Synchrotron x-ray exploration of growth and structure in 2D dichalcogenides

Roberto Sant

Communauté
UNIVERSITÉ Grenoble Alpes

THÈSE

Pour obtenir le grade de

DOCTEUR DE LA COMMUNAUTE UNIVERSITE GRENOBLE ALPES

Spécialité : **Physique de la matière condensée et du rayonnement**

Présentée par

Roberto SANT

Thèse dirigée par **Johann CORAUX,** chargé de recherche au **CNRS (Institut Néel)**, et codirigée par **Gilles RENAUD,** ingénieur-chercheur au **CEA-Grenoble (IRIG/DEPHY/MEM)**,

préparée au sein de l'**Institut Néel (CNRS) à Grenoble** dans **l'École Doctorale de Physique de Grenoble**

Exploration par rayonnement synchrotron X de la croissance et de la structure de dichalcogénures 2D

Thèse soutenue publiquement le **17 décembre 2019**, devant le jury composé de :

M. Benjamin Grévin
Directeur de recherche, CNRS - Grenoble, President
M. Carsten Busse
Professeur, Universität Siegen, Rapporteur
M. Fréderic Leroy
Professeur, Université d'Aix-Marseille et CINAM, Rapporteur
M. Yves Garreau
Professeur, Université de Paris, Examinateur
Mme. Rosanna Larciprete
Docteur de recherche, CNR / ISC - Rome, Examinateur

A Laura ed Enrico.
Stavate anche voi per terminare la vostra tesi.
Sappiate che questa tesi è anche un po' vostra,
perché vivete ancora nella memoria di chi l'ha scritta.

Aknowledgements

My highest gratitude goes to my thesis directors, Johann Coraux and Gilles Renaud, for having guided me along these three years. My growth as young scientist implied a big effort and a lot of time. They had the patience to wait for me, being the first to believe in my skills. Always positive and enthusiastic, they reinforced my passion for this job. I had never felt alone with them, but actually part of a team and with a major role.

I feel honoured to have worked with Athanasios Dimoulas and his team from the NCSRD laboratories in Athens. A far-sighted researcher, he opened my horizons towards a multiplicity of interesting subjects and he contributed strongly to enrich my background.

Special thanks go also to Matthieu Jamet, group leader at CEA/IRIG/SPINTEC, and his group, especially to Alain Marty. With them I moved the very first steps and I created a close-knit collaboration and friendship that is still going on.

I am very thankful to Pierre Rodiere, researcher at Institut Néel, for the selfless interest toward my work and the useful discussions we had together about charge density waves. He contributed to make me more autonomous as a scientist.

I thank Alexej Bosak, responsible for ID28 (ESRF) for the trust that he put in me by ceding a beamtime for my personal research initiatives. As the same I thank also Philip Hoffman and Marco Bianchi, from Aarhus University, for welcoming me at ASTRID2 and giving me the opportunity of carrying out experiments in their beamline.

I thank also the referees of this thesis together with the jury president and all the other members. Their critical analysis aimed at improving this work represented for me an important step. I can say I had something new to learn also the day of my defense.

All this work would have been not possible without the technical assistance of Olivier Geaymond and Olivier Ulrich at BM32 and Valerie Guisset and Philippe David at Institut Néel. Efficient people, always ready to lend an hand, they made nice also the hardest moments in the lab.

Among the many people I worked with during these three intense years, a special mention goes to my colleagues and friends Simone Lisi and Tao Zhou, for the precious time, the words and the work they shared with me. Although very young, I could learn a lot from them. Another special thank you goes to Arianna, dear friend of mine inside and outside ESRF. Without her, I could not have done one of the experiments I am most proud of.

I would like to thank all the members of the Hybrid group at Institut Néel, the per-

manent and the non-permanent, the old and the newest. I spent really great time with them and I considered them my little family in Grenoble. I thank also all the members of French CRG at ESRF for their friendship and the attention they had towards me.

I thanks all my friends here in Grenoble, with whom I spent three awesome years. If this PhD thesis was a great experience, it is also because I felt good in this city, inside and outside the lab.

Last but least, a huge thank you go to my parents, who suffered for not having me at home but always encouraged me to go on. To them and to all my friends in Italy my apologies if sometimes I made them miss me. I hope I can say I deserved this experience.

Abstract

Two-dimensional transition metal dichalcogenides (TMDCs) are promising materials for a variety of applications, especially in optoelectronics. However, the lack of understanding of their epitaxy, *i.e.* growth mechanism, microscopic structure, nature of the 2D layer-substrate interaction, etc, is still a crucial issue to address. In this PhD thesis we explored a series of epitaxial growths of monolayer and thin film TMDCs grown by molecular beam epitaxy (MBE) on a variety of substrates. We studied their atomic structures and we attempted the modifications of some of them with various *in situ* methods. Several systems and processes have been investigated: (*i*) transition metal ditellurides, $ZrTe_2$, $MoTe_2$ and $TiTe_2$ on InAs(111) substrate, (*ii*) the intercalation of alkali metal species between single layer MoS_2 and its Au(111) substrate, (*iii*) the growth and the thermal treatments in H_2S atmosphere of monolayer $PtSe_2$ on Pt(111). Our work relies on both phenomenological and quantitative methods based on surface X-ray diffraction, often complemented by parallel analysis performed with other probes, *e.g.* STM, TEM, XPS, ARPES. Most notably, we found that: (*i*) a metastable orthorhombic phase and a charge density wave phase can be stabilized at room temperature in $MoTe_2$ and $TiTe_2$ owing to the epitaxial strain in the materials; (*ii*) the intercalation of Cs atoms under MoS_2 induces structural and electronic decoupling of the 2D MoS_2 layer from its Au(111) substrate; (*iii*) the sulfurization of $PtSe_2$ promotes the Se-by-S substitution in one (or both) of its two chalcogen layers, leading either to the full conversion of the selenide into a sulfide or even to an ordered *Janus* alloy.

Resumé

Les dichalcogenures de métaux de transition bidimensionnels (2D) suscitent un grand interêt pour des applications variées, principalement en optoelectronique. Toutefois, la faible compréhension des mécanismes liés à leur épitaxie, de leur microstructure et de la nature de leur interaction avec le substrat représentent encore des problèmes ouverts. Nous avons exploré un certain nombre de croissances épitaxiales des dichalcogenures 2D préparés par épitaxie à jets moleculaires sur des substrats différents. Nous en avons examiné la structure atomique et essayé d'en modifier certains *in situ*. Plusieurs systèmes et processus ont été étudiés: (*i*) des tellurures de métaux de transition, $ZrTe_2$, $MoTe_2$ et $TiTe_2$, épitaxiés sur un substrat de InAs(111), (*ii*) l'intercalation d'espèces atomique alcalines entre une monocouche de MoS_2 et son substrat d'Au(111), (*iii*) la croissance et le traitement thermique sous atmosphère de H_2S d'une monocouche de $PtSe_2$ sur Pt(111). Notre travail s'appuie sur des approches à la fois phénoménologiques et quantitatives de diffraction de rayons X de surface, souvent complétées par ses analyses effectuées à l'aide d'autres techniques (STM, TEM, XPS et ARPES). Les principaux resultats sont que: (*i*) une phase orthorhombique et une onde de densité de charge sont stabilisées à température ambiante dans les couches de $MoTe_2$ et $TiTe_2$ par un effet de déformation induite par l'épitaxie; (*ii*) l'intercalation de cesium (Cs) au-dessous du MoS_2 induit un découplage structurel mais aussi électronique de la monocouche de son substrat; (*iii*) la sulfurisation de $PtSe_2$ à chaud en conditions controlées permet de substituer des atomes de Se par des atomes de S dans la couche supérieure du dichalcogenure, formant ainsi un alliage ordonné de SPtSe, structure de type *Janus*.

Introduction

Two-dimensional transition metal dichalcogenides (TMDCs) host unique properties related to their low-dimensionality and they are considered for a variety of applications, especially in optoelectronics. The main advantages of TMDCs compared to graphene consist in their sizable bandgap and in the tunability of their properties with the thickness, *i.e.* the number of layers. In the last ten years, the advent of sophisticated experimental probes in combination with new recent theoretical studies have paved the way to an important number of new fundamental domains of investigation, for instance related to topologically non trivial electronic band structures and the physics of excitons, also linked to the peculiar electronic band structure. These trends are also promising in view of new technological applications and devices based on 2D TMDCs. A strong hurdle to industrial-scale applications is the fact that the 2D TMDCs which are objects nowadays of the majority of publications are mostly prepared by top-down methods, *i.e.* in-solution or dry exfoliation. These methods allow flakes of good crystal quality, but they are not compatible with industrial fabrication, which requires instead epitaxial processes. In this respect, the bottom-up growth of high-quality crystalline epitaxial TMDCs over large surfaces is an attractive alternative, yet it is still a major challenge. It follows that the moderate structural quality of the 2D TMDCs achievable up to date hinders the access to the intrinsic properties of the materials and limits the device performances. Moreover, solid state bottom-up methods, such as physical vapor deposition, are often performed on metallic substrates requiring afterwards a transfer step onto other semiconducting technological substrates. On another note, achieving a good control over chemical functionalization of 2D TMDCs is a crucial challenge to address in order to control/modify with always better efficiency the physical properties of these materials. To have a technological repercussion in this sense, research on new fundamental physical phenomena should be accompanied by adequate efforts in synthesis and engineering, also at fundamental level.

Within this PhD thesis we tried to go down this path: we performed epitaxial growths by molecular beam epitaxy (MBE) under ultra-high vacuum (UHV) of different types of TMDCs on a variety of substrates (metallic and semiconducting), and we subsequently attempted to modify the materials with various *in situ* methods. (*i*) The growth of little studied ditellurides such as $ZrTe_2$ and $TiTe_2$ on unconventional - for TMDCs - semiconducting substrates, (*ii*) the intercalation of atomic guest species between the epitaxial 2D overlayer and its metallic substrate with the prospect to enable phase transitions and elec-

tronic doping, (*iii*) the thermal treatments in suitable precursor gas atmosphere in view of the anionic substitution in one (or both) of the chalcogen layers by other chalcogen species, represent three main challenging experiments with non-obvious outcome that we carried out along these three years, and they constitute the three main thematic threads of the experimental part of this manuscript.

Materials properties are inevitably affected by the surroundings. This is particularly true for two-dimensional materials, where a distinction between bulk and interface is meaningless in practice. The so-called van der Waals (vdW) epitaxy experienced by TMDC materials grown on substrates is cited as a relevant advantage of TMDCs compared to more traditional non-layered semiconductors. It leads to systems with very sharp interfaces and weak bondings with the substrate. It is known however that in some systems, TMDCs are perturbed by the presence of the substrate, *e.g.* orbital hybridization. We wondered if such perturbations, when active, are accompanied by visible structural effects such as strain and/or in-plane deformation. This question comes every now and then in the text and we hope that these works could help addressing this issue more rigorously in the future. To this purpose, we tried to clarify the criteria that define vdW epitaxy and we discussed, within the characterization capabilities of our probes, the nature of the interface interaction between 2D layers and substrates in our systems, which *a priori* might not be exclusively vdW-like, but comprises a certain covalent character.

A large part of our work has relied on the unique features of the INS2 instrument installed at the BM32 CRG/IF beamline at ESRF, which is a diffractometer optimized for grazing incidence with synchrotron light, coupled with a UHV chamber equipped with all the basic tools required for nanostructure growth and *in situ* diagnostics. Grazing incidence and surface x-ray diffraction are in fact the main techniques exploited along this PhD thesis. The scope of our investigations are the processes, the 2D systems and the fundamental questions that each time will be introduced to the reader at the beginning of the experimental chapters. In fact, we made use of a wide range of experimental probes bringing complementary characterizations of our systems, which were in some cases decisive to answer the starting questions. Measurements other than X-ray diffraction/scattering have been performed in other external setups - sometimes other synchrotrons - either with the goal of enriching our study with information non achievable with X-rays, *e.g.* STM, XPS or cross-sectional-TEM, or to correlate the structural observations with the related material electronic properties, as we did for instance with ARPES. All the measurements performed during this thesis and the respective authors are reported in the appendix.

This manuscript is organized in two main parts. Part I is a transversal introduction to the topics discussed in the chapters afterwards. It includes: a detailed description of the TMDC structures and their polymorphic phases (*Chapter 1*); a discussion of the main features of vdW epitaxy, followed by a summary of the state-of-the-art of the methods used nowadays to synthesize 2D TMDC epitaxial layers (*Chapter 2*); an overview of the physical and chemical routes used to engineer TMDCs and modify some of their physical

properties (*Chapter 3*). A simplified introduction to synchrotron light and surface x-ray diffraction (SXRD) has also been inserted with the purpose to give the readers who are less familiar an easy access to the main concepts of the discipline (*Chapter 4*). All these chapters are not meant to be comprehensive from the theoretical point of view - several textbooks exist for that - but are thought to give the reader the basic ideas to address the second part more "comfortably".

Part II is the experimental part. Therein, the description and the results of the experiments carried out along these three years are reported. The first chapter (*Chapter 5*) reports the preparation and the structural characterization of three ditelluride materials, *i.e.* $ZrTe_2$, $MoTe_2$ and $TiTe_2$, grown on InAs(111), with particular attention to the strain effects induced by the substrate. In the case of $TiTe_2$ a charge density wave phase stable at room temperature was found, which is discussed with a large overview encompassing several physical aspects of the phenomenon. This work has been developed within the strong collaboration of Dr. Dimoulas' group in Athens - responsible for the growth, the STM and ARPES characterization and of the theoretical calculations - and thanks to the contribution of Dr. C. Alvarez and Dr. H. Okuno from the CEA-INAC laboratories in Grenoble, who provided the cross-sectional-STEM images.

Chapter 6 is devoted to the study of the *in situ* intercalation of single layer MoS_2 grown on Au(111) by alkali metal species. Intercalation is a well studied and known process in bulk TMDC, but it has been never attempted with 2D MoS_2 and almost never with monolayer epitaxial TMDCs in general. In this work we wanted not only to demonstrate the feasibility of the process itself, but also to discuss how this method can open a viable route for controlling and modifying charge density inside 2D TMDCs, and how it can solve the issue of decoupling the 2D layer from the interaction with its substrate. This work has been possible thanks to the close collaboration with the colleagues of the Hybrid team at the Institut Néel and it combines reciprocal space (diffraction and reflectivity) and real space (STM) characterizations. The chapter is completed by a photoemission study performed at the GSM-3 beamline at ASTRID2 synchrotron in Aarhus (Denmark) with the collaboration of the group led by P. Hoffmann.

The last chapter (*Chapter 7*) is devoted to the growth of 2D $PtSe_2$ prepared by selenization of the Pt(111) surface. It is divided in two sub-parts: the first describes the 2D layer preparation, the fine characterization of its outstanding diffraction pattern and the quantitative analysis of the atomic displacements within the surface layers; the second is a description of the sulfurization process through which we attempted to convert $PtSe_2$ in an asymmetric configuration called "Janus", characterized by the complete substitution of the top chalcogen selenium layer with sulfur atoms. This study is still a work in progress, based on results collected both by *operando* experiments performed in our beamline and at CEA-IRIG labs - in collaboration with the group of M. Jamet - and by chemical analysis, performed by M. Gay and O. Renault at the CEA-LETI laboratories in Grenoble.

Contents

Part I

Chapter 1

Structure and properties of 2D transition metal dichalcogenides

1.1 The new frontier of 2D materials

Two-dimensional (2D) materials are a new class of crystalline materials consisting of a single or few layers of atoms, thus having an ultimately small - even irreducible, in the case of single layers - thickness of few nanometers or ångströms. Most belong to the class of layered *van der Waals* (vdW) materials: each layer consists of covalently bonded atoms with no dangling bonds at the layer surface. One can easily overcome the weak interlayer vdW interaction by *exfoliating* them into single stable layer units via mechanical or chemical methods[1; 2]. Moreover, the opposite process is also feasible: single layer 2D crystals even of different nature can be piled up in artificial vertical heterostructures purposely designed to achieve on-demand properties[3].

The most famous example is *graphene*, a single layer of sp^2 hybridized carbon atoms arranged in a honeycomb lattice. Each carbon atom forms three covalent σ-bonds in the plane with three other nearest neighbors at a characteristic angle of 120°. A remaining non-hybridized p_z orbital is involved in a π-bonding that contributes to the formation of double bonds. In graphene valence orbitals are fully occupied and no dangling bonds are left on the layer surface. If, ideally, a vertical stack of graphene sheets is made, each layer can interact with the adjacent ones only by means of weak vdW forces. A graphene layer stacking actually exists in nature: graphite. As everyone has experienced, graphite can be readily cleaved mechanically and in fact exfoliation represents an effective method to isolate graphene sheets.

However, it is not the extreme down-scaling alone that makes 2D materials so noteworthy. When dimensions are reduced to the nanoscale, the size affects how materials behave. In 2D materials the third dimension is effectively (sub)-nano-sized. This boosts deeply modifies the electronic, optical and mechanical properties. Hence, when electrons are confined in two-dimensional materials novel quantum transport phenomena can be observed. For instance, in graphene the peculiar linear dispersion and topology of the

band structure give rise to the massless Dirac fermion behaviour of the charge carriers[4] and to a distinctive half-integer (anomalous) quantum Hall effect.

Though several theoretical studies on "single layer graphite" - as graphene was called back then - date back to the Forties[5], it is the first isolation of graphene sheets operated in 2004 by A. Geim and K. Novoselov[6] that inaugurates the "2D materials age". The two scientists were awarded the Nobel Prize in 2010 for their achievements. The success of graphene generated great enthusiasm in the scientific community and soon after the acquired theoretical and technological know-how has been transferred to the search for new 2D materials. Soon material scientists attempted the exfoliation of a wide range of layered materials, as hexagonal boron-nitride (h-BN), transition metal dichalcogenides (TMDCs) and complex oxides[7], succeeding to isolate and manipulate single layers and subsequently to directly grow them by bottom-up methods. Fifteen years later hundreds of other layered materials have been identified and/or predicted[8] and still nowadays a lot of efforts are being made in order to synthesize layered species not occurring in nature that could however be grown and stabilized in 2D form, like silicene[9] and the family of X-enes.

Hereafter and in the next chapters we dwell on the description of the transition metal dichalcogenides (TMDCs), since this material class represents the case study of this thesis. TMDCs have been known since very long time and they have been at the heart of hundreds of publications since the Sixties[10; 11]. As we just said, the isolation and study of graphene triggered new interest for their 2D counterparts, as witnessed by the explosion of the number of publications since 2010[12]. Such interest is justified also by the variety of properties TMDCs show in combination with their tunability. If one major drawback in graphene is the lack of a bandgap, in TMDCs bandgap is sizable and it can be engineered by varying the number of layers, as demonstrated in MoS_2, whose indirect bandgap becomes direct when prepared as single layer, with strongly enhanced light emission[13]. The TMDC family includes nowadays about 60 different members[12] that, despite their similar structures, cover a very wide spectrum of properties and phases. We will give some more details on the fundamental properties discovered in TMDCs at the end of this chapter. Before that, it is necessary to spend few words to examine their chemistry and structure.

1.2 Atomic structure, polymorphs and polytypes in TMDCs

In this section, the main polymorphic phases and polytypes of TMDCs will be described. The topic is supported by many studies carried out since the Seventies and very detailed information concerning a large group of TMDC structures can be found in the work of Wilson and Yoffe[10]. For the sake of completeness, we will describe the TMDCs structures having in mind bulk TMDC compounds. The validity of the statements contained in this section can be extended to the 2D case, except when explicitly indicated.

Layered TMDCs have generic formula MX_2 where M is a transition metal from the IV to VII or X group of the periodic table and X is a chalcogen, *i.e.* a sulfur, selenium or tellurium atom. Individual layer units are actually triple layers consisting of one layer of hexagonally packed metal atoms sandwiched between two other layers of hexagonally packed chalcogen atoms, as in figure 1.1. The M-M bonds length generally varies between 3Å and 4Å depending mainly on the atomic size, while the thickness of the layer is typically about 6-7Å[12]. Most of the chemistry and physics of TMDCs is determined by the non-bonding *d*-orbitals of the transition metal atoms and by the lone pair electrons inside chalcogen atoms. While the progressive filling of the *d*-orbitals determines the variety of electronic properties that can be found in TMDCs - essentially the insulating, semiconducting or metallic character of TMDCs - the lone-pair electrons located on the sp^3 hybridized orbitals of the chalcogen atoms are not involved in bonding, but terminate the layer surface. The lack of dangling bonds makes the TMDCs surfaces very stable and accounts for the weak vdW interlayer interactions between TMDC layers.

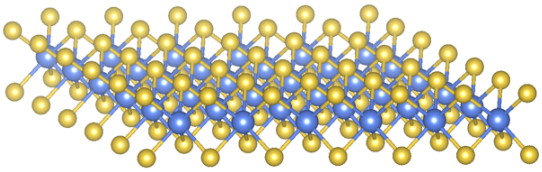

Figure 1.1: Prospective three-dimensional view of a typical monolayer TMDC with formula MX_2, with metal atoms (M) in blue and chalcogen atoms (X) in yellow.

Typical TMDC polymorphs can be distinguished on the basis of the metal center *coordination* inside the unit cell, as well as the layer *stacking* order. The unit cell is defined with the *c* axis perpendicular to the TMDC layer, whereas the *a* and *b* axes lie in the TMDC plane along the minimal metal-metal distance, as in figures 1.2. Within the layer, each metal center is surrounded by six nearest neighbour chalcogen atoms according to either trigonal prismatic (D_{3h}) or octahedral (O_h) coordination (figure 1.2). Layers of the same type can be stacked in a variety of different ways, whose most common ones are the 2H and 1T polytypes. In the labelling, the letters refer to the lattice type (hexagonal or trigonal), whereas the digits specify the number of layers contained inside the unit cell and it descends from the characteristic stacking. In figures 1.3 it is shown that the 2H polytype has two layers inside the unit cell where the stacking sequence is AbA BaB (the capital and lower case letters refer to chalcogens and metal atoms respectively), whereas the 1T polytype contains only one layer per unit cell, each one having AbA stacking sequence. Another explanatory example, though less frequently encountered, is the 3R polytype, typically found in $NbSe_2$ and rather common among non-stoichiometric TMDC compounds[14; 15]. In this phase, the metal center is characterized by a trigonal prismatic coordination (D_{3h}), but the periodical stacking is instead in the form of a rhombohedral

lattice where three layers are necessary to describe the unit cell and the stacking sequence is AbA CaC BcB (the third on the right in figure 1.3). Many different TMDC stacking polytypes are known, which exist in nature. The 2H polytype, for instance, exist under a rich set of sub-varieties: the one described above and reported in figure 1.3 with typical AbA BaB stacking sequence is only the most common case occurring for instance in group VI TMDCs (MoS_2, $MoSe_2$, WS_2 WSe_2). Other varieties also exist, denoted as $2H_a$, $2H_b$, etc., to mention a few, which present slightly different stacking sequences. For a complete list of TMDC polytypes we refer to Ref.[10].

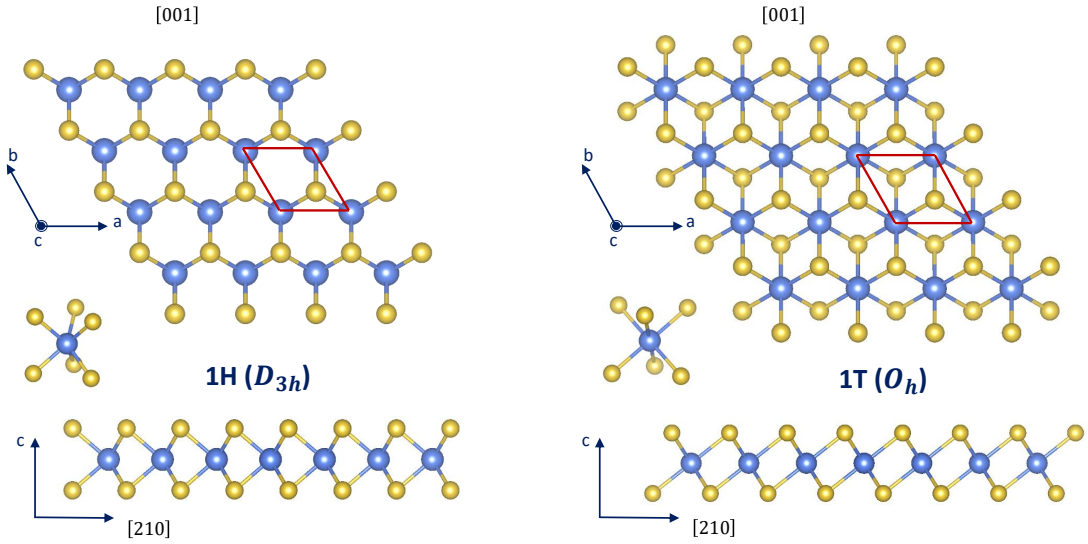

Figure 1.2: From the top to the bottom: in plane projection, prospective view and side projection of trigonal prismatic (left) and octahedral (right) TMDC structures. Typical corresponding polytypes are the 2H and the 1T respectively. The surface projected unit cells are drawn in red and contain three atoms, 1 metal and 2 chalcogen; for the 2H polytype, the two chalcogen atoms are superimposed.

For monolayer TMDCs, classification is much simpler, since the "stacking order degree of freedom" is dropped and eventually it is determined exclusively by the coordination of the metal center. Conventionally, they are known as 1H (essentially the 2H polytype where digit 2 is changed to 1 because the layer is unique), 1T and 1T', *i.e.* a distorted 1T coordination.

Sometimes the same TMDC can be found in multiple polytype structures: for example the same TMDCs can coexist in different phases at the same temperature and pressure, owing to the history of their formation. Furthermore, phase transitions can also occur, which transform for instance the 1H phase into 1T or 1T' under the effect of specific external stimuli[16]. All these topics will be the addressed along the next chapters of this manuscript.

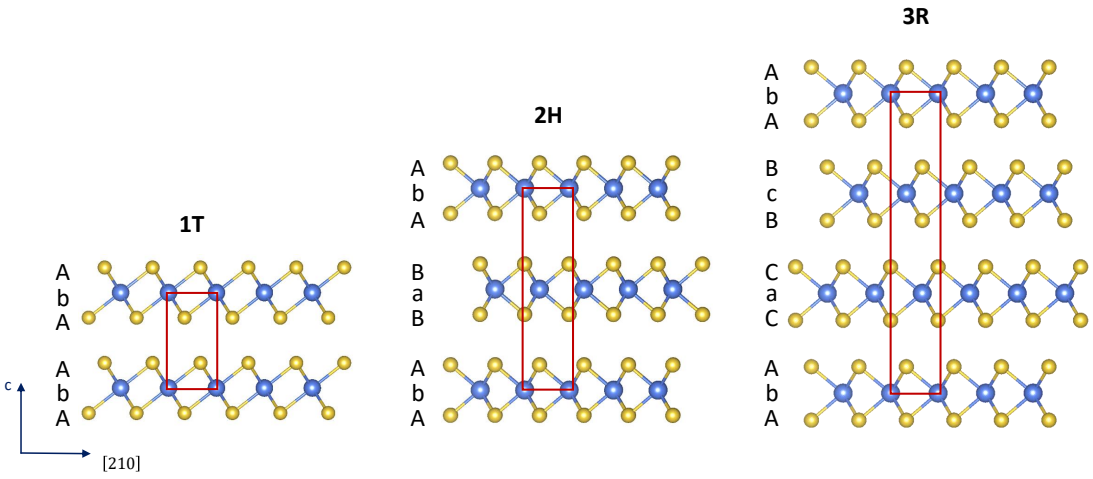

Figure 1.3: From left to right 1T (trigonal symmetry, one layer per unit cell, octahedral coordination), 2H (hexagonal symmetry, 2 layers per unit cell, trigonal prismatic coordination) and 3R (rhomboedral symmetry, 3 layers per unit cell, trigonl prismatic coordination) TMDC polytypes projected along the $[2\bar{1}\bar{1}0]$ direction. Unit cell projection is in red.

1.3 Distorted structures

1.3.1 1T' phases

Some TMDCs crystallize in a lower symmetry structure known as 1T'. This polymorph is a periodic distortion of the more common 1T phase characterized by a collective displacement of the metal atoms out of their equilibrium sites inside the octahedra along the high symmetry direction in the layer plane, as reported in figure 1.4. Blue metal atom rows in the 1T structure slide along the b direction toward the adjacent parallel row, forming zig-zag chains extending in the direction of a. In the side view at the bottom of figure 1.4, the pairing of nearest neighbour metal atoms along b is evident. The pairing doubles the typical hexagonal surface unit cell (in blue in figure 1.4) of the non-distorted 1T structure and the use of a rectangular primitive unit cell becomes more convenient to represent the 1T' lattice. Such a distortion is found in some ditellurides, such as WTe_2 and $MoTe_2$[17; 18], but also in common 2H TMDCs, as bulk group VI sulphides/selenides, when intercalated by alkali metals[19]. In order to accommodate the distortion, chalcogen atoms shift both horizontally and vertically. It results that 1T' layers are rather buckled with some metal-chalcogen bonds elongated and other shrunk.

1T' phase stabilization in dichalcogenides has been explained in terms of electronic *Peierls* or *Jahn-Teller* instabilities[12; 20], similarly to microscopic mechanisms adopted to describe distortions in charge density wave phases (discussed in the next section). According to these models, whether a distortion occurs or not in ideal 1T structures is established by the competition between two driving forces, *i.e.* an energy gain in the electronic band structure (related to a gap opening or a band lowering in the dispersion diagram) and the elastic energy cost accumulated with the deformation. When the ener-

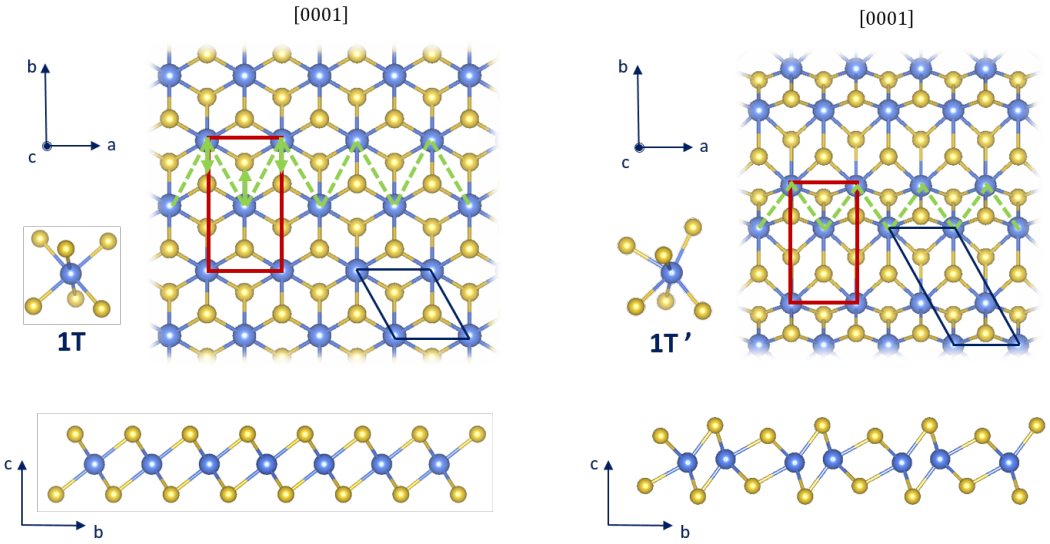

Figure 1.4: In plane projection, prospective view and side projection of the single layer structure of 1T octahedral (left) and 1T' distorted octahedral (right) TMDC structures. The distortion is due to the metal displacement along *b* (green arrows) and by the consequent pairing of the metal rows in zig-zag chains (dashed green lines) running along *a*. In the 1T' the hexagonal (blue) unit cell has double sized side along one direction compared to the 1T structure. A rectangular (dark red) unit cell is typically preferred instead of the hexagonal one

getic balance is favorable, metal atoms tend to form pairs or clusters with their neighbours, while metal-chalcogen bonds are shortened or lengthened, similarly to what happens in transition metal molecular complexes owing to Jahn-Teller distortions.

In figure 1.5 the Jahn-Teller mechanism is illustrated for the simple case of a tetragonal distortion in a molecular transition metal complex MX_6 having octahedral (O_h) coordination. Initially, according to crystal field theory, the metal atom has two sets of degenerate *d* orbitals at the ground state, notably three t_{2g} levels at lower energy and two e_g levels at higher energy (figure 1.5, left). Any stretching or compression of the metal-ligand bonds along the fourfold axis introduces a tetragonal distortion in the system and lifts the pristine degeneracy by splitting the t_{2g} and the e_g levels in sublevels, with concomitant electron rearrangement. It is straightforward that an odd number of electrons occupying the e_g orbitals constitutes a source of instability for the octahedral system that evolves towards a more energetically favorable tetragonal structure (figure 1.5, right). Intuitively, the total electron counting is thus crucial to determine the distortion, which appears more likely in the octahedral complexes where the transition metal has d^4, d^7 or d^8 electronic configuration. Although the Jahn-Teller effect is characteristic of molecules, there seems to be an intimate analogy with the structural instabilities found in certain crystalline solids[21]. This concerns in particular distorted structures showing intralayer metal atom pairing/clustering and large metal-chalcogen bond deformations, a scenario not very far from that of 1T' polymorphs. In this framework, "band type" Jahn-Teller microscopic theories have been already proposed to account for instabilities in crystalline solids[22]. However, so far it mostly concerns charge density waves.

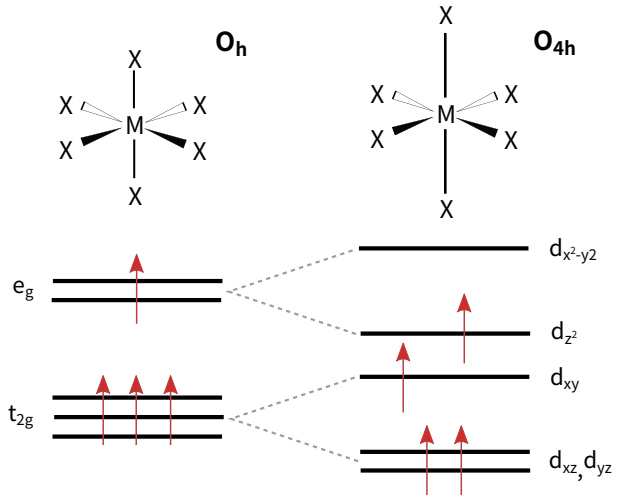

Figure 1.5: tetragonal distortion (elongation along the fourfold axis) of an octahedral molecular complex due to Jahn-Teller effect.

1.3.2 Charge density waves in TMDCs

Another typical example of distortion occurring in TMDCs are charge density waves (CDWs). It is now more than forty years that charge density waves have been observed the first time just in TMDCs. Although a huge number of cases has been described in the literature for bulk systems and new ones are being published about 2D materials, we are still far from a full understanding of the CDW formation. Several scenarios have been considered and whether one or the other prevails in the case of a specific TMDC is sometimes still a matter of debates. Peierls instability, Kohn anomaly, Fermi surface nesting, Jahn-Teller effect have been invoked, but a fully comprehensive microscopic theory has not emerged yet. We will not treat deeply the CDW theory in this manuscript - a detailed dissertation on CDWs in TMDCs can be found in the review paper written by Rossnagel[20] - but we will limit to a short description based on the most fundamental results of the Peierls' theory, useful to introduce the necessary basic elements for the discussion of the experimental results reported later in this work (chapter 5).

Predicted the first time by R. Periers in the 1930s, CDWs are a periodic wavelike modulation of the electron density in a crystal. Mathematically, Rossnagel[20] describes the CDWs as:

$$\rho(\vec{r}) = \rho_0(\vec{r})[1 + \rho_1 cos(\vec{q_0}\vec{r} + \phi)] \tag{1.1}$$

where ρ_0 is the unperturbed density in the crystal while the second term in the bracket represents a standing wave with wavelength $\lambda_0 = 2\pi/q_0$. $\vec{q_0}$ and ϕ are respectively the characteristic wavevector and phase of the CDW. The CDW acts as an additional potential causing the lattice ions to move to a new equilibrium position, the distortion along one direction being:

$$u_n = u_0 sin(n|\vec{q_0}|a + \phi) \tag{1.2}$$

where a is the lattice constant. Conversely, any periodic distortion of the lattice necessarily redistributes the electron density with the same periodicity. Hence, whether the periodic lattice distortion (PLD) is the source or the cause of the CDW is an open (almost philosophical) question. The CDW and the PLD thus can simply be seen as two sides (electronic and structural) of the same coin and they often come together.

In the Peierls model any CDW/PLD occurring in a linear chain of atoms with regular spacing a alters the periodicity in the system and opens a gap at the Fermi surface, thereby lowering the energy of the occupied electron states. A simple example is reported in figure 1.6. By pairing up the atoms, the periodicity in the chain doubles (figure 1.6a), while it is divided by two in reciprocal space. Within a simple tight binding model and assuming weak electron-phonon interaction, a gap opens halfway from the Brillouin zone edges (figure 1.6b). All the occupied states are below the Fermi level, so the overall electron energy is lower than in the absence of a distortion. If this net energy gain at least compensates the elastic energy cost of the distortion, the CDW is self-sustaining and the crystal undergoes a phase transition to a structure with a larger unit cell.

Fundamental ingredient in Peierl's theory of CDWs is the electron-phonon interaction, which affects both electron and phonon dispersions. Peierls deduced that in correspondence of the CDW wavevector $\vec{q_0}$ the electronic susceptibility diverges while the phonon frequencies are strongly "softened" - phenomenon which is known as *Kohn anomaly* (figure 1.6c). Susceptibility divergence and complete phonon softening ($\omega_{q_0}^2 = 0$) are usually interpreted as signals of structural instability and phase transition towards a CDW phase where the lattice distortion is completely frozen. Such a distortion shows up in a diffraction pattern as additional reflections at fractional positions.

The Peierls' model leads sometimes to inconsistencies in describing CDWs in layered compounds as TMDCs. Main weaknesses are connected to the various approximations made, in particular the weak electron-phonon interaction and the linear atomic chain. When electron-phonon coupling is instead strong and dimensionality increases to two, as is always the case of TMDCs, Peierls' formulas cannot be applied anymore. This topic is however beyond the scope of this manuscript.

Rossnagel points out that, compared to weak coupling, strong coupling CDWs are in general characterized by larger atomic displacements, often involving metal atom clustering, as well as shortening and lengthening of the other metal-chalcogen bonds[20]. Qualitatively, an analogy can be established between CDW effects in low-dimensional solids and Jahn-Teller distortion in molecules[21]. A microscopic CDW model based on "band type" Jahn-Teller effect was proposed firstly by Motizuki[22]. Experimental works supporting this theory came few years later when Whangbo and Canadell tried to account for the Se p-band shift to lower binding energy and other hybridization features observed in the electronic band structure of $TiSe_2$ after the transition to a CDW phase[23]. They demonstrated that the changes in band diagram are originated from a stronger Ti-Se hybridization and that, as a consequence, the CDW was intimately correlated to the Ti-Se bond shortening[21; 24] (figure 1.7).

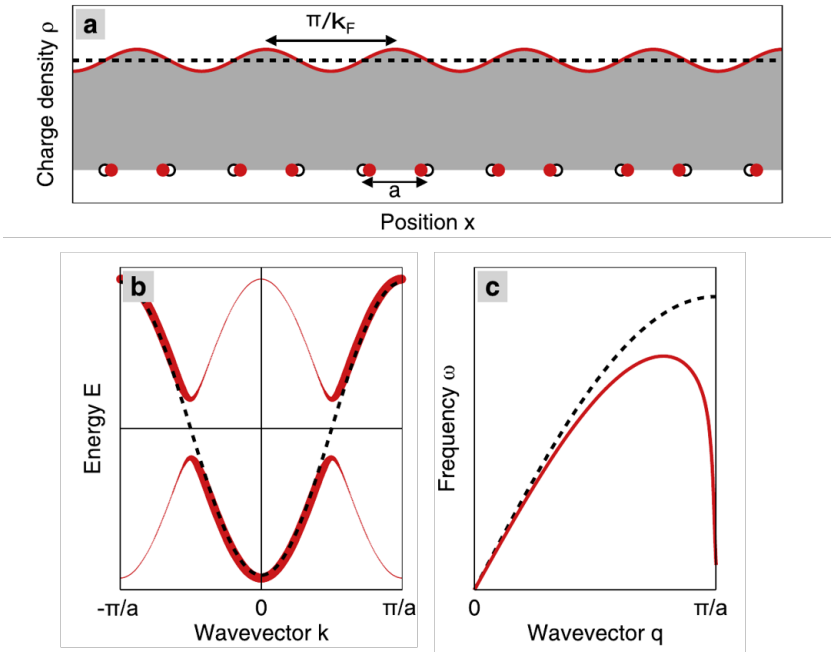

Figure 1.6: The three basic ingredients of a CDW according to the Peierls' model: PLD, energy gap below Peierls transition temperature, Kohn anomaly occurring at CDW vector. (a) schematic view of CDW/PLD for a 1D lattice whose atoms are equispaced by a regular distance a: dashed line and empty circles are the electron density and the ion lattice in the absence of the CDW, whereas the red curve and red filled circles represent the density wave modulation and the atomic position upon the distortion where the lattice unit cell is equal to $2a$; (b) electronic band dispersion above the Peierls' transition temperature T_0 (dashed black line) and the CDW phase band dispersion below T_0 (solid red line); due to the distortion the Brillouin zone reduces to one half and bandgaps open at the edges; (c) acoustic phonon dispersion above (dashed black line) and below (solid red line) T_0. The images are taken from Ref[20]

Several examples of CDW phases have been found among bulk TMDCs. They show that a wide variety of superstructures, displacement magnitude and temperature transitions exist even inside the same family of materials. 1T-TaS_2 for instance shows a series of transition between different kinds of CDWs phases, from incommensurate to nearly commensurate and finally to perfectly commensurate superstructures in the temperature range from 560K down to 183K. In the commensurate phase Ta atoms rearrange by group of 13 in a peculiar David star-like reconstruction rotated by 13.9° with respect to the non-distorted lattice[25]. In 1T-$TiSe_2$[26] and in 2H $NbSe_2$[27] the CDW phases are instead commensurate with the pristine lattice and develop a (2×2) and a (3×3) superstructures respectively. Moreover, in the case of 1T-$TiSe_2$, the PLD shows a 3D long range ordering - hence, the reconstruction would be better defined as a $(2 \times 2 \times 2)$ - due to the peculiar ordered layer stacking. In general, PLDs in TMDCs have wide amplitudes, sometimes with in-plane atomic displacement as large as 0.24Å, as for Ta in TaS_2[28], in agreement with what is expected from a strong electron-phonon interaction. Remarkably, the known CDWs in dichalcogenides show relatively high transition Peierls' temperatures, well above 77K, or even above room temperature[26]. External factors such as strain and pressure[29] can have influence on the CDW transition temperature.

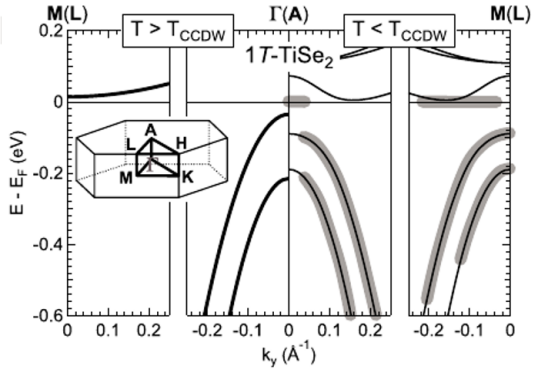

Figure 1.7: Schematic of $TiSe_2$ electronic band structure reproducing the ARPES results of Kidd et al.[23]. The spectrum on the left corresponds to the normal phase, while the one of the right corresponds to a (2×2) CDW phase. Remarkably in the CDW phase the VB maximum at Γ is shifted to lower energy and the CB minimum near M has changed profile. Reproduced from Ref.[20].

1.4 A wide spectrum of properties

The range of properties and consequently of potential applications of 2D TMDCs is wide. Although underperforming compared to graphene in several respects, carrier mobility and mechanical strength to name a few, TMDCs possess some fundamental properties graphene does not have, such as a tunable band gap and a large spin-orbit coupling. This allowed 2D TMDCs to become a cutting edge topic in materials science in few years after graphene discovery.

Moreover, despite their similar structures, TMDCs constitute a large family and the variety of transition metal elements that can form stable MX_2 type dichalcogenides cover a wide range of properties. Concerning the electronic structure, for instance, among TMDCs we find insulators (as bulk HfS_2), semiconductors (such as MoS_2 and WSe_2), semimetals (*e.g.* $TiSe_2$) and metals (*e.g.* NbS_2). This diversity is linked to the coordination environment of the transition metals and the progressive filling of their non-bonding *d*-bands[1]. A pictorial view of the density of states in the surrounding of the Fermi level is shown in figure 1.8 for different transition metal groups in the periodic table: trivially, group 6 TMDCs having fully occupied *d*-orbitals are semiconducting, while group 5 TMDCs with partially occupied *d*-states are metallic. Amazingly, by introducing additional electronic charge in the material and thus progressively filling the d-bands, phase transitions can be induced: it is well known in fact that 2H semiconducting MoS_2 transforms into the 1T metallic polymorph when alkali metal donor species intercalates inside its vdW gap[1]. The reverse scenario was observed instead by intercalating Li in TaS_2 [30]. Band gap engineering and phase transition via charge transfer will be addressed more in detail in chapter 3.

Furthermore, the number of layers constituting the 2D materials can drastically change the electronic band dispersion with also dramatic effect on the bandgap nature. For instance, it is well known that bulk group VI TMDCs (MoS_2, $MoSe_2$, WS_2 and WSe_2) are indirect band-gap semiconductors, while single layers have direct band gap and intense

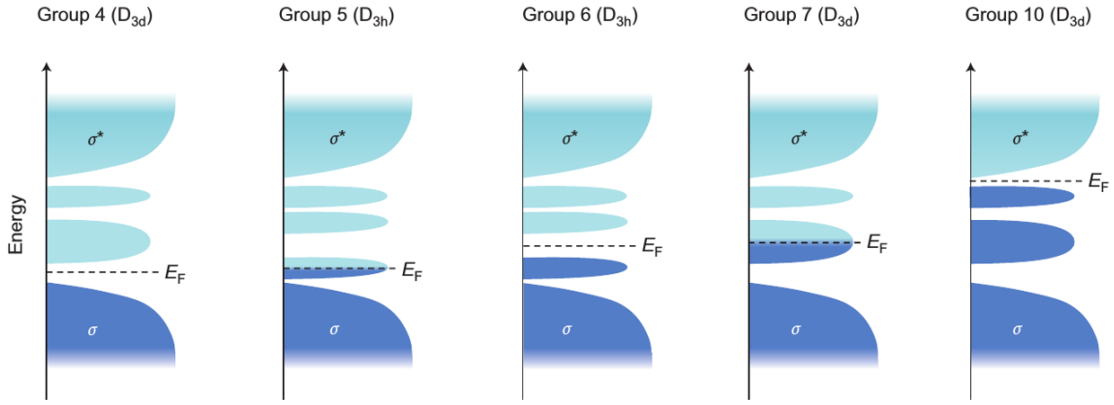

Figure 1.8: Pictorial view showing the progressive filling of *d*-orbitals between bonding (σ) and antibonding (σ^*) states in groups 4,5,6,7,10. D_{3h} and D_{3d} (equivalent to O_h) refer to the point groups associated with trigonal prismatic and octahedral coordination. Filled and empty states are in dark and light blue respectevely. The image is taken from Ref:[1]

emission in the visible light spectral range. Notably, in the case of MoS_2 the indirect to direct gap transition occurs from bilayer to single layer [13]. Another interesting example is $PtSe_2$, which has metallic band structure until the monolayer limit is achieved and a (indirect) band gap opening occurs[31].

Another remarkable property of 2D TMDCs concerns excitons. Typical exciton binding energy in these materials is one order of magnitude higher than in traditional semiconductors [32] owing to the extremely small thickness. Confined in an ultrathin layer, electron-hole pairs experience minor dielectric screening and consequently higher attractive Coulomb interaction. In extra charge conditions trions (a bound state of two electrons and one hole, *i.e.* a charged exciton) also form[33].

Monolayer TMDCs have become promising candidate materials also for manipulation of the spin degrees of freedom in future spintronics devices. The transition metal center is in fact responsible for intense spin-orbit interaction that, in presence of inversion symmetry breaking, lifts the spin degeneracy of the valence band. Spin energy splitting was predicted and measured in many TMDCs and it is exceptionally large in WSe_2 (about 500meV)[34].

What we described so far is just a short list of the most important properties encountered by physicists with 2D TMDCs. Ferromagnetism, superconductivity, electronic band structures with non trivial topology can also be found in these materials. However, a detailed discussion of such properties goes beyond the goals of this manuscript. The present rapid and biased overview is meant to introduce the motivation for the experimental work discuss in the second part of this thesis, where some peculiar properties described above will reappear as examples of potential applications of the structural engineering of the TMDCs studied by us.

Bibliography

[1] M. Chhowalla, H. S. Shin, G. Eda, L.-J. Li, K. P. Loh, and H. Zhang, "The chemistry of two-dimensional layered transition metal dichalcogenide nanosheets," *Nature Chemistry*, vol. 5, no. 4, p. 263, 2013.

[2] Q. H. Wang, K. Kalantar-Zadeh, A. Kis, J. N. Coleman, and M. S. Strano, "Electronics and optoelectronics of two-dimensional transition metal dichalcogenides," *Nature Nanotechnology*, vol. 7, no. 11, p. 699, 2012.

[3] K. Novoselov, A. Mishchenko, A. Carvalho, and A. C. Neto, "2D materials and van der Waals heterostructures," *Science*, vol. 353, no. 6298, p. aac9439, 2016.

[4] K. S. Novoselov, A. K. Geim, S. V. Morozov, D. Jiang, M. I. Katsnelson, I. Grigorieva, S. Dubonos, and A. A. Firsov, "Two-dimensional gas of massless Dirac fermions in graphene," *Nature*, vol. 438, no. 7065, p. 197, 2005.

[5] P. R. Wallace, "The band theory of graphite," *Physical Review*, vol. 71, no. 9, p. 622, 1947.

[6] K. S. Novoselov, A. K. Geim, S. V. Morozov, D. Jiang, Y. Zhang, S. V. Dubonos, I. V. Grigorieva, and A. A. Firsov, "Electric field effect in atomically thin carbon films," *Science*, vol. 306, no. 5696, pp. 666–669, 2004.

[7] K. S. Novoselov, D. Jiang, F. Schedin, T. Booth, V. Khotkevich, S. Morozov, and A. K. Geim, "Two-dimensional atomic crystals," *Proceedings of the National Academy of Sciences*, vol. 102, no. 30, pp. 10451–10453, 2005.

[8] G. Cheon, K.-A. N. Duerloo, A. D. Sendek, C. Porter, Y. Chen, and E. J. Reed, "Data mining for new two-and one-dimensional weakly bonded solids and lattice-commensurate heterostructures," *Nano Letters*, vol. 17, no. 3, pp. 1915–1923, 2017.

[9] C. Grazianetti, E. Cinquanta, and A. Molle, "Two-dimensional silicon: the advent of silicene," *2D Materials*, vol. 3, no. 1, p. 012001, 2016.

[10] J. A. Wilson and A. Yoffe, "The transition metal dichalcogenides discussion and interpretation of the observed optical, electrical and structural properties," *Advances in Physics*, vol. 18, no. 73, pp. 193–335, 1969.

[11] B. Clayman and R. Frindt, "The superconducting energy gap of $NbSe_2$," *Solid State Communications*, vol. 9, no. 22, pp. 1881–1884, 1971.

[12] A. V. Kolobov and J. Tominaga, *Chalcogenides: metastability and phase change phenomena*, vol. 164. Springer Science & Business Media, 2012.

[13] A. Splendiani, L. Sun, Y. Zhang, T. Li, J. Kim, C.-Y. Chim, G. Galli, and F. Wang, "Emerging photoluminescence in monolayer MoS_2," *Nano Letters*, vol. 10, no. 4, pp. 1271–1275, 2010.

[14] M. Leroux, I. Errea, M. Le Tacon, S.-M. Souliou, G. Garbarino, L. Cario, A. Bosak, F. Mauri, M. Calandra, and P. Rodière, "Strong anharmonicity induces quantum melting of charge density wave in 2H-$NbSe_2$ under pressure," *Physical Review B*, vol. 92, no. 14, p. 140303, 2015.

[15] W. G. Fisher and M. Sienko, "Stoichiometry, structure, and physical properties of niobium disulfide," *Inorganic Chemistry*, vol. 19, no. 1, pp. 39–43, 1980.

[16] D. Voiry, A. Mohite, and M. Chhowalla, "Phase engineering of transition metal dichalcogenides," *Chemical Society Reviews*, vol. 44, no. 9, pp. 2702–2712, 2015.

[17] W. Dawson and D. Bullett, "Electronic structure and crystallography of $MoTe_2$ and WTe_2," *Journal of Physics C: Solid State Physics*, vol. 20, no. 36, p. 6159, 1987.

[18] C.-H. Lee, E. C. Silva, L. Calderin, M. A. T. Nguyen, M. J. Hollander, B. Bersch, T. E. Mallouk, and J. A. Robinson, "Tungsten Ditelluride: a layered semimetal," *Scientific Reports*, vol. 5, p. 10013, 2015.

[19] Y. Guo, D. Sun, B. Ouyang, A. Raja, J. Song, T. F. Heinz, and L. E. Brus, "Probing the dynamics of the metallic-to-semiconducting structural phase transformation in MoS_2 crystals," *Nano Letters*, vol. 15, no. 8, pp. 5081–5088, 2015.

[20] K. Rossnagel, "On the origin of charge-density waves in select layered transition-metal dichalcogenides," *Journal of Physics: Condensed Matter*, vol. 23, no. 21, p. 213001, 2011.

[21] M. H. Whangbo and E. Canadell, "Analogies between the concepts of molecular chemistry and solid-state physics concerning structural instabilities. electronic origin of the structural modulations in layered transition metal dichalcogenides," *Journal of the American Chemical Society*, vol. 114, no. 24, pp. 9587–9600, 1992.

[22] K. Motizuki, N. Suzuki, Y. Yoshida, and Y. Takaoka, "Role of electron-lattice interaction in lattice dynamics and lattice instability of 1T-$TiSe_2$," *Solid State Communications*, vol. 40, no. 11, pp. 995–998, 1981.

[23] T. Kidd, T. Miller, M. Chou, and T.-C. Chiang, "Electron-hole coupling and the charge density wave transition in $TiSe_2$," *Physical Review Letters*, vol. 88, no. 22, p. 226402, 2002.

[24] K. Rossnagel, L. Kipp, and M. Skibowski, "Charge-density-wave phase transition in 1T-$TiSe_2$: Excitonic insulator versus band-type Jahn-Teller mechanism," *Physical Review B*, vol. 65, no. 23, p. 235101, 2002.

[25] J. A. Wilson, F. Di Salvo, and S. Mahajan, "Charge-density waves and superlattices in the metallic layered transition metal dichalcogenides," *Advances in Physics*, vol. 24, no. 2, pp. 117–201, 1975.

[26] F. J. Di Salvo, D. Moncton, and J. Waszczak, "Electronic properties and superlattice formation in the semimetal $TiSe_2$," *Physical Review B*, vol. 14, no. 10, p. 4321, 1976.

[27] R. Fleming, D. Moncton, J. Axe, and G. Brown, "High-q-resolution scattering using synchrotron X-radiation: 2H-$TaSe_2$ and $NbSe_3$," *Physical Review B*, vol. 30, no. 4, p. 1877, 1984.

[28] R. Brouwer and F. Jellinek, "Superstructure of 1s TaS_2," *Materials Research Bulletin*, vol. 9, no. 6, pp. 827–829, 1974.

[29] M. Wei, W. Lu, R. Xiao, H. Lv, P. Tong, W. Song, and Y. Sun, "Manipulating charge density wave order in monolayer 1T-$TiSe_2$ by strain and charge doping: a first-principles investigation," *Physical Review B*, vol. 96, no. 16, p. 165404, 2017.

[30] P. Ganal, W. Olberding, T. Butz, and G. Ouvrard, "Soft chemistry induced host metal coordination change from octahedral to trigonal prismatic in 1T-TaS_2," *Solid State Ionics*, vol. 59, no. 3-4, pp. 313–319, 1993.

[31] Y. Wang, L. Li, W. Yao, S. Song, J. Sun, J. Pan, X. Ren, C. Li, E. Okunishi, Y.-Q. Wang, *et al.*, "Monolayer $PtSe_2$, a new semiconducting transition-metal-dichalcogenide, epitaxially grown by direct selenization of Pt," *Nano Letters*, vol. 15, no. 6, pp. 4013–4018, 2015.

[32] K. He, N. Kumar, L. Zhao, Z. Wang, K. F. Mak, H. Zhao, and J. Shan, "Tightly bound excitons in monolayer WSe_2," *Physical Review Letters*, vol. 113, no. 2, p. 026803, 2014.

[33] K. F. Mak, K. He, C. Lee, G. H. Lee, J. Hone, T. F. Heinz, and J. Shan, "Tightly bound trions in monolayer MoS_2," *Nature Materials*, vol. 12, no. 3, p. 207, 2013.

[34] D. Le, A. Barinov, E. Preciado, M. Isarraraz, I. Tanabe, T. Komesu, C. Troha, L. Bartels, T. S. Rahman, and P. A. Dowben, "Spin–orbit coupling in the band structure of monolayer WSe_2," *Journal of Physics: Condensed Matter*, vol. 27, no. 18, p. 182201, 2015.

Chapter 2

Epitaxial 2D materials

2.1 Top-down vs bottom-up preparation of 2D materials

In nanofabrication it is common to distinguish between two fundamental approaches, which are referred to as *top-down* and *bottom-up*. Within the context of TMDCs, top-down methods consist in the mechanical or chemical *exfoliation* of layers from the bulk compounds enabled by the weak vdW nature of the interlayer forces, whereas by bottom-up methods one refers to those techniques that aim to *grow* the TMDC layers directly from their atomic components on a suitable target substrate.

Nowadays exfoliation is a widely applied preparation technique of 2D materials since large sub-millimetric sized flakes of high crystalline quality can be readily obtained. In dry *mechanical exfoliation*, TMDC layers are peeled off from the bulk compounds with adhesive tape and brought into contact with a substrate. Thereon, the tape is removed and a single or few layers of the TMDC remain bonded on the support. This method yields the cleanest and highest crystalline quality monolayer samples, often used in high-performance device demonstrations. *Liquid/chemical exfoliation* is also commonly adopted in the preparation of 2D TMDC nanosheets: direct sonication in organic solvents, Li intercalation (sometimes promoted and controlled by galvanostatic discharge) and electrochemical exfoliation are common chemical approaches that aim to separate TMDC layers in solution by overcoming the vdW interlayer forces[1]. Even though chemical purity of the obtained flakes is considered lower than in mechanically cleaved flakes, liquid exfoliation is generally preferred when a large amount of product is needed.

Despite that, top-down methods are not down-scalable and they do not allow any control over the size, the thickness, the orientation and the purity of the exfoliated flakes. These major drawbacks prevent these methods to be used for large area electronic material manufacturing, where properties as high electronic mobility and pure optical response, to mention a few, are desired and for which *epitaxial* (bottom-up) techniques, such as chemical and physical vapor deposition (CVD/PVD) are instead more suitable. It follows that the preferable route to prepare TMDC materials embedded in solid state devices involves necessarily reliable epitaxial processes. The peculiar case of 2D materials epitaxy

is the object discussed in the next paragraphs. Before that, few basic concepts concerning "conventional" 3D epitaxy will be introduced.

2.2 3D material epitaxy

Epitaxial growth is considered the cornerstone of semiconductor technology since it is the only reliable method for preparing high crystal quality thin films compatible with Si-CMOS technology and scalable according to the Moore's Law. The term *epitaxy* comes from the Greek words *epi*, meaning "above" and *taxis*, meaning "in ordered manner". Using a turn of phrase instead of a literal translation, we can state that epitaxy occurs whenever a crystalline thin film, *i.e.* the *overlayer*, grown on top of a *substrate* aligns its own crystallographic axes with the ones of the crystalline material below. This way the substrate *orients* the film growth. In principle, the overlayer can have the same chemical nature as the substrate (*homoepitaxy*). This is applied for instance when a higher purity than in the substrate is to be achieved. More frequently, however, film and substrate are different species and in this case one speaks about *heteroepitaxy*.

In conventional epitaxy, the possible issues to address during growths are surface energy discrepancy, chemical intermixing at the interface and lattice mismatch. The latter is defined as the relative difference in lattice constant between substrate (a_s) and overlayer film (a_f):

$$m = \frac{a_f - a_s}{a_s} \tag{2.1}$$

For simplicity, we will restrict the number of possible cases to a very specific one. As a first hypothesis, we consider that the growth occurs in conditions very close to the thermodynamic equilibrium and all the kinetics limitations are irrelevant. As second hypothesis we assume that the surface thermodynamics is in favour of a flat film growth. It should be noted that this scenario, usually referred to as Franck-van der Merwe growth (or layer-by-layer growth), is typical of homoepitaxial systems as well as of situations where atoms form more stabilizing bonds with the substrate than with each other. The deposited atoms rearrange on the surface in order to minimize the interfacial energy, which is often achieved in first approximation, by reaching the highest possible matching at the interface, *i.e.* the highest density of lattice coincidences. At the same time, however, the lattice might also accumulate defects and strain energy which lead to detrimental effects for the thin film transport properties.

For a typical heterointerface between semiconductors and in presence of lattice mismatch, we can simplify the possible scenarios with the three cases schematized in figure 2.1. When the two lattice constants of substrate and overlayer nearly match, atomic rows continuity is observed at the interface and the number of defects is minimized. In such a case the growth is said *pseudomorphic* (figure 2.1a). When the mismatch is large, two pos-

sible scenarios may occur. As the first case, deformation of the overlayer lattice constant allows to accommodate the mismatch. Along the hypothesis of flat film growth, the material grows pseudomorphic and strained in the early stages of the process until a critical elastic energy is accumulated at a certain critical thickness. At this point, the overlayer relaxes either by nucleating defects, *e.g. misfit dislocations* (figure 2.1b), or by changing its growth mode from 2D to 3D forming clusters. Alternatively, if no lattice accommodation is not possible, misfit dislocations directly form at the interface and overlayer grows relaxed above (figure 2.1c).

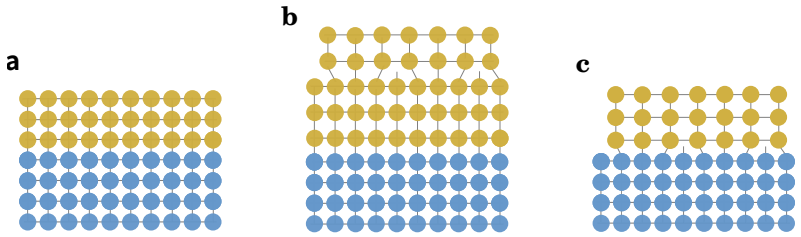

Figure 2.1: Typical lattice matching issues encountered in 3D epitaxy: (a) perfect or nearly perfect lattice matching allows pseudomorphic growth; (b)small mismatch: strained growth; (c) elevated mismatch: unstrained growth, the film grows relaxed after misfit dislocations form at the interface.

The picture we just described is typical of many non-layered semiconductor and metal epitaxial systems, where overlayer atoms bond with the atoms of the substrate surface (3D/3D epitaxy). In fact, because the substrate is truncated, the atoms in the topmost layer do not have a full coordination - unless the surface is reconstucted - and some of their electrons are free to form new bonds with the atomic species landing on during the growth process.

2.3 Van der Waals epitaxy

Different is the case when the substrate has no dangling bonds but a fully terminated surface, as in 2D and bulk vdW materials. This scenario leads to appreciably different behaviours in contrast with those valid for conventional epitaxy, where the relaxation of the lattice mismatch is a costly process. In 1984 A. Koma, demonstrated that ultrathin $NbSe_2$ films can be grown unstrained and defect-free on a cleaved 2H-MoS_2 surface in spite of a lattice mismatch as large as 10%[2]. The interface interaction between the two dichalcogenides, notably two vdW materials, is rather similar to the interlayer interaction within the bulk. Koma et al. introduced the concept of "*van der Waals epitaxy*" to describe every unstrained growth of layered materials on other layered materials (2D/2D epitaxy). The comparison between conventional and vdW epitaxy is sketched in figures 2.2a-b. Included are not only growths where overlayer and substrate are two layered

materials of the same family, *e.g.* two TMDCs, but also when the two have completely different structures. Remarkable is the growth of $MoSe_2$ and $NbSe_2$ on cleaved muscovite, where lattice mismatch is about of 50%[3].

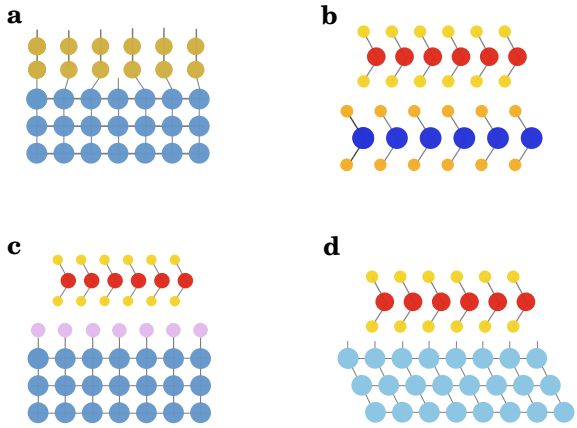

Figure 2.2: (a) conventional 3D epitaxy characterized by covalent bonding at the interface and (sometimes) misfit dislocations (3D/3D); (b) vdW epitaxy between two layered materials (2D/2D); (c) quasi vdW epitaxy between a 2D layered material and a chemically passivated surface (2D/3D); (d) growth of 2D layered material can sometimes occurs on metal and semiconductor 3D surfaces with dangling bonds (2D/3D).

After their first work, Koma and coworkers extended the concept of vdW epitaxy also to large mismatched systems of 2D layered materials and three-dimensional non-layered substrates (2D/3D epitaxy). The unstrained growth is possible after the substrate surface has been chemically passivated in order to saturate all the dangling bonds (figure 2.2c). Several proofs of concept arrived with the growth of various TMDCs on different chemically treated semiconductor surfaces such as S-GaAs(111)[4], H-Si(111) and F-CaF_2[5]. These types of heteroepitaxy were thus named "*quasi-vdW*".

In the same way as fcc noble metals like Cu, Ag and Au can form epitaxial (111) oriented films and abrupt interfaces on (0001) dichalcogenide faces (3D/2D epitaxy)[6], one may argue that, viceversa, also epitaxial 2D TMDC can be grown on close packed (111) metal surfaces (figure 2.2d). Many successful results have been achieved recently using Au(111)[7; 8; 9; 10]. However, whether the epitaxial growth of 2D TMDCs on metallic substrates could still be considered within the frame of (quasi)vdW epitaxy rather than conventional epitaxy is still matter of debate.

To this purpose, it is recommended to point out which other experimental and theoretical criteria can define vdW epitaxy beyond the mismatch one already mentioned. In their review on TMDC and topological insulator growths[11], L.A. Welsh and C.L. Hinkle analyzed the peculiar structural features common to most 2D epitaxial TMDCs grown on 3D substrates. They highlighted a set of criteria that, although still qualitative, may help to discern vdW epitaxy on the basis of experimental observations. In short, 2D TMDCs grown by vdW epitaxy show:

- *strain free* lattices, in spite of large mismatch with the substrate;
- *abrupt interfaces* without dislocations and point defects;
- *rotational alignment* of the grown islands along the high symmetry direction of the substrate.

To them we add a fourth point, commonly emphasized in this contest:

- only *vdW interactions* occur between 2D layer and substrate.

We already discussed about the two first items, which may be considered a sort of "definition" of vdW epitaxy. Whether the third and the fourth are always verified is a point that should be questioned, since a variety of "nuances" can actually be found. Let us go by order. Generally, if in vdW epitaxy the interaction strength between overlayer and substrate is not strong enough to induce strain (despite the large mismatches), it appears to be at least sufficient to orient the growing flakes. This has been demonstrated in several works showing oriented but strain-free 2D TMDC films grown on a large variety of substrates. However, in most of the cases the proofs of the alignment come from electron diffraction measurements, *e.g.* RHEED, LEED or SAED, which sometimes are not able to measure quantitatively the "degree" of rotational misalignment between a film and the respective substrate. This is enabled instead by synchrotron x-rays scattering techniques optimized for surface sensitive measurements, *e.g.* grazing incidence x-ray diffraction (GIXRD), which offer in combination also the possibility to accurately model and solve the structure. We will demonstrate in the second part of this manuscript that the so called film *mosaic spread*, *i.e.* measurements of the angular distribution of an in-plane reflection signal obtained by rotating the sample around its azimuthal axis (*rocking scans*), might become a clue of the interaction strength on the basis of the epitaxial alignment.

About the nature of the interaction established at the interface, whether it is purely vdW or not remains an open question. Ideally the growth of a 2D TMDC on a pure vdW material - or onto a passivated surface - is driven by vdW forces, generally originated either by dipolar interactions between couples of atoms or London dispersion forces. However, in a 2D material grown onto a metal or semiconductor surface, we can expect the interfacial interaction to be at least partially hybridized and the interface to exhibit strain and/or local defects typical of conventional epitaxy. In the second part of this manuscript we will address this question several times. Observations of non-zero strain, misfit dislocation networks and rearrangements of atoms both in the film and in the substrate are some examples that will be discussed in the light of non-purely vdW interaction.

2.4 State of art of the 2D TMDC epitaxial growths

The synthesis of ultra-thin epitaxial TMDC layers, especially MoS_2, has been demonstrated so far using several approaches. Chemical vapour deposition (CVD) and molecular beam epitaxy (MBE) are the most often used techniques. CVD supplies the atomic species via gaseous precursors and it allows achieving excellent growth uniformity as well as thickness and stoichiometry control. However, defects and impurity levels might be high due to the low vacuum conditions in which the growth is performed. On the contrary, MBE is carried out in ultra-high vacuum (UHV) environment, where pressure is kept lower than 10^{-9} mbar and source materials are of high purity. Very low pressure and slow evaporation rate allow for a highly accurate control of the composition, while the concomitant presence of *in situ* diagnostics makes MBE an ideal process both for fundamental studies and device fabrication. In this paragraph we are going to outline the state-of-art in the synthesis of epitaxial TMDCs prepared by either CVD or MBE methods. Particular attention is given however to MBE growth, as this technique was used for the synthesis carried out within this thesis.

In general, two main strategies are adopted to prepare 2D TMDCs. The first consists essentially in the *chalcogenation* of a predeposited metal layer in order to form a dichalcogenide of the same metal species. A school example is reported by Zhan et al[12]: firstly Mo is predeposited onto a SiO_2 substrate to form a 1 nm thin metal layer. After that, the sample is transferred inside a CVD setup where a sulfur precursor is supplied and reacts with Mo at 750°C forming single or few-layers MoS_2 flakes. The advantage of this method is that the overall dichalcogenide thickness is related to the thickness of the predeposited metallic layer and hence can be very accurately controlled.

However, the most common approach for preparing epitaxial TMDCs is by *codeposition* of the metal and chalcogen precursor reagents and their direct reaction on the target substrate. Initially, sulfur and MoO_3 powders were widely used as chalcogen and metal precursors to synthesize MoS_2 on SiO_2/Si(111) substrates inside CVD setups[13]. Codeposition allowed to produce MoS_2 sheets of triangular shapes of 1-3 monolayers thickness and micrometric lateral size and then it was extended also to preparation of other TMDC species, also on different substrates.

Growth strategies based on MBE do not differ too much from the methods adopted to grow TMDCs by CVD. Walsh et Hilke[11] report that the majority of the MBE growths of TMDCs published in literature share the following growth conditions:

- chalcogen to metal flux ratio of 20:1 at least;
- slow growth rates in the order of 1ML/h;
- substrate temperatures in the range of 300-500°C.

Essentially the ideal growth consists in metal deposition under a rich chalcogen atmosphere on a heated substrate. The temperature condition matches the compatibility

standards required by Si-CMOS technology, which limit the growth temperature. In general, metals are evaporated in UHV from high purity rods by electron beam evaporators, whereas chalcogen atoms (Se, Te) are mostly provided from Knudsen cells containing pure element powder. Their vapor pressure is rather high[14], so that they can be easily evaporated in UHV by applying modest resistive heating. Regarding sulfur (S), hydrogen disulfide (H_2S) gas has been widely preferred to powder precursors for the growth of MoS_2 on Au(111)[7]. The metallic substrate is a crucial element in the synthesis since it acts at the same time as growth template and catalyst for the H_2S pyrolisis, by lowering the energy barrier required to crack the H_2S molecules[15]. The growth is carried out in conditions halfway between a standard MBE growth and a CVD process: first, while the metal atoms are evaporated in molecular regime from an electron beam evaporator, the gas is supplied in the UHV growth chamber at relatively high partial pressure, typically 4-5 orders of magnitude higher than the base pressure. Second, the H_2S gas molecules directly react with the metal substrate surface to decompose to H_2 (immediately desorbed) and S atoms that remain adsorbed on the surface. Owing to these reasons, we call the process "*reactive*" MBE. This method was developed at Aarhus University in the early 2000s to prepare MoS_2 nanostructures for catalysis applications and it has been very recently extended successfully to the synthesis of other 2D transition metal disulfide crystals, such as VS_2[8], TaS_2[9] and WS_2[10].

2.5 Challenges related to domain size and oriented growth

The problem of growing TMDCs by MBE under the conditions discussed above is that they lead to high nucleation density and favor in turn small average domain size and high grain boundary density, with detrimental effects for carrier transport. Typical single grain size in TMDC samples prepared by MBE go from tenth to few hundreds nanometer, definitely too small to enable large area material production. Increasing flake size thus constitutes one of the biggest challenges to overcome in view of real world devices production based on high-quality TMDCs. The use of higher growth temperatures might represent a solution to this problem. In fact, higher substrate temperature during growth might reduces the nucleation density by favoring atom desorption and increasing adatom mobility on the surface. The latter decreases the probability for two or more atoms meeting stochastically on the surface, thereby reducing the TMDC island nucleation density. This allows to grow large TMDCs flakes before they coalesce. In this respect, *Yue et al.* reported that to achieve 2D WSe_2 with domain size as large as 1.2 μm, the reduction of the metal deposition rate in conjunction with elevated substrate temperature (higher than 500°C) and Se richer environment was necessary[16].

Several substrates have also been tested for TMDC growth. SiO_2/Si(111) was widely used in the past in view of the possible integration of TMDCs in Si-CMOS technology.

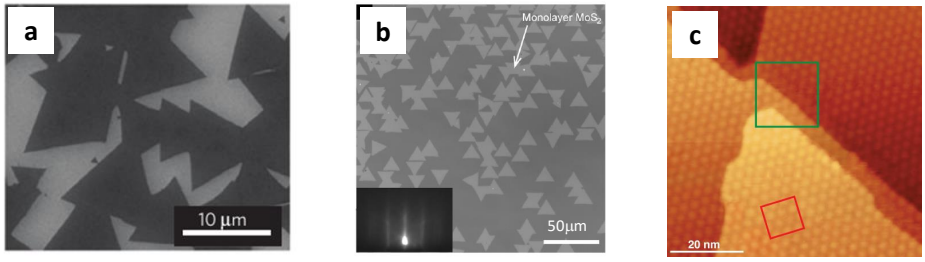

Figure 2.3: (a) TMDC flakes grow with random orientation and shape on amorphous SiO_2/Si(111)[17]; (b) multiple orientatons in MoS_2 on single crystal sapphire[18]; (c) epitaxial MoS_2 grown on Au(111) with single a orientation. Note the what is shown in the image is a moiré pattern (description in the next section), not the atoms[19].

Although CVD growth led sometimes to micrometric size flakes, this amorphous substrate prevents the control over flake orientation which turns out to be completely random[17] (figure 2.3a). Single crystal insulating substrates such as mica and sapphire[18] were considered next to address this challenge. Even though TMDCs grow epitaxially on these substrates, several orientations were systematically observed (figure 2.3b). Control of the growth orientation is of fundamental importance in view of technological applications. The occurrence of multiple orientations implies in fact the formation of grain boundaries when the domains coalesce. This is detrimental to the charge carrier electronic transport or to radiative recombination of excitons, especially when combined with the high nucleation densities and the small average size of the nanoscrystals. The choice of metallic single crystal substrates, especially cubic (111) surfaces, has offered a possible solution allowing the growth of epitaxial TMDCs with unique preferential orientation[7; 19] (figure 2.3c). So far, high quality growth has been obtained only on Au(111) single crystal substrates. However, TMDCs grown on metal substrates are not immediately employable for technological applications. A transfer step on other insulating substrates is in fact mandatory.

2.6 Superstructures in TMDC epitaxial single layers

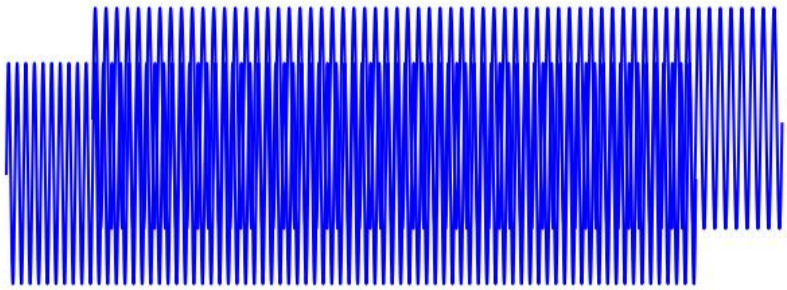

Figure 2.4: Two sinusoidal patterns with slightly different wavelength are superimposed. The superposition area shows a different additional modulation which is called optical moiré.

We already stated that the peculiarity of vdW epitaxy is to preserve the intrinsic lattice constant of the freestanding layer while promoting a well-defined crystallographic orientation of the overlayer on the substrate, in spite of their natural mismatch. The structural mismatch - we should better say mis-registry since a similar effect can be produced either by lattice parameter mismatch or misalignment, *i.e.* rotation between overlayer and substrate - often leads to the observation of a superlattice effect, similar to the optical moiré effect, which is referred to as *moiré superstructure*[20]. An optical moiré is sketched in figure 2.4: the superposition of two regular patterns with different periodicity generates a modulation having a longer period than the individual patterns. Likewise, in 2D epitaxial crystal systems the superposition of two lattices with different lattice constants gives rise to an additional modulation in real space, both electronic and topographic, which can be detected by certain microscopy techniques, *e.g.* scanning tunneling microscopy (STM, figure 2.5a), and to additional satellite reflections in the reciprocal space, which can be measured by diffraction methods (figure 2.5b).

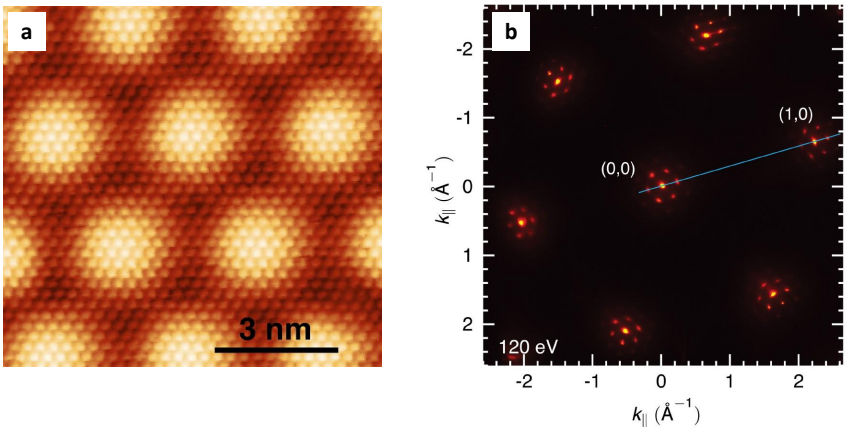

Figure 2.5: moiré superstructures can be detected both in real space and in reciprocal space: (a) atomically resolved STM characterization of MoS_2/Au(111): small spots are atoms while the larger-scale (∼3 nm) apparent height bumps correspond to the moiré and have both electronic and topographic origin; (b) SPA-LEED (spot profile analysis low energy electron diffraction) image shows the Au substrate bright reflections surrounded by six weaker satellites; the short satellites' periodicity measured in reciprocal space corresponds to the large moiré supercell in real space. The images are taken from Ref.[19]

Such wavelike modulations are strongly related to the periodical variation of the overlayer-substrate distance and the atomic stacking. In the absence of rotational misorientation between the overlayer and the substrate, and considering only the simplest moiré lattices, the period of the modulation is the period of the moiré supercell and it is given by:

$$\frac{1}{a_{moire}} = \left| \frac{1}{a_{ov}} - \frac{1}{a_{sub}} \right| \tag{2.2}$$

where a_{sub} and a_{ov} are the lattice constants of the two substrate and overlayer sublattices.

According to the ratio between overlayer and substrate lattice parameters, the super-

structure can be either *commensurate* or *incommensurate*. The first case happens when the supercell length is an integer multiple of the sublattice ones and in diffraction the corresponding superstructure reflections occur at simple fractions of the reciprocal lattice unit vectors. In this case, the two lattices coincide over a certain distance, and the moiré supercell is also called *coincidence supercell*. Not all the systems are commensurate, and incommensurate ones occur when the sublattice lengths ratio is not a rational number. In this scenario a strict coincidence is never observed. A typical case is the moiré pattern observed in graphene on Ru(0001) which was first reported as (12×12) graphene matching (11×11)Ru[21], then as (11×11) graphene matching (10×10)Ru[22], and finally as (25×25) graphene matching (23×23)Ru[23].

The moiré effect has not only a geometric relevance. The periodic variation of the overlayer-substrate distance goes along with the chemical reactivity of the layer, since it induces preferential sites for adsorption and it can drive nanopatterning. Moreover, it influences the interaction with the substrate. This topic was abundantly studied in the case of graphene. Some substrates impose to graphene only a weak interaction dominated by vdW forces - it is the case for instance of graphene grown on SiC(0001)[24] and on Ir(111)[25]. In these cases, the moiré can be interpreted as a smooth superpotential which does not affect dramatically the electronic properties. On the other hand, other substrates interact more strongly with the overlayer, establishing partial covalent bondings. A noteworthy example is graphene on Re(0001) where interaction manifests itself with a pronounced nanorippling of the graphene surface quantified with 1.6Å nanorippling amplitude[26].

Moiré patterns are ubiquitous in 2D materials. Also 2D TMDCs host fascinating moiré superstructure of various kinds according to the nature of the substrate and the interaction that it imposes. Along this thesis we will have the chance to discuss some examples. We will carefully describe the encountered superstructures both in real and reciprocal space and we will discuss the possible effects induced on the overlayer electronic properties.

2.6.1 Moiré pattern as an array of misfit dislocations

Actually, a moiré pattern observed on a 2D epitaxial layer - for instance by scanning probe microscopy - can be seen as a misfit dislocation network at the hetero-epitaxial interface[27]. In conventional 3D/3D epitaxy misfit dislocations occur to relieve the misfit strain accumulated when the film reaches a critical thickness. Generally, the misfit dislocation core widths are small (they encompass few atoms) forming a network of defects where the lattices are locally deformed. In 2D/2D or 2D/3D heteroepitaxy, misfit dislocations can periodically occur at the interface to accommodate the mis-registry between two materials having different lattice parameters. Between a vdW material and its substrate interactions are much weaker than in covalent solids: this gives to the misfit dislocation a much larger core width accompanied by a weak deformation field.

Figure 2.6a-c show the different cases we can find by superimposing two incommensurate chains of atoms, having slightly different lattice parameters. In all the cases a superlattice is formed, which is made of 15 (overlayer) and 16 (substrates) atomic units. In the first case (figure 2.6a) interaction between layers is zero: yellow and blue atoms pass from a situation of coincidence where one is on top of the other, *i.e.* in phase, to the one where the top atom is settled on a bridge site above two bottom atoms, *i.e.* out-of-phase. The Peierls-Nabarro model[28] predicts that in the limit of zero interactions between the layers, the *dislocation core* extends across the entire supercell with zero lattice deformation. In the second case (figure 2.6b), the layers are instead weakly interacting. The supercell size does not change, but the upper layer is slightly deformed and the dislocation core is less than the superlattice period. If the periodic strain increases further (case (c)), the situation encountered in (b) is brought to the extremes: the deformation field is very localized, the dislocation core size is much smaller and the atoms inside are sensibly displaced. This situation is similar to misfit dislocations in covalent epitaxial systems.

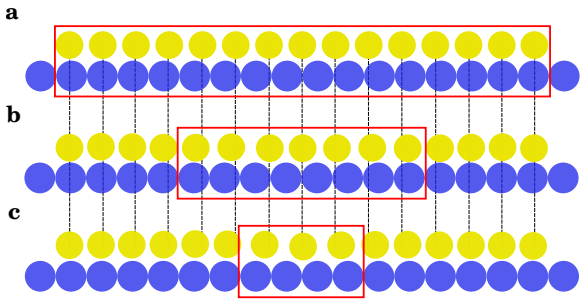

Figure 2.6: Two generic one-dimensional lattices, respectively in yellow and in blue, having slightly different lattice parameters are superimposed. Due to the lattice mismatch, the mutual positions between atoms in the first and second layers varies periodically between two extremes and a misfit dislocation is thus produced. Misfit dislocation is identified in the figure through its core (red box) where the lattice deformation is localized and its size is depending on the interface interaction strength: (a) zero interaction between the layers, (b) weak interaction, (c) strong interaction.

All of these types of misfit dislocations manifest with an optical moiré pattern in STM or by an additional periodicity signal in a diffraction pattern. In this manuscript we will refer to this phenomenon as *"moiré patterns"* for the sake of intuition, but we actually imply that microscopically a network of misfit dislocations is actually at the origin of the superperiodicity.

Note that the observation of a moiré pattern itself is not indicative of the strength of the interface interaction. In other words, a moiré pattern observed by STM or the simple presence of a dislocation network imaged by cross-sectional scanning transmission electron microscopy (STEM) do not mean that two layers at the interface are necessarily strongly interacting, since it exists also for weakly interacting vdW epitaxial systems. Dislocation core size, local strain and atomic displacement distribution may instead provide further insights of that, and they can be quantitatively estimated both by microscopy tools such as

cross sectional scanning transmission electron microscopy (STEM) and grazing incidence x-ray diffraction (GIXRD).

Bibliography

[1] M. Chhowalla, H. S. Shin, G. Eda, L.-J. Li, K. P. Loh, and H. Zhang, "The chemistry of two-dimensional layered transition metal dichalcogenide nanosheets," *Nature Chemistry*, vol. 5, no. 4, p. 263, 2013.

[2] A. Koma, K. Sunouchi, and T. Miyajima, "Fabrication and characterization of heterostructures with subnanometer thickness," *Microelectronic Engineering*, vol. 2, no. 1-3, pp. 129–136, 1984.

[3] K. Ueno, K. Saiki, T. Shimada, and A. Koma, "Epitaxial growth of transition metal dichalcogenides on cleaved faces of mica," *Journal of Vacuum Science & Technology A*, vol. 8, no. 1, pp. 68–72, 1990.

[4] K. Ueno, T. Shimada, K. Saiki, and A. Koma, "Heteroepitaxial growth of layered transition metal dichalcogenides on sulfur-terminated GaAs(111) surfaces," *Applied Physics Letters*, vol. 56, no. 4, pp. 327–329, 1990.

[5] A. Koma, "Van der waals epitaxy — a new epitaxial growth method for a highly lattice-mismatched system," *Thin Solid Films*, vol. 216, no. 1, pp. 72–76, 1992.

[6] W. Jaegermann, F. Ohuchi, and B. Parkinson, "Interaction of cu, ag and au with van der waals faces of WS_2, and SnS_2," *Surface Science*, vol. 201, no. 1-2, pp. 211–227, 1988.

[7] S. S. Grønborg, S. Ulstrup, M. Bianchi, M. Dendzik, C. E. Sanders, J. V. Lauritsen, P. Hofmann, and J. A. Miwa, "Synthesis of epitaxial single-layer MoS_2 on Au(111)," *Langmuir*, vol. 31, no. 35, pp. 9700–9706, 2015.

[8] F. Arnold, R.-M. Stan, S. K. Mahatha, H. Lund, D. Curcio, M. Dendzik, H. Bana, E. Travaglia, L. Bignardi, P. Lacovig, *et al.*, "Novel single-layer vanadium sulphide phases," *2D Materials*, vol. 5, no. 4, p. 045009, 2018.

[9] C. E. Sanders, M. Dendzik, A. S. Ngankeu, A. Eich, A. Bruix, M. Bianchi, J. A. Miwa, B. Hammer, A. A. Khajetoorians, and P. Hofmann, "Crystalline and electronic structure of single-layer TaS_2," *Physical Review B*, vol. 94, no. 8, p. 081404, 2016.

[10] M. Dendzik, M. Michiardi, C. Sanders, M. Bianchi, J. A. Miwa, S. S. Grønborg, J. V. Lauritsen, A. Bruix, B. Hammer, and P. Hofmann, "Growth and electronic structure of epitaxial single-layer WS_2 on Au(111)," *Physical Review B*, vol. 92, no. 24, p. 245442, 2015.

[11] L. A. Walsh and C. L. Hinkle, "van der waals epitaxy: 2D materials and topological insulators," *Applied Materials Today*, vol. 9, pp. 504–515, 2017.

[12] Y. Zhan, Z. Liu, S. Najmaei, P. M. Ajayan, and J. Lou, "Large-area vapor-phase growth and characterization of MoS_2 atomic layers on a SiO_2 substrate," *Small*, vol. 8, no. 7, pp. 966–971, 2012.

[13] Y.-H. Lee, X.-Q. Zhang, W. Zhang, M.-T. Chang, C.-T. Lin, K.-D. Chang, Y.-C. Yu, J. T.-W. Wang, C.-S. Chang, L.-J. Li, *et al.*, "Synthesis of large-area MoS_2 atomic layers with chemical vapor deposition," *Advanced Materials*, vol. 24, no. 17, pp. 2320–2325, 2012.

[14] Wikipedia, "Vapor pressures of the elements — wikipedia, l'enciclopedia libera."

[15] A. Startsev, O. Kruglyakova, Y. A. Chesalov, S. P. Ruzankin, E. Kravtsov, T. Larina, and E. Paukshtis, "Low temperature catalytic decomposition of hydrogen sulfide into hydrogen and diatomic gaseous sulfur," *Topics in Catalysis*, vol. 56, no. 11, pp. 969–980, 2013.

[16] R. Yue, Y. Nie, L. A. Walsh, R. Addou, C. Liang, N. Lu, A. T. Barton, H. Zhu, Z. Che, D. Barrera, *et al.*, "Nucleation and growth of WSe_2: enabling large grain transition metal dichalcogenides," *2D Materials*, vol. 4, no. 4, p. 045019, 2017.

[17] S. Najmaei, Z. Liu, W. Zhou, X. Zou, G. Shi, S. Lei, B. I. Yakobson, J.-C. Idrobo, P. M. Ajayan, and J. Lou, "Vapour phase growth and grain boundary structure of molybdenum disulphide atomic layers," *Nature Materials*, vol. 12, no. 8, p. 754, 2013.

[18] D. Dumcenco, D. Ovchinnikov, K. Marinov, P. Lazic, M. Gibertini, N. Marzari, O. L. Sanchez, Y.-C. Kung, D. Krasnozhon, M.-W. Chen, *et al.*, "Large-area epitaxial monolayer MoS_2," *ACS Nano*, vol. 9, no. 4, pp. 4611–4620, 2015.

[19] H. Bana, E. Travaglia, L. Bignardi, P. Lacovig, C. E. Sanders, M. Dendzik, M. Michiardi, M. Bianchi, D. Lizzit, F. Presel, *et al.*, "Epitaxial growth of single-orientation high-quality MoS_2 monolayers," *2D Materials*, vol. 5, no. 3, p. 035012, 2018.

[20] M. Ritter, W. Ranke, and W. Weiss, "Growth and structure of ultrathin FeO films on Pt(111) studied by stm and leed," *Physical Review B*, vol. 57, no. 12, p. 7240, 1998.

[21] J. Coraux, A. T. N 'Diaye, C. Busse, and T. Michely, "Structural coherency of graphene on Ir(111)," *Nano Letters*, vol. 8, no. 2, pp. 565–570, 2008.

[22] A. V. De Parga, F. Calleja, B. Borca, M. Passeggi Jr, J. Hinarejos, F. Guinea, and R. Miranda, "Periodically rippled graphene: growth and spatially resolved electronic structure," *Physical ReviewLetters*, vol. 100, no. 5, p. 056807, 2008.

[23] D. Martoccia, P. Willmott, T. Brugger, M. Björck, S. Günther, C. Schlepütz, A. Cervellino, S. Pauli, B. Patterson, S. Marchini, *et al.*, "Graphene on Ru(0001): a 25×25 supercell," *Physical Review Letters*, vol. 101, no. 12, p. 126102, 2008.

[24] J. Hass, R. Feng, J. Millán-Otoya, X. Li, M. Sprinkle, P. N. First, W. De Heer, E. Conrad, and C. Berger, "Structural properties of the multilayer graphene/4H-SiC(0001) system as determined by surface x-ray diffraction," *Physical Review B*, vol. 75, no. 21, p. 214109, 2007.

[25] N. Blanc, J. Coraux, C. Vo-Van, O. Geaymond, G. Renaud, *et al.*, "Local deformations and incommensurability of high-quality epitaxial graphene on a weakly interacting transition metal," *Physical Review B*, vol. 86, no. 23, p. 235439, 2012.

[26] C. Tonnoir, A. Kimouche, J. Coraux, L. Magaud, B. Delsol, B. Gilles, and C. Chapelier, "Induced superconductivity in graphene grown on Rhenium," *Physical Review Letters*, vol. 111, no. 24, p. 246805, 2013.

[27] P. Pochet, B. C. McGuigan, J. Coraux, and H. T. Johnson, "Toward moiré engineering in 2D materials via dislocation theory," *Applied Materials Today*, vol. 9, pp. 240–250, 2017.

[28] F. Nabarro, "Dislocations in a simple cubic lattice," *Proceedings of the Physical Society*, vol. 59, no. 2, p. 256, 1947.

Chapter 3

Tuning TMDC properties through control of their structure and chemistry

3.1 Phase transitions between TMDC polymorphs

The existence of several polymorphic phases in TMDCs (see chapter 1) with peculiar distinctive properties is of potential interest for their technological applications. This fact sets another difference with respect to graphene, which requires instead chemical functionalization to engineer its properties. Associated to each TMDC polymorph, *e.g.* 1T or 2H, there is a specific electronic behaviour. It is the case of group VI dichalcogenides, *e.g.* MoS_2, whose 2H phase shows semiconducting behaviour, while the 1T phase is metallic. Although the 1T polymorph is metastable at room temperature, it can be stabilized under certain conditions. There are numerous potential applications for a material that can be switched from one phase to another at room temperature by applying an external stimulus, e.g an electric field or a directional strain. For instance, metal-semiconductor transitions can be used in applications where a drastic resistance change is required, as in information storage devices. One can also exploit polymorphism by making lateral domains of dissimilar phases of the same material coexisting on the same substrate. This case was firstly demonstrated in TMDCs by Eda and coworkers[1], who realized lateral MoS_2 junctions of chemically exfoliated 1T and 1H lattice matched polymorphs, and more recently by Lin et al. who obtained the same result in epitaxial $PtSe_2$ by controlling the annealing temperature and the deposited amount of selenium[2]. Moreover, one could also simply wonder how a metastable phase can be stabilized under thermodynamically unfavorable conditions - for instance, direct synthesis of metallic 1T MoS_2 is demanded to obtain catalytic properties that can be combined with carrier transport - or how to make the transition process fully reversible.

Owing to the variety of possible compounds and polymorphs, the study of phase transition seems a vast field of investigation. As we mentioned elsewhere, learning how to

manipulate single layer TMDC structures is also part of this thesis work. Hereafter we briefly discuss some of the methods reported in the literature for obtaining and stabilizing metastable TMDCs phases.

A fundamental approach to TMDC phase transitions is to understand the tight correlation between structure and electronic states. In chapter 1 we noticed that the progressive filling of the *d*-band with electrons establishes the semiconducting or metallic nature of the TMDCs. We know also from crystal field theory that each TMDC coordination type, *i.e.* trigonal prismatic (D_{3h}) or octahedral (O_h), corresponds to a characteristic energy splitting of the *d*-levels. In figure 3.1a, an MoS_6 D_{3h} coordinated atomic unit is used as an example. The structure coincides with the 1H unit cell in single layer MoS_2. The five Mo 4*d* orbitals are induced by symmetry to split into three sub-groups characterized by different energies. From the bottom to the top they are: Mo $4d_{z^2}$ (completely occupied), Mo $4d_{xy}$ and Mo $4d_{x^2-y^2}$ (semi-occupied), and finally Mo $4d_{xz}$ and Mo $4d_{yz}$ (empty). If the MoS_6 unit adopts an octahedral (O_h) coordination instead, as in figure 3.1b, the degenerated *d*-levels split into two groups: lower in energy we find Mo $4d_{xy}$, Mo $4d_{xz}$ and Mo $4d_{yz}$ levels (semi-occupied), while the remaining ones are located at higher energies and they are empty. Density functional theory predict that the trigonal prismatic configuration is the most energetically stable. However, if one electron is added to this system (figure 3.1a), it will occupy one of the Mo $4d_{xy}$ and $4d_{x^2-y^2}$ levels, increasing the overall energy. On the contrary, if the same electron is added to the O_h structure (figure 3.1b), it will occupy one of the remaining still free positions available in the semi-occupied orbitals at the same energy. Overall, an electron donation to the MoS_6 atomic unit ends up to stabilize the 1T phase and destabilize the 2H one, favoring the transition of 2H MoS_2 towards the metallic 1T phase[3]. This qualitative picture can be applied to the other TMDCs of the VI group, and similar reasoning can be followed for other TMDC compounds.

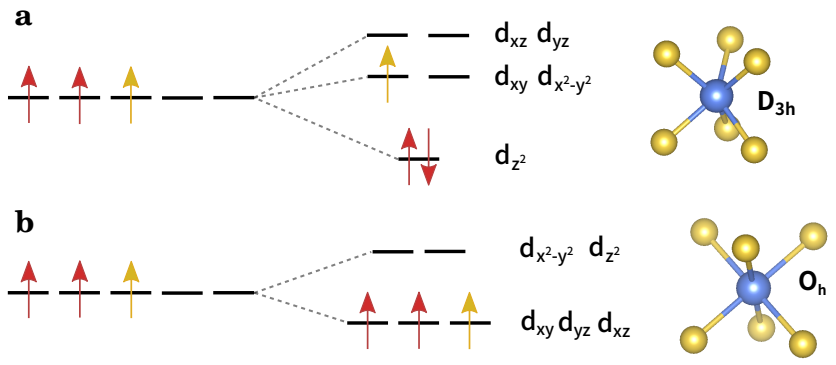

Figure 3.1: simplified representation of *d*-bands energy splitting diagram within crystal field theory for trigonal prismatic (a) and octahedral (b) MoS_6 units.

Excess charge is thus a driving force towards the 2H to 1T transition in bulk and 2D dichalcogenides and it can be achieved by several ways. 1T phases have been obtained

the first time by exfoliation of bulk TMDCs in solution using intercalating agents such as n-butil-lithium[4]. This method has been widely applied since the pioneering work of Py and Hearing in the Eighties[5]. Alkali metals are in fact well known electro-donors: once intercalated in the vdW gap between two TMDC layer planes, they provide electrons to the TMDC, and can thereby induce a phase transition of the flakes from 2H to 1T (or even 1T') structures. Intercalation of TMDCs by alkali metal is a well-explored topic in material science and we will have the chance to discuss it more deeply in the next section and in the experimental part.

Alternative solid-state compatible methods to induce phase transitions in TMDCs by charge transfer have also been experimentally demonstrated or theoretically suggested. Duerloo and coworkers calculated that changing carrier density in monolayer 2H $MoTe_2$ can induce a semiconducting-to-semimetal transition and they proposed an electrostatic gating device configuration to n-dope semiconducting 2H $MoTe_2$ and transform it into a semimetallic 1T' phase[6]. Lin and Dumcenco instead succeeded in obtaining 2H-1T phase transition in Re-doped single layer MoS_2 at 600°C triggered by electron beam irradiation[7]. Their atomically resolved *operando* investigations offered a first valuable contribution to the comprehension of the atomic mechanisms of 1T phase nucleation in a pristine 2H layer, involving gliding plane shifts, intermediate phase mediation and grain boundary formation.

3.2 Intercalation of TMDCs

In this section we are going to describe the main structural and electronic effects of intercalation in TMDCs, as it will be at the heart of the experiment discussed in chapter 7. Intercalation is the insertion of atomic or small molecular guest species inside the interlayer spacing of a host layered material, *e.g.* graphite or a bulk TMDC. This process has been intensively studied since the Sixties with numerous articles and reported case studies[8]. Typical intercalating guest elements are either transition metal or alkali metal atoms, but organic molecules have been used as well. The interaction of these species with the host materials is generally weak: no ionic or covalent bonds are formed with the atoms of the host structure - with some exceptions regarding intercalation of transition metals - but charge transfer represents the main form of interaction. Because of that, intercalating species are very mobile inside the vdW gaps of the host material and they can easily channel in and out. It results that intercalation is a reversible process. Common ways to intercalate alkali metals are by dip-coating in alkali solution, electrochemistry or deposition in UHV (*in situ* intercalation). With the latter, intercalation occurs spontaneously through the layers after deposition of the intercalating atoms on the top surface of the host material. Besides the preparation of the so-called *intercalation compounds* useful in battery applications, intercalation has been considered for several decades an optimum way

to *decouple* individual layer from the rest of the structure and hence to observe the effects of reduced dimensionality and carrier confinement in quasi isolated 2D layers. Moreover, thanks to the charge transfer from the guest atom to the host material, intercalation became a simple and controllable way to modify intrinsic properties in TMDCs, to inject extra carriers in the system and to induce phase transitions from semiconductor to metal or even from metal to superconductor.

In this work we will be interested in studying the structural and electronic effects of intercalating alkali atoms under a single layer TMDC. Inquiring the feasibility of the intercalation process with a 2D material directly anchored to a substrate is a topic that we will address later in the second part of the manuscript. We focus for the moment only on the structural effects expected and observed within the "classical" intercalation of bulk layered TMDCs. In general, upon intercalation TMDCs show:

- increased spacing between layers to accomodate the guest atoms;
- modified interlayer interaction: the interaction is not anymore between two inert vdW surfaces but it might imply partial ionic bonding or charge transfer due to the insertion of metal electron donor species between TMDC layers;
- structural changes also within the layers, *e.g.* altered metal-chalcogen bond lengths.

The impact of the structural changes is variable as function of the size of the intercalated species. It is straightforward that larger layer separation is needed to accommodate bigger alkali metals like Cs than smaller species such as Li or Na. This is not however the only effect that intercalation can induce in the host material. Charge transfer from intercalants can also modify the bond lengths within the layers[8] and induce numerous kinds of electronic instability effects leading for instance to CDW superstructure[9], superconducting phases[10] and magnetic domains[11]. Depending on the elastic energy cost of the deformation they induce, alkali metal atoms may not intercalate inside all the available vdW gaps of the host TMDC, but occupy one every n gaps (stage n intercalation compound). For example, in $LiMoS_2$, Li atoms fill all the gaps available in MoS_2 (stage 1). However, since TMDCs bonds are quite rigid, stage numbers 2 and 4 are more common.

Owing to the characteristic topography of the TMDC surfaces, one can expect that alkali atoms occupy octahedral or trigonal prismatic sites on top of the chalcogen atoms and that the density is homogeneous everywhere inside the gap thanks to the high mobility of the atoms. Actually, the numerous existing studies depict a more complex scenario. Situations vary in fact from cases where alkali metals occupy both type of sites in the same TMDC, to others where the 2D phases may change as function of the intercalated dose. Disordered intercalated phases where no reconstructions are observed are also considered. Also very likely, coverage and reconstructions may vary as function of the fractional charge transferred to the host material. The intercalated atoms ionize by donating part of their charge to the TMDC and simultaneously effectively reduce their size. However,

as they cede electrons, they become more positively charged and their mutual interaction increases[12]. For this reason, low density phase are often observed.

3.3 The influence of the substrate

2D TMDCs can be influenced by the supporting substrate. Surface roughness, the presence of defects or impurities at the interface, charge transfer and dielectric surroundings can in fact drastically alter the intrinsic properties of the 2D material and their influence becomes particularly crucial in the case of the single layer. Although vdW heterostructures and suspended layers (obtained by etching the substrate, for instance) allow for fabrication of *quasi-freestanding* materials, in many other cases getting rid completely of the substrate, and with it of any related form of perturbation, is an almost impossible task: 2D materials need in fact a physical support. This issue prompts fundamental questions on the intrinsic nature of low dimensional systems: are 2D materials the same when supported by a substrate and when they are suspended? How far? In this section we will address the problem in a transversal and general fashion. Special cases will be studied more in details in the experimental part.

Performances of transistors based on 2D materials can increase substantially when the 2D layer is placed on a substrate with which it forms a clean and sharp surface, as demonstrated for graphene and TMDCs transferred on h-BN[13]. Impurities and/or structural point defects act as electronic scattering centers, which decreases charge carrier mobility.

Besides transport, the substrate can perturb the intrinsic opto-electronic properties of the supported 2D material more deeply in the band structure. Signatures of these perturbations can be captured by spectroscopy techniques such as photoluminescence (PL), Raman scattering or photoemission. Strain may have great influence on electronic properties since modified lattice constants or induced structural transitions can drastically change the electron energy band structure. This does not occur only on epitaxial systems but also to exfoliated suspended 2D TMDCs. Conley at al. demonstrated that direct to indirect bandgap transition with strongly suppressed and redshifted PL is achieved by applying uniaxial tensile strain up to 1.8% in suspended MoS_2[14]. In parallel, strain can also affect the Raman-active phonon dispersion of TMDC by softening certain sensitive in-plane phonon modes, like the E^1_{2g} mode in MoS_2, as demonstrated in several Raman spectroscopy studies[15]. Out-of-plane modes of TMDCs appear instead more robust against strain perturbation.

Major effects in the electronic band structure occur, however, for single layer epitaxial TMDCs when the interaction with the substrate is particularly strong. As result of the hybridization between the atomic orbitals of the overlayer and the substrate, interface states may form. This effect was demonstrated by Bruix et al. for single layer MoS_2 grown

on Au(111) where the experimental photoemission spectrum shows remarkable differences with respect to DFT predictions[16] (fig 3.2a). This observation was then confirmed by Krane and coworkers, who measured quasi-freestanding electrical and optical bandgaps for MoS_2 flakes suspended on nanometer sized vacancy islands of the substrate formed during the growth process. Interestingly, the gap values differ from those measured from other MoS_2 flakes of the same sample lying instead in direct contact with the gold substrate[17] (see figure 3.2b-d) .

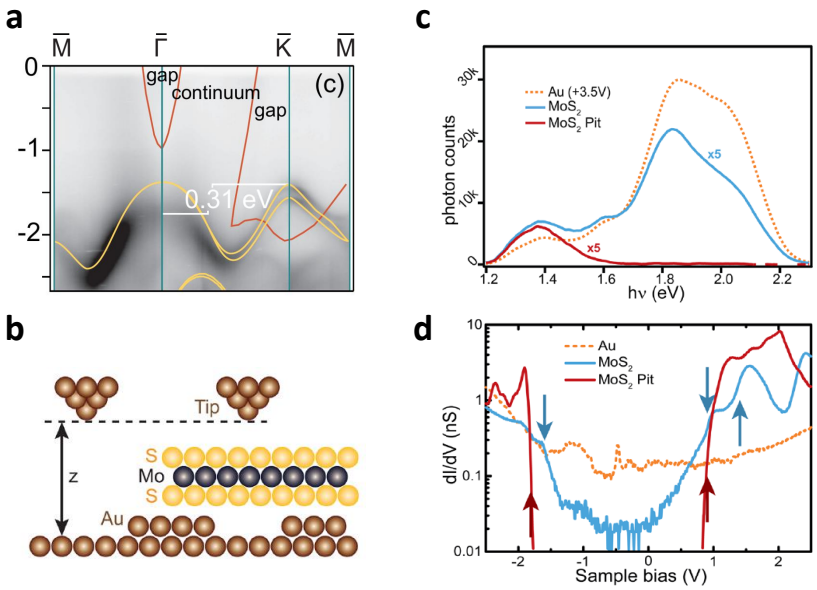

Figure 3.2: (a) experimental photoemission intensity of epitaxial single layer MoS_2 on Au(111) and comparison with the theoretical dispersion for a free standing layer (yellow solid lines), respectively measured and calculted by Bruix et al.[16]; (b) sketch of MoS_2 flake suspended on a MoS_2 vacancy island during scanning tunneling spectroscopy (STS) measurements; (c-d) dI/dV and PL spectra taken on Au(111) (orange), MoS_2on Au(111) (blue) and MoS_2 on a vacancy (red). Images (b-d) are taken from Krane et al.[17].

Besides orbital hybridization, charge transfer between the TMDC layer and its metallic substrate can also occur, the efficiency and direction of the process being linked to the difference in the work function between the two materials. Metallic substrates act in fact as real charge reservoirs that, by injecting (or draining) electrons to (from) a 2D semiconductor, can substantially dope it. This effect is visible as a rigid band shift in photoemission spectra and it may give rise to novel properties for the overlayer. It is well known that extra charge transfer towards 2D TMDCs can tune the concentration of neutral and charged excitons in the material and affect the electron-hole recombination process, with visible effects on PL efficiency and exciton lifetime. In fact, in absence of doping, emission from neutral excitons is dominant, whereas in presence of net n-doping, the population of charged excitons, *i.e.* trions, is increased. Due to the larger binding energy and the lower quantum yield, trions correspond to light emission at lower frequencies and they are weaker emitters than excitons[18].

PL properties of 2D TMDCs have also strong correlations with the surrounding dielectric environment. A substrate in fact can "screen" the Coulomb repulsive interaction between electrons in the thin film and modify the excitonic binding energy and, as a consequence, its optical bandgap. This occurs especially when the substrate possess a large dielectric constant compared to the 2D overlayer. This effect was demonstrated by Ugeda et al. who measured 51% reduction in exciton binding energy for $MoSe_2$ grown on cleaved graphite (HOPG), due to the stronger substrate screening compared to the case when it is grown on bilayer graphene on SiC[19].

This short discussion aimed to highlight the numerous ways a substrate can alter the intrinsic properties predicted for a freestanding 2D TMDCs. Obviously, the extent to which these properties are altered varies according to the *coupling* strength between the 2D layer and its substrate. In broad terms, the coupling strength relates to the interaction forces acting between overlayer and substrate and the degree of hybridization of their bands. From a structural standpoint, in epitaxial systems, it can also be visualized in terms of corrugation of the 2D layer. We already referred to that at the end of chapter 2 while discussing different types of moiré superstructures: in weakly interacting (coupled) systems, *e.g.* graphene on Ir[20], the 2D layer is only slightly deformed and this is associated to a smooth superpotential, whereas for a strongly interacting (coupled) systems, *e.g.* graphene on Ru[21], large corrugation and in-plane deformation are measured in both the 2D film and the substrate. While numerous studies have already been published concerning graphene, not much is known in the case of 2D TMDCs, perhaps because only on a limited number of substrates compared to graphene.

Like it was shown with other 2D materials, the interaction is not always deleterious: it can be exploited to modify the intrinsic properties or to enrich them in a desirable way. Whenever its influence needs to be eliminated, transfer of the 2D material to another one, onto which the interaction is less severe, may be considered. While transfer is well-suited starting from weakly interacting substrates, it does not seem feasible in the case of strongly bonded TMDC grown on metals and semiconductors. In these cases one may want to reduce or even suppress the interaction with the substrate, *i.e.* to decouple the 2D material from its substrate. Also in this case, pioneering works have been attempted with graphene grown on metals, specifically by intercalating atomic species between the 2D layer and substrate in order to decouple them both physically and electronically[22]. To our knowledge, at the moment only one single case has been reported of metal intercalation of a single layer TMDC epitaxially epitaxially grown on a metal substrate[23]. To this work, we will add our investigations carried out on MoS_2 intercalation by alkali metal and described in chapter 7 of this manuscript.

3.4 Dichalcogenide alloys and Janus materials

Alloying semiconductors has been a widely used strategy to tailor opto-electronics properties in bulk semiconducting materials, and a key ingredient in the elaboration of vertical heterostructures. By gradually varying the stoichiometric composition between elements in a semiconductor alloy, one can continuously tune the bandgap between the two extreme values corresponding to the pure stoichiometric compounds. This goal has been achieved also in TMDCs by synthesizing ternary alloy MX_xY_{1-x} nanosheets with a variable content of the two chalcogen species X and Y. Several methods have been reported in literature to obtain TMDC ternary alloys, going from the codeposition of the two chalcogen species from the pure powder precursors in a CVD setup [24], to the anionic substitution of the chalcogen X atoms by annealing in the gaseous atmosphere of a Y species precursor. Both sulfurization and selenization of selenides and sulfides respectively were reported in literature[25; 26]. Taghinejad et al.[25] used a controlled sulfurization process implemented in a CVD setup to replace Se atoms from as grown $MoSe_2$ crystal. The temperature was varied along the process from 750°C to 950°C, enabling the gradual substitution of Se atoms until the full conversion into MoS_2. PL and Raman spectra measured at different steps along the process, *i.e.* at different temperatures, demonstrate a continuous shift of the emission wavelength and vibration mode energy between those of pure $MoSe_2$ and MoS_2. Although it is not clear if the time variable plays a role into that, the temperature ramp is justified because a series of kinetic barriers need to be overcome, whose height is related to diffusion, presence of defects, etc. DFT calculations suggest a "vacancy-mediated mechanism" for the anionic substitution in dichalcogenides where the substituting element (S in the above case) binds to host material vacancies (Se) and then diffuses through the lattice. In this proposed picture, it turns out that a defective materials is more prone towards anionic substitution than a less defective one.

A careful choice of temperature can be operated to selectively overcome kinetics barriers. For instance one could try to control the reaction in order to promote substitution of the chalcogens located on the top layer but not those at the bottom. Intuitively, in fact, the energetic barrier associated to the substitution of bottom chalcogens is higher, since a diffusion step through the lattice is necessary to reach the atomic site. This fact was experimentally proved by Zhang et al. who demonstrated that if sulfurization is carried out at temperatures above 750 °C but below 850°C an ordered S-Mo-Se alloy can form, whereas if the process is carried out at higher temperature a full conversion of $MoSe_2$ into MoS_2 is obtained[27]. This peculiar kind of ordered XMY alloy where the metal plane is sandwiched between two different chalcogen planes, X and Y, has been called *Janus* after the bi-face roman god. This configuration breaks the out-of-plane mirror symmetry characteristic of all the TMDCs and introduces an intrinsic built-in electric dipole in the structure owing to the vertical electronic density imbalance. In Janus dichalcogenides a series of appealing properties can be found, which do not exist in conventional TMDC ones such as Rashba type spin splitting in the electronic bands[28] and natural strong out-

of-plane piezoelectricity (TMDCs have strong piezoelectric coefficient only in-plane)[29].

The opposite process, namely the selenization of a disulfide species to form a Janus structure, was demonstrated by Lu and coworkers[30]. The native species (MoS_2) is firstly exposed to H_2 plasma to strip the top layer S atoms and replace them with H. This intermediate step preceeding the selenization is fundamental since diselenides are thermodynamically less stable than corresponding disulfides - most probably because of the larger atomic size of selenium and the relative chalcogen-metal bond lengths - and the substitution process is thermodynamically unfavored. Also in this case the optimized temperature for selenization is found between 350°C and 450°C, whereas higher temperature leads to vacancies and disordered alloy.

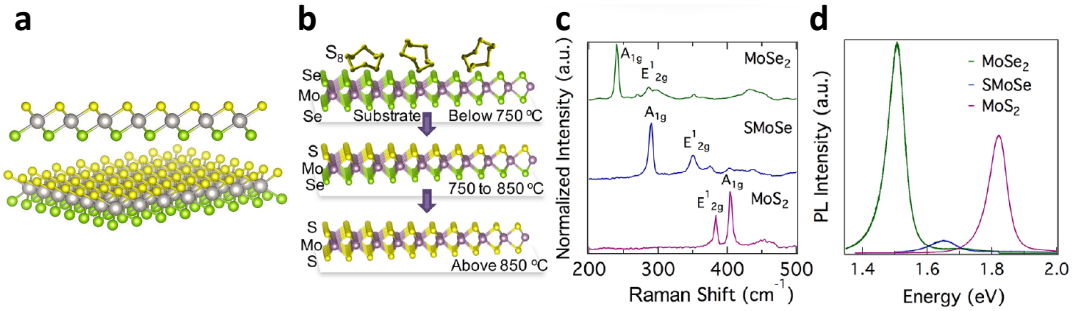

Figure 3.3: (a) sketch of Janus dichalcogenide structure; (b) mechanism proposed by Zhang et al. for the sulfurization of monolayer $MoSe_2$ in a CVD setup leading to Janus type MoSeS and to pure MoS_2 ; (c-d) Raman and PL spectra (532nm laser excitation) of $MoSe_2$, Janus type MoSeS alloy and MoS_2 corresponding to diagram in (b); images (b-d) are taken from Ref.[27].

Bibliography

[1] G. Eda, T. Fujita, H. Yamaguchi, D. Voiry, M. Chen, and M. Chhowalla, "Coherent atomic and electronic heterostructures of single-layer MoS_2," *ACS Nano*, vol. 6, no. 8, pp. 7311–7317, 2012.

[2] X. Lin, J. Lu, Y. Shao, Y. Zhang, X. Wu, J. Pan, L. Gao, S. Zhu, K. Qian, Y. Zhang, *et al.*, "Intrinsically patterned two-dimensional materials for selective adsorption of molecules and nanoclusters," *Nature Materials*, vol. 16, no. 7, p. 717, 2017.

[3] A. N. Enyashin, L. Yadgarov, L. Houben, I. Popov, M. Weidenbach, R. Tenne, M. Bar-Sadan, and G. Seifert, "New route for stabilization of 1T-WS_2 and MoS_2 phases," *The Journal of Physical Chemistry C*, vol. 115, no. 50, pp. 24586–24591, 2011.

[4] G. Eda, H. Yamaguchi, D. Voiry, T. Fujita, M. Chen, and M. Chhowalla, "Photolumi-

nescence from chemically exfoliated MoS_2," *Nano Letters*, vol. 11, no. 12, pp. 5111–5116, 2011.

[5] M. Py and R. Haering, "Structural destabilization induced by lithium intercalation in MoS_2 and related compounds," *Canadian Journal of Physics*, vol. 61, no. 1, pp. 76–84, 1983.

[6] Y. Li, K.-A. N. Duerloo, K. Wauson, and E. J. Reed, "Structural semiconductor-to-semimetal phase transition in two-dimensional materials induced by electrostatic gating," *Nature Communications*, vol. 7, p. 10671, 2016.

[7] Y.-C. Lin, D. O. Dumcenco, Y.-S. Huang, and K. Suenaga, "Atomic mechanism of the semiconducting-to-metallic phase transition in single-layered MoS_2," *Nature Nanotechnology*, vol. 9, no. 5, p. 391, 2014.

[8] H. P. Hughes and H. Starnberg, *Electron spectroscopies applied to low-dimensional structures*, vol. 24. Springer Science & Business Media, 2001.

[9] C. Pettenkofer and W. Jaegermann, "Charge-density-wave transformation induced by Na intercalation into 1T-TaS_2," *Physical Review B*, vol. 50, no. 12, p. 8816, 1994.

[10] J. A. Woollam and R. B. Somoano, "Physics and chemistry of MoS_2 intercalation compounds," *Materials Science and Engineering*, vol. 31, pp. 289–295, 1977.

[11] R. Friend and A. Yoffe, "Electronic properties of intercalation complexes of the transition metal dichalcogenides," *Advances in Physics*, vol. 36, no. 1, pp. 1–94, 1987.

[12] J. L. LaRue, J. D. White, N. H. Nahler, Z. Liu, Y. Sun, P. Pianetta, D. J. Auerbach, and A. M. Wodtke, "The work function of submonolayer cesium-covered gold: A photoelectron spectroscopy study," *The Journal of Chemical Physics*, vol. 129, no. 2, p. 024709, 2008.

[13] C. R. Dean, A. F. Young, I. Meric, C. Lee, L. Wang, S. Sorgenfrei, K. Watanabe, T. Taniguchi, P. Kim, K. L. Shepard, *et al.*, "Boron nitride substrates for high-quality graphene electronics," *Nature Nanotechnology*, vol. 5, no. 10, p. 722, 2010.

[14] H. J. Conley, B. Wang, J. I. Ziegler, R. F. Haglund Jr, S. T. Pantelides, and K. I. Bolotin, "Bandgap engineering of strained monolayer and bilayer MoS_2," *Nano Letters*, vol. 13, no. 8, pp. 3626–3630, 2013.

[15] C. Zhu, G. Wang, B. Liu, X. Marie, X. Qiao, X. Zhang, X. Wu, H. Fan, P. Tan, T. Amand, *et al.*, "Strain tuning of optical emission energy and polarization in monolayer and bilayer MoS_2," *Physical Review B*, vol. 88, no. 12, p. 121301, 2013.

[16] A. Bruix, J. A. Miwa, N. Hauptmann, D. Wegner, S. Ulstrup, S. S. Grønborg, C. E. Sanders, M. Dendzik, A. G. Čabo, M. Bianchi, *et al.*, "Single-layer MoS_2 on Au(111):

Band gap renormalization and substrate interaction," *Physical Review B*, vol. 93, no. 16, p. 165422, 2016.

[17] N. Krane, C. Lotze, J. M. Lager, G. Reecht, and K. J. Franke, "Electronic structure and luminescence of quasi-freestanding MoS_2 nanopatches on Au(111)," *Nano Letters*, vol. 16, no. 8, pp. 5163–5168, 2016.

[18] K. F. Mak, K. He, C. Lee, G. H. Lee, J. Hone, T. F. Heinz, and J. Shan, "Tightly bound trions in monolayer MoS_2," *Nature Materials*, vol. 12, no. 3, p. 207, 2013.

[19] M. M. Ugeda, A. J. Bradley, S.-F. Shi, H. Felipe, Y. Zhang, D. Y. Qiu, W. Ruan, S.-K. Mo, Z. Hussain, Z.-X. Shen, *et al.*, "Giant bandgap renormalization and excitonic effects in a monolayer transition metal dichalcogenide semiconductor," *Nature Materials*, vol. 13, no. 12, p. 1091, 2014.

[20] N. Blanc, J. Coraux, C. Vo-Van, O. Geaymond, G. Renaud, *et al.*, "Local deformations and incommensurability of high-quality epitaxial graphene on a weakly interacting transition metal," *Physical Review B*, vol. 86, no. 23, p. 235439, 2012.

[21] D. Martoccia, P. Willmott, T. Brugger, M. Björck, S. Günther, C. Schlepütz, A. Cervellino, S. Pauli, B. Patterson, S. Marchini, *et al.*, "Graphene on Ru(0001): a 25×25 supercell," *Physical Review Letters*, vol. 101, no. 12, p. 126102, 2008.

[22] M. Petrović, I. Š. Rakić, S. Runte, C. Busse, J. Sadowski, P. Lazić, I. Pletikosić, Z.-H. Pan, M. Milun, P. Pervan, *et al.*, "The mechanism of caesium intercalation of graphene," *Nature Communications*, vol. 4, p. 2772, 2013.

[23] S. K. Mahatha, M. Dendzik, C. E. Sanders, M. Michiardi, M. Bianchi, J. A. Miwa, and P. Hofmann, "Quasi-free-standing single-layer WS_2 achieved by intercalation," *Physical Review Materials*, vol. 2, no. 12, p. 124001, 2018.

[24] H. Li, X. Duan, X. Wu, X. Zhuang, H. Zhou, Q. Zhang, X. Zhu, W. Hu, P. Ren, P. Guo, *et al.*, "Growth of alloy $MoS_{2x}Se_{2(1-x)}$ nanosheets with fully tunable chemical compositions and optical properties," *Journal of the American Chemical Society*, vol. 136, no. 10, pp. 3756–3759, 2014.

[25] H. Taghinejad, D. A. Rehn, C. Muccianti, A. A. Eftekhar, M. Tian, T. Fan, X. Zhang, Y. Meng, Y. Chen, T.-V. Nguyen, *et al.*, "Defect-mediated alloying of monolayer transition-metal dichalcogenides," *ACS Nano*, vol. 12, no. 12, pp. 12795–12804, 2018.

[26] S.-H. Su, Y.-T. Hsu, Y.-H. Chang, M.-H. Chiu, C.-L. Hsu, W.-T. Hsu, W.-H. Chang, J.-H. He, and L.-J. Li, "Band gap-tunable molybdenum sulfide selenide monolayer alloy," *Small*, vol. 10, no. 13, pp. 2589–2594, 2014.

[27] J. Zhang, S. Jia, I. Kholmanov, L. Dong, D. Er, W. Chen, H. Guo, Z. Jin, V. B. Shenoy, L. Shi, *et al.*, "Janus monolayer transition-metal dichalcogenides," *ACS Nano*, vol. 11, no. 8, pp. 8192–8198, 2017.

[28] Y. Cheng, Z. Zhu, M. Tahir, and U. Schwingenschlögl, "Spin-orbit–induced spin splittings in polar transition metal dichalcogenide monolayers," *EPL (Europhysics Letters)*, vol. 102, no. 5, p. 57001, 2013.

[29] L. Dong, J. Lou, and V. B. Shenoy, "Large in-plane and vertical piezoelectricity in janus transition metal dichalchogenides," *ACS Nano*, vol. 11, no. 8, pp. 8242–8248, 2017.

[30] A.-Y. Lu, H. Zhu, J. Xiao, C.-P. Chuu, Y. Han, M.-H. Chiu, C.-C. Cheng, C.-W. Yang, K.-H. Wei, Y. Yang, *et al.*, "Janus monolayers of transition metal dichalcogenides," *Nature Nanotechnology*, vol. 12, no. 8, p. 744, 2017.

Chapter 4

Methods and working environment

4.1 Elements of kinematical diffraction theory

4.1.1 X-ray interaction with matter

Since their discovery in 1895 by W. C. Röntgen, who was awarded the first Nobel prize six years later, X-rays have been established as a very powerful and versatile tool to probe matter, whose applications span a wide and ever growing range of scattering, spectroscopy and imaging techniques. We may wonder which are the properties that make X-rays so special. Without aiming to be exhaustive, we can point out some main characteristics. Firstly, X-rays are able to probe condensed matter deeply and non destructively, with penetration depths varying with energy and material density. This allows scientists to study selected inner regions in the samples which are not directly accessible from outside - for instance buried interface in heterostructures or inclusions in crystalline solids - by preserving the sample during the measurements. Secondly, *hard* X-rays (with photon energies above 5-10keV), have wavelengths comparable to interatomic distances in crystalline materials. Because of that, crystals act as interference gratings for X-ray radiation, producing diffractive phenomena that unveil the atomic structure. In addition, all along their spectral range, *hard* and *soft* (energies typically below 5keV) X-rays might be absorbed by the atoms, enabling electronic transitions from core and valence levels respectively. X-rays absorption subsequently leads to a range of relaxation phenomena from photoelectric effect to fluorescence, that enable several types of spectroscopy techniques.

It might be appropriate already at this point to highlight another property of X-rays particularly important in surface X-ray diffraction (SXRD), which is the X-rays surface sensitivity under grazing incidence conditions. It stems from *Snell's law* and the nature of X-rays refractive index, which is known to be lower than 1 for X-rays travelling in any medium. Snell's law is expressed as following:

$$\frac{n_1}{n_2} = \frac{cos\alpha'}{cos\alpha} \tag{4.1}$$

where α and α' represent the angle formed with the surface by the incident and refracted

beams respectively, and n_1 and n_2 are the refractive index of the propagation medium and the probed material. Typically, in a X-ray experiment performed in vacuum ($n_1 = 1$) - as all the ones reported in this work - a travelling X-ray beam impinges onto the material surface ($n_2 < 1$) and is refracted inside the second medium with an angle α' smaller than α. Intuitively from Snell's law if we continue to reduce the incidence angle α, we will get to a point where $\alpha' = 0$. This limit case is called *total external reflection* since the X-ray beam cannot be transmitted beyond the interface. The *critical angle* α_c at which it occurs can be calculated as follows:

$$\alpha_c = \sqrt{2\delta} \tag{4.2}$$

where δ is a small value usually of the order of magnitude of 10^{-5} - 10^{-6} in solids. It results that the critical angles are in practice lower than 0.3mrad. This expression descends from the complex X-rays refractive index definition, where δ is included in the real part, whereas β represents the imaginary part:

$$n = 1 - \delta + i\beta. \tag{4.3}$$

It can also be demonstrated that for any $\alpha < \alpha_c$ the imaginary part of the refractive wave becomes prominent: the wave amplitude is strongly damped and propagation is confined to few nanometers below the interface - the wave is usually said *evanescent*. In a qualitative picture, it turns out that below the critical angle the penetration of the X-ray beam inside matter is limited to a dozen of nanometers and the surface sensitivity is extremely enhanced at the expense of the bulk signal. This is the reason why surface science experiments are usually performed at grazing incidence conditions.

4.1.2 Diffraction from a bulk crystal

It is universally known that crystalline materials display long range positional order. Ideally, crystals are in fact described as an infinite array of identical unit cells, each containing a finite number of atoms, periodically repeated on a lattice, the *Bravais Lattice*, along the three space dimensions. Inside each unit cells the atomic positions can be described according to a specific *symmetry point group*. Translational and point symmetry in crystals were established shortly after the advent of the X-ray sources by von Laue and the Braggs and are at the basis of the analysis of diffraction data. In this section we will not develop in detail all the aspects of diffraction theory which are reported in common solid state physics and crystallography books. The goal is instead to recall the main concepts that will be used later in this manuscript. In order to introduce the fundamental quantities more clearly, we will build the crystal "in stages", starting from the scattering of X-rays with a single free electron and then considering in sequence more complex systems such as atoms, unit cells and finally the ideal infinite crystal.

Diffraction theory is a purely classical description. In such a picture, electrons are the most elementary scattering particle for X-rays. The electric field component of the electromagnetic wave makes electrons re-irradiate at exactly the same frequency. This process is therefore *elastic*. Energy transfer to electrons, *i.e.* inelastic scattering, is also possible, but we will not consider it here. Besides that, the theory relies on two approximations: first, the point of observation is in the far field limit, *i.e.* at long distance from the scattering objects (*Fraunhofer limit*). This allows treating both incoming and outgoing waves as plane waves. Second, multiple scattering is neglected (*kinematical approximation*). For a single free electron in the space the scattering event is described by the *Thomson's model*, depicted in figure 4.1a. Neglecting the polarization, an incident plane wave with amplitude E_0 and wavevector $\vec{k_0}$ is elastically scattered by an electron located at $\vec{r_e}$ from the observer. The outgoing plane wave has the same wavevector modulus as the incident one ($|\vec{k_1}| = |\vec{k_0}|$) by virtue of the elasticity of the scattering process and the scattered amplitude is given by :

$$E_1 = E_0 r_0 \frac{1}{R_0} e^{i\vec{k_1}\cdot\vec{r_e}} e^{-i\vec{k_0}\cdot\vec{r_e}} \tag{4.4}$$

where $r_0 = e^2/4\pi\epsilon_0 mc^2$ is the electron *Thomson scattering length*, which is equal to 2.82×10^{-5}Å, and $\frac{1}{R_0}$ is the distance to the observer . Its small value justifies the use of the kinematical approximation - *i.e.* multiple scattering does not occur - by keeping the probability of the scattering event very low.

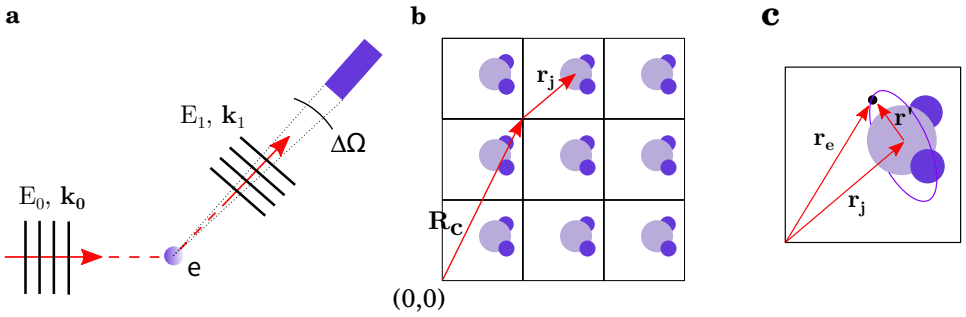

Figure 4.1: (a)Thompson scattering: a plane electromagnetic wave with amplitude E_0 and momentum $\vec{k_0}$ is scattered by a free electron that re-irradiates the wave elastically. In a scattering experiment a detector located at a distance R intercepts a portion of scattered radiation under the solid angle $\Delta\Omega$ along the direction $\vec{k_1}$; (b) sketch of a crystal: an array of square unit cells located at the generic position $\vec{R_c}$ contains a number j of atoms at position $\vec{r_j}$. (c) inside each atom an electron is pointed out by the vector $\vec{r_e}$ with respect to the unit cell origin, $\vec{r'}$ with respect to atom.

Now we add one step of complexity and we consider a whole atom j in place of a single electron. The most effective approach to accounts for scattering from multiple electrons around an atomic nucleus located at $\vec{r_j}$ is to use the electron density distribution function $\rho(\vec{r'})$, where $\vec{r'} = \vec{r_e} - \vec{r_j}$, instead of the sum of discrete charges. The total scattered amplitude turns out to be the integral of different volume element contributions located

at a distance $\vec{r'}$ from the atomic core with mathematical expression:

$$E_1 = E_0 r_0 \int \rho(\vec{r'}) e^{i\vec{Q}\cdot(\vec{r_j}+\vec{r'})} d^3\vec{r'} \tag{4.5}$$

where:

$$\vec{Q} = \vec{k_1} - \vec{k_0}$$

is known as *momentum transfer vector*. It keeps track of the phase difference between two waves scattered from different volume elements in the electronic cloud, as shown in figure 4.1b. The expression in (4.5) can be rearranged in a more compact way as following:

$$E_1 = E_0 r_0 f(\vec{Q}) e^{i\vec{Q}\cdot\vec{r_j}} \tag{4.6}$$

where:

$$f(\vec{Q}) = \int \rho(\vec{r'}) e^{i\vec{Q}\cdot\vec{r'}} d^3\vec{r'}. \tag{4.7}$$

f($\vec{Q}$) is called the *atomic form factor* and represents the *Fourier transform* of the electron density within the atom. Remarkably, in the limit of $\vec{Q} \longrightarrow 0$ all the volume elements scatter in phase and $f = Z$, *i.e.* the atomic number.

Generally, a unit cell may contain more than one atom, even of different types. Its periodic replication along the three space directions generates the ideal crystal. Figure (4.1b) depicts this model and clarifies the adopted labelling, where $\vec{R_c}$ defines the positions of the unit cells in the crystal and $\vec{r_j}$ the position of the j-th atom within the unit cell. The total amplitude scattered by the crystal can be now re-written as in 4.8, where two terms have been highlighted, a sum over all the j atoms in the unit cell and one over all the unit cells in the lattice:

$$E_1 = E_0 r_0 \sum_{\vec{r_j}} f_j(\vec{Q}) e^{i\vec{Q}\cdot\vec{r_j}} \sum_{\vec{R_c}} e^{i\vec{Q}\cdot\vec{R_c}}. \tag{4.8}$$

Similarly to 4.6, the scattering amplitude formula can be rearranged as:

$$E_1 = E_0 r_0 F(\vec{Q}) \sum_{\vec{R_c}} e^{i\vec{Q}\cdot\vec{R_c}} \tag{4.9}$$

$$F(\vec{Q}) = \sum_{\vec{r_j}} f_j(\vec{Q}) e^{i\vec{Q}\cdot\vec{r_j}}. \tag{4.10}$$

The summation over all the atoms in the unit cell coincides with the *Fourier transform* of the electron density in the unit cell an it is known as the *unit cell structure factor F($\vec{Q}$)*. The amplitude of the structure factor is a combination of all atomic factors and it is directly related to the electronic density of the elements, while the phase term encloses the information about the relative positions of the atoms inside the unit cell.

The second sum in eq. (4.8) runs over all the unit cells in the crystal and it is commonly known as the *lattice sum*. It accounts for the constructive interference of the waves

scattered from the whole crystal and determines the peak positions in the diffraction pattern. To highlight this fact it is sufficient to rewrite eq. (4.9) as follows, considering for the sake of simplicity a block shaped unit cell lattice with primitive vectors $\vec{a_1}$, $\vec{a_2}$, $\vec{a_3}$:

$$E_1 = E_0 r_0 F(\vec{Q}) \sum_{n_1=0}^{N_1} \sum_{n_2=0}^{N_2} \sum_{n_3=0}^{N_3} e^{i\vec{Q}\cdot(n_1\vec{a_1}+n_2\vec{a_2}+n_3\vec{a_3})} \tag{4.11}$$

$$= E_0 r_0 F(\vec{Q}) S_{N_1}(\vec{Q}\cdot\vec{a_1}) S_{N_2}(\vec{Q}\cdot\vec{a_2}) S_{N_3}(\vec{Q}\cdot\vec{a_3}) \tag{4.12}$$

The scattering amplitude depends on the geometric sums $S_{N_i}(\vec{Q}\cdot\vec{a_i})$ over all the cells inside the crystals, which are called the *N-slit interference functions*. Because experimentally one always measures an intensity, *i.e.* the square of the scattering amplitude, we are interested to know the absolute square of the $S_{N_i}(\vec{Q}\cdot\vec{a_i})$ which can be expressed as[1]:

$$|S_{N_i}|^2 = \frac{|sin^2(\frac{1}{2}\vec{Q}\cdot N_i\vec{a_i})|}{|sin^2(\frac{1}{2}\vec{Q}\cdot\vec{a_i})|} \tag{4.13}$$

It can be demonstrated that as long as the number of unit cells is large enough, *i.e.* for large values of (n_i), the interference sum is sharply peaked whenever $Q = 2\pi m$, (m is integer). It follows that the diffracted intensity of the crystal has a strong maximum whenever $\vec{Q}$ meets simultaneously the three following conditions:

$$\vec{Q}\cdot\vec{a_1} = 2\pi h \tag{4.14}$$

$$\vec{Q}\cdot\vec{a_2} = 2\pi k \tag{4.15}$$

$$\vec{Q}\cdot\vec{a_3} = 2\pi l \tag{4.16}$$

These relationships are known as *Laue's conditions* for diffraction and they are verified for all the generic vectors $\vec{Q} = h\vec{b_1} + k\vec{b_2} + l\vec{b_3}$ belonging to the *reciprocal lattice* associated to the crystal. (h, k, l) are integer numbers known as *Miller indices*. They univocally define the reciprocal space points where a diffraction spot is expected. According to these results, the diffracted intensity pattern of an ideal infinite crystal can be described mathematically as a three-dimensional set of Dirac δ function centered on the $\vec{Q}$ vectors which fulfills the Laue's conditions. In reality, instead of Dirac functions, finite size and intensity functions are observed, due to the finite size of the crystal.

It can be demonstrated that Laue's conditions are equivalent to the Bragg's law historically established in a separated framework:

$$\lambda = 2d_{hkl}\sin\theta \tag{4.17}$$

where θ is the incidence and outgoing angle (also called Bragg's angle) of the X-ray beam with respect to a set of parallel planes whose interplanar distance is d_{hkl}. Bragg's law is the first elementary description of X-ray diffraction in a crystal, where diffraction is interpreted as the constructive interference of waves reflected by parallel atomic planes

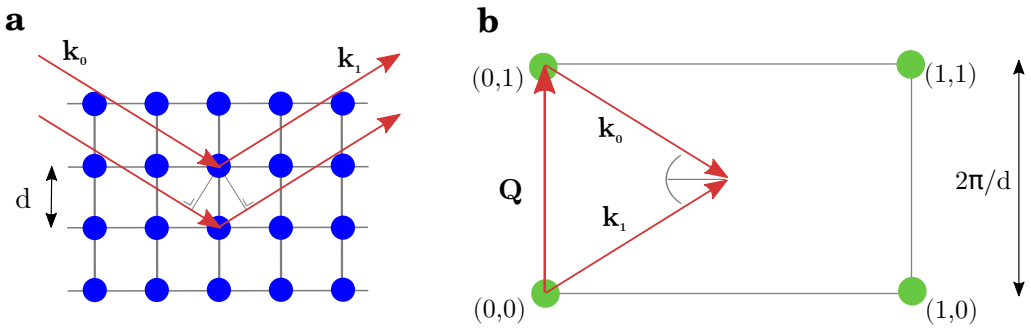

Figure 4.2: (a) Bragg's law: a set of parallel planes in a crystal with interplanar distance d reflects the incident X-ray beam with Bragg angle θ. (b) Laue's conditions: the momentum transfer vector belongs to the reciprocal lattice and its length is inversely proportional to d.

(figure 4.2a). An intimate relationship descends from the equivalence between Laue's and Bragg's laws:

- each set of Miller index that satisfy Laue's conditions defines a vector Q perpendicular to the diffracting planes.
- the distance d between the scattering planes is inversely proportional to the modulus of the Q vector.

4.1.3 Direct and indirect methods for solving crystal structures

During a diffraction experiment only the scattered intensity is measurable, which is a scalar quantity proportional to the structure factor square. As shown by eq.4.10, the structure factor is a complex number made up of an amplitude and a phase component. While calculating the intensity, *i.e.* the product of the structure factor by its complex conjugate, only the amplitude is conserved while the information contained in the phase is lost. This is referred to in diffraction as the *phase problem*. If instead the intensity were accessible experimentally, we would be able to retrieve all the structural information contained in a crystal by simply Fourier back-transforming the measurement. On the contrary, only interplanar distances can be known through Bragg's law from a diffraction experiment, whereas absolute atomic positions are not directly accessible.

In crystallography, structure solution usually proceeds by two distinct steps. Firstly, an algorithm which assumes no preconceived models is used to estimate the phases and find an approximated model of the real structure; secondly a process of structural refinement simulates the experimental data by a systematic variation of free parameters of a fitting function. In general, the fitting step is performed by algorithmic processes that aim at minimizing the deviation of the calculated intensities from the experimental one, *e.g. Levenberg-Marquardt* method. Other methods are also employed, *e.g. simulated annealing*, etc. The first step could be replaced in alternative by so-called *indirect* methods as *Patterson function* or *Fourier Difference map*. These methods apply the Fourier back-transform

to the experimental available data, *e.g.* intensity, and offer a partial but useful insight into the atomic structure even without knowing the phase. Although indirect methods do not return the real structure, a trial model can be derived from their results, which might contain a likely configurations of atoms in the unit cell that could be better refined by means of model-fitting procedures. We present here the Patterson function method, which has been used to perform the diffraction analysis of $PtSe_2$/Pt(111), a 2D epitaxial system studied during this thesis (see Chapter 7).

By calculating the *inverse fourier tranform* (IFT) of the measured intensity instead of the complex structure factor, one obtains:

$$P(\vec{r}) = \int \rho(\vec{r'})\rho(\vec{r} - \vec{r'})d\vec{r'} \tag{4.18}$$

The function is called *Patterson function* and mathematically represents the electronic density $\rho(\vec{r})$ auto-correlation. The function yields the *relative* distances and angles between atoms in the unit cell. This method is widely applied in surface diffraction. By measuring a set of in-plane reflections it is possible to obtain a 2D *Patterson map*, *i.e.* a contour plot where maxima correspond to interatomic vectors. An experimental example is reported in chapter 7, where the Patterson map has been obtained by calculating the IFT of the in-plane projected intensities of some $PtSe_2$ diffraction rods measured within a range of l-values close to zero:

$$P(xy) = \sum_{h,k} |F_{hkl}|^2 cos[2\pi(hx + ky)] \tag{4.19}$$

The intensity of the Patterson peaks is proportional to the electron density of the atoms that produce that peak. It results that heavy atoms dominate the plot whereas light atoms are only scarcely visible. Intuitively, because two generic $\overrightarrow{AB}$ and $\overrightarrow{BA}$ vectors - A and B are two generic atoms in the unit cell - contribute in the same way to the Patterson function, the latter is always centrosymmetric with respect to the origin. This fact descends straightforwardly from Friedel's law, which states that pairs of opposite reflections (h, k, l) and $(\overline{h}, \overline{k}, \overline{l})$ have the same intensity $|F_{hkl}|^2 = |F_{\overline{hkl}}|^2$ in reciprocal space[1]. In general, the Patterson map possesses the same symmetry as the unit cell plus an inversion center. The origin is the most intense point in the map, since it is proportional to the sum of the of the square electron density of all the atoms.

Generally in a surface diffraction experiment the intensity of integer Bragg peaks of the substrate is much larger than that of the overlayer reflections. In the Patterson map it results that the bulk fully hides the surface structure information. For this reason, it is common practice to remove bulk Bragg reflections and crystal truncation rods - defined later - from the list of experimental structure factor which feed the Patterson function. The Patterson function calculated by omitting integer order reflections is said *distorted*.

[1]This is correct when the X-ray energy is far from the absorption edges of the atoms in the crystal, *i.e.* out of anomalous scattering conditions

The corresponding map shows also negative peaks which do not carry physical information and the positions of the positive peaks might be displaced. When only fractional order peaks are taken into account the Patterson map allows to identify possible distortions inside the 2D lattice.

4.1.4 Diffraction from a surface

In this section we consider the special case of the diffraction by a surface. In first approximation a surface can be defined as a two-dimensional crystal whose thickness is limited to one unit cell (figure 4.3a). In order to calculate the scattering amplitude from a surface, the equation 4.12 can be used with the difference that summation runs only over the two in-plane directions. By assuming that the out-of-plane direction is represented by $\vec{a_3}$, because of the lack of periodicity along this direction, N_3 is equal to 1 and the lattice sum output is independent of the product $\vec{Q} \cdot \vec{a_3}$. Along the $\vec{a_1}$ and $\vec{a_2}$ directions diffraction instead still occurs when Laue's conditions are fulfilled.

$$E_1 = E_0 r_0 F(\vec{Q}) \sum_{n_1,n_2}^{N_1,N_2} e^{2\pi i(hn_1+kn2)} \tag{4.20}$$

Pictorially, we deduce that the diffraction pattern of a pure surface is represented by a set of *rods* of (almost) constant intensity perpendicular to the surface, passing through the nodal points (h, k) in the reciprocal space plane (figure 4.3b).

Although a freestanding single layer might be realized in certain conditions, in reality the closest objects to the idea of surface that scientists commonly handle are either truncated crystals or 2D films grown on bulk substrates (figures 4.3c). The simplest way to calculate the total scattered intensity is to split the problem into two, by calculating the "*bulk*" and the "*surface*" contributions separately. For a rectangular bulk unit cell, the following formula is given by Vlieg[2]:

$$E_1 = E_0 \sum_{n_1,n_2}^{N_1,N_2} e^{2\pi i(hn_1+kn2)} [\underbrace{\sum_{n_3=-\infty}^{0} e^{2\pi i l n_3} e^{\alpha n_3}}_{bulk} + \underbrace{\sum_j f_j e^{-M_j} e^{2\pi i(hx_j+ky_j+lz_j)}}_{surf}] \tag{4.21}$$

The left-most summation yields the rod profile as presented above. The first contribution in the brackets is instead over the bulk unit cells. It sums up a single column of unit cells with identical structure factors and appropriate phase. An attenuation factor α takes into account the X-ray beam absorbed by the crystal. If we evaluate the bulk summation separately and we discard the attenuation factor, which has an effect only near Bragg peaks, one can obtain[2]:

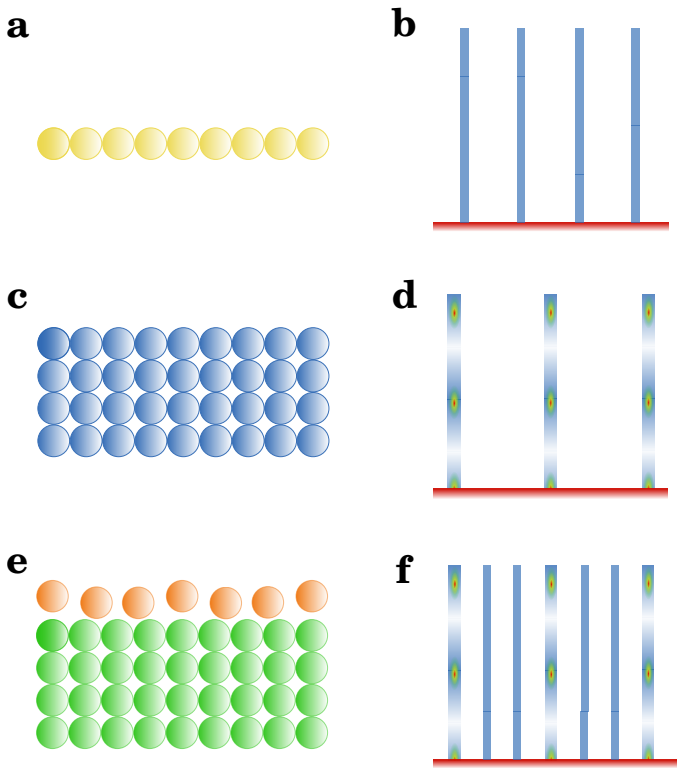

Figure 4.3: two-dimensional real space structures are shown with the corresponding reciprocal space sketches. (a-b): freestanding 2D SL layer crystal: the reciprocal space is made up of diffraction rod with constant intensity; (c-d): truncated crystal: reciprocal space is made by crystal truncation rods (CTRs) having maxima at Bragg positions and non-zero intensity in between; (e-f): 2D layer grown on crystal substrate: the reciprocal space is the sum of CTRs and diffraction rods located at fractional substrate Miller indices.

$$F_{bulk} = \frac{F^{u}_{bulk}}{2\sin(\pi l)} \tag{4.22}$$

This function rapidly rises to high values at integer l, unless symmetry constraints in the unit cell suppress it. However, amplitude is non-zero along the surface normal at any non-integer l-values. Such rods are called *crystal truncation rods* (CTRs) because they arise from the truncated crystal surface. The corresponding reciprocal space is sketched in figure 4.3d.

The second summation within the bracket in equation 4.21 represents the surface contribution. Similarly to the bulk, we evaluate separately the structure factor:

$$F_{surf} = \sum_{j} f_j e^{-M_j} e^{2\pi i(hx_j + ky_j + lz_j)} \tag{4.23}$$

where f_j is the atomic form factor of the elements in the surface unit cell. As we anticipated the surface unit cell can either contain:

- topmost layers of the substrate which may be relaxed (the interlayer distance is different than in the bulk) or reconstructed to reduce the surface energy.

- 2D crystals or ordered arrays of adsorbed atoms, in general chemical species different from the bulk (figure 4.3e). In this case, the surface unit cell could be either the same or a multiple of the bulk unit cell.

The diffraction pattern contains both CTRs and surface rods (figure 4.3f). The total structure factor of a diffraction rod is the interference sum of bulk and surface contributions and, assuming they scatter coherently, the total scattered intensity is the square of their sum:

$$I \propto |F_{tot}|^2 = |F_{bulk} + F_{surf}|^2 \tag{4.24}$$

Rods and CTRs are the study object of *surface X-ray diffraction* (SXRD)[3; 4]. This technique has been applied since the Eighties[5] - when the emergence of synchrotrons boosted the investigation of structural phenomena on surfaces, like for instance relaxation of topmost layers in metals, reconstructions of atoms adsorbed on the surface, interfaces between two heterogeneous crystals and, more recently, new 2D materials. Nowadays, surface physics has been attracting new interest since when 2D materials broke through material science. Two features are essential in SXRD: the use of grazing incidence geometry and a synchrotron X-ray source. We have already explained at the beginning of this chapter that grazing incidence geometry allows total external reflection and enhances surface sensitivity. However the amount of scatterers confined in a surface is much less than in the bulk, which explained why the surface signal is very weak. As we will be able to explain in the next section, the high synchrotron beam brilliance is able to solve this problem.

4.2 Working environment

4.2.1 The synchrotron X-ray source

Most of the experiments described in this work have been carried out using synchrotron X-ray radiation at the *European Synchrotron Radiation Facility* (ESRF) in Grenoble. In this section, we will write a few words describing synchrotron light generation and properties with the goal of highlighting its benefits with respect to standard X-ray sources.

First of all, before being big scientific research laboratories, synchrotrons are big machines built for high quality X-ray beam production. In their storage rings electrons are accelerated to relativistic velocities and forced to maintain a closed path. A broad spectrum of electromagnetic waves spanning from far infrared to hard X-rays is emitted when electrons pass through bending magnets inside the curved sectors of the storage ring and their trajectory is deflected by the Lorentz force. Initially in the Sixties, the *first generation* of synchrotrons was primarily designed for nuclear physics experiments, essentially to

study particles collision events occurring in the tunnel. At that time, emitted synchrotron radiation was actually seen as an unavoidable parasitic effect that however physicists tried to harness. SURF I in Maryland, DESY in Hamburg, or LNF in Frascati (Italy) are examples among the first generation of synchrotrons. Only in 1981 the first dedicated facility designed specifically to generate synchrotron radiation for experimental purposes was opened at *Daresbury* (England) and together with others which came after, they belong to the so-called *second generation*. The *third generation* of synchrotrons, almost all currently operative worldwide, makes use of *insertion devices* to produce X-rays. Thanks to insertion devices X-ray beam has achieved outstanding *brilliance*, *i.e.* the amount of emitted flux per unit area, frequency and solid angle, up to 10^{10} times higher compared to when the first generation of synchrotrons was abandoned. ESRF was the first third generation synchrotron to be completed and at the moment of writing an upgrade is in progress, which will lead to even more powerful performances in terms of beam brilliance and coherence. ESRF-EBS will be the first *fourth generation* synchrotron operative in 2020[6].

We have already introduced bending magnets and insertion devices as the "spots" where electrons generate X-rays while their trajectory is deflected. We make now one step back to proceed with order in describing the synchrotrons most important components. Figure 4.4 shows as example an ESRF sketch. Inside the *LINAC* (1), *i.e.* a linear accelerator, electrons are extracted by thermionic emission from a hot cathode and then pre-accelerated up to hundreds of MeV before entering the *booster* ring (2). In the booster electrons are further accelerated up to the relativistic velocity chosen for their injection in the *storage ring* (3). Once in the storage ring, electrons possess already the designed synchrotron energy necessary to X-ray emission, which is of 6GeV in the case of ESRF. All along their path, electrons move in an evacuated environment with pressure maintained as low as 1×10^{-9} mbar. This condition is essential for operations, because otherwise electrons would lose energy in collisions with air particles. However, collisions with residual gas atoms and molecules cannot be completely avoided and regular supply of electrons in storage ring is effectuated in order to conserve the set current (200 mA at ESRF). A storage ring is made by curved sectors, where electrons are deflected by the Lorentz force applied by the *bending magnets* (4), and straight sectors, where *insertion devices* (5) are positioned. Other elements are also present in between, which are needed for electron beam reshaping (*focusing magnets*) (6) and energy refilling (*RF cavities*).

In a third generation synchrotron like ESRF, the X-ray beam is generated by bending magnets and insertion devices installed all along the storage ring. Each of them is an individual source from which each experimental station, *i.e.* the *beamline*, drains and shapes the X-ray beam to the needs of each experiment. In 2019 ESRF counts 48 beamlines, 14 collect X-rays from a bending magnet source and are labelled *BM* after that, while the remaining use insertion devices and are referred to as *ID* beamlines. Essentially, bending magnets allow radiation emission from the curvature of the electron beam and their spectrum depends both on the applied magnetic field strength B and the energy ε of the

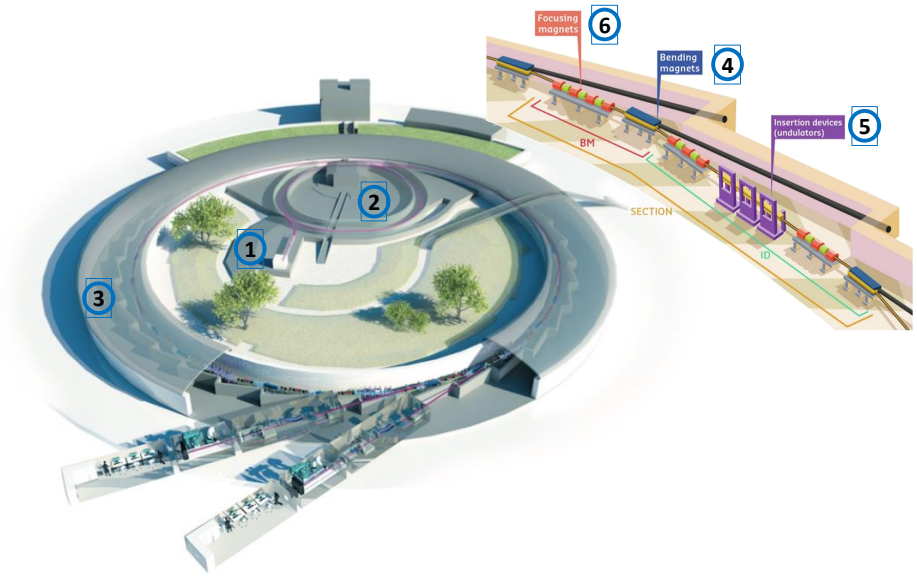

Figure 4.4: Pictorial view of ESRF-the european synchrotron. The numbers show: (1) the LINAC, (2) the booster, (3) the storage ring. In the inset: (4) bending magnets at curved sectors, (5) insertion devices at straight sectors, (6) focusing magnets in between. The image is taken from ESRF website.

electrons in the storage ring, with a *characteristic energy* $\hbar\omega_0$ given by [7]:

$$\hbar\omega_0 = 0.665\varepsilon^2 B. \tag{4.25}$$

Every bending magnet generates a broad continuous spectrum of wavelengths and the *characteristic energy* divides the emitted power exactly in half. The characteristic energy at BM32 - the beamline where most of the experiment described in this work were performed - is 20.6keV. This energy, typical of hard X-rays, makes the beam ideal for diffraction studies.

Insertion devices are instead arrays of magnets arranged in sequence in order to produce magnetic fields that point alternately up and down. When electrons are travelling inside, they are forced to slalom in the plane, emitting radiation at every direction change. If deviations are smaller than the electron beam aperture, the X-ray wave cones emitted at each curve interfere constructively and intensities sum up coherently, *i.e.* the sum of the intensities is elevated to square power. In this case the insertion device is commonly called *undulator*. On the contrary, when the intensity is summed incoherently the insertion device is a *wiggler*. Insertion devices achieve at least three order of magnitude higher brilliance than bending magnets. Moreover, their energy spectrum is almost monochromatic, typically characterized by relative spectral bandwidth of the order of 10^{-2}.

Evidently, insertion device performances outclass bending magnets. Nevertheless, for experiments which do not need neither a high degree of monochromaticity (or even require broad energy tunability) nor high spatial resolution, as in the case of SXRD, bending magnets still constitutes an acceptable solution.

Hereafter we make a list of those properties that distinguish synchrotron radiation from

standard X-rays obtained from common laboratories sources. Each of these properties depends on a large set of construction variables such as storage ring dimensions, electron beam energy, magnetic field strength, number and periodicity of magnetic elements in undulators, etc., and can bring different benefits according to the specific requirements of the single technique:

- *brilliance*: the number of photons per second emitted from a source area unit (mm^2) under a solid angle unit ($mrad^2$) and - since the emission spectrum might be quite different from one source to another - within a certain energy range fixed by the 0.1% of the relative energy bandwidth (BW):

$$Brilliance = \frac{n_{ph}(counts/s)}{A_0(mm^2)\Omega(mrad^2)\Delta\omega(0.1\%bandwidth)}. \tag{4.26}$$

  The maximum brilliance of a state-of-art fourth generation undulator (ESRF-EBS) can be even 14 orders of magnitude higher than a rotating anode. By virtue of that, the beam could be further monochromatized, gaining energy/wavevector resolution while keeping adequate intensity. In the case of grazing incidence SXRD, the main advantage of the synchrotron light brilliance is to dramatically enhance the surface to bulk signal ratio: in grazing incidence conditions in fact, the amount of scattering events occurring inside an extremely thin layer of matter (the surface) relative to the remaining sample volume (the bulk) is sensibly increased. The same is not achievable with standard available X-rays sources, the reason why SXRD is considered a purely "synchrotron technique".

- *continuous energy spectrum*: as already explained, synchrotron radiation is emitted in a broad band of wavelengths, whose spectrum depends on the characteristics of the source. This fact allows both to choose the working energy which is the most suitable for the experimental needs - *e.g.* in anomalous scattering experiments when the energy must be set at the absorption edge of one of the atoms - and to perform spectroscopy experiments.

- *divergence*: due to relativistic effects, the radiation emitted by electrons moving in a circular orbit is compressed in very tightly collimated cones of light tangential to the electron orbit, whose opening angle in the vertical plane is $\gamma^{-1} = mc^2/E$, where γ is the relativity Lorentz factor. It turns out that vertical beam divergence at the source is exceptionally low, typically around 0.1 mrad (0.08 mrad at ESRF). This allows measuring the true shape of diffraction peaks, limited by intrinsic sample characteristics such as grain size, and not by resolution. In the horizontal plane the natural opening is instead much larger as the electrons radiate continuously along the orbit. To heal this and in order to match other experimental requirements, the X-ray beam is corrected by a series of optical devices (slits, mirrors, filters, monochromator, etc.) installed in the optical hutch of each beamline.

Other significant properties of a synchrotron beam are important: high longitudinal and transverse *coherency*, useful for instance in imaging applications; beam *polarization* - that could be either linear or circular - used in magnetic scattering experiment. The x-ray radiation is also pulsed, enabling time-resolved experiments. To the purposes of this work, we will not discuss these properties here.

4.2.2 The BM32 beamline

Most of the experiments described in this manuscript have been performed at the BM32, a french CRG beamline at ESRF. The beamline receives X-rays from a bending magnet and reshapes and focus them through the optical apparatus installed in the optical hutch. Table 4.2.2 summarizes the most important source and beam properties measured at the outlet of the optical hutch.

Characteristic energy	20.6 keV
Energy range	7-30 keV
Energy resolution	10^{-4}
Beam size	(0.5×0.3) mm^2 (H×V)
Vertical divergence	0.13 mrad
Horizontal divergence	1.0 mrad
Source - sample distance	60 m

Although flux and beam size cannot compete with those of beams generated by insertion devices, the beam characteristics suit adequately the requirements of the scattering techniques used at BM32. Those are the hard X-ray spectral range available (7-30keV), ideal for diffraction experiments, the good energy/wavevector resolution (10^{-4}) and above all the very low beam vertical divergence (0.13 mrad). The latter allows high resolution measurements of in-plane geometries in vertically mounted samples, as in INS2 at BM32 (see next section), and it suits perfectly the requirements for a fine structural characterization of two-dimensional systems. On the other hand, horizontal divergence is one order of magnitude higher than vertical divergence. This however does not constitutes a problem but it is actually sufficient to probe with adequate resolution the structure factor modulations of out-of-plane rods extending perpendicularly to the surface, while realizing an experimental integration over a corresponding interval of the rods, thus enhancing the measured intensity.

4.2.3 INS2: the growth chamber

The BM32 beamline is dedicated to surface and interface structural characterization and it is divided in two experimental hutches connected in series which share the same optics and hence operate alternately. GIXRD/SXRD experiments described here have been

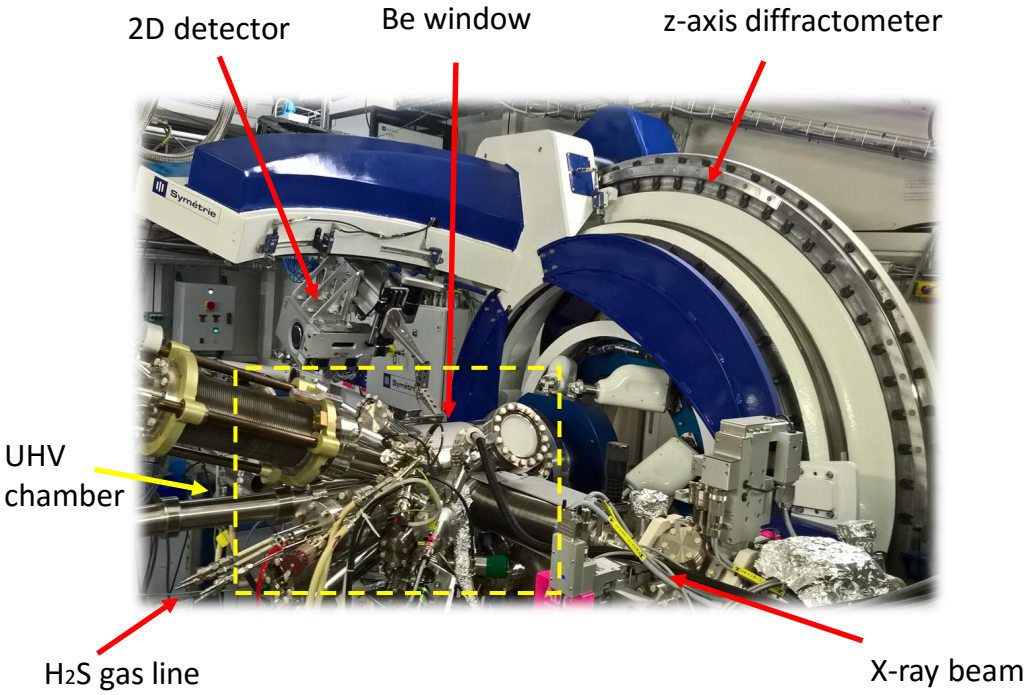

Figure 4.5: INS2 diffractometer and growth chamber at BM32 beamline (ESRF).

performed in the *Interface and Nanostructure and Surfaces 2 (INS2)* hutch, where a UHV chamber fully equipped for nanostructure epitaxial MBE/CVD growths is coupled with a z-axis diffractometer optimized for grazing incidence geometry and surface diffraction. The peculiarity of this instrument - the current (*INS2*, figure 4.5) has replaced a former one (INS) and it is operative since 2016 - is that MBE and diffraction chambers are the same, therefore growths and X-ray characterization can be performed *in-situ* and *operando* without moving the sample from a stage to another during the process. It follows that structural characterizations can be performed in real time during growth. Firstly, we will focus the attention on the UHV-growth chamber, after that a detailed description of the diffractometer will be given.

INS2 is provided with a UHV chamber where the background pressure is 3×10^{-10} mbar. UHV pressure is maintained by means of three different capacity turbo pumps (connected to primary pumping), one ion pump and one Ti sublimation pump. Samples mounted on molybdenum sample holder are firstly loaded in the *modutrack*, a long module usually kept at slightly higher pressures than the main chamber (1×10^{-9} mbar) used for various pre-experimental purposes (sample loading, storage, degassing, transfer to external UHV suitcase, etc.), and then transferred in the main chamber by a mechanical manipulator. The sample is vertically fixed on the stage which allows rotations along X axis, as required by the diffractometer geometry. Behind the sample holder, a oven can be used to heat the sample up to 1300°C by irradiation and electron bombardment. Temperature can be measured by two pyrometers: a low-T single wavelength pyrometer operates between 75

and 1300°C, whereas a second high-T double wavelength pyrometer operates between 450 and 1700°C. An ion gun is used to sputter the sample in Ar plasma during the substrate surface preparations. An O_2 bottle is also connected to the system and it can provide oxygen gas to assist the cleaning of carbon-contaminated surfaces (*e.g.* platinum). Various kinds of sources, typically electron beam metal evaporators, Knudsen cells and an alkali metal dispenser, are mounted on the chamber according to the experiments planned by the users. Concerning the growths performed during this PhD thesis, platinum (Pt) and molybdenum (Mo) were evaporated from electron beam evaporators, while sulfur was provided from an automatic H_2S gas line designed to comply with the high safety standard of ESRF. The gas line system consists of the following parts: a gas cabinet with internal turbo pump extraction containing a H_2S bottle; a mass flow controller; a pneumatic valve system supplying the gas into the chamber (the system is designed to deal with up to three gas lines); a quartz tube that can be approached up to few millimeters close to the sample; a He line for purging; a control unit governing the valve opening and closure over the whole gas line. Other tools are also installed for fast structural and chemical characterization: a RHEED and an Auger spectrometer. Finally, a quartz balance is also installed to calibrate the deposition rate of the substances to be evaporated.

4.2.4 The z-axis diffractometer

Figure 4.6 shows a schematic of the *z-axis* diffractometer operative at BM32[8]. The sample can be moved along three orthogonal x, y, z directions and rotated (ω circle) around the azimuthal axis passing through the homocenter. A 2D detector can rotate following the δ and β circles, defining the in-plane and out-of-plane component of the Bragg angles, *i.e.* the angle under which the diffracted intensity is measured after the scattering process. The incident angle formed between the incoming X-ray beam and the sample is called α and it describes a circle common to both sample and detector. χ_1 and χ_2 represent two additional angular degrees of freedom for the sample that are used to adjust the surface alignment perpendicularly to the z-axis.

With this geometry we are able to sample a large portion of the reciprocal space at $l > 0$, taken into account that the measurable extension in reciprocal space depends on the X-ray energy and it is restricted by the physical limits imposed by the growth chamber and the motion of the detector arm. Typical scans that can be performed during experiments are:

- *radial scans*: they are linear scans between two set points in reciprocal space plane ($l = 0$), performed by rotating simultaneously the sample and the detector along ω and δ circles in order to keep on probe the reciprocal space along a specific (usually high-symmetry) direction. With radial scans we probed the in-plane geometries of the 2D crystals.

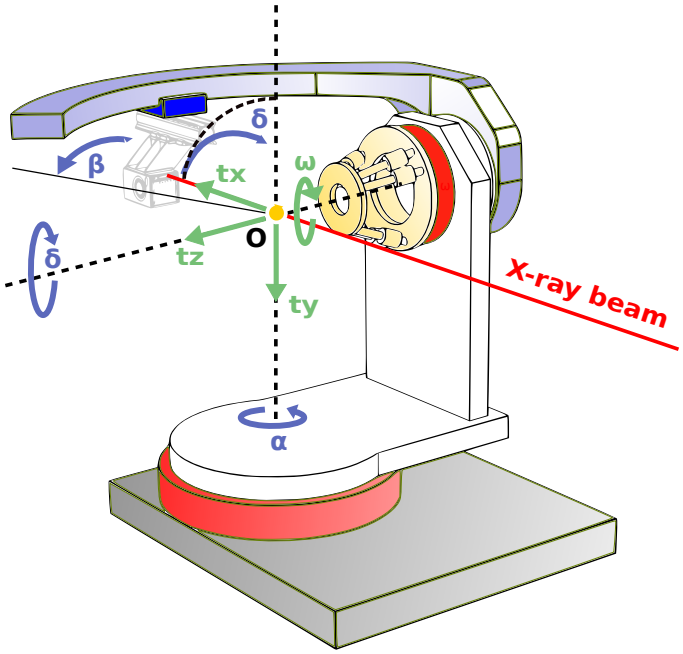

Figure 4.6: Schematic of the INS2 diffractometer at the BM32 beamline.

- *rocking scans*: the detector is fixed while the sample rotates around ω (this is said "rocking the sample"). Rocking scans collect information about the degree of in-plane alignment (*mosaic spread*) of the epilayer with respect to the substrate. While rocking the sample a certain thickness Δl of the diffraction rod intensities is intercepted. For this reasons rocking scans performed at different height in reciprocal space, *i.e.* different l, were the commonly used method to measure rod/CTR intensity.

- *l-scans (stationary scans)*: rod intensities can be measured also by "cutting" the rod in "slices" with a 2D detector, by moving the latter along the β circle at different height l in reciprocal space at fixed (h, k) coordinates.

- *reflectivity scans*: the (0,0) specular rod is measured using a specific geometry. Intensity can be measured by simultaneously varying α and β so that $\alpha = \beta$. A more detailed description is reported in the next section.

4.2.5 The special case of XRR: X-ray specular reflectivity

Among all the diffraction rods/CTRs, the "specular" rod, with Miller indices h and k equal to zero, is a somewhat special case. *X-ray reflectivity* (XRR) is a widely employed technique that can be used to measure the "specular" reflectivity of a large range of materials, from crystalline to non-crystalline, from homogeneous slabs to superlattices. As schematized in figure 4.7, incident and outgoing wavevector form the same angle $\alpha = \beta$

with the surface plane and the resulting momentum transfer vector $\vec{Q}$ has only a purely perpendicular component. In absence of any in-plane momentum transfer, the specular rod is sensitive only to the electron density profile perpendicular to the surface and it does not carry any information about lateral in-plane arrangement of atoms. Hence it is a special probe, very suitable for layer and interface thickness measurements.

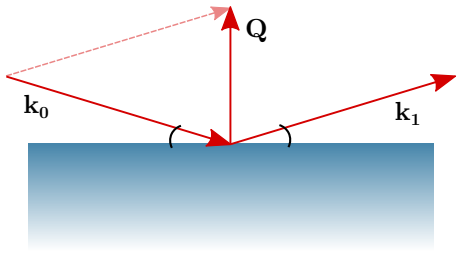

Figure 4.7: Schematic of a reflectivity experiment: Incident and outgoing wavevectors form the same angles α and β with the surface. The (0,0) rod is perfectly perpendicular to the surface and the momentum transfer has zero in plane component.

Owing to its special nature, XRR requires an experimental geometry different from the other rods. Generally, using BM32 notations, intensity is collected by varying simultaneously the incident and the outgoing angles α and β in order to always keep $\alpha = \beta$. Standard XRR instruments are built to probe portions of the reciprocal space limited to some fractions of the $\vec{Q}$ vector close to the origin (few degrees beyond the critical angle for total external reflection). *Kiessig fringes* are observed in multi-layer systems. These fringes are interference features due to the scattering of X-rays with the encountered interfaces, which oscillate along $\vec{Q}_{perp}$ with a period inversely proportional to the layer thickness. This standard geometry is ideal for measuring layers and superlattices with sub-micrometric thickness. 2D materials are few or less than 1nm thick and are associated to specular rods with interference features extending over some $\vec{Q}$ vector units. Their exploration does not necessitate of high resolution, but an extended inspection in angular space. At BM32, XRR measurements are performed by rotating the sample (and the whole chamber in joint motion with the sample) along the α-circle, while the detector is moving by the same angle steps $\Delta\beta = \Delta\alpha$ along the β-circle at $\delta = 0$. INS2 can span a α angular range from 0° to 19°, allowing to span a large range of $\vec{Q}_{perp}$. $\vec{Q}$ vector resolution depends on the beam divergence, the surface bending and the angular step size $\Delta\alpha$, and it could be as small as 0.0005°. In chapter 6 we will study the evolution of the XRR profile of a 2D material as a result of the intercalation of alkali atoms performed at BM32. We will demonstrate how our approach could be interesting for the investigation of 2D material-substrate interfaces.

4.2.6 2D detectors and data acquisition

Single photon counting area (2D) detectors for synchrotron X-ray scattering data acquisition are a relatively new technological achievement which has brought many advantages compared to the former point (0D) detectors such as fast read-out time, lower electronic noise and the faster measurement procedures[9]. In fact, previous generation 0D point detectors were characterized by low angular acceptance and poor spatial resolution limited by the detector size. SXRD technique in addition suffers from other drawbacks, for instance the weak diffracted intensity and the background signals coming from the sample mounting, which is usually reduced by closing the slit apertures. Main consequence for SXRD is that point detectors could not intercept the full part of the rod that intersects the Ewald's sphere, but only a smaller part, and sample rotation around the surface normal is required to acquire the total rod integrated intensity. Because of that, before the advent of 2D detectors, rod scans were carried out by a succession of rocking scans performed at different l values[10].

2D detectors such as the PILATUS (developed at Swiss Light Source) or MAXIPIX (developed at ESRF) ones are instead large area pixel detectors. The MAXIPIX model used during our experiments at BM32 consists of 5×1 chips of 256×256 pixels each with a size of 55 μm. Compared to point detectors, 2D ones allows much larger spatial resolution and angular acceptance. Thanks to that, rod intensity can be acquired at once just by moving the detector along the β-circle to different heights in reciprocal space, cutting this way the CTR/rods into slices of thickness Δl. This scan geometry has been called *stationary* because it does not require sample rotations. It turns out that in stationary geometry a single count at each l position can be performed in place of a rocking scan, thus speeding up the measurement time.

The second difference with respect to point detectors is that in 2D ones not only the full reflection is acquired but also its surrounding. Once connected to the work station, angular and reciprocal space can be visualized in 2D images and spurious signals can be identified and corrected during the data treatment. Typical spurious signals might come for instance from scratches and contaminants present on the sample surface or from the pollution encountered by the beam in the beam path.

Last but not least, with a 2D detector a set of coordinates can be assigned to each pixel. Each collected image is thus an array of points containing spatial and intensity information that can be stored into binary (edf) files and handled as matrix elements in order to reconstruct a 2D/3D images of the reciprocal space after the experiment. Integration of the intensity within specific volumes in the reciprocal space can be performed as well by *slicing* the images by means of modern scientific computing packages. In the next section we will give an example of data acquisition and treatment developed and used during this PhD thesis for rod and CTR measurements and analysis.

4.2.7 Rod measurements and data treatment

In most of the experiments performed in the past at BM32, and also in part for this thesis, rod intensity was measured according to a combined approach of stationary and rocking scans[10]. In fact, provided that the in-plane detector acceptance is large enough, stationary scans measures at once the full diffraction rod (or CTR) at a specific height in reciprocal space. As shown in figure 4.8, each scan image acquired by the 2D detector looks as a rod slice of thickness Δl. The measuring time is greatly reduced when using stationary scans in place of rocking scans. However, at small out-of-plane angle β, the detector angular acceptance does not encompass the full cross section of the rod. To deal with this issue, rocking scans are measured at the base of the rod. While rocking the sample in fact, a portion Δl of the rod profile is captured and the intensity is integrated following classical procedures. Hence, a succession of rocking scans can be used to measure rod profiles.

Once rod intensity has been measured, a proper estimation of the diffracted intensity and the structure factor extraction have to be performed. A robust method adopted at the beginning of this thesis is described in Drnec et al.[10], which combines stationary scans and rocking scans at low l-values. By these approaches the rod intensity is integrated in real angular space and it needs then to be corrected by the Lorentz factor $\sin^{-1}\gamma$ in order to be expressed as function of the reciprocal space momentum transfer $\vec{Q}$[11].

We propose here a different method based on direct integration in reciprocal space. In short, we calculate the reciprocal space coordinates (q_{xy}, q_z) for each pixel in all the acquired stationary scan images of a specific rod or CTR, and we reconstruct the 2D projection on the q_{xy}-q_z plane as shown in figure 4.8. Thereby, the rod intensity is integrated along the q_{xy} axis perpendicular to q_z. As shown in the schematics in figure 4.9, the q_z axis is parallel to the out-of-plane component $\vec{Q}_{perp}$ of the momentum transfer $\vec{Q}$.

In practice the procedure is divided in two steps, the first carried out by the CUT function of the *PyRod* code, the second by the "*Rod2Dplot*" macro that we wrote for this purpose. The *PyRod* code is a python based software developed by T. Zhou at BM32 for the visualization, the analysis and the simulation of SXRD data acquired by 2D detectors[12]. The PyRod GUI displays the 2D images collected by the area detector at a given scan point. Suitable region of interest (ROIs) can be edited even after the experiment in order to restrict the portion of data to integrate - for instance to exclude from the analysis possible intruded signals - and adapt the resolution as function of the scan type. The PyRod "CUT" functions rearrange pixel data collected during one scan, *e.g.* stationary scans, in a reshaped 2D or 3D data volume, and displays a cross-sectional view of it. Moreover, they provide a data ouput containing the intensity and the angular space coordinates (α, β, etc.) for each pixel within the selected ROI.

Once the data are extracted, the "*Rod2Dplot*" macro is used to reconstruct the rod in a 2D projection. A detailed description of the procedure goes beyond the goals fixed for this manuscript. Hereafter we limit to point out the main steps and highlight some figures

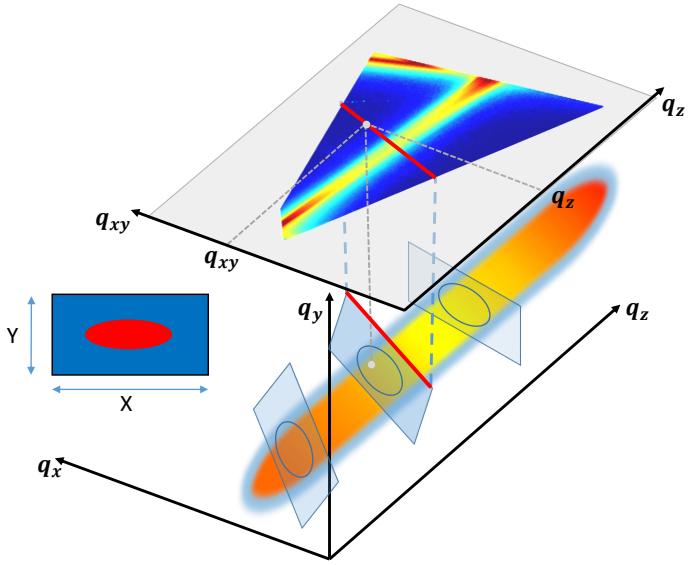

Figure 4.8: 3D pictorial view in reciprocal space of the vectorial basis (q_x, q_y, q_z) of a diffraction rod perpendicular to the surface of a vertical sample and cut into "slices" by a 2D detector during a rod scan in stationary geometry. In the inset the 2D detector screen is shown with a preselected ROI having X and Y horizontal and vertical sizes. The intensity in each 2D image is integrated along Y and the data set passes from a 2D (ROI image) to a 1D array of points (red stripes). We aim to reconstruct a 2D image of the rod by projecting it on the (q_{xy}, q_z) plane after calculating the coordinates for each pixel.

of merit.

In figure 4.8 a pictorial view of a diffraction rod during the l-scans in stationary geometry is shown. The rod is lying along the q_z direction perpendicular to the sample surface. During a stationary scan the 2D detector cuts the rod into slices. Each image thus shows a rod cross-section tilted with respect to the sample surface plane. We would like to build a 2D view of the rod and plot the intensity as function of l (or equivalently $\left|\vec{Q}_{perp}\right|$). We will do that by projecting the rod intensity on the q_z-q_{xy} plane as shown in figure 4.8 and integrating it along (q_{xy}) directly in reciprocal space. How the intensity is distributed around the rod center in each scan (see the inset in figure 4.8) is irrelevant: this is the reason why as preliminary step intensity in each 2D image is integrated along δ in angular space (Y, in practice, as shown in the inset) within the ROI. Thanks to that, every 2D image is converted into a one-dimensional array of points reducing the final data volume size.

From the sketch in figure 4.9a we can understand how the coordinates q_{xy} and q_z of a generic pixel inside the rod are calculated. The q_z coordinate is defined as the modulus of the $\vec{Q}_{perp}$ out-of-plane component of the momentum transfer $\vec{Q}$, and it can be simply obtained as the difference between the out-of-plane components of the incident and outgoing wavevectors $\vec{k}_0$ and $\vec{k}_1$. The q_{xy} coordinate instead must not be confused with the momentum transfer component parallel to the plane, $\vec{Q}_{par}$, but it corresponds to the distance of each pixel from the detector homocenter and it can be calculated as explained in figure 4.9b from simple geometric and instrumental considerations. The formulas are reported below: α and β are the out-of-plane X-ray beam incident and outogoing angles

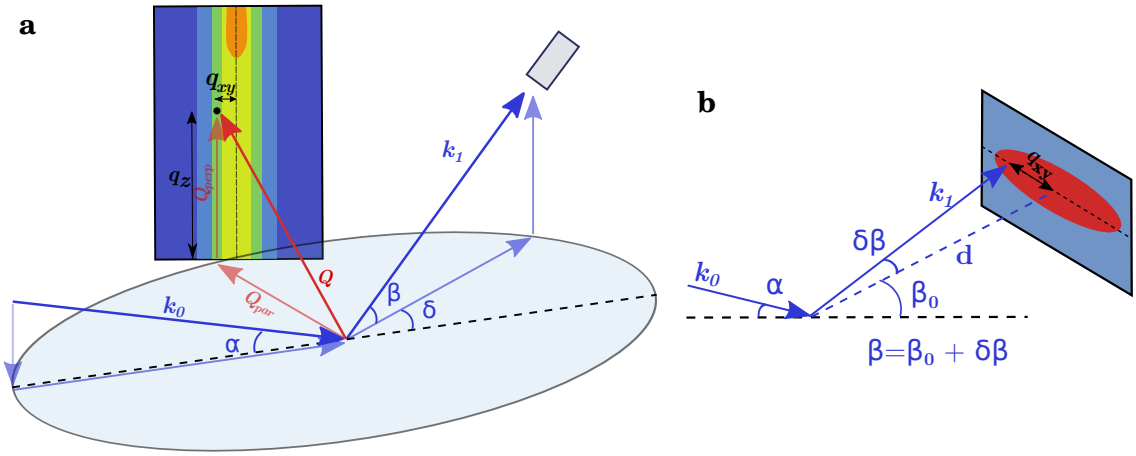

Figure 4.9: (a) Pictorial view of the scattering process leading to diffraction rod formation in reciprocal space. The incident and outgoing wavevectors ($\vec{k_0}$ and $\vec{k_1}$) are shown with their orthogonal components. $\vec{k_0}$ forms an angle α with the surface. instead forms an out-of-plane angle β with the surface and its deviated by an azimuthal angle δ in the plane. $\vec{Q}$ is the momentum transfer vector. Its components are $\vec{Q}_{par}$ and $\vec{Q}_{perp}$. A generic point in the surrounding of the rod has coordinates q_{xy} and $q_z = |\vec{Q}_{perp}|$. (b) The schematic shows how to calculate the q_{xy} position for a generic pixel in a 2D-detector. β_0 represents the out-of-plane angle of the detector homocenter, whereas d is the distance between the homocenter and the sample. $\delta\beta$ is the difference in angle between the $\vec{k_1}$ vector pointing to the chosen pixel and the vector connecting the detector homocenter to the sample surface.

as defined before in this chapter; we should clarify that β_0 is the angular position of the detector homocenter, while each pixel has a slightly different absolute value $\beta = \beta_0 + \delta\beta$. Finally d, n_{pix} and s_{pix} are respectively the distance of the detector homocenter from the sample, the distance in pixels separating the point of which we want to calculate the coordinates from the detector homocenter, and the pixel size.

$$\begin{cases} q_z = \frac{2\pi}{\lambda}(\sin\alpha + \sin\beta), \beta = \beta_0 + \delta\beta \\ \\ q_{xy} = \frac{2\pi}{\lambda}\sin\beta_0\delta\beta = \frac{2\pi}{\lambda}\sin\beta_0\frac{n_{pix}\cdot s_{pix}}{d} \end{cases} \tag{4.27}$$

At this stage the 2D projection of a generic rod is plotted as in figure 4.10a. In the zoom within the inset, the point array is unstructured, appearing as bunches of points grouped in straight lines with different orientation. These are the lines of pixels corresponding to the detector ROI images projected on the q_{xy}-q_{xy} plane after the integration along Y within the ROI. A 2D interpolation of these points on a regular orthogonal grid is thus needed in view of the subsequent integration. The result is shown in figure 4.10b. At this point the rod intensity is integrated along q_{xy} and plotted as function of l (or $|\vec{Q}_z|$). The final result is shown in figure 4.10c.

As next steps, the background is subtracted and the structure factor is calculated as the square root of the measured intensity corrected by the following instrumental factors: monitor, polarization, shined area, gaussian beam profile and refraction effect at the surface[11]. Remarkably, because the rod is integrated directly in reciprocal space, the correction by the Lorentz's factor is not needed.

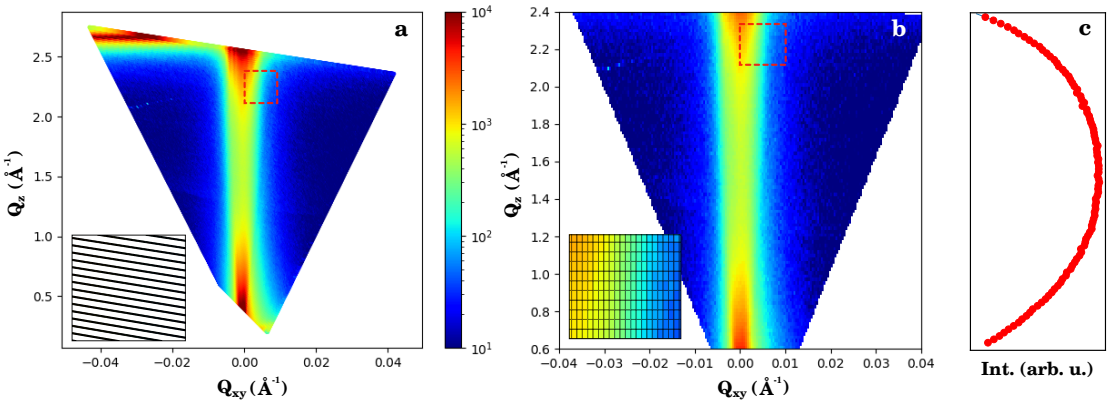

Figure 4.10: (a) experimental intensity 2D plot of the specular rod *00l* in the q_z-q_{xy} plane between (000) and (111) Bragg reflection obtained with the procedure described in the text; the inset at the bottom left is a zoom of the squared area with red boundary and it shows that the image is made by dense lines of points corresponding to the detector images integrated along δ in angular space, or Y, the vertical detector dimension; (b) the same image in (a) interpolated between $q_z = 0.6$ and $q_z = 2.4$; now the zoom in the inset at the bottom left is an orthogonal array of pixels filling the whole space where it is possible to integrate the intensity along q_{xy}; (c) integrated intensity profile of the Au specular rod obtained by summing the pixel intensity along along the q_{xy} direction; the vertical axis is the same as in (b).

Bibliography

[1] J. Als-Nielsen and D. McMorrow, *Elements of modern X-ray physics*. John Wiley & Sons, 2011.

[2] E. Vlieg, "Surface and interface science, vol. 1, concepts and methods," 2012.

[3] I. Robinson and D. Tweet, "Surface x-ray diffraction," *Reports on Progress in Physics*, vol. 55, no. 5, p. 599, 1992.

[4] R. Feidenhans, "Surface structure determination by x-ray diffraction," *Surface Science Reports*, vol. 10, no. 3, pp. 105–188, 1989.

[5] P. Eisenberger and W. C. Marra, "X-ray diffraction study of the Ge (001) reconstructed surface," *Physical Review Letters*, vol. 46, no. 16, p. 1081, 1981.

[6] "ESRF-EBS." https://www.esrf.eu/about/upgrade.

[7] P. Willmott, *An introduction to synchrotron radiation: techniques and applications*. Wiley, 2019.

[8] V. Cantelli, O. Geaymond, O. Ulrich, T. Zhou, N. Blanc, and G. Renaud, "The in situ growth of nanostructures on surfaces (INS) endstation of the ESRF BM32 beamline," *Journal of synchrotron radiation*, vol. 22, no. 3, pp. 688–700, 2015.

[9] C. Schlepütz, R. Herger, P. Willmott, B. Patterson, O. Bunk, C. Brönnimann, B. Henrich, G. Hülsen, and E. Eikenberry, "Improved data acquisition in grazing-incidence x-ray scattering experiments using a pixel detector," *Acta Crystallographica Section A: Foundations of Crystallography*, vol. 61, no. 4, pp. 418–425, 2005.

[10] J. Drnec, T. Zhou, S. Pintea, W. Onderwaater, E. Vlieg, G. Renaud, and R. Felici, "Integration techniques for surface x-ray diffraction data obtained with a two-dimensional detector," *Journal of Applied Crystallography*, vol. 47, no. 1, pp. 365–377, 2014.

[11] E. Vlieg, "Integrated intensities using a six-circle surface x-ray diffractometer," *Journal of Applied Crystallography*, vol. 30, no. 5, pp. 532–543, 1997.

[12] T. Zhou, *In Situ Synchrotron X-ray Scattering of SiGe NWs: Growth, Strain and Bending*. PhD thesis, Université Grenoble-Alpes, 2015.

Part II

Chapter 5

2D transition metal ditellurides grown on InAs(111)

5.1 Introduction

Inside the large family of TMDCs, ditellurides have received initially a minor attention compared to disulphides and diselenides, presumably due to synthesis issues and poor stability in air. Only in a second moment, the efforts in order to synthesize and characterize ditellurides have increased conspicuously, also boosted by the prediction of fascinating non trivial topological states, such as in 3D Dirac or Weyl semimetals[1], and the possibility in some of them, *e.g.* $MoTe_2$, to drive robust transitions between 2H and 1T' polymorphs[2; 3].

Unlike disulphides and diselenides, most ditellurides are semimetals and are affected by electronic instabilities that drive the transition towards a lower symmetry phase. In Chapter 1 we have already introduced the 1T' polymorph as a distorted 1T structure where metal atoms pair up and form zig-zag rows in the layer plane. This intralayer atomic displacement breaks the in-plane hexagonal symmetry typical of 2H and 1T structures and doubles the periodicity of the crystal along the displacement direction such that the primitive unit cell becomes rectangular. Several ditellurides adopt a stable 1T' structure in conditions close to atmospheric pressure and room temperature. For instance, WTe_2 is stable at room temperature in the 1T' phase[4; 5], whereas for $MoTe_2$ the 1T' phase is metastable and lies only 31meV above the more stable 2H phase[6]. Former studies report that the 1T' phase in $MoTe_2$ can be stabilized by post growth treatments consisting in high temperature annealing followed by rapid cooling[4; 5]. Due to the energy proximity of the the two phases, also external stimuli such as an electric field (set by an electrostatic bias)[7] and mechanical strain[3] have been suggested to drive metal-semiconductor transitions in monolayer $MoTe_2$, which can be exploited in room temperature devices.

Another reason that makes ditellurides appealing target materials for material science research nowadays is the discovery of topological properties in some of them. WTe_2 and $MoTe_2$ have been already demonstrated to exhibit topological Weyl states associated to

1T' type structures[8; 9]. One peculiarity of Weyl states is that they appear in pairs of opposite chirality (right and left handed) that can be manipulated as special degrees of freedom. Such properties bring novel concepts for electronic devices to be used in information technologies.

However, most of the knowledge on ditellurides synthesis comes from 3D crystals preparations following bulk growth methodologies, whereas the realization of solid state devices requires epitaxial processes and possibly down-scaling. It implies that improving the current synthesis methods has become compelling and epitaxial growths on new suitable substrates must be attempted. For this thesis we used InAs(111) grown on Si(111) as substrate for some ditelluride growths. The reason behind this choice is to find new large area substrates for high-quality TMDC growth in alternative to metals, the latter being non-compatible with standard semiconductor microelectronics processes and requiring a transfer step in view of technological use. Furthermore, a 2D material is not a guarantee of ideal vdW epitaxy - *i.e.* absence of actual bonds with the substrate and yet perfect alignment of crystallographic directions - when a non-vdW material with dangling bonds on the terminating surface is chosen as substrate (2D/3D epitaxy). It might happens in fact that the 2D overlayer grows strained on the substrate because of stronger epitaxial bonding. Such a strained growth however may result in modified - and sometimes new - properties of the material that are not found in the bulk or in freestanding layers.

In this framework, we have studied a set of different transition metal ditellurides (both multilayers and monolayers films) going from the well-known $MoTe_2$ to less studied species such as $ZrTe_2$ and $TiTe_2$. Our goals were to check and discuss the feasibility of the epitaxial growth of these materials on an unconventional substrate for TMDCs such as InAs(111), identify which phases they show at room temperature, and eventually study possible unexpected fundamental properties. In Table 5.1 we report the list of the ditellurides we have characterized by GIXRD at BM32. It shows the measured in-plane lattice constants in comparison with those of referenced bulk compounds, the mismatch with respect to InAs(111) substrate (whose lattice parameter is 4.284Å) and the residual strain calculated with respect to the relaxed bulk values. Notably, the ditellurides studied in this work are not lattice matched with InAs(111) - the natural mismatch with InAs(111) varying from 7 to 19% would be too large to be sustainable - but they accumulate a non negligible amount of tensile strain varying between 0.7 and 2.3%. In this chapter we will focus our attention mostly on the samples in Table 5.1 that are highlighted in bold. For each of them we will devote one of the next three sections, whereby we will deal with the peculiar physical aspects that directly descend from the specific structure the materials have adopted. Before that, we will briefly describe the common growth procedure used.

sample	thickness	a_{exp}(Å)	a_{3D}(Å)	mismatch	strain(%)
$ZrTe_2$	**1ML**	**4.003**	**3.953[10]**	**-0.066**	**1.265**
$ZrTe_2$	4ML	3.984	3.953[10]	-0.070	0.784
$MoTe_2$	**3ML**	**3.501**	**3.469[4; 9]**	**-0.183**	**0.922**
$TiTe_2$	1ML	3.833	3.777[11]	-0.105	1.483
$TiTe_2$	**50ML**	**3.863**	**3.777[11]**	**-0.098**	**2.277**

Table 5.1: Experimental in-plane lattice constants for the set of ditelluride samples measured by GIXRD. For each of them we report reference values from bulk samples taken from articles and/or crystallographic databases, experimental lattice mismatch with the InAs(111) substrate as defined in eq.(2.1), and residual strain with respect to the referenced bulk expected values.

5.2 Epitaxial growth of 2D ditellurides on InAs(111)

The InAs substrates used during our experiments are 200nm thick [111] oriented films grown on Si(111) wafers by T. Baron and his coworkers inside the LTM laboratories of Grenoble. Before TMDC growth, the substrates were chemically cleaned in 5N solution of HF diluted in isopropyl alcohol and then annealed at 400°C in UHV. After the treatment, the surfaces are flat and In-terminated (they present the characteristic 2×2 reconstruction, as shown in the RHEED patterns in figure 5.1). The as-prepared material does not tolerate annealing temperatures higher than 400°C. Above this temperature the pristine structure of the material is altered, probably due to the formation of substoichiometric phases in the topmost layers following As desorption, (as verified by GIXRD measurement not shown in this work). This drawback strictly limits the possibility to perform post-growth annealing treatments.

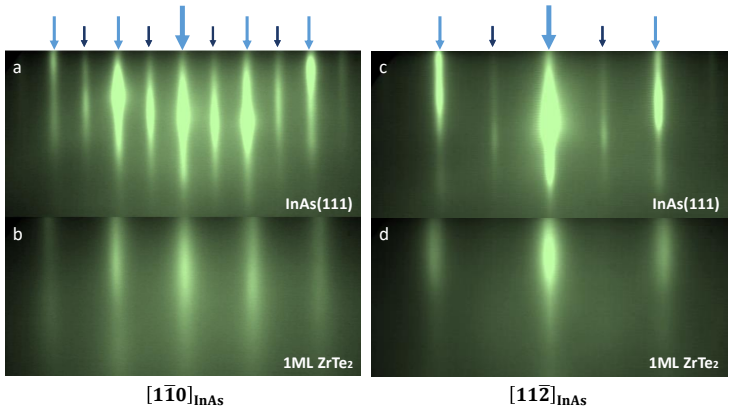

Figure 5.1: RHEED patterns along the $[1\bar{1}0]$ and $[11\bar{2}]$ of InAs(111) (a,c) and 3ML $ZrTe_2$ (b,d) films along two high symmetry directions of InAs(111). Light blue arrows point to streaks originating from the unreconstructued InAs(111) surface, while small dark blue arrows point to 2×2 reconstruction streaks related to the In-terminated surface reconstruction.

$MoTe_2$, $ZrTe_2$ and $TiTe_2$ (essentially all the samples described in this chapter) have been grown by MBE on the as-prepared InAs(111) substrates at the NCSRD laboratories

in Athens by the group led by A. Dimoulas and subsequently delivered to Grenoble (ESRF) for the structural characterization, *i.e.* grazing incidence x-ray diffraction (GIXRD) and cross sectional scanning transmission electron microscopy (STEM)[1]. The chosen growth conditions are reminiscent of those used for other TMDCs (see chapter 2): low metal deposition rate (typically 0.5ML/min), high Te/metal flux ratio (100/1) and mild annealing temperature (between 280°C and 400°C). In the case of $MoTe_2$, a "beam-interrupted method" was adopted, similar to the one reported for WTe_2[12]: in this recipe the metal evaporator shutter is opened and closed alternately every 30s, while the Te flux is kept constant on the sample. The goal is to obtain a sufficient "tellurization" of the deposited metal atoms, and to circumvent the tendency of both W and Mo to form clusters instead of covalent metal-Te bonds, which otherwise leads to low quality crystals.

Non obviously, we proved that the MBE of ditellurides on InAs(111) leads to good quality crystals characterized by a rather sharp and clean interface and excellent orientational alignment with respect to the InAs(111) crystallographic directions (see figure 5.1b,d reporting the case of 1ML $ZrTe_2$ growth). In the next section we present the structural characterization of 1ML $ZrTe_2$ grown on InAs(111)/Si(111) as an example of the just mentioned results.

5.3 Epitaxy of 2D $ZrTe_2$ on InAs(111)

Figure 5.2a is a 80° reciprocal space cut parallel to the surface plane measured by GIXRD at BM32. It shows the intensity diffracted by a 1ML $ZrTe_2$ sample using 11keV synchrotron x-ray radiation (1.13Å) impinging on the surface with the grazing angle of 0.2°. Because $ZrTe_2$ has hexagonal planar symmetry, a 60° map comprised between the two high symmetry axes h and k is sufficient to fully describe the planar geometry of the surface layer. Eight couples of spots, three aligned along each h and k axes, and two along the $h = k$ axis, are observed. They are located at the center of each first Brillouin zone (FBZ) of $ZrTe_2$ depicted in the figure as yellow hexagonal cells. Within all of these couples of spots, the reflection closest to the origin is from InAs, whereas the second is from $ZrTe_2$. The spacing between these spots is consistent with the smaller lattice parameter of $ZrTe_2$ (3.953Å) compared to that of InAs(111) (4.284Å). Along the h axis, we distinguish the first (100), second (200) and third order (300) reflections of $ZrTe_2$. For InAs(111) the $(22\bar{4})$ Bragg reflection is close to the third order $ZrTe_2$ peak, preceded at $\frac{1}{3}$ and $\frac{2}{3}$ by two CTR intersections with the $l = 0$ plane. Along $h = k$ axes instead we find (110) $ZrTe_2$ and $(02\bar{2})$ InAs reflections. The ring with an intensity maximum at the center of the map is due to the polycrystal signal from the 5 nm thick Al capping layer, used to protect the sample during the transfer from Athens to Grenoble. Highly resolved radial scans have been also measured along the high symmetry crystallographic axes h

[1]STEM measurements have been performed by C. Alvarez and H. Okuno at CEA-LETI

and $h = k$ shown in figure 5.2c-d. Our measurements show that the 2D material has a good epitaxial alignment with the substrate, with the following orientational relationship: $ZrTe_2[11\bar{2}0](0001) \parallel InAs[01\bar{1}](111)$. No additional phases, *e.g.* at the interface, or rotational variants, can be detected in these measurements.

In the first part of the manuscript we have discussed the nature of the interaction occurring between 2D TMDCs and their substrates, debating the meaning of vdW epitaxy. Hereafter, we are interested to know if the epitaxial growth of $ZrTe_2$ meets the characteristics of vdW epitaxy: unstrained growth in spite of large lattice mismatch, sharp and clean interface, good rotational alignment. To answer this question, we will proceed with a systematical crosschecking of these three criteria.

Unstrained growth. From radial scans in figure 5.2c-d we can derive the in-plane lattice parameter of 1ML $ZrTe_2$ knowing the Si(111) and InAs(111) lattice constants which are used as references. The measured value of (4.003 ± 0.002)Å is 1.26% larger than the one referenced for bulk $ZrTe_2$ (3.95Å)[10]. Although structural information about $ZrTe_2$ is very limited, the discrepancy between the bulk relaxed value and that measured in our sample is reminiscent of other published results for $MoTe_2$ and $TiTe_2$[13; 14] that exhibit expanded lattice constants when grown on InAs(111). It seems thus that InAs(111) exerts epitaxial constraints on $ZrTe_2$ so that the monolayer is strained.

The radial scan in figure 5.2c shows a weak but significant peak at $h = 2.0628$ (highlighted by the blue arrow), approximately halfway between the second InAs CTR ($h = 2.000$) and the $ZrTe_2$ (200) peak ($h = 2.1402$). The same distance separates each spot from the central one in the hexagonal shaped set of six satellites surrounding the first InAs CTRs along the h and k axes (see magnified view in the inset of figure 5.2a). All these peaks are satellites of a superperiodicity (moiré) pattern. As discussed in chapter 2, a 2D hetero-epitaxial system where overlayer and substrate have different lattice parameters generates a network of regularly spaced misfit dislocations. Misfit dislocations at the interface between InAs and $ZrTe_2$ are in fact observed by cross-sectional STEM and shown in figure 5.3: the relative position of $ZrTe_2$ atoms with respect to InAs ones varies periodically from point A/B (bridge site) to point C (on top site). This configuration is expected to have long range order and constitutes a network of dislocations which is responsible for the superperiodicity visible by diffraction through the above-mentioned satellites peaks. From the radial scan we can derive accurately the superlattice periodicity by measuring the distance of the satellite peak from one between the adjacent InAs and $ZrTe_2$ peaks. We found a 6.2nm long superstructure unit cell, corresponding to nearly (14×14) InAs unit cells and nearly (15×15) $ZrTe_2$ unit cells. This result is in agreement with the moiré pattern observed on the $ZrTe_2$ surface by STM (6.6nm) - images are shown in the in the article that we published based in part on the present work[15]. The so-measured superperiodicity is twice the distance between the two misfit dislocation centers A and B observed in figure 5.3, i.e. $\overline{AB}$=3.1nm. Along the $[10\bar{1}0]$ $ZrTe_2$ zone axis, atoms on two adjacent vertical $ZrTe_2$ $(2\bar{1}\bar{1}0)$ planes are staggered, i.e. alternatively slightly forward (a)

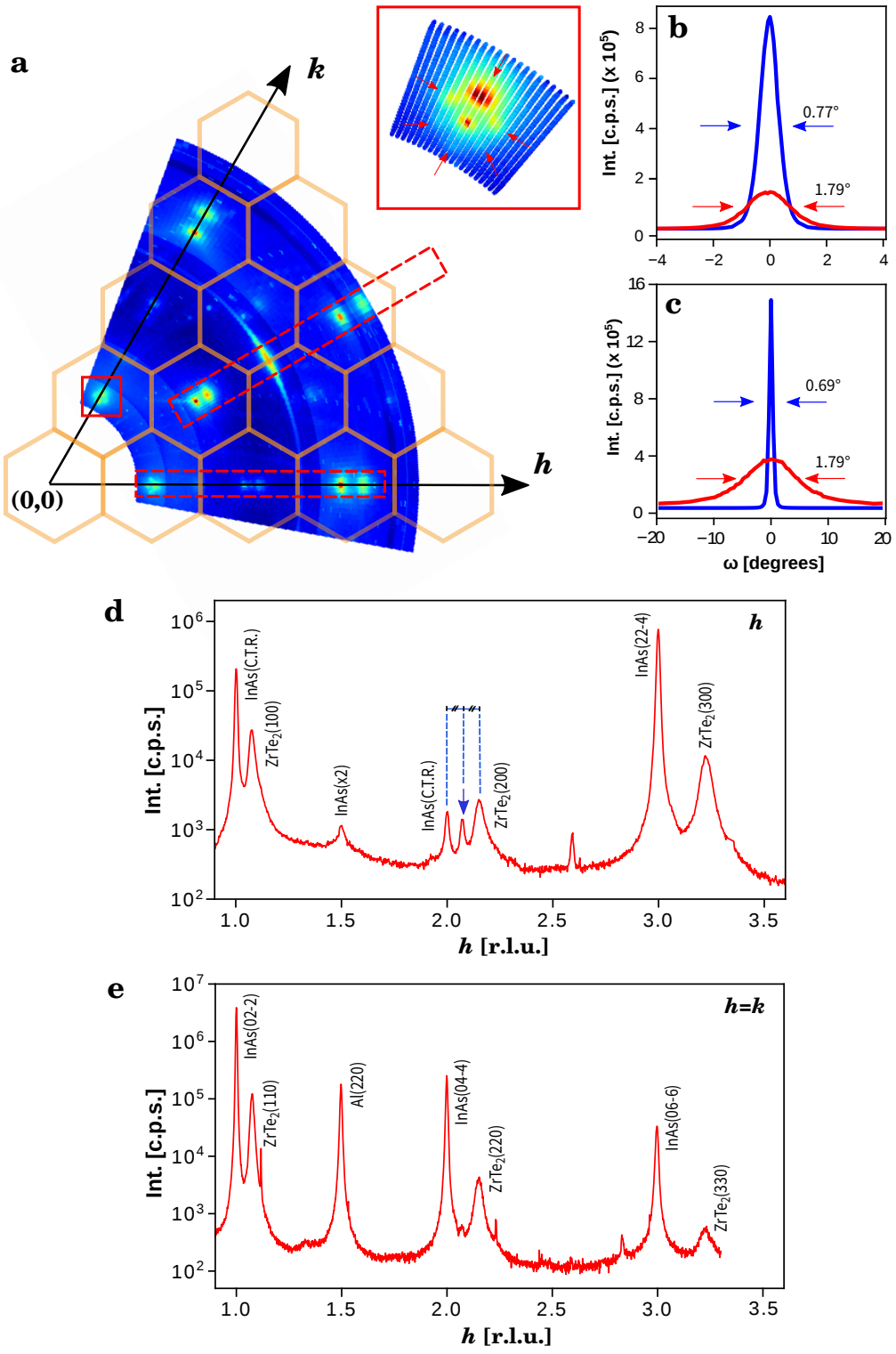

Figure 5.2: GIXRD measurements of 1ML $ZrTe_2$/InAs(111). (a) Reciprocal space in-plane map with pictorial view of the FBZ of InAs(111). Dashed red boxes show high symmetry directions h and $h = k$ of the substrates and the overlayer. The several white spots aligned along arcs are glitches due to a non-perfect design of the detector arm "flight tube", affecting the measurements performed during the first months of operation of the new INS2 diffractometer (this problem has then been now resolved); in the inset a zoom of the superlattice pattern around the first InAs(111) CTR is shown; (b) rocking scans of $ZrTe_2$ (110) reflection compared with the $(02\bar{2})$ reflection of InAs(111); (c) rocking scan of $MoSe_2$ (100) reflection compared with the one of AlN (1000) reflection; this measurements are relative to a 1ML $MoSe_2$ layer grown on Al(0001) substrate; (d,e) radial scans along the direction h and $h = k$ highlighted in the map by red dashed boxes.

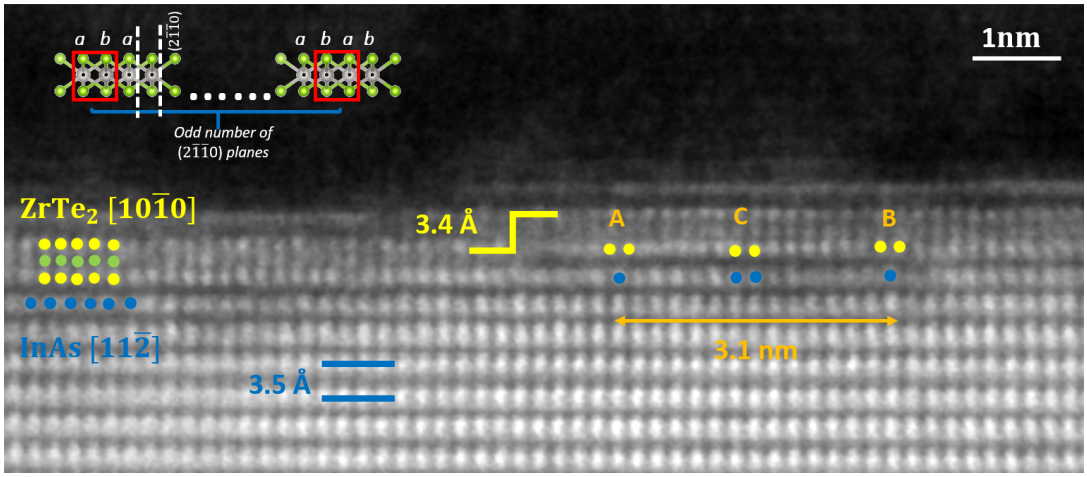

Figure 5.3: cross-sectional STEM of 1ML $ZrTe_2$/InAs(111) along the [112] InAs zone axis: A and B points highlight mismatch dislocation cores at the interface between $ZrTe_2$ and InAs(111) (bridge configuration); the C point indicates another region where the relative atomic positions are different (on-top configuration); the yellow step line indicates an InAs monoatomic surface step.

and backward (b). It results that after an odd number of $ZrTe_2$ (2$\bar{1}\bar{1}$0) planes, configuration in B is not as in A *i.e.* *ab*, but inverted *i.e.* *ba* (figure 5.3, inset). It results that the actual superlattice length is $2\overline{AB}$, coherently with what we extrapolated by GIXRD.

Sharp interface. The cross-sectional-STEM image in figure 5.3 complements our diffraction results with real space information about the interface quality. It shows a good film uniformity, a sharp and defect-free crystalline interface without intermixing, and provides an estimation of the interfacial distance (3.5Å), which is comparable to the size of the substrate interlayer distance (3.4Å). The continuity of the film is however interrupted by the presence of monoatomic steps on the substrate surface. The irregular morphology of the substrate thus limits the grain size of monolayer $ZrTe_2$ to some tens of nanometers. Within this average distance, which is more than one moiré superlattice unit cell, $ZrTe_2$ appears however very flat, indicating almost zero amplitude corrugation.

Rotational alignment. Another remarkable observation is the relatively low mosaic spread shown by $ZrTe_2$ reflections compared to other epitaxial dichalcogenides grown on non-metallic substrates. In epitaxy, mosaic spread is the angular distribution of the slightly rotated overlayer domains with respect to the substrate crystallographic axes. As explained in chapter 2, non-negligible mosaic spread is one of the main issues related to TMDCs growths on non-metal substrates, very likely due to the weakness of the interface forces. Albeit still far from on-metal references (see next chapters), ditellurides grown on InAs(111) show relatively small in-plane mosaic spread, almost limited by the substrate 1.79° for $ZrTe_2$ (110) reflection vs 0.77° of InAs (02$\bar{2}$) reflection, as shown in figure 5.2b. This result can be compared with other cases studied by us, *e.g.* 2D $MoSe_2$ grown on AlN(0001) and on graphene/SiC(0001)[16], where mosaic spread of the 2D layer is about

one order of magnitude higher.

The sharpness and cleanliness of the interface as well as the good registry of the growth in spite of the large mismatch between the 2D $ZrTe_2$ layer and the substrate seem a good practical realisation of a vdW epitaxy. The fact that the $ZrTe_2$ lattice is not fully relaxed but significantly strained (1.26%) is nevertheless indicative of a non negligible interaction with the substrate. The lower mosaic spread compared to other 2D TMDCs grown on non-metal substrates goes along this interpretation: where interaction is stronger the overlayer is better locked to the substrate crystallographic axes and the orientation distribution is narrower.

The dislocations observed in figure 5.3 cannot be understood as strained-induced defects as in conventional 3D/3D epitaxy, but they are simply the manifestation of the lattice mismatch existing between the 2D overlayer and the substrate. Based on that, we cannot conclude whether the interaction between $ZrTe_2$ and InAs(111) is purely vdW or it has stronger character. However, the identification of the dislocation core size, the analysis of the local strain distribution and eventually a measurement of the corrugation of the interface could lead to at least a qualitative answer.

The detection of the superperiodicity satellite network by GIXRD provides the most important argument to this disquisition. We do not have sufficient data information to launch a quantitative study and we should limit to a rather qualitative interpretation. We can develop some simple considerations. Given two superimposed non-interacting lattices, A and B, having slightly different lattice constants, the diffraction pattern relative to the system is the sum of the two lattice Fourier transforms, *i.e.* $FT(A+B) = FT(A)+FT(B)$, due to the linearity of the Fourier transform operation. The diffraction pattern thus shows two fundamental harmonics: k_A and k_B. If the two lattices instead are interacting, even weakly, a deformation field would perturb at least one of the two atomic chains. It follows that A and B cannot be considered anymore as independent, but must be described by additional superperiodicity, *i.e.* $FT(A+B) = FT(A)+FT(B)+FT(deformation)$. The fast Fourier transform (FFT) of a similar system gives an additional harmonic k_m, which accounts for the moiré perodicity. Therefore, the observation of a misfit dislocation peak in the diffraction pattern is possible only if a non-zero deformation occurs in either one of the lattices. It follows that in our case $ZrTe_2$ necessarily interacts with InAs(111). In support of this assumption we add that the growth of various kinds of selenide 2D films on AlN(0001) substrate studied by us but not reported in this work does not lead to similar superperiodicities in GIXRD scans and are instead characterized by larger mosaic spread, two signs of a weaker interface interaction compared to the $ZrTe_2$/InAs(111) system. However, the small intensity of the satellite peaks, the moderate corrugation and the large dislocation core size (which seems comparable to the moiré cell according to the STEM observations) indicate that, although non negligible, epitaxial constraints exerted by InAs(111) on $ZrTe_2$ are overall weak and close to what is expected for vdW epitaxy.

5.4 RT stabilization of an orthorhombic γ-phase in few-layer thick $MoTe_2$

At room temperature bulk $MoTe_2$ is stable as a 2H polymorph but the distorted 1T' phase is only a fraction of eV higher in energy and it could be stabilized by post growth thermal treatments[4]. The 1T' phase is in fact an in-plane distortion of the more common 1T phase, but when the material is more than one monolayer thick, stacking must also be taken into account and the variety of possible polytypes increases. According to Brown et al.[4], the 1T' $MoTe_2$ that we can find at room temperature is monoclinic and centrosymmetric with 2 layers in the unit cell (β-$MoTe_2$). At temperature lower than 250K $MoTe_2$ transforms into a non-centrosymmetric orthorhombic structure that lacks inversion symmetry. This phase is known by crystallographers as γ-$MoTe_2$, but it is commonly referred to as the T_d phase. From the top, β-$MoTe_2$ and γ-$MoTe_2$ structures look identical, however their stacking order is slightly different (see figure 5.4). The lateral view along the $[11\bar{2}0]$ direction shows in fact that the out-of-plane angle ϕ of the unit cell is perfectly right in orthorhombic ($Pnm2_1$) γ-$MoTe_2$, whereas it is slightly larger than 90° ($\sim 94°$) for monoclinic ($P2_1/m$) β-$MoTe_2$. The distinction is of great relevance in topology, since inversion symmetry breaking is a fundamental condition for Weyl semimetallicity to manifest. Stabilizing orthorhombic γ $MoTe_2$ at room temperature is therefore mandatory to access the properties that descend from the non trivial topology of this phase, as reported by Tsipas et al.[13]. Low-dimensionality and built-in strain can have an important influence over the phase adopted by an epitaxial layer. We wondered whether we could stabilize $MoTe_2$ in the T_d phase thanks to the interfacial built-in strain by growing the 2D layer on a substrate with rather different in-plane lattice constant such as InAs(111).

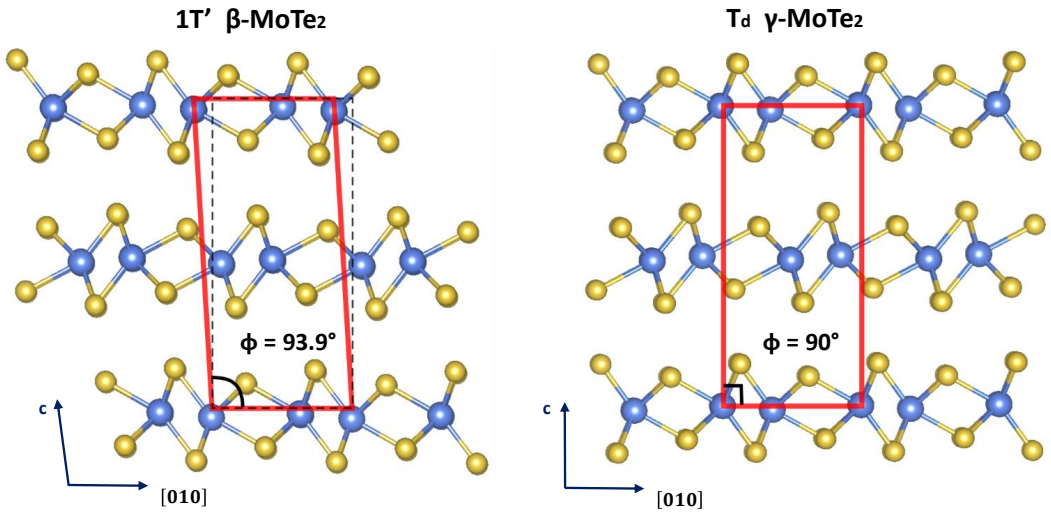

Figure 5.4: monoclinic ($P2_1/m$) β phase (left) and orthorhombic ($Pmn2_1$) γ phase (right) of $MoTe_2$ projected along the [100] direction. The two phases are distinguishable through the out-of-plane angle, perfectly right for orthorhombic phase, sligthly larger than 90° for the monoclinic one.

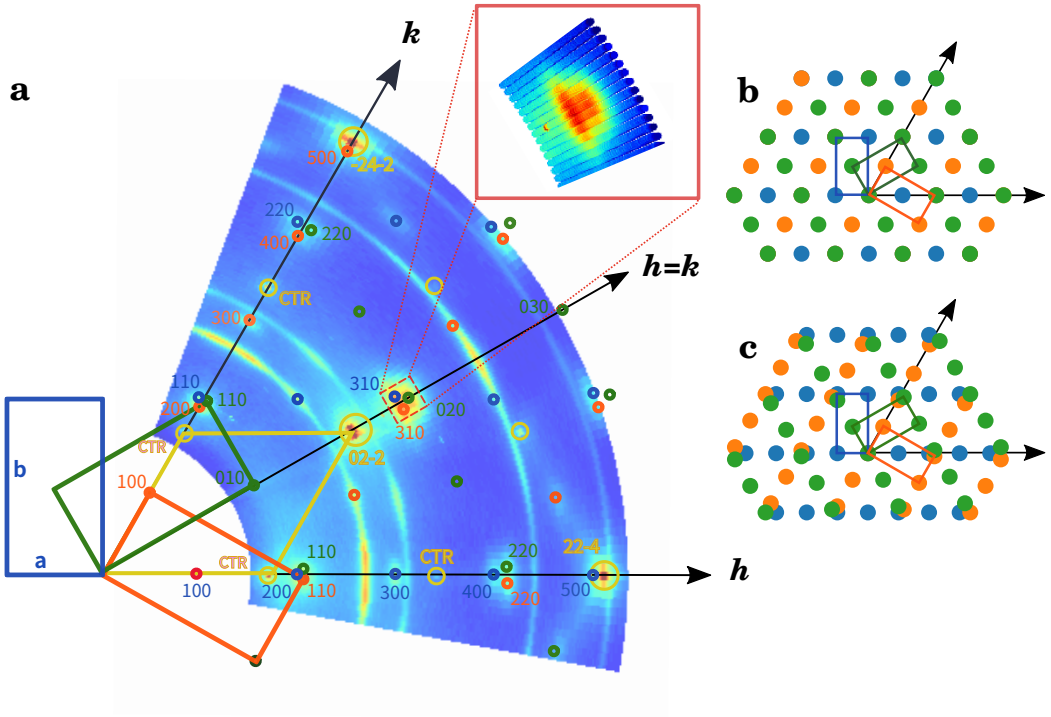

Figure 5.5: (a) Reciprocal space in-plane map of 3ML $MoTe_2$/InAs(111). The diffraction pattern is the result of the superposition of three rectangular Brillouin zones, corresponding in real space to three orientational variants of the same rectangular 1T' surface unit cell rotated by 0, 60, 120°. They are highlighted in blue, green and orange respectively. The hexagonal InAs(111) lattice is highlighted in yellow. When the 1T' unit cell sides are in $\sqrt{3}$ ratio, reflections with the same Miller indices coming from different variants coincide on the same spot (b), when they are not, the same set of reflections splits into triplets (c). The inset in (a) shows a magnification of a triplet located along the $h = k$ axis in the map.

We grew $MoTe_2$ by MBE on InAs(111)/Si(111), obtaining the first experimental observation of an orthorhombic $MoTe_2$ T_d stable at room temperature[13]. Before, only two other groups provided evidences of epitaxial 1T' $MoTe_2$ grown by MBE on graphene/SiC[17], but without distinguishing between monoclinic and orthorhombic phases. Our result was obtained for a 3ML $MoTe_2$ sample grown following the "beam interruption" method used by Walsh et al. to grow WTe_2[12]. Besides the T_d structure, we observed also a triclinic polytype, which however does not comply the symmetry requirements for non-trivial topology.

The experimental evidence has been obtained by the combination of x-ray diffraction and electron microscopy. GIXRD allowed to recognize the rectangular geometry of the primitive surface unit cell in the layer plane and to accurately calculate the in-plane lattice parameters. Cross-sectional-STEM images instead allowed to identify the γ phase by imaging the vertical stacking. In fact, our SXRD methods are not adequate to resolve the few degrees-difference in tilt angle ϕ between the out-of-plane axes of the β and γ-$MoTe_2$ unit cells.

Figure 5.5a shows the in-plane reciprocal space intensity map while figure 5.6 shows the radial scans along the directions denoted as h and $h = k$ in the map. With respect to a simple 1T TMDC compound (comparison can be done with the map discussed in

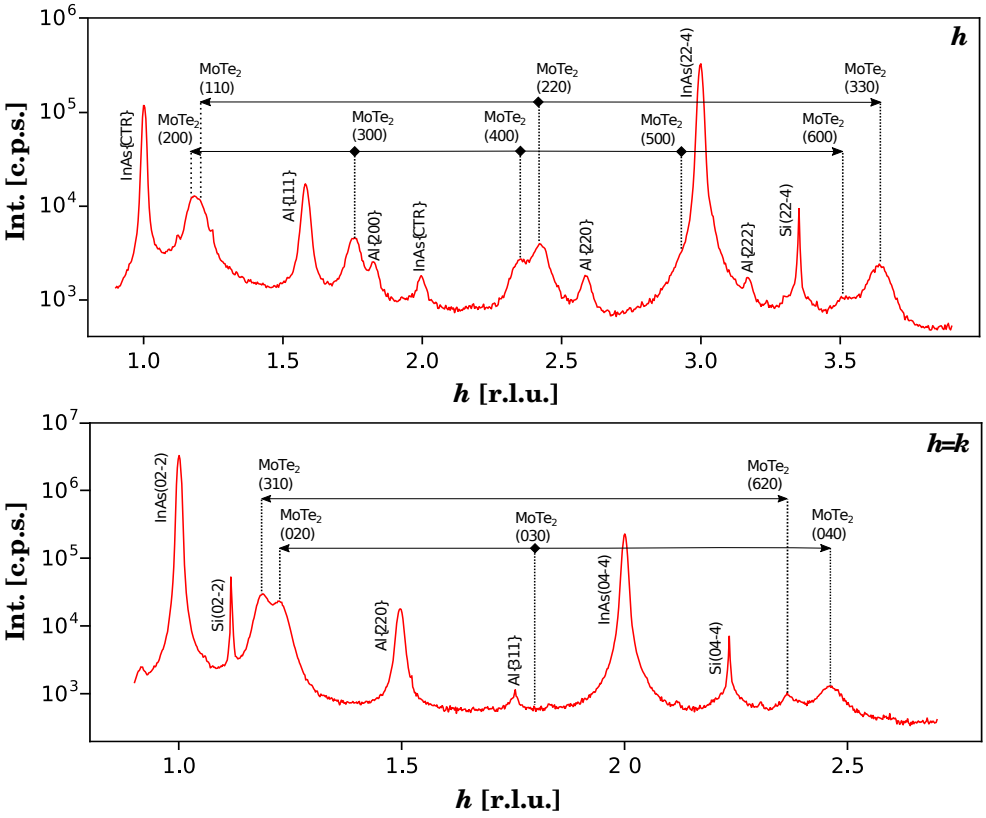

Figure 5.6: GIXRD radial scans taken along h (top) and $h = k$ (bottom) directions in the map as indicated in figure 5.5.

the previous section for $ZrTe_2$), the 3ML $MoTe_2$ map exhibits more reflections, most of them characterized by broaden trilobed shapes (inset in figure 5.5a). The higher density of diffraction spots than in the typical 1T diffraction patterns is due to the doubling of the periodicity of the crystal in real space. As explained in chapter 1, when a 1T-1T' distortion occurs in TMDCs, the pristine symmetry is degraded and the primitive unit cell becomes rectangular with one side, *i.e.* the one parallel to the atomic displacement, twice longer than the other. The trilobed shapes of the diffracted signals is in fact a triplet of reflections. The diffraction pattern could be "disentangled" by considering multiple crystal domains with a primitive rectangular unit cell rotated by 0°, 60° and 120°, generating the rotational variants shown in figure 5.5a in blue, green and orange. In the inset, the triplet is actually the superposition of a single "on-axis" (020) reflection plus a couple of "off-axis" (310) reflections. This interpretation allows for the full indexing of the diffraction pattern. It is worth noting that the triplets are direct consequence of the distortion. If $MoTe_2$ were 1T, a (non primitive) rectangular patterning of the diffraction space with all the three variants would be possible as well. The ratio between two unit cell sides, a and b, would be exactly $\sqrt{3}$ and all the three closely spaced reciprocal lattice nodes would coincide on the same point (figure 5.5b). On the contrary, in distorted $MoTe_2$ $a > \sqrt{3}b$, hence the reciprocal space nodes do not match on the same point, but they split into triplets (figure 5.5c). Radial scans in figure 5.6 confirm such interpretation with

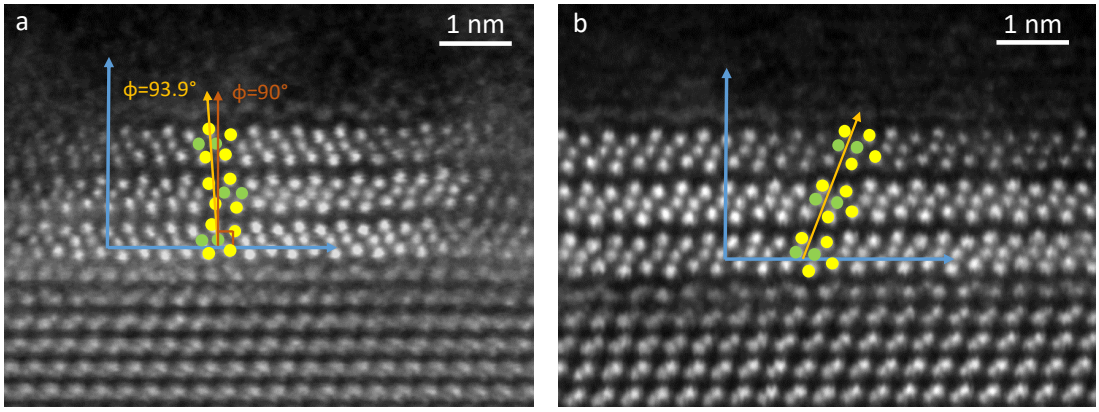

Figure 5.7: Cross-sectional-STEM of 3ML $MoTe_2$/InAs(111) along the [11$\bar{2}$0] zone axis. (a) Orthorhomic stacking: the second layer is 180° rotated with respect to the adjacent ones. First and third layers are vertically aligned as shown by the red arrow forming a 90° angle with the atomic plane. The orange arrow instead shows the direction of an ideal monoclinic unit cell vertical axis forming an almost 94° angle with the atomic plane (not found in this sample); (b) Triclinic stacking: the second layer is not rotated but slightly translated with respect to the adjacent ones.

the difference that in one-dimensional scans the triplets appear as doublets. The long and short sides of the rectangular unit cell extracted from the radial scans are (6.340 ± 0.005)Å and $(3.501 \pm 0.003$Å$)$ respectively. We conclude that, similar to the case of $ZrTe_2$, $MoTe_2$ grown on InAs(111) shows non-negligible in-plane lattice expansion, of the order of 0.9% (see Table 5.1).

By GIXRD we proved so far that the surface unit cell of the grown $MoTe_2$ is not the conventional 1T, but the distorted one. In order to distinguish between the β monoclinic (1T') and the γ orthorhombic (T_d) phases, further information is needed. The cross-sectional-STEM image in figure 5.7a demonstrates that the first and third layers in the unit cell are almost exactly superimposed and the out-of-plane angle ϕ is a right angle, whereas a slightly tilted structure with $\phi \sim 94°$ is expected if the stacking is monoclinic. This proves that the observed phase is the γ orthorhombic one. No traces of the β-$MoTe_2$ phase were found instead. The vertical lattice parameter c is measured by STEM to be 14.15Å, significantly larger than experimental values reported in the literature for bulk T_d $MoTe_2$, which are in the range between 13.86 and 13.89Å[4; 9]. Remarkably, besides T_d $MoTe_2$, an unconventional triclinic structure was also observed for the first time (figure 5.7). The stacking in the triclinic system differs from the T_d phase. In the latter one every second layer is 180° rotated with respect to the others, whereas in the triclinic all the layers have the same orientation but displaced along the [10$\bar{1}$0] direction. It turns out that the unit cell is made up of one single layer. However, this stacking preserves inversion symmetry and is topologically trivial.

We refer to our recent publication [13] for a detailed discussion of the topological properties descending from these peculiar structures. We limit ourselves to report that first principle calculations performed at NCSRD predicted for the measured T_d $MoTe_2$ structure four couples of Weyl nodes of opposite chirality located below and very close

to the Fermi level. This result is of great interest because it establishes that topological properties can be accessible in combination with electronic transport at room temperature.

5.5 Charge density wave phase in multilayer $TiTe_2$

In this section we address a third case study concerning the observation at room temperature of a commensurate charge density wave (CDW) phase associated to a periodic lattice distortion (PLD) in multilayer (50ML) $TiTe_2$ grown on InAs(111)/Si(111). CDWs are common in 3D layered TMDCs, as witnessed by many studies since the Seventies. New interest recently arose alongside the capacity of preparing TMDCs in the 2D ultimate limit. No clues had been found of CDW instabilities in $TiTe_2$ until 2017, when Chen et al. recognised a replica band within the FBZ in the ARPES band diagram of a 1ML $TiTe_2$ film[18], which they ascribed as an evidence of a commensurate (2×2) CDW. The replica is visible below 92K but it is suppressed at higher temperatures and in samples thicker than 1ML. Shortly after, Dutta et al. observed the same commensurate CDW at room temperature when non-hydrostatic pressure was applied on a bulk $TiTe_2$ sample[19].

We performed GIXRD experiments on a multilayer film of 50ML (about 32nm) $TiTe_2$ grown on InAs(111)/Si(111). The data were collected by using 11keV x-ray energy and the beam was directed on the sample at a 0.2° grazing incidence angle. Both in in-plane radial scans along h and $h = k$ and out-of-plane rod scans along l, we observed reconstruction peaks at half-integer Miller indixes (figures 5.8a-d). Such additional reflections are found along all the three hexagonal system axes in reciprocal space (h, k, l) and represent a clear evidence of doubling of periodicity in the 1T-$TiTe_2$ lattice, consistent with a $(2 \times 2 \times 2)$ superlattice. In real space, the distorted unit cell is double of the pristine one. Viceversa, in reciprocal space the FBZ is half that of the undistorted 1T-$TiTe_2$. Moreover, similar to $ZrTe_2$ and $MoTe_2$, also in the $TiTe_2$ multilayer film the experimental in-plane lattice constant is found larger than the reference value expected for the bulk, *i.e.* (3.863±0.002)Å compared to 3.777Å (see Table 5.1).

Based on the recent publications on the CDWs discovered in $TiTe_2$ (bulk and thin layer), we wondered whether the $(2 \times 2 \times 2)$ superlattice in this system could be linked to a CDW and which factors may have contributed to its stabilization. CDW is a complex phenomenon, which manifests both through structural and electronic effects. In chapter 1 we disregarded this complexity and considered that the fundamental ingredients accompanying a CDW phase formation are essentially three: the presence of a *Kohn anomaly* in the phonon dispersion, the existence of a *periodic lattice distortion (PLD)* of the crystal structure and a *band gap opening* in the electronic band diagram. To address the above question, we sought for evidences of one or the other ingredient in the samples we studied. To this purpose, we used a combination of approaches, *e.g.* theoretical arguments, first principle calculations, as well as scattering and photoemission experiments.

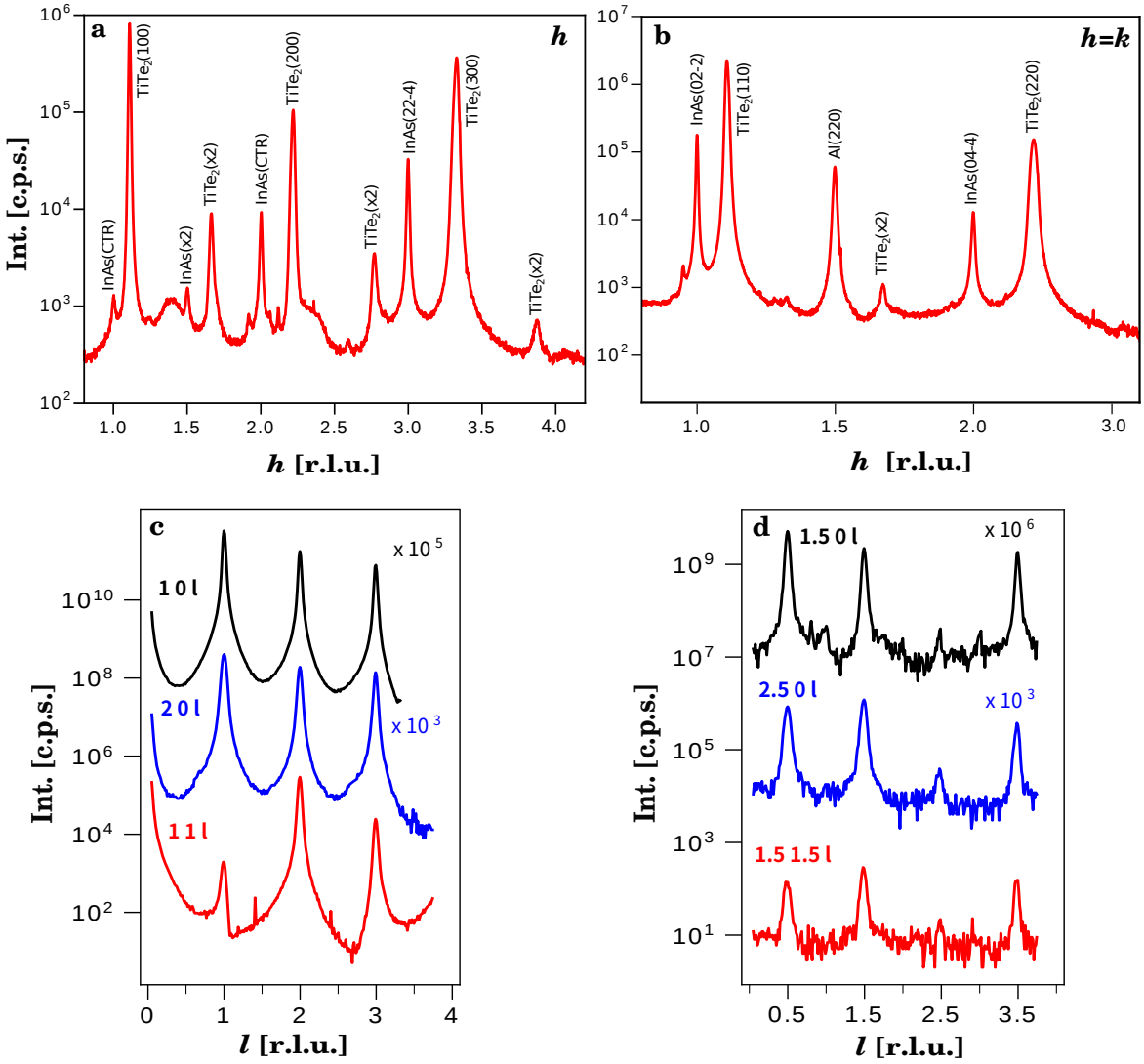

Figure 5.8: GIXRD measurements of 50ML $TiTe_2$/InAs(111) showing a $(2 \times 2 \times 2)$ PLD: (a-b) radial scans along h and $h = k$ high-symmetry directions of the InAs(111) substrate; (c) l-scans measured along some integer $(h, 0)$ and (h, h) rods; (d) l-scans measured along some half-integer $(h, 0)$ and (h, h) rods.

5.5.1 Phonon mode dispersion and computed structure

Using the experimentally found lattice parameters and adopting Heyd-Scuseria-Ernzerhof (HSE) hybrid functionals, density functional theory (DFT) calculations of the phononic band dispersion for a monolayer 1T-$TiTe_2$ were performed at the NCSRD. The calculations predict a strong and broad dip at the M point of the $TiTe_2$ FBZ for one of the three acoustic phonon branches (figure 5.9a), which can be interpreted as a phonon softening associated to Kohn anomaly. A strong and broad dip is typical of the CDWs characterized by large electron-phonon coupling, as those that are expected for 2D TMDCs[20].

Remarkably, the phonon mode in M is totally suppressed and assumes negative frequency values. This fact is usually interpreted as a signal of phase transition in the crystal towards a lower symmetry structure. Coherently with that, energy minimization calcula-

tions carried out for this system established that $TiTe_2$ should relax towards a periodically distorted structure, 90meV more stable in energy than the original 1T phase. The distorted monolayer unit cell structure is drawn in orange in figure 5.9b in contrast to the pristine 1T unit cell in yellow. The Ti atoms (light blue) at the vertices of the distorted cell are fixed on their original positions, while the remaining ones shift by about 0.021 unit cell fractions in the directions pointed out by the black arrows; Te atoms (white and gold) move accordingly in the directions of the red arrows, but their displacements are one order of magnitude shorter compared to metal atoms. This picture reproduces very closely the well-known $TiSe_2$ (2×2) commensurate CDW reported in previous works[21; 22]. $TiSe_2$ is very similar material to $TiTe_2$, both structurally and electronically, and it is plausible that $TiTe_2$ behaves in a similar way.

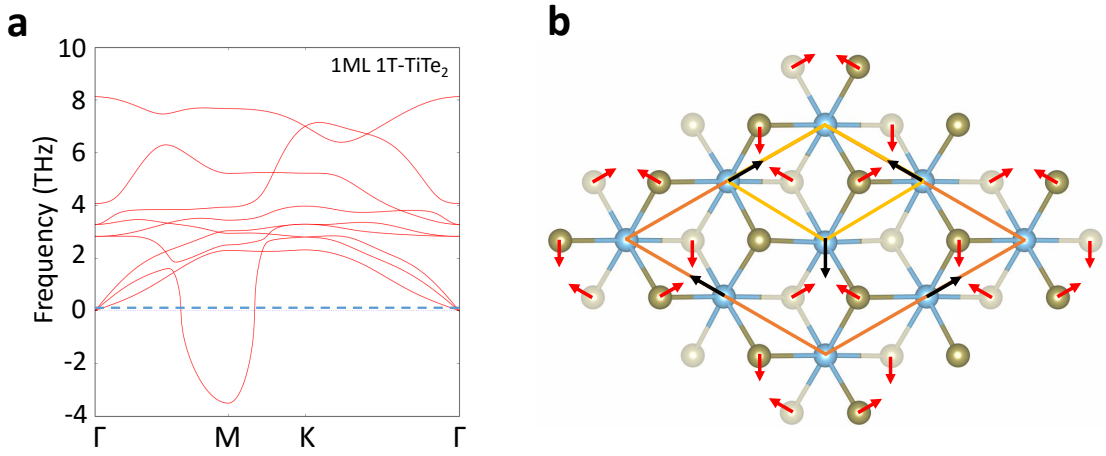

Figure 5.9: (a) phonon dispersion calculated by DFT for 1ML 1T-$TiTe_2$; (b) 1T-$TiTe_2$ in plane projection showing atomic displacements (black and red arrows) due to a (2×2) PLD as calculated by DFT. Ti atoms are in blue; top Te atoms are in gold while bottom Te atoms are in white.

5.5.2 Study of the PLD

Diffuse scattering experiments were performed at the ID28 diffraction side station at ESRF to further investigate the nature of the PLD observed by GIXRD. This new experiment was motivated essentially by two reasons, one theoretical, the other more practical. From a theoretical standpoint, the distribution in reciprocal space of the diffuse scattering signal carries information about the lattice dynamics in a crystal, including thermal phonons whose dynamics may be altered by the interaction with other phonons or electrons. A CDW is therefore expected to leave signatures such as periodic satellite spots and/or diffuse scattering streaks associated to the PLD or to the inelastic scattering of x-rays with the softened phonons. From a practical point of view, a diffuse scattering experiment allows to rapidly map the reciprocal space volume and it provides preliminary information

of lattice dynamics prior to any other deeper investigation, saving measurement time. Further information on the diffuse scattering technique and recent examples can be found in Ref.[23]. At the ID28 beamline diffuse scattering measurements are carried out with the use of a large area PILATUSx1M 2D detector in combination with undulator x-rays - typically the beam brilliance is three orders of magnitude higher than at BM32 - enabling high signal to noise ratio and faster acquisitions[24]. The data were collected using a 17.8keV (0.697Å) x-ray beam with fixed 1° incident angle.

In figures 5.10a-b two reciprocal space maps parallel to the sample surface are shown at $l = 1$ and $l = 0.5$ respectively, while figures 5.10c-d represent two reciprocal space perpendicular cuts containing the h and $h = k$ axis. Globally the diffraction patterns can be described as the superposition of intense Bragg peaks located at integer Miller indices, characteristic of the non-distorted 1T structure, and a superstructure pattern of satellite peaks located at half integer indices, having from two to three orders of magnitude lower intensity. This difference in intensity is substantial to support the idea of a CDW as the cause of the observed PLD. A common 1T' distortion in fact would not present such a large intensity contrast between integer and non integer reflections, *i.e.* between Bragg peaks and satellites.

We can state as general rule that when l is an integer number (figure 5.10a), intense Bragg peaks corresponding to the periodicity of the non-distorted structure occupy integer h, k positions at the new Brillouin zone centers Γ. In between two Bragg reflections, very weak signals are found at M points on the zone edges, which are instead due to the distortion. When l is half-integer (figure 5.10b), Bragg peaks are absent while those due to the superstructure are centered at half integer (h, k) values. Since periodicity is doubled also along the vertical direction, a new FBZ must be defined that contains an additional (non equivalent) plane passing through A,H,L points, which are the projection of Γ,K,M points in the intermediate plane, as shown in the inset of figure 5.10. In this new FBZ, satellite peaks at half-integer l values are all located at L points, whereas no intensity should be measured in A. The finite intensity which is instead effectively measured in A corresponds either to the Bragg peaks of the Si substrate - Si in-plane lattice constants are very close to those of $TiTe_2$ - or to scattered intensity due to the finite film thickness. The intensity stripes passing through integer spots are other typical features of Si due to thermal phonon scattering.

All these observations are confirmed by the vertical cuts shown in figures 5.10c-d. $TiTe_2$ Bragg peaks are located along integer (h, k) rods at integer l values (Si substrate Bragg reflections and thermal diffuse scattering intensity sometimes superimpose to them), whereas satellites are along the rods occupying half-integer (h, k) positions. These are much weaker when l is integer than when it is half integer. This observation opens a debate about the nature of the PLD, which cannot be purely sinusoidal but should be described by a more complex Fourier synthesis.

At this point, we may wonder which structural model can reproduce best the experimental diffraction pattern just described. We can consider as a plausible structure to

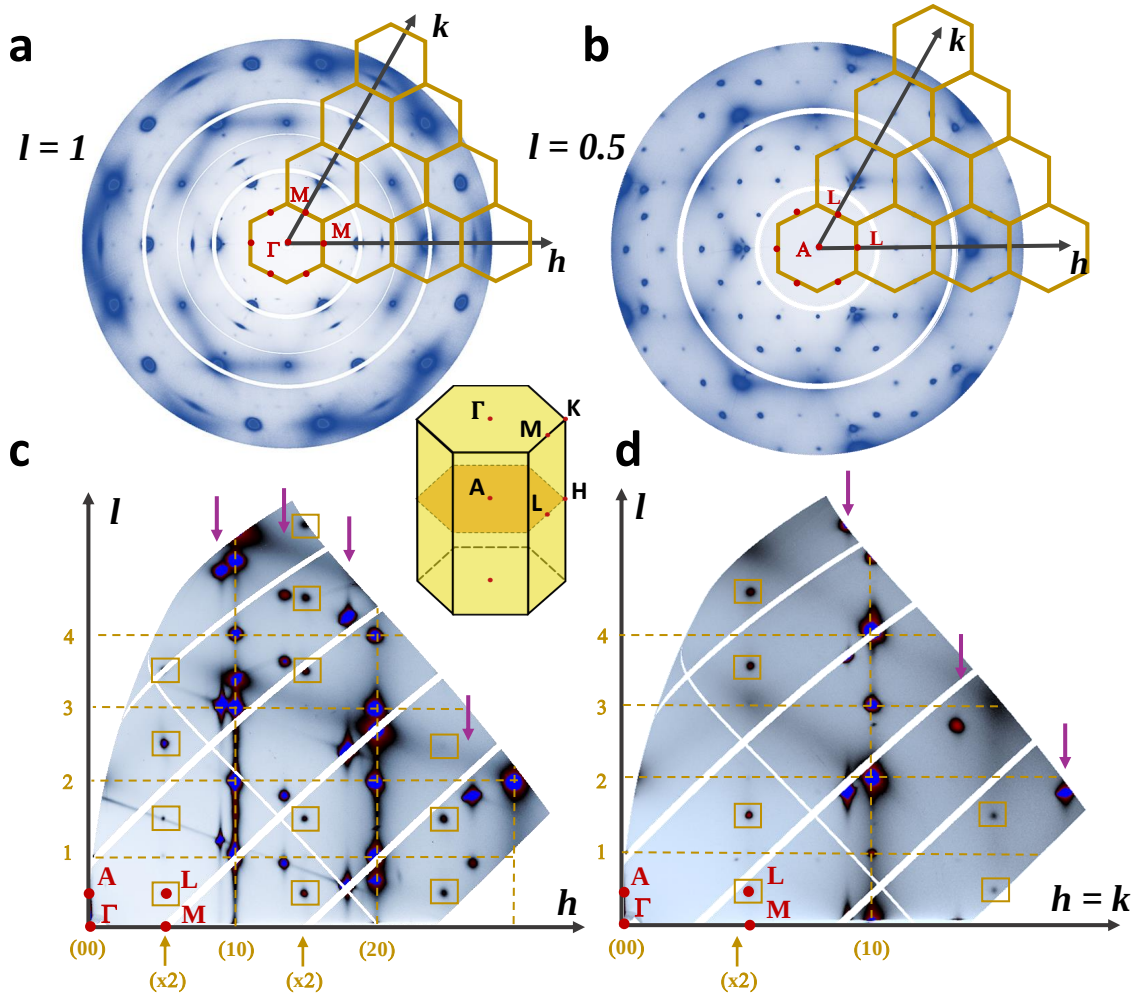

Figure 5.10: Reciprocal space mapping of PLD in 50ML $TiTe_2$/InAs(111) collected by diffuse scattering. (a) in-plane map at $l = 1$; (b) in-plane map at $l = 0.5$; (c) vertical cut parallel to h axis; (d) vertical cut parallel to $h = k$ axis. In the vertical cuts dashed lines, square boxes and purple arrows indicate respectively the integer Bragg reflections, the satellite spots from the PLD and the Bragg reflections from InAs. In the inset: schematics of the FBZ in $TiTe_2$ presenting $(2 \times 2 \times 2)$ PLD.

account for the in-plane (2×2) reconstruction the DFT output schematized in figure 5.9b, since the PLD shown therein was already established as the PLD in a $TiSe_2$ CDW phase[21; 22]. With only a 2D model we cannot however account for the vertical component of the distortion. The latter is a non-trivial problem that lies very likely in the layer stacking order. The total scattered intensity along a $TiTe_2$ rod is given by the scattering from all the 50 layers in the mulitlayer film. It is easy to verify that, if two adjacent identical $TiTe_2$ layers A and B ($A = B$) are shifted by half a unit cell along one of the two hexagonal h or k axes, *e.g.* $B = A + (\frac{1}{2}, 0, \frac{1}{2})$, the total structure factor is given by:

$$F_{tot} = F_A + F_B = F_A(1 + e^{2\pi i(\frac{h}{2}+\frac{l}{2})}) \tag{5.1}$$

When h or k are even, F_{tot} is non zero at even l-values, whereas when h or k are odd the scattering signal is located at odd l-values. "Even" and "odd" are equivalent to "integer"

hk	**n=even**		**n=odd**	
n0	l=even: F=2F$_A$	l=odd: F=0	l=even: F=0	l=odd: F=2F$_A$
0n	l=even: F=2F$_A$	l=odd: F=0	l=even: F=2F$_A$	l=odd: F=0
nn	l=even: F=2F$_A$	l=odd: F=0	l=even: F=0	l=odd: F=2F$_A$

Table 5.2: summary of the results obtained by applying equation 5.1 to a set of $(n,0)$, $(0,n)$ and (n,n) rods located along h and $h=k$ high symmetry directions, with n assuming even/odd (h,k) Miller indices values, at the intersection with even or odd l planes.

and "half-integer" in the reference frame we have been using so far. Table 5.2 summarizes all the possible extinctions for rod along h, k and $h=k$ hexagonal high symmetry axes. Although the calculations lead to different results for $(n,0)$ and $(0,n)$ rods when n is odd, we verified throughout the simulations that the incoherent scattering of 30° rotated equivalent domains reduces the possible cases to those shown in the table for the $(n,0)$ rod. In conclusion, the ABA stacking breaks the translation symmetry in the vertical direction, and the peculiar shift of the B plane along either h or k (but not both) described above allows to reproduce the intensity pattern observed in the diffusion scattering maps and in the rod scans.

We built then a 50ML $TiTe_2$ model based on the 2×2 in-plane PLD reproduced in figure 5.9b and the above described stacking. Inside each layer atomic positions were set as in a perfect 1T structure. The PLD is introduced by adding a displacement factor s to the (x,y) atomic coordinates, allowing the atoms to move out of their sites in the directions specified in figure 5.9b. The in-plane and out-of-plane total structure factor was then calculated and plotted using PyRod (description in Chapter 4) in the form of in-plane Fourier maps and rod scans as reported in figure 5.11. The distortion parameter values were adjusted in order to obtain the best qualitative agreement with the experimental data. In general we observed that:

- when the distortion parameter s is set to zero the output is the one expected for a 1T structure.
- the best agreement is obtained when s is of the same order of magnitude as the displacement calculated by DFT ($s=0.021$)
- Only Ti atom displacements affect substantially the results. Te atoms displacements have negligible influence.
- Only when B is shifted parallel to either h or k axes, but not both, Bragg peaks and satellites occupy the position shown in the experimental scans. All the other possibilities lead to at least one situation of disagreement.

The model does not account for the peak suppression that we systematically observe in the l-scans at $l=2.5$ and half-integer h (or k). We believe that a more complex stacking is the cause of this systematic absence. The structural refinement of the model has not been accomplished finally since it represents a pure 3D crystallography problem, whereas our

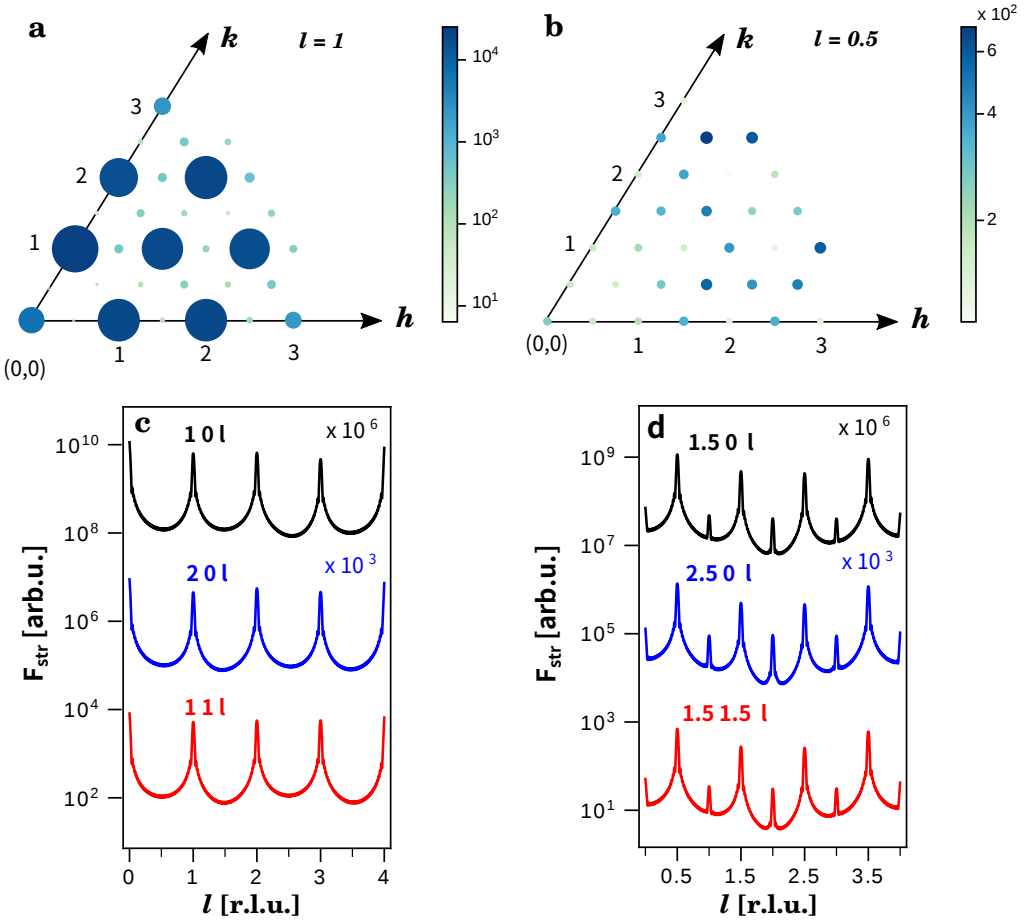

Figure 5.11: Simulations of in-plane diffraction maps and rod scans in 50ML $TiTe_2$ exhibiting $(2 \times 2 \times 2)$ PLD (to be compared with figures 5.8a-d and 5.10). (a) In-plane map calculated at $l = 0$; (b) in-plane map calculated at $l = 0.5$; (c) l-scan along some integer $(h, 0)$ and (h, h) CTRs; (d) l-scan along some half-integer $(h, 0)$ and (h, h) rods. The simulations are based on 50 layers of $TiTe_2$ distorted structure model described in the text and are calculated using the "PyRod" code (see chapter 4).

software tools are specific for 2D surface and rod analysis. Nevertheless, the analysis done untill now shows already a convincing picture of how the PLD of $TiTe_2$ should appear in real space, indeed very similar to $TiSe_2$.

5.5.3 Study of the electronic band structure

So far we have discussed the structural aspects related to a CDW/PLD. We still have to address the third point listed at the beginning of this section, namely the CDW effects on the electronic band dispersion. It is worth anticipating that we do not have at this stage a sufficient set of data and theoretical calculations to give robust conclusions. Nevertheless we may have a phenomenological discussion by comparing our results with other works reported in the literature for similar systems.

Peierls' model establishes that as consequence of the PLD, energy gaps open at Fermi level at a wavevector corresponding to that of the CDW ($\vec{q}_{CDW}$). The comparison between

the cost in elastic energy stored in the PLD and the lowering of the electron energy states associated with the bandgap opening tells whether the CDW is self-sustainable or not. Peierls' model gives a proper description of one-dimensional systems in weak electron-phonon coupling regime, but it is not reliable for 2D systems in presence of strong coupling, as it is most often the case with TMDCs. More recent microscopic models predict larger bandgap opening and atomic displacement for these situations[25]. Figure 1.7 in chapter 1 shows the changes occurring in the electronic band dispersion diagram for $TiSe_2$ upon the transition to the commensurate $(2 \times 2 \times 2)$ CDW phase below the critical Peierls' temperature. It is worth noting that $TiSe_2$ above the CDW transition is an indirect 50meV bandgap semiconductor. Se 4p states form the valence band (VB) maximum at Γ, while Ti 3d states contribute to the conduction band (CB) minimum at M(L) point. Upon transition to the CDW phase, the VB maximum shifts down to lower energies, resulting in a band gap increase from 50meV to 100meV[26; 27]. Further studies highlighted that this experimental observation cannot be interpreted on the basis of a rigid band downshift only, but rather by taking into account the hybridization of Se 4p and Ti 3d states[26; 28]. Besides the gap increase in fact, strong p-d band interactions manifest in the flattening and in the spectral weight suppression of the Se 4p VB maximum, as well as in the rebound of the bottom of the Ti 3d CB. The PLD/CDW is intimately connected to this effect because the shortening of the Se-Ti bonds favors stronger wavefunction hybridization. For this reason, the CDW should be understood in the spirit of a "local chemical bonding picture" and of a "band-type" Jahn-Teller mechanism[26; 28].

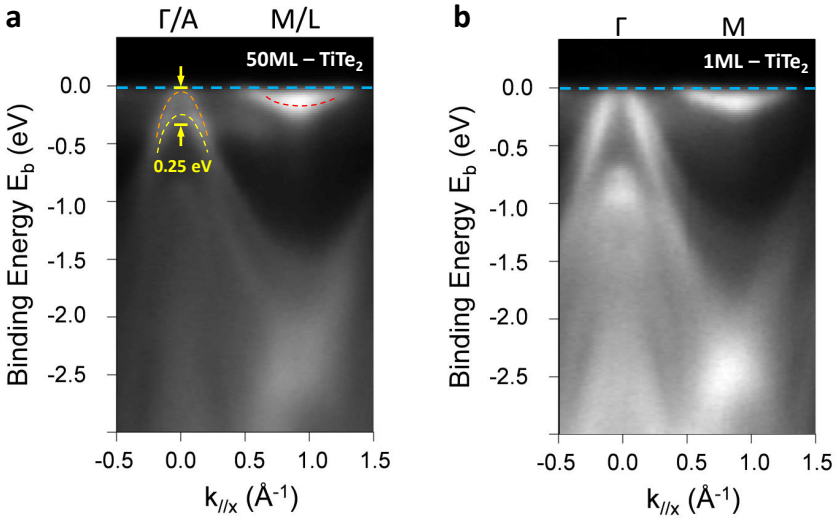

Figure 5.12: Electronic band structure of (a) 50ML and (b) 1ML $TiTe_2$/InAs(111) along Γ(A)-M(L) direction, obtained by ARPES. The two Te 5p CB bands dispersing around Γ(A) are shown in orange and yellow. The Ti 3d CB crosses the E_F in M(L) and it is highlighted in red.

In contrast to $TiSe_2$, $TiTe_2$ is instead a semimetal. Two strongly dispersive Te 5p bands (VB) cross E_F near the Γ point and overlap in energy with the Ti 3d band located

at M(L) by 0.2-0.4eV[29; 30]. The experimental ARPES measured at the NCSRD, is shown in figure 6.12a-b for 50ML and 1ML films respectively. The VB and CB overlap in energy below E_F. In contrast to $TiSe_2$, no bandgap opening is visible here, but in figure 6.12a one of the two Te 5p bands near Γ shifts down by 0.25eV with respect to the other and the E_F. This indicates the energy lowering of some of the electronic states near E_F, which is referred to as partial gap (or *pseudogap*) opening. This splitting and downshifting is not observed neither in the $TiTe_2$ band structure calculated by Rossnagel et al.[29] nor in the ARPES data of a 1ML $TiTe_2$/InAs(111) sample of us that does not exhibit the PLD[14] that is found for the multilayer film (figure 6.12b). Drawing conclusions seems premature at this stage in the absence of supporting calculations. However this observation is suggestive of the same Jahn-Teller mechanism proposed for $TiSe_2$ and it calls for deeper investigations.

To confirm the occurrence of a CDW is not simple task, given the complexity and the multiple features it goes with. In this work we gave a substantial contribution in this sense analyzing multiple aspects typical of CDWs, *i.e.* the corresponding PLD, a Kohn anomaly, (partial) bandgap opening, giving theoretical and experimental evidences to support and enriching the discussion by comparing former and widely accepted works published in the past.

5.5.4 CDW origin and self-sustainability

We performed diffuse scattering experiments also on commercial bulk $TiTe_2$. The result are reported in the Supplementary Information of the paper of this work[14]. As expected, the bulk material does not present any kind of PLD, but only the 1T phase. Such counterproof is the demonstration that the CDW/PLD is specific to our system, owing to the peculiar epitaxy or the growth history. In fact, as already said, no CDW had ever been found in $TiTe_2$ before the work of Chen et al., who reported a (2×2) CDW phase in monolayer $TiTe_2$. This CDW is stable below 92K and anyway it is not found in samples thicker than one monolayer. We claim instead that a CDW could have formed in our system at room temperature. So, why should it be possible? Why a CDW phase can self-sustain in $TiTe_2$ grown on InAs(111), whereas it has never been observed in bulk $TiTe_2$?

Recently, Dutta et al. measured a $(2 \times 2 \times 2)$ CDW in bulk $TiTe_2$ when they applied 0.5GPa uniaxial pressure on it[19]. In parallel, theoretical studies published at the same time suggest that strain may affect the CDW transition temperature and stabilize the PLD out of the normal conditions. In particular, biaxial compressive strain was found to lower the Peierls' temperature while tensile strain is supposed to increase it[31]. As mentioned several times in this chapter, tellurides grown on InAs(111)/Si(111) all show expanded lattice constants. In the case of $TiTe_2$ the residual strain measured with respect to our reference value is 2.2% larger than the relaxed value (see Table 5.1), whereas the out-of-plane lattice constant (c=6.349Å) results 2.3% smaller than in the pure bulk compound

(c=6.498%). In other words, $TiTe_2$ grown on InAs(111) undergoes in-plane tensile built-in strain while it is vertically compressed. This compressive strain state can be considered somehow similar to the case reported by Dutta. Therefore, the epitaxial strain imparted by the InAs(111) substrate could be indeed a stabilizing factor for the CDW phase in multilayer $TiTe_2$.

Finally, one may wonder also up to which temperature the observed PLD distortion is preserved and if other commensurate or uncommensurate CDW phases exist in other temperature ranges. GIXRD measurements have been repeated on this sample at BM32 in order to investigate the temperature stability of the PLD. Figures 5.13a-b show the (1,0) $TiTe_2$ CTR and the (1.5 0) satellite rod measured at room and high temperature. It is evident in figure 5.13b that the PLD is conserved almost identical far above room temperature, at least up to 300°C, although background signal has increased significantly because of the enhanced diffuse thermal scattering due to the higher temperature. Unfortunately, above 350°C structural changes occur in the sample, as evidenced by GIXRD measurements not shown here (several new additional peaks comes out in the radial scans), which are related to the substrate degradation. As mentioned at the beginning of this chapter, the InAs(111)/Si(111) substrate is stable only at low temperatures and it is expected to degrade below 400°C. We cannot thus identify the critical temperature of CDW found in our sample.

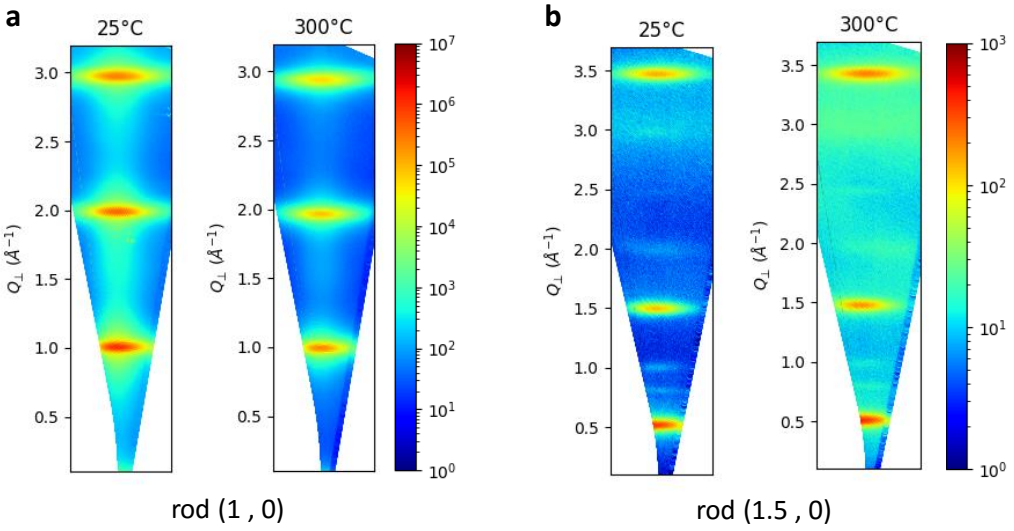

Figure 5.13: 2D views of (a) $TiTe_2$ (1,0) CTR and (b) (1.5) satellite rod of the (2x2) PLD, measured at room temperature and 300°C and plotted using methods described in chapter 4.

5.6 Conclusions and outlooks

Single and multi-layer ditellurides as $ZrTe_2$, $MoTe_2$ and $TiTe_2$, grown on InAs(111)substrates have been characterized by GIXRD, as well as with other complementary techniques, above all cross-sectional-STEM and ARPES. All these studied dichalcogenides present larger in-plane lattice parameters than in the corresponding relaxed bulk structures. We believe they are tensile strained due to a non-negligible interaction occurring with their InAs(111) substrate, this one having a lattice constant up to 0.2% larger. Signs of this interaction are found by GIXRD in the low mosaic spread of the 2D layers, almost limited by the substrate, and, for SL $ZrTe_2$, in the superstructure pattern of satellites around the main InAs reflections in the plane. The epitaxial constraint is assumed as the main factor for the stabilization of phases which are not encountered in their bulk analogs at room temperature. First, the orthorhombic γ-phase of $MoTe_2$ was found at room temperature in a 3ML compound. This phase is topologically non-trivial and it has been predicted to carry Weyl states. Second, a $(2 \times 2 \times 2)$ periodic lattice distortion connected to a CDW was found for a 50ML sample of $TiTe_2$. This discover is supported also by theoretical calculations, which predict a deep Kohn anomaly in the phonon dispersion of the 1T-$TiTe_2$ structure - sign of phase instability - and by some simulations of the measured diffraction patterns based on structural models involving AB layer stacking and in-plane distortions of the atoms similar to those found in $TiSe_2$. Finally, our ARPES measurements indicate a possible down-shift of a Te p-state at Γ. A similar behaviour was measured in $TiSe_2$ and associated to an energy gain of the electronic band states, which sustains the charge density wave and it is explained in the frame of a local bonding picture and band-type Jahn-Teller mechanism.

Bibliography

[1] A. A. Soluyanov, D. Gresch, Z. Wang, Q. Wu, M. Troyer, X. Dai, and B. A. Bernevig, "Type-II weyl semimetals," *Nature*, vol. 527, no. 7579, p. 495, 2015.

[2] D. H. Keum, S. Cho, J. H. Kim, D.-H. Choe, H.-J. Sung, M. Kan, H. Kang, J.-Y. Hwang, S. W. Kim, H. Yang, *et al.*, "Bandgap opening in few-layered monoclinic $MoTe_2$," *Nature Physics*, vol. 11, no. 6, p. 482, 2015.

[3] S. Song, D. H. Keum, S. Cho, D. Perello, Y. Kim, and Y. H. Lee, "Room temperature semiconductor–metal transition of $MoTe_2$ thin films engineered by strain," *Nano Letters*, vol. 16, no. 1, pp. 188–193, 2015.

[4] B. E. Brown, "The crystal structures of wte2 and high-temperature $MoTe_2$," *Acta Crystallographica*, vol. 20, no. 2, pp. 268–274, 1966.

[5] W. Dawson and D. Bullett, "Electronic structure and crystallography of $MoTe_2$ and WTe_2," *Journal of Physics C: Solid State Physics*, vol. 20, no. 36, p. 6159, 1987.

[6] Y. Zhou and E. J. Reed, "Structural phase stability control of monolayer $MoTe_2$ with adsorbed atoms and molecules," *The Journal of Physical Chemistry C*, vol. 119, no. 37, pp. 21674–21680, 2015.

[7] Y. Li, K.-A. N. Duerloo, K. Wauson, and E. J. Reed, "Structural semiconductor-to-semimetal phase transition in two-dimensional materials induced by electrostatic gating," *Nature Communications*, vol. 7, p. 10671, 2016.

[8] C. Wang, Y. Zhang, J. Huang, S. Nie, G. Liu, A. Liang, Y. Zhang, B. Shen, J. Liu, C. Hu, *et al.*, "Spectroscopic evidence of type II weyl semimetal state in WTe_2," *arXiv preprint arXiv:1604.04218*, 2016.

[9] A. Tamai, Q. Wu, I. Cucchi, F. Y. Bruno, S. Riccò, T. Kim, M. Hoesch, C. Barreteau, E. Giannini, C. Besnard, *et al.*, "Fermi arcs and their topological character in the candidate type-II weyl semimetal $MoTe_2$," *Physical Review X*, vol. 6, no. 3, p. 031021, 2016.

[10] R. W. G. Wyckoff, *Crystal structures*. Krieger, 1964.

[11] Y. Arnaud and M. Chevreton, "Etude comparative des composés TiX_2 (X=S, Se, Te). structures de $TiTe_2$ et TiSeTe," *Journal of Solid State Chemistry*, vol. 39, no. 2, pp. 230–239, 1981.

[12] L. A. Walsh, R. Yue, Q. Wang, A. T. Barton, R. Addou, C. M. Smyth, H. Zhu, J. Kim, L. Colombo, M. J. Kim, *et al.*, "WTe_2 thin films grown by beam-interrupted molecular beam epitaxy," *2D Materials*, vol. 4, no. 2, p. 025044, 2017.

[13] P. Tsipas, S. Fragkos, D. Tsoutsou, C. Alvarez, R. Sant, G. Renaud, H. Okuno, and A. Dimoulas, "Direct observation at room temperature of the orthorhombic weyl semimetal phase in thin epitaxial $MoTe_2$," *Advanced Functional Materials*, vol. 28, no. 33, p. 1802084, 2018.

[14] S. Fragkos, R. Sant, C. Alvarez, A. Bosak, P. Tsipas, D. Tsoutsou, H. Okuno, G. Renaud, and A. Dimoulas, "Room temperature commensurate charge density wave in epitaxial strained $TiTe_2$ multilayer films," *Advanced Materials Interfaces*, vol. 6, no. 5, p. 1801850, 2019.

[15] P. Tsipas, D. Tsoutsou, S. Fragkos, R. Sant, C. Alvarez, H. Okuno, G. Renaud, R. Alcotte, T. Baron, and A. Dimoulas, "Massless dirac fermions in $ZrTe_2$ semimetal grown on InAs(111) by van der waals epitaxy," *ACS Nano*, vol. 12, no. 2, pp. 1696–1703, 2018.

[16] M. T. Dau, M. Gay, D. Di Felice, C. Vergnaud, A. Marty, C. Beigne, G. Renaud, O. Renault, P. Mallet, T. Le Quang, *et al.*, "Beyond van der waals interaction: The case of $MoSe_2$ epitaxially grown on few-layer graphene," *ACS Nano*, vol. 12, no. 3, pp. 2319–2331, 2018.

[17] Y. Yu, G. Wang, S. Qin, N. Wu, Z. Wang, K. He, and X.-A. Zhang, "Molecular beam epitaxy growth of atomically ultrathin mote2 lateral heterophase homojunctions on graphene substrates," *Carbon*, vol. 115, pp. 526–531, 2017.

[18] P. Chen, W. W. Pai, Y.-H. Chan, A. Takayama, C.-Z. Xu, A. Karn, S. Hasegawa, M.-Y. Chou, S.-K. Mo, A.-V. Fedorov, *et al.*, "Emergence of charge density waves and a pseudogap in single-layer $TiTe_2$," *Nature Communications*, vol. 8, no. 1, p. 516, 2017.

[19] U. Dutta, P. Malavi, S. Sahoo, B. Joseph, and S. Karmakar, "Pressure-induced superconductivity in semimetallic 1T-$TiTe_2$ and its persistence upon decompression," *Physical Review B*, vol. 97, no. 6, p. 060503, 2018.

[20] K. Rossnagel, "On the origin of charge-density waves in select layered transition-metal dichalcogenides," *Journal of Physics: Condensed Matter*, vol. 23, no. 21, p. 213001, 2011.

[21] D. Di Salvo, FJ Moncton and J. Waszczak, "Electronic properties and superlattice formation in the semimetal $TiSe_2$," *Phys. Rev. B*, vol. 14, p. 4321, 1976.

[22] B. Guster, R. Robles, M. Pruneda, E. Canadell, and P. Ordejón, "2×2 charge density wave in single-layer $TiTe_2$," *2D Materials*, vol. 6, no. 1, p. 015027, 2018.

[23] A. Bosak, D. Chernyshov, B. Wehinger, B. Winkler, M. Le Tacon, and M. Krisch, "In-between bragg reflections: thermal diffuse scattering and vibrational spectroscopy with x-rays," *Journal of Physics D: Applied Physics*, vol. 48, no. 50, p. 504003, 2015.

[24] "ID28 - inelastic scattering II." https://www.esrf.eu.

[25] K. Motizuki, N. Suzuki, Y. Yoshida, and Y. Takaoka, "Role of electron-lattice interaction in lattice dynamics and lattice instability of 1T-$TiSe_2$," *Solid State Communications*, vol. 40, no. 11, pp. 995–998, 1981.

[26] K. Rossnagel, L. Kipp, and M. Skibowski, "Charge-density-wave phase transition in 1T-$TiSe_2$: Excitonic insulator versus band-type jahn-teller mechanism," *Physical Review B*, vol. 65, no. 23, p. 235101, 2002.

[27] T. Kidd, T. Miller, M. Chou, and T.-C. Chiang, "Electron-hole coupling and the charge density wave transition in $TiSe_2$," *Physical Review Letters*, vol. 88, no. 22, p. 226402, 2002.

[28] M. H. Whangbo and E. Canadell, "Analogies between the concepts of molecular chemistry and solid-state physics concerning structural instabilities. electronic origin of the structural modulations in layered transition metal dichalcogenides," *Journal of the American Chemical Society*, vol. 114, no. 24, pp. 9587–9600, 1992.

[29] K. Rossnagel, L. Kipp, M. Skibowski, C. Solterbeck, T. Strasser, W. Schattke, D. Voß, P. Krüger, A. Mazur, and J. Pollmann, "Three-dimensional fermi surface determination by angle-resolved photoelectron spectroscopy," *Physical Review B*, vol. 63, no. 12, p. 125104, 2001.

[30] R. Claessen, R. Anderson, G.-H. Gweon, J. Allen, W. Ellis, C. Janowitz, C. Olson, Z. Shen, V. Eyert, M. Skibowski, *et al.*, "Complete band-structure determination of the quasi-two-dimensional fermi-liquid reference compound $TiTe_2$," *Physical Review B*, vol. 54, no. 4, p. 2453, 1996.

[31] M. Wei, W. Lu, R. Xiao, H. Lv, P. Tong, W. Song, and Y. Sun, "Manipulating charge density wave order in monolayer 1 T-$TiSe_2$ by strain and charge doping: A first-principles investigation," *Physical Review B*, vol. 96, no. 16, p. 165404, 2017.

Chapter 6

MoS_2/Au(111) growth and decoupling

6.1 Introduction

Single layer MoS_2 is a direct bandgap semiconductor TMDC whose most stable structure is 1H. The interest for MoS_2 nanostructures arose at the end of the Nineties, as they were considered suitable catalysts for the production of low sulfur fuels[1]. The earliest MoS_2 flakes with nanometric lateral size and monolayer thickness were synthesized at the Aarhus University by the group of F. Besenbacher, following a reactive MBE synthesis on Au(111) substrates using H_2S gas as sulfur precursor[1]. In this chapter we will refer to this synthesis approach as the "*Aarhus' recipe*". The Au(111) (non reconstructed) surface is an optimum substrate for MoS_2: firstly, its three-fold symmetry complies with the hexagonal planar symmetry of TMDCs and it acts as a suitable template to grow nanostructures with a unique orientation determined by the substrate; secondly, Au catalyzes the dissociation reaction of the H_2S molecules, which would not occur otherwise at low temperature. More recently, on the wake of the graphene discovery and the "search" for new 2D materials, the achievement of electrostatic switching[2] and the demonstration of bright light emission in the visible spectral range[3] made the interest in SL MoS_2 rise again, so that nowadays MoS_2 is considered a very promising candidate for future 2D optoelectronics.

To reach the kind of structural quality found in mechanically exfoliated samples, intense efforts have been done to grow MoS_2 via bottom-up approaches such as CVD[4], chalcogenation of metal surfaces[5], or MBE[6; 7; 8]. MBE growth of MoS_2 is currently still based on the *Aarhus' recipe*. This process allows for the growth of high crystalline quality and highly oriented monolayer MoS_2 islands. Since the first attempts[1], some variations in the method were reported, such as cycling the process[7] or carrying out the Mo deposition directly on the hot Au surface rather than at room temperature[8]. Notably, by depositing Mo on the Au(111) substrate heated up to 500°C, Bana et al. achieved MoS_2 islands with large-area domains and monolayer thickness, covering Au surface without grain boundaries, even across the atomic steps.

However, as-prepared SL MoS_2 is not suited to the study of some of the key properties of the 2D MoS_2: excitons become very short-lived due to the immediate vicinity of a metallic substrate and electrical transport is also shunt by the conductive substrate. Besides that, MoS_2 does not retain the properties of the freestanding material. Significant interaction between the electronic bands of MoS_2 and Au(111) entails strong changes in the electronic band structure[9] and the existence of an intense moiré pattern was found to induce a nanometer-scale modulation of this interaction[10].

A way to weaken this interaction is to "lift" MoS_2 from its surface. Such lifting occurs spontaneously across the regions where MoS_2 is suspended over some Ångström deep vacancy islands of the substrate[11]. Effective lifting may be achieved also using an alternative strategy, namely by intercalating a layer of alkali species in order to decouple MoS_2 from its substrate. Intercalation of bulk TMDCs in solution has been widely investigated since the Seventies. However, our goal is to intercalate epitaxial SL MoS_2 flakes that are in direct contact with the substrate, under UHV conditions. At the moment of writing, intercalation has never been achieved on SL MoS_2 lying on metal substrates, and almost never on other 2D TMDC systems, with the only exception of SL WS_2 grown on Ag(111)[12]. As with graphite, using layers of alkali atoms, molecules, or transition metals as intercalants, unique properties including superconductivity and (anti)ferromagnetism have been found and/or predicted in intercalated TMDC systems[13]. The ability to store and release alkali atoms by intercalation and de-intercalation, i.e. the reverse process, in perfectly reversible way, makes TMDCs possible electrode materials for Li-ion batteries[14]. Moreover, electro-donor intercalants promote a structural phase transition in MoS_2, *i.e.* from semiconducting 1H to metallic 1T phase[15], that can be used in several applications, as already discussed in chapter 3.

During this PhD thesis we studied the growth, intercalation and de-intercalation of MoS_2 on Au(111) using cesium (Cs) as intercalating agent. Cs is the largest atom among alkali - and among the largest in the periodic table - but also the most electro-positive. Electro-donation is an attractive property for intercalation compounds and we expect from Cs an intense charge transfer towards MoS_2. Moreover, SL MoS_2/Au(111) represents a well-studied and documented TMDC reference to check the feasibility of the intercalation between a TMDC and the substrate. Our analysis combines a broad set of complementary measurements which aim at investigating the intercalation-induced effects on the atomic structure and the electronic properties of SL MoS_2 by using both real and reciprocal space probes installed on two different UHV systems of our laboratories, equipped for *in-situ* growth and diagnostics: a room temperature scanning tunneling microscope (STM) available at Institut Néel, and the grazing incidence diffractometer at BM32-ESRF (described in chapter 4).

In this chapter we are going to describe the process leading to the preparation of monolayer MoS_2 flakes on Au(111) with typical total surface coverage spanning between 0.4ML and 0.8ML and some tens of nanometer lateral size. The description of the surface morphology and the MoS_2 atomic structure is supported by STM images and GIXRD

measurements. Subsequently, we will report the effects observed in the system after Cs deposition, always through a combined approach of STM and diffraction. Intercalation will be demonstrated by the vanishing of the characteristic moiré superstructure satellite peaks from the diffraction pattern, a clear sign of the weakening of the interface interaction between the substrate and the 2D epitaxial layer, and it is accompanied by a series of other structural effects, including in-plane lattice constant expansion. We will show that this process is also reversible, since a high temperature annealing promotes desorption (and so de-intercalation) of the Cs atoms. A quantitative analysis of the sample reflectivity (XRR) will be also discussed to investigate the increase of the interface thickness following Cs intercalation and confirm the "structural decoupling" of MoS_2 from Au. Finally, a last section is devoted to the photoemission study of the effects induced by intercalation on the as-grown and intercalated MoS_2/Au(111) band structures. This analysis aims at providing insights also on the "electronic decoupling" of MoS_2 from Au, described in terms of charge transfer and orbital hybridization. Electronic structure characterization has been performed in a third UHV system installed at the SGM-3 endstation of ASTRID2 synchrotron radiation source (Aarhus, Denmark).

6.2 Growth and characterization of MoS_2/Au(111)

6.2.1 The growth

We grew SL MoS_2 following *Aarhus' recipe* as described by Grønborg et al[7]. This procedure consists in cycles of Mo deposition and annealing under H_2S partial pressure on a UHV-clean herringbone-reconstructed Au(111) surface. Cycling the process is aimed at progressively increasing the total coverage and the average size of the MoS_2 flakes. Hereafter we summarize the cycle steps adopted in this thesis for the MoS_2 growth inside the INS2 UHV chamber at BM32. A similar process has been applied for the MoS_2 growths carried out in the other mentioned setups. Before growth, the Au(111) single crystal surfaces have been sputtered and reconstructed in UHV by means of several cycles of Ar-ion bombardment at 0.8-1kV and annealing at 600°C, until a well developed herringbone reconstruction was deduced by RHEED observations, as *e.g.* in figures 6.1a-b. After that, the MoS_2 growth process consists of the following steps:

1. A clean Au(111) single crystal surface showing the herringbone reconstruction is exposed to a 10^{-5}mbar partial pressure of H_2S.

2. Mo is then deposited on the Au(111) surface kept at room temperature at the very slow rate of 0.02ML/min by an e-beam evaporator in H_2S atmosphere. The depositions had a 8 to 12 minutes long duration.

3. The Mo flow is then stopped and the sample is annealed at 600°C for 15 minutes

always in H_2S atmosphere.

4. The sample is cooled down to RT. H_2S is either maintained constant all along the process or turned off below 200°C. Too high temperature lead to the formation of sulfur vacancy in the MoS_2.

The as described process represents one growth cycle and it is calibrated to increase the surface coverage by 0.2ML of MoS_2. At BM32, between two consecutive cycles, a set of GIXRD measurements was performed to monitor the evolution of the MoS_2 structure. This sequence of operations was usually repeated up to three/four times to achieve a MoS_2 nominal surface coverage between 0.6 and 0.8ML. At the 0.8ML coverage Grøngborg et al. report that a second layer of MoS_2 begins to seed.

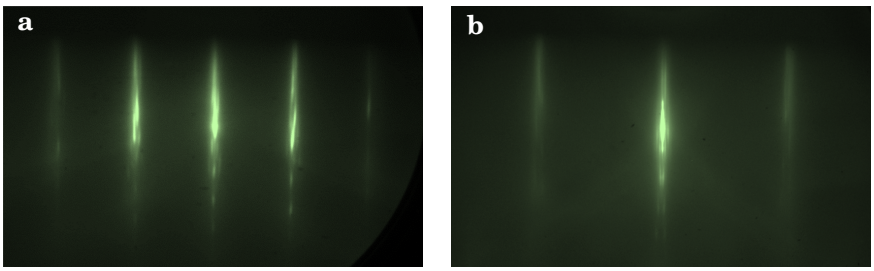

Figure 6.1: RHEED diffractograms at 17keV along (a) the $[1\bar{1}0]$ and (b) the $[11\bar{2}]$ azimuths of Au, showing the characteristic herringbone reconstruction as weak intensity fringes on the sides of the Au streaks.

6.2.2 Morphology and structure of the MoS_2/Au(111) surface

A bare Au(111) surface free from any contaminant appears at room temperature with the characteristic *herringbone* reconstruction, so-called after the peculiar profile visible by STM (figures 6.2a-b). To release part of the tensile stress and lower the surface energy, the Au(111) topmost layer spontaneously densifies and forms *fcc* and *hcp* domains separated by domain walls where Au atoms occupy bridge sites[16]. The as-reconstructed surface is described by a large rectangular $(22 \times \sqrt{3})$R30° unit cell, that in reciprocal space manifests with a dense pack of fringes on the side of the main Au(111) reflections. This is visible in the RHEED images in figure 6.1a-b, in the radial scans in figure 6.3d, and in the insets of the latter showing high-resolution in-plane maps acquired around the three Au reflections along the h axis.

The concomitant exposure of the Au substrate to H_2S gas molecules and Mo atoms allows the nucleation of MoS_2 islands on the gold surface. The low Mo deposition rate (0.02ML/min) prevents metal atom clusterization and favors instead the sulfurization of Mo atoms species. The temperature chosen for the annealing of the nucleated crystals (600°C) is also crucial: lower temperatures might lead in fact to incomplete sulfurization

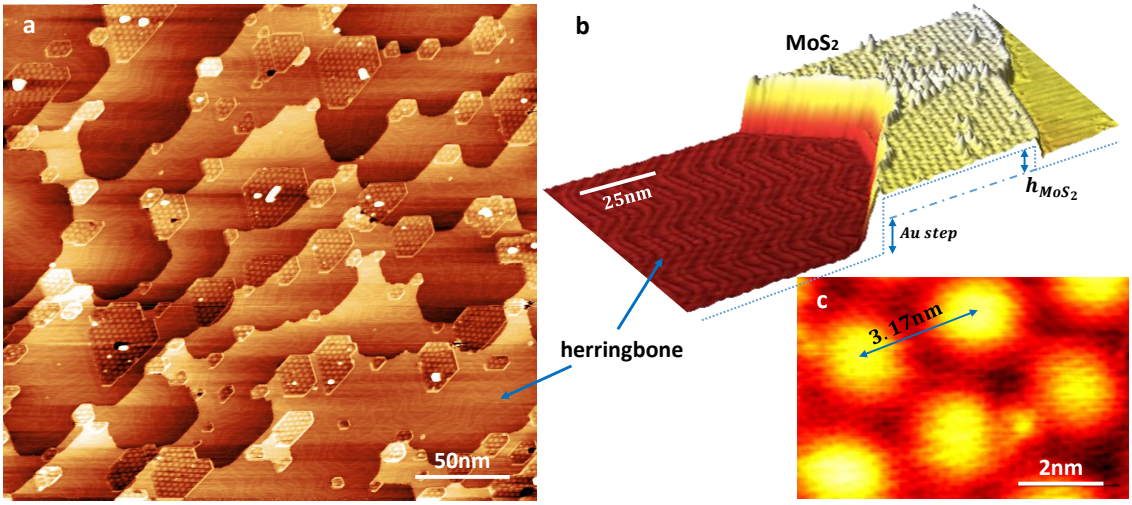

Figure 6.2: STM topographic images of SL MoS_2 islands formed on Au(111), with the herringbone reconstruction still visible on the MoS_2-free surface, exhibiting moiré pattern: (a) panoramic view (1.1nA, -1.0V) on the Au surface with MoS_2 islands nucleated mostly on along the Au terrace edges; (b) three-dimensional view (2.0nA, -2.0V) of a single layer MoS_2 island grown on top of Au(111) and close to a terrace edge; the Au surface shows the herringbone reconstruction while MoS_2 shows the moiré pattern; defects in the moiré appear as higher bumps; (c) atomically resolved image (0.8nA, -1.9V) of an MoS_2 surface displaying a marked moiré patterning (yellow bumps).

and at the same time limit the mobility of Mo atoms on the surface. On the other hand, higher temperatures might make Mo segregate in the bulk or create S vacancies in the MoS_2 lattice. Figure 6.3a shows the evolution of the diffraction pattern in the surrounding of the (200) MoS_2 reflection at each stage of a three cycle growth leading to 0.6ML MoS_2. When the growth starts, soon the herringbone reconstruction is lifted and the (200) MoS_2 Bragg reflection forms at $h = 1.8266$. At each cycle the peak intensity constantly increases, but the full-width at half maximum (FWHM) remains nearly constant. Intuitively, since the longitudinal width of the peaks measured in radial scans is inversely proportional to the finite lateral size of the domains - and neglecting any distribution of lattice parameter - we can infer that the average grain size of MoS_2 domains does not increase by repeating the cycles. We will come back to this point later.

The STM image in figure 6.2a shows how the surface looks at the end of two growth cycles, *i.e.* 0.4ML of MoS_2 surface coverage. The MoS_2 flakes exhibit triangular/hexagonal shapes with straight edges and have an extension of the order of a few 10nm. In between the flakes the herringbone reconstruction of the bare Au(111) is still visible but it often appears irregular. Nucleation occurs mostly along the Au steps were the largest islands (up to 30nm) are found. All these observations are consistent with those in previous reports[6; 7]. On the MoS_2 flakes a pronounced pattern is visible. The zoom in figure 6.2c shows that the apparent height modulation has a 3.17nm periodicity and it is aligned with the high symmetry directions of MoS_2. This pattern is an example of moiré superlattice described in chapter 2. The intensity modulation visible in the STM topographs is in fact a combined effect of corrugation and electronic density modulation imparted by the lattice mismatch between MoS_2 and the Au(111) substrate.

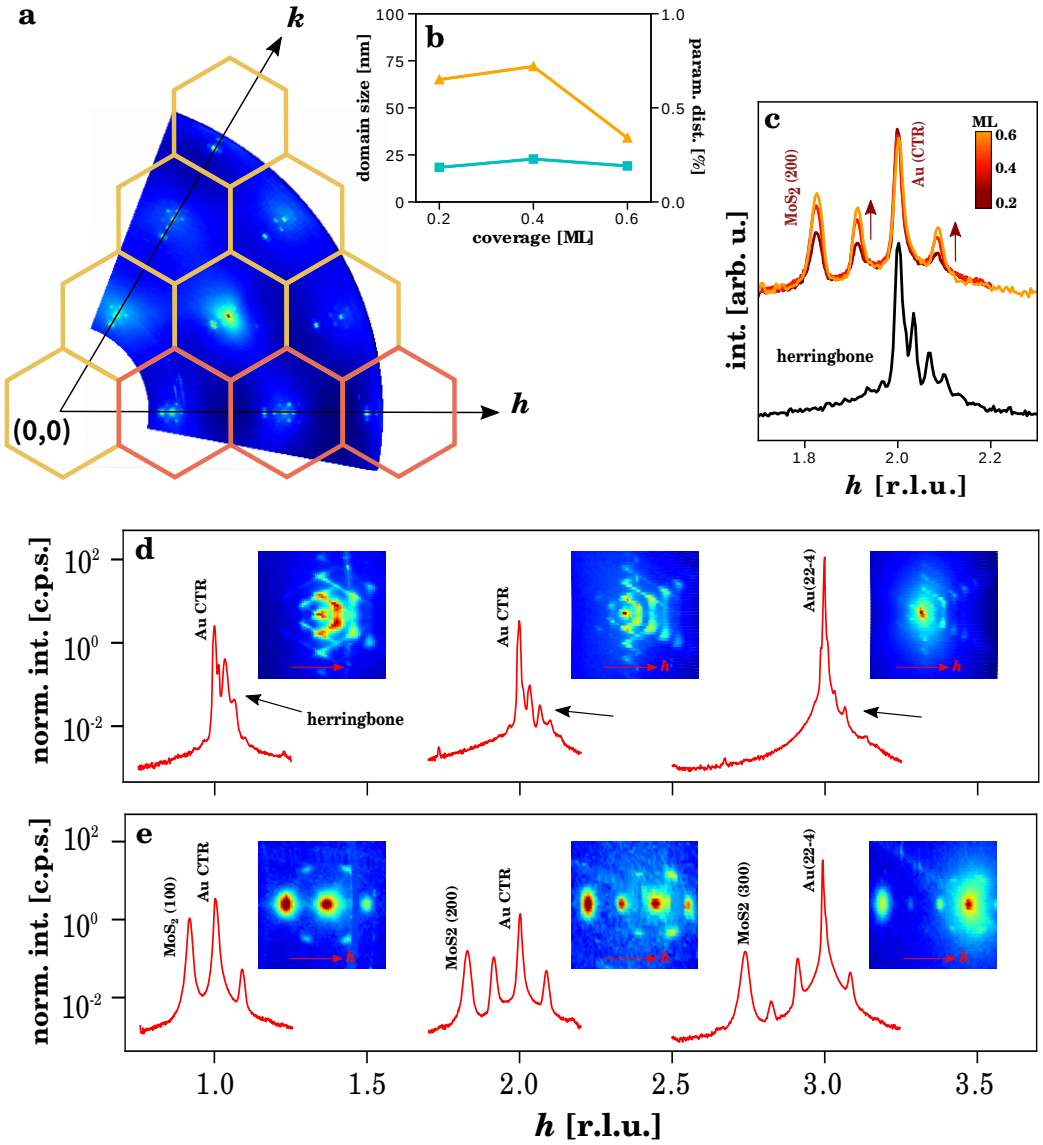

Figure 6.3: GIXRD characterization of as-grown 0.6ML MoS_2 on Au(111). (a) in-plane cut of the reciprocal space lattice; the hexagonal patterning shows the subdivision of the reciprocal space in Au(111) Brillouin zones whereby the Au CTR/Bragg reflection is at the center (Γ) point; the red hexagons point out the first, second and third Brillouin zone along h axis; (b) average domain size (cyan) and lattice parameter distribution (orange) as function of the coverage during growth of MoS_2; (c) radial scans of the diffracted intensity direction in the map in the second Brillouin zone of the reciprocal space plane along h at three different steps of the MoS_2 growth: pristine herringbone reconstructed Au surface (black), 0.2ML MoS_2 (dark red), 0.4ML MoS_2 (red) and 0.6ML MoS_2 (yellow); (d-e) radial scans measured along h at each of the three Brillouin zones highlighted in red in (a), before (top) and after (bottom) the MoS_2 growth; besides each radial scan, the corresponding two-dimensional highly resolved reciprocal space map is shown in the inset.

GIXRD measurements in figures 6.3, *i.e.* in-plane maps and high resolution radial scans along the high symmetry h direction, confirm this scenario. The first result we can observe is that Au(111) and MoS_2 crystallographic directions are precisely aligned (figure 6.3a). Careful analysis of the peak positions in radial scans allows to determine the MoS_2 in-plane lattice parameter which measures (3.157 ± 0.001)Å, very close to the values reported in the literature for multilayer and two-dimensional compounds[7; 8]. Besides MoS_2 peaks, an additional pattern of satellite reflections equispaced between each other is present. The periodicity associated to this superlattice is (33.35±0.01)Å, consistent with the modulation length of the moiré pattern observed by STM. If we compare this length with the unit cell lattice constants of Au(111) and MoS_2, we discover they are respectively in 10.5 and 11.5 ratio. We can deduce that the superlattice unit cell might correspond either to the precise coincidence of 10 MoS_2 unit cells onto 11 Au(111) unit cells, *i.e.* a (10×11) consistent with other recent reports[8], or - with equal probability - to 11 MoS_2 unit cells onto 12 Au(111) unit cells, *i.e.* a (11×12). This ambiguity could be explained by the fact that MoS_2 lattice parameter is not homogeneous but slightly varies from one domain to the other. Looking at the maps in the insets of figure 6.3e, we note that the satellite signals are distributed as hexagonal patterns around Au CTRs or Bragg reflections. These patterns are reminiscent of that observed in chapter 5 for $ZrTe_2$ and, similarly, they can be understood in terms of the mismatch existing between the overlayer and the substrate. However, in MoS_2/Au(111) the satellites are remarkably more intense: this translates a significant lattice distortion either in MoS_2 or in the topmost Au(111) planes (or both). We will come back to this point shortly later.

The longitudinal width of the peaks along a radial direction provides the average lateral size D of the single domains. This information can be extracted by fitting a few points in the Δq^2 vs q^2 plot of the momentum transfer vectors associated to the MoS_2 peaks measured along the radial direction h, according to the relationship[17]:

$$\Delta q^2 \propto \frac{4\pi^2}{D^2} + q^2 \cdot \frac{\Delta a^2}{a^2} \tag{6.1}$$

where q and Δq are respectively the modulus of the momentum transfer vectors at which the peaks are found and the peaks FWHM, D is the average domain size and $\frac{\Delta a}{a}$ the distribution of the in-plane lattice parameter over the whole sample. We calculated that the FWHM of MoS_2 peaks in a 0.6ML sample increases from (0.32±0.05)nm^{-1} to (0.51±0.05)nm^{-1} from first to third order. This corresponds to an average domain size of about 20nm. Strikingly, the domain size is here smaller than the typical flake sizes that we determined by visual inspection of STM images (not reported here). This difference simply shows that globally the flakes are not single-crystal, but each consists of smaller single-crystal grains. Equation 6.1 applied to data from the 0.2ML and 0.4ML samples, *i.e.* at intermediate stages of the growth, leads to similar domain extensions (figure 6.3b). Our interpretation is that at each step of the MoS_2 cyclic preparation, new MoS_2 islands nucleate, grow, and coalesce with pre-existing ones, but no lattice re-organisation occurs

that would eliminate the grain boundaries and yield large single-crystal flakes.

6.2.3 Structure and coupling at the interface between MoS_2 and Au(111)

To learn more about the out-of-plane structure of the material, we measured the x-ray reflectivity (XRR) of the sample. As explained in chapter 4, the amplitude of the Fourier transform of the total electronic density of the system along the out-of-plane direction l can be determined by measuring the (0,0) specular rod, whose intensity profile is sensitive only to the out-of-plane component of the momentum transfer. The experimental XRR curves of the bare Au(111) sample and of 0.8ML of MoS_2/Au(111) appear respectively in figures 6.5 and 6.6. For both we report the 2D projection of the experimental intensity of the Au(0,0) CTR obtained from 2D detector data and the integrated structure factor, F_{str}, profile as function of l. Compared to the pristine Au(111), in the MoS_2 sample we observe a bump in the reflectivity between the (000) and (111) crystallographic reflections of Au(111), *i.e.* respectively between $l = 0$ and $l = 3$. Qualitatively, the distance between the two minima in the XRR curve is set by destructive interferences between the Au(111) planes and the MoS_2 layer. Our simulations of the (0,0) CTR structure factor along l (in figure 6.6c) demonstrate how the distance between the minima becomes shorter - the profile is more "oscillating" - by physically separating the substrate and the 2D layer, namely by increasing the distance d_{Au-S} between the first superficial Au layer and the bottom S layer in MoS_2. In order to obtain a reliable estimation of the MoS_2-Au distance, we refined the parameter values of a structural model by fitting the experimental data. The fitting has been performed using the ROD code[18].

As explained in chapter 4, the most simple way to model a surface atomic structure is to consider the substrate as a semi-infinite column of piled *bulk unit cells*, on top of which we put the exact number of layers that constitute the *surface unit cell*, *e.g.* the overlayer - the single layer TMDC for instance - and any substrate layer below which is allowed to relax or deform and does not present long range periodicity perpendicular to the surface.

In our case the bulk unit cell is common for the two domains and it consists simply of a three layer set of Au (111) planes with the typical bulk interplanar distance of 2.35Å. Regarding the surface unit cell, we assumed in this model two regions scattering incoherently - *i.e.* the square of the total structure factor is the sum of the squared single contributions - whereas the scattering between substrate and surface within the same domain is necessarily coherent - *i.e.* the square of the total structure factor is the square of the sum of the single contributions. The two domains describe respectively the Au(111) regions covered by the MoS_2 flakes and the bare Au(111) surface, consistently with the MoS_2 coverage of the surface, *i.e.* between 60% and 80%. We disregard the possible periodic corrugation due to the moiré in order to keep low the number of free parameters and ensure a reliable fit, and we consider only "flat" layers.

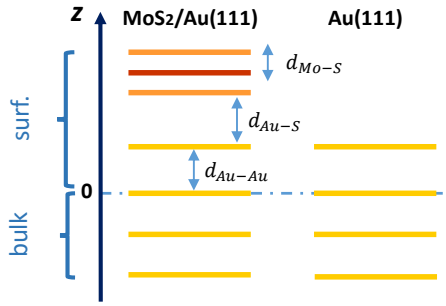

Figure 6.4: Sketch of the out-of-plane (z) layer stacking model used to fit the experimental XRR curve. The colored horizontal stripes display the different atomic layers: Au (yellow), S (orange) and Mo (red); $z = 0$ corresponds to the blue dashed line: it separates the substrate unit cells (negative z, only the first three layers are shown) from the surface unit cell (positive z).

As shown in figure 6.4, the free parameters in this model are: the interplanar distance between Mo and S planes in MoS_2 (d_{Mo-S}), the gap between the bottom S plane in MoS_2 and the outermost Au (111) atomic plane of the substrate (d_{Au-S}), and the distance between the same superficial Au plane from the next one underneath (d_{Au-Au}). As opposed to the bulk interplanar distances between Au planes in the bulk, which are fixed, the latter is let free to vary in order to account for possible surface relaxation in the z direction. Notably the possible displacements are only vertical and no atomic in-plane displacements have been considered since the specular rod is not sensitive to in-plane scattering vector components. Other free parameters in the fit are atomic occupancy within the planes and the out-of-plane Debye Waller (DW) coefficients which have been added to the calculations to model the thermal and static disorder. Finally, the roughness of the surface is modeled within the so-called *beta*-model[19], with β as another free parameter.

We obtained the very good fit to the experimental data ($R = 0.026$) reported in figure 6.6b corresponding to the electronic density profile shown in the inset. The fitting procedure yields the refined parameter values as listed in Table 6.1. The 2D layer-substrate interface distance (d_{Au-S}) amounts to (2.46±0.21)Å^{-1}, a value significantly lower than the characteristic vdW gap of bulk MoS_2 (3.17Å)[20]. A straightforward conclusion is that a strong interaction is active at the interface in place of weak vdW forces between MoS_2 layers in bulk, which structurally bonds the MoS_2 to the substrate. Such interaction is responsible for the orbital hybridization between S and Au found by ARPES[9] and might lead also to structural deformation in the lattice, *e.g.* corrugation and/or lateral atomic displacements, as the pronounced superstructure pattern seems to indicate. The intralayer Mo-S distance (d_{Mo-S}), equal to (1.53±0.22)Å^{-1}, is instead very close to the values already reported in the literature[20]. Finally the fit lead to a modest relaxation of the first Au layer where MoS_2 is grown, estimated about 0.8% larger than typical 2.35Å interplanar distance in bulk.

	fit-value	**uncertainty**	**ref.**
$\mathbf{d_{Au\text{-}S}}$	2.46 Å	0.21 Å	3.17 Å
$\mathbf{d_{Mo\text{-}S}}$	1.53 Å	0.22 Å	1.49 Å
$\mathbf{d_{Au\text{-}Au}}$	2.37 Å	0.05 Å	2.35 Å

Table 6.1: Interplanar spacings and relative uncertainties as estimated by fitting the experimental XRR curve in figure 6.6 and based to the model described in the text. The reference values reported are relative to diffraction measurement of bulk compounds[20]

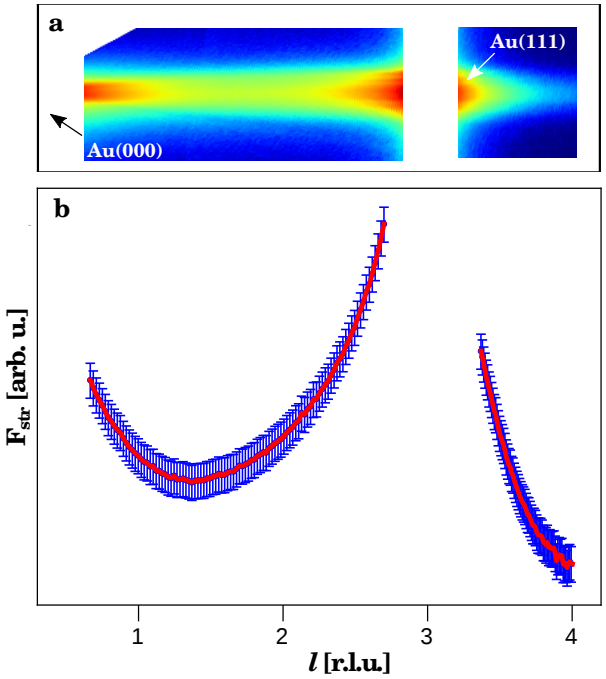

Figure 6.5: Specular rod analysis by XRR of Au(111) substrate before MoS_2 growth. (a) Two-dimensional view of the (0,0) specular rod intensity along l; (b) integrated structure factor F_{str} (blue dots) displayed along l, and best fit ($R = 0.018$, red curve).

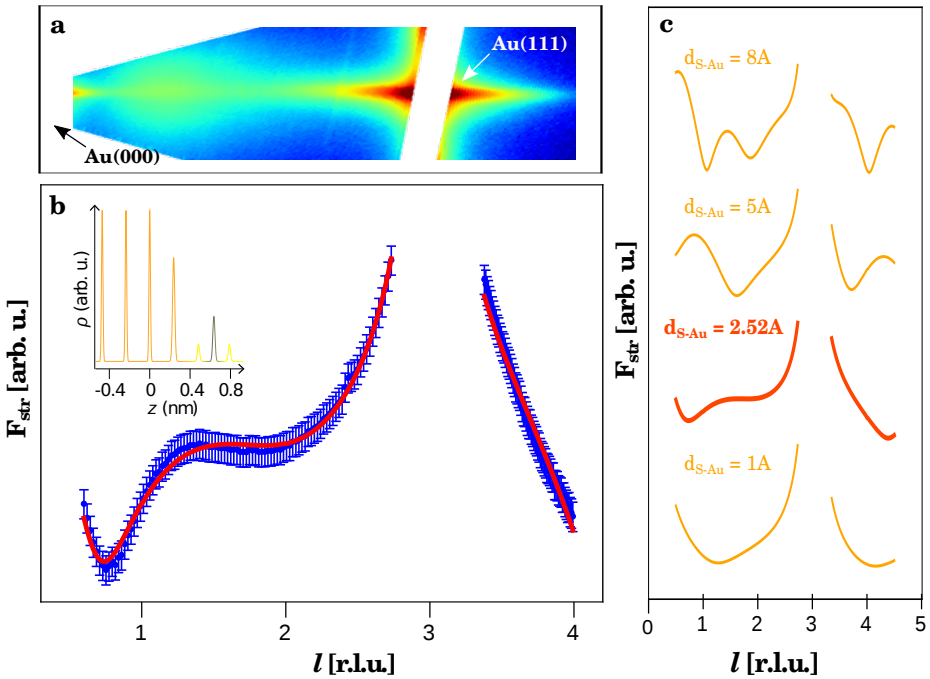

Figure 6.6: Specular rod analysis by XRR of the as-grown MoS_2 on Au(111). (a) Two-dimensional view of the (0,0) specular rod intensity along l; (b) integrated structure factor F_{str} (blue dots), displayed along l, and best fit ($R = 0.025$, red curve); the inset shows the electronic density for the different planes in the model along z (see figure 6.4) and corresponding to the best fit. (c) simulations of the (0,0) specular rod as function of l calculated from the best fit model by varying the distance d_{Au-S} between the topmost Au layer and the bottom S layer.

6.3 Intercalation of SL MoS_2/Au(111) by Cs atoms

We move now to the study of the MoS_2/Au(111) intercalation in UHV. We want to verify if intercalating some alkali metal species, i.e. cesium (Cs), inside the heteroepitaxial gap between SL MoS_2 and Au is a feasible and effective route to decouple a MoS_2 from its substrate both structurally and electronically. Cs is evaporated by resistive heating from an home-made source: two inox rods are used as electrodes to carry the current through a SAES GETTER alkali dispenser inside the UHV chamber. When a threshold current is overcome, the dispenser metal case opens along the traced groove and Cs atoms sublimates in the chamber. Typically a pressure as low as 10^{-9}mbar is measured during deposition after the source has been degased. For three times the sample was exposed to the Cs vapors at room temperature for 30 minutes, while the process was monitored by GIXRD. After each deposition step, the sample was heated at low temperature (200-250°C). We verified that the post deposition annealing speeds up intercalation, whereas annealing the sample during the Cs deposition reduces the sticking of the alkali species on the surface. No reliable Cs flux measurements were collected to estimate accurately the deposited Cs dose on the Au surface, neither during the experiment nor *a posteriori*. In the next sections we will comment the main effects observed by STM, GIXRD, and XRR after Cs evaporation and we will systematically compare them with the as-grown MoS_2 case.

6.3.1 Main effects of Cs deposition on the MoS_2 structure

Cs deposition has several effects on SL MoS_2, which are evident in figure 6.7a, showing the evolution of the diffraction pattern after each Cs evaporation stage in the surrounding of the (200). First, the diffraction signal associated to MoS_2 progressively shows two components that are fitted in figure 6.7c: one of them at higher h-values ($h = 1.8238$) is located at the same position in reciprocal space where we observed MoS_2 peak in the as grown diffraction pattern; the other, at lower h-values ($h = 1.8114$) instead corresponds to a $\sim$0.85% expansion of the lattice (in-plane lattice constant a=3.184Å). The longitudinal peak FWHM is similar for both cases and to as-grown MoS_2, which indicates that no substantial changes occur in MoS_2 domain size upon intercalation. We also observe in figure 6.7a an overall decrease of the MoS_2 peak intensity as the Cs dose increases, together with a broadening of their angular width, as shown by the rocking scans in figure 6.7d. Both point to increased disorder in the form of in-plane strain and mosaic spread.

Remarkably, also the signals associated with the moiré lattice decrease in intensity (figure 6.7a). This observation suggests a reduction of the amplitude of the periodic lattice distortions associated with the spatially varying interaction between Au(111) and MoS_2. These effects become more prominent when the sample is annealed a few 100°C above room temperature - typically at 250°C - after Cs deposition, which suggests that kinetics governs the processes at play. After three steps of room temperature deposition

radial scans along h and associated planar cuts in reciprocal space (figure 6.7c) essentially feature the Au and MoS_2 peaks with almost no sign of a moiré contribution. However a new superstructure manifests at higher h-values close to the Au peaks.

A straightforward way to interpret all these observations is to invoke intercalation of Cs in between MoS_2 and Au(111). Without Cs significant hybridization and periodic lattice distortion are expected, which accounts for the strong moiré signals initially observed in figures 6.3. Conversely, the vanishing signal upon Cs deposition and annealing indicates that the Au atomic distortion related to the moiré are significantly reduced and the hybridization between Au and MoS_2 orbitals almost canceled. In the absence of a significant hybridization between MoS_2 and Au orbitals, the MoS_2 is no more strongly pinned on the substrate. According to this view, the MoS_2 layer is expected to relax upon Cs intercalation and this hypothesis finds its confirmation in the 1.4% lateral expansion mentioned before.

Besides the weakening of the epitaxial forces, several other effects may explain this expansion. First, MoS_2 is grown at 600°C, a temperature at which the ratio of lattice parameters for MoS_2 and Au(111) is precisely 1.10, *i.e.* the 11/10 ratio determined experimentally after the sample is cooled down to room temperature. Individully the thermal compression of bulk MoS_2 and Au(111) is different at 600°C and room temperature, though, amounting to 0.02Å and 0.026Å respectively. The relief of the corresponding thermal compressive strain in MoS_2 upon intercalation should amount to a $\sim$0.2% expansion, a quantity much smaller than what we observed.

We wonder then what is the main effect contributing to the lattice expansion. A structural phase transition, e.g. 1H-1T or 1H-1T', is expected upon electron doping[21], and Cs, a well-known electro-donor species, might indeed donate the required amount of charges to MoS_2. The 1T phase is not expected to have a significantly different lattice constant from the 1H phase, on the contrary the 1T' phase should[22]. As we saw several times along this manuscript, a 1T' phase is characterized by a doubling of periodicity along three out of six in-plane hexagonal axes, which is easily detectable in reciprocal space by additional reflections at fractional order positions. However our diffraction measurements do not detect such doubling of the MoS_2 unit cell.

There are two other reasons why an increasing amount of alkali atoms in the vicinity of MoS_2 could actually lead to an increased lattice constant. In the related system of potassium inserted in between MoS_2 layers, DFT calculations predicted a significant lattice expansion. This is ascribed to either the stronger charge density within the Mo-S bonds or to repulsive interactions between the alkali atoms[23], which due to electron donation actually behave as cations, and in turn end up to stretch the MoS_2 layer.

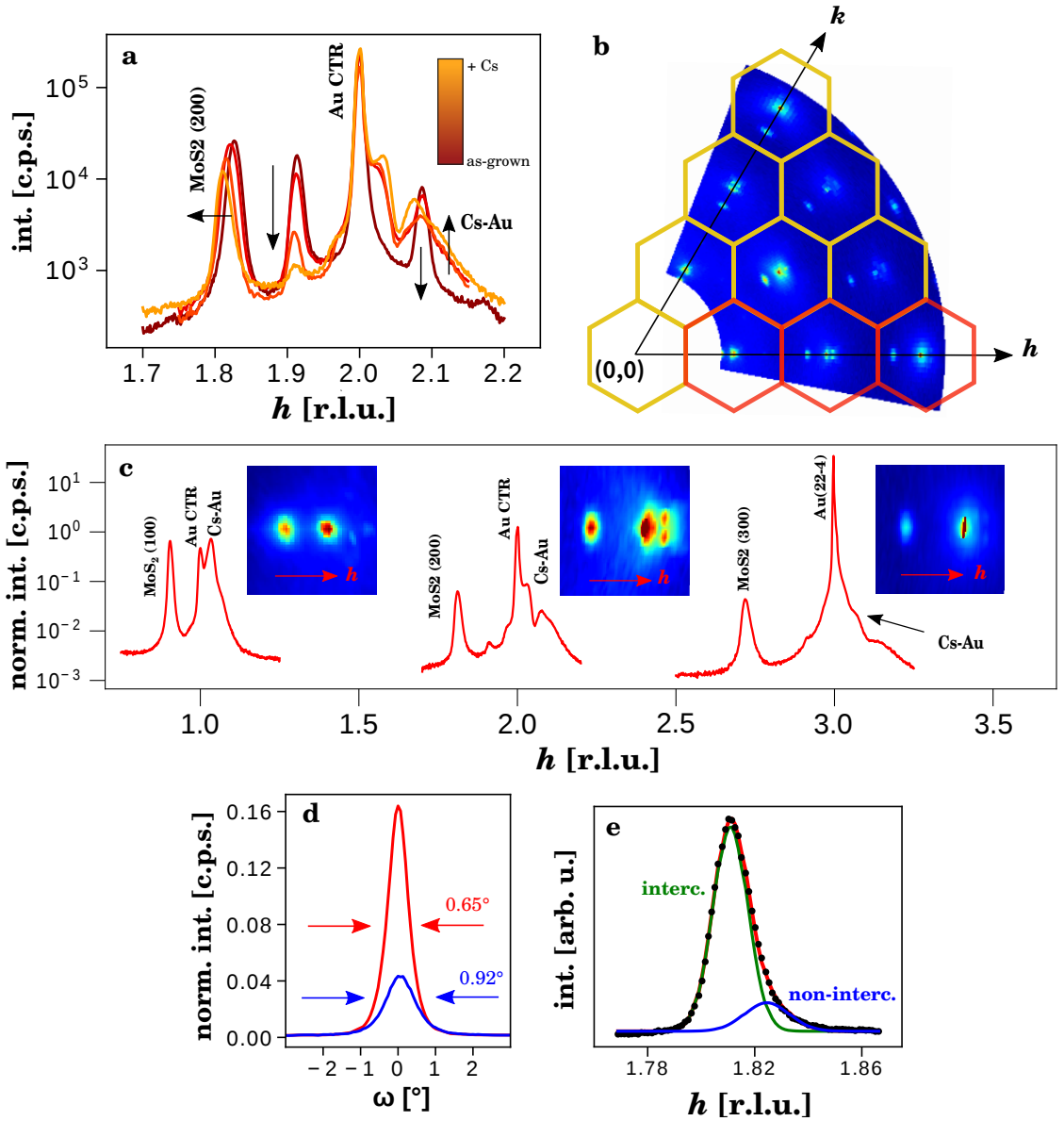

Figure 6.7: Structural changes in MoS_2 upon Cs intercalation observed by GIXRD. (a) radial scans of the x-ray scattered intensity along h before (brown) and after (from red to yellow) three cycles of 30 minutes Cs deposition at room temperature followed by annealing at 250°C; (b) in-plane reciprocal lattice cut after the deposition of 0.6 ML of Cs; hexagons show the Au Brillouin zones; (c) radial scans measured along h after the MoS_2 intercalation for each Au Brillouin zone highlighted in red in (b); the insets show the corresponding two-dimensional maps; (d) rocking scan of the (300) MoS_2 peak before (red) and after (blue) intercalation; (e) (200) MoS_2 peak fitted by two (pseudo-voigt) components that we attributed to intercalated (green) and non-intecalated (blue) MoS_2; total fit curve is in red;

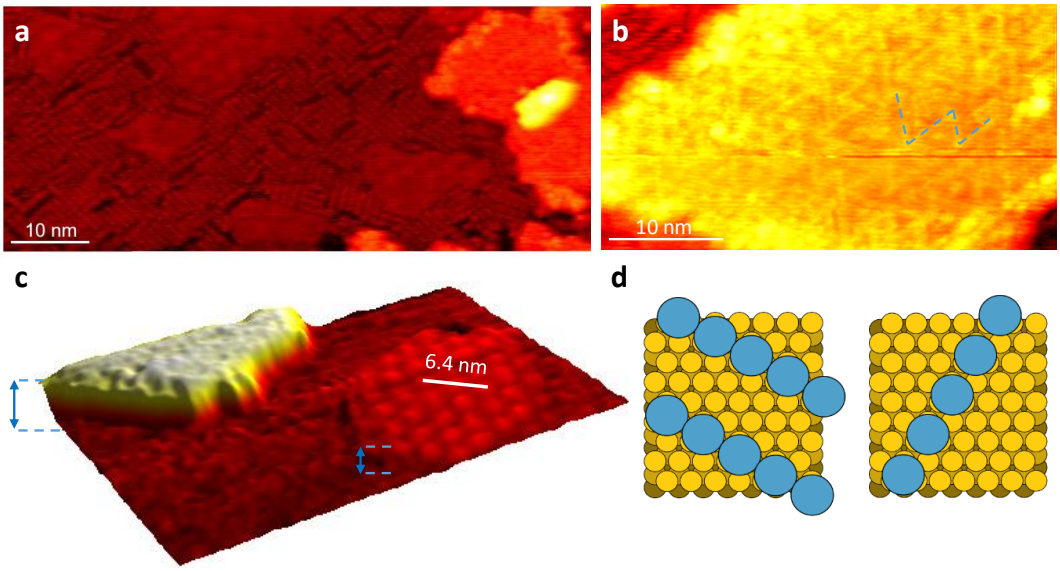

Figure 6.8: Structural changes in MoS_2 upon Cs intercalation observed STM. (a) STM view (0.2nA, -2V) revealing Cs nanosticks on Au(111); (b) close-up STM view (0.2nA, -2V) of a Cs-intercalated MoS_2 island revealing a pattern of lines; (c) three-dimensional view of an STM topograph (0.65nA, -0.5V) after room temperature Cs deposition, showing MoS_2 islands with and without intercalated Cs; (d) sketch of two possible nanostick patterns of Cs on the bare Au(111) surface, respectively 30° rotated (on top) and aligned (bottom) with the main Au(111) crystallographic directions.

6.3.2 Cs structures on bare Au and underneath MoS_2

In principle diffraction can inform us on the nature of the intercalated Cs phases, provided that they are reasonably well-ordered. However we do not detect such order with RHEED or GIXRD. Radial scans and maps in figure 6.7c measured after Cs deposition show broaden peaks on the higher h-values side of the Au CTRs and Bragg reflections but their periodicity in reciprocal space is actually linked to the Au one, suggesting more probably a Cs-Au surface alloy rather than an ordered Cs reconstruction. This kind of effect of Cs on are Au has already been reported in the literature[24].

In contrast, the STM image shown in figure 6.8a, performed after room temperature deposition of Cs - thus not annealed yet - reveals that on MoS_2 free regions, Cs atoms form a pattern of about 5nm long nanosticks, some bunching across several 1nm to several 10nm, and having different orientations on the surface. Two possible atomic configurations of Cs nanosticks, either 30° rotated or perfectly aligned with respect to the Au(111) symmetry axes are proposed in figure 6.8d. The strong structural disorder evident on the STM image explains the absence of a long range order Cs signal in the diffraction pattern.

On MoS_2-covered regions, we are not able to detect this structure. The moiré pattern is not visible anymore (figures 6.8b) on most of the MoS_2 islands, suggesting they are intercalated or lifted at a larger distance from the substrate. However, some STM images reveal that not all the MoS_2 flakes have the same appearance (figure 6.8c). Part of them are apparently higher, and exhibit no moiré pattern, while the others have the same appearance as in the pristine MoS_2 /Au(111) samples. This finding is consistent with

the two-component character of the MoS_2 signal in GIXRD (figure 6.3c), and indicates that Cs intercalation is not homogeneous. The fact that the islands seem either fully intercalated or not intercalated at all might also suggest that the limiting kinetic step in the intercalation process corresponds to the opening of an intercalation channel, for instance a point defect or the unbinding of part of the flake edges from the substrate. Once this channel is opened, mass transport underneath the flake is presumably very efficient at the scale considered here, and the flake is fully intercalated.

Whether Cs forms an ordered structure or not underneath MoS_2 cannot be observed directly based on our STM measurements. Yet, we observe a nanoscale pattern of lines oriented along the three highest-symmetry direction of Au(111) and MoS_2 (figure 6.8b). This pattern may be related to that observed in another intercalated two-dimensional material grown on a metal substrate, such as graphene/Bi/Ir(111)[25]. There, the pattern was interpreted as a network of dislocations in the intercalant's lattice, where the lines correspond to the boundaries between different intercalated domains being shifted by a fraction of the lattice vector of the intercalant's lattice.

6.3.3 Structure and coupling at the interface after Cs intercalation

Just like we did in the absence of Cs, we now address the structure of the sample in the direction perpendicular to the surface. As expected from intercalation, the experimental XRR curve in figure 6.10a,b shows an additional bump before $l = 3$, that we can qualitatively interpret as a decrease of the oscillation length due to the increase of the layer thickness under the intercalated MoS_2 flakes. To get more quantitative insights, we tested several structural models that would allow us to reproduce the experimental XRR data and eventually to refine the structural parameters via a fit procedure. Among the many models with a reasonably simple structure that we considered, the only one that produces good fits to the data and gives reasonable values for the structural fitting parameters contains a bilayer stack of a AuCs alloy intercalated between Au(111) and MoS_2. The guessed model is shown in figure 6.9. Also for this case, we assumed that the sample surface is characterized essentially by two main types of domains: one with fully intercalated MoS_2 islands, the other with the bare Au surface covered by Cs. By STM we also observed MoS_2 islands that are not intercalated, but exhibit a moiré pattern. They however represent a minority that we neglect in order to reduce the amount of free parameters in the fit. Based on the fit results obtained from the non intercalated sample, we assumed that MoS_2 occupies the 65% of the surface.

As we did for as-grown MoS_2/Au(111), we introduced in the model a common "bulk" unit cell for the two domains, consisting of three Au (111) planes having the typical bulk interplanar distance of 2.35Å. The set of "surface" cells differs instead for the two domains. As anticipated, if we intercalated MoS_2 with a single Cs layer, the fit converges systematically toward a structure with non-realistic parameter values. However, we know that

Cs forms surface alloys with Au[24], as our GIXRD measurements also suggest, and it is very likely that the Cs atoms landed on the bare Au surface or intercalated under MoS_2 partially segregated within Au layers. This tendency is expected to be even more prominent for the samples studied by diffraction, which has been thermally annealed. Hence, we introduced in the surface cells two layers of Au-Cs alloy. Each of them is modeled as a Cs layer on top of a Au layer with a short mutual separation d_{Cs-Au} between the two. The MoS_2 layer is lifted at a height d_{S-CsAu} above the first Cs-Au layer. Likewise, the second surface, representing the MoS_2-free regions, contains the two CsAu layers, but no MoS_2 on top. Analog to the MoS_2 model, the two domains are allowed to scatter incoherently and no in-plane displacements parameters have been taken into account, since we know that the specular rod is not sensitive to in-plane scattering vector components. Atomic occupancies within the planes and out-of-plane Debye Waller (DW) coefficients have been also introduced.

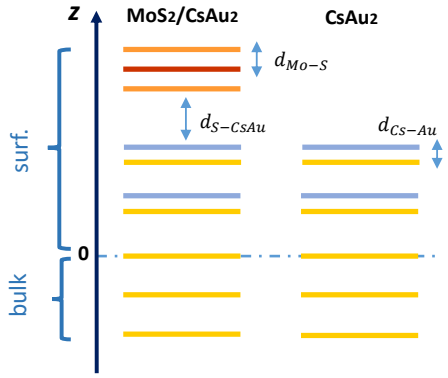

Figure 6.9: Sketch of the out-of-plane (z) layer stacking model used to fit the experimental XRR curve. The colored horizontal stripes display the different atomic layers: Au (yellow), S (orange), Mo (red) and Cs (blue); $z = 0$ corresponds to the blue dashed line: it separates the substrate unit cells (negative z, only the first three layers are shown) from the surface unit cell (positive z). Two domains are considered, with and without MoS_2 on the surface.

As shown in figure 6.10, we obtained again a very good fit to the experimental data ($R = 0.20$) corresponding to the electronic density profile shown in the inset. Some of the refined fit parameters are listed in Table 6.2. From the occupancies of Cs in the plane we can deduce a 1:2 Cs:Au alloy composition, compatible with a low Cs surface density. A low density reconstruction is nevertheless expected for Cs deposited on metal surfaces or intercalated in bulk TMDCs, both because of the large Cs atomic radius and the mutual electrostatic repulsion acting between alkali dipoles - Cs is in fact a strong electro-donor. We will come back later on this point. The refined parameter d_{S-CsAu} that quantifies the separation between the bottom S plane in MoS_2 and the topmost intercalated Cs layer amounts to (6.26±0.10)Å. We deduce from that a gap size increment between MoS_2 and the (alloyed) Au of as much as 3.77Å. This result confirms the increment of the overlayer thickness expected by effect of Cs intercalation. However such an increment is notably high, expecially if compared with the original MoS_2-substrate distance (2.52Å) found in the previous fit of MoS_2 in contact with Au(111). A previous work also report a smaller expansion (1.83Å) for the vdW gap of bulk MoS_2 intercalated by Cs, approximately twice less than what we found[26]. This value should be taken with caution given the possible oversimplification of the structural model that we assumed, but at the same time establishes that an increment of the MoS_2-Au gap is necessary to account for the oscillation of the XRR curve. Within MoS_2 instead, the fit provides for the distance d_{Mo-S} between the Mo plane and the S one a lower value, *i.e.* (1.10±0.07)Å than the one obtained in the case of the as-grown

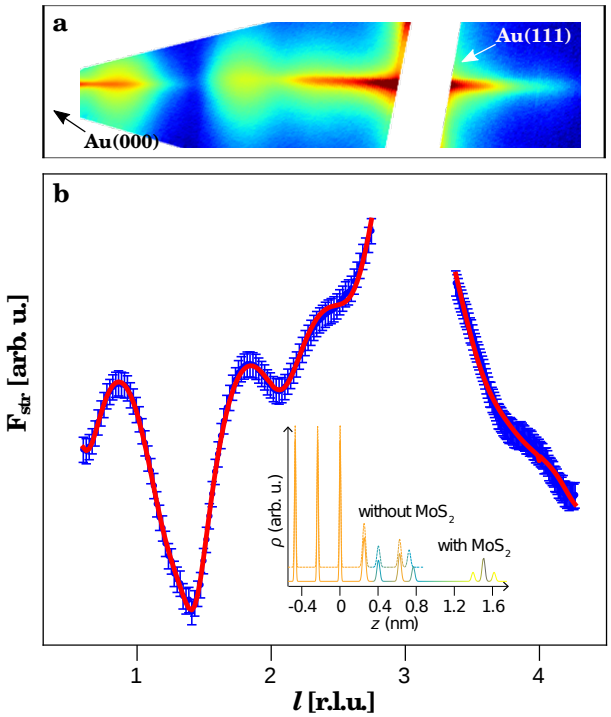

Figure 6.10: Specular rod analysis by XRR of intercalated MoS_2. (a) two-dimensional view of the (0,0) specular rod intensity along l; (b) integrated structure factor F_{str} (blue dots), displayed along l, and best fit ($R = 0.020$, red curve); the inset shows the electronic surface density profiles versus out-of-plane coordinate (z), for regions of the sample covered and not covered with MoS_2, corresponding to the best fit.

MoS_2 model (1.53Å). Even though a vertical compression of the MoS_2 can be expected in presence of the large lateral expansion observed by GIXRD, which stretches the Mo-S bonds significantly, this value could be as well underestimated by the fitting due to the lower scattering cross-section of S compared to the Mo.

	fit-value	**uncertainty**		**ref.**
$\mathbf{d_{S\text{-}CsAu}}$	6.26 Å	0.10 Å	$\mathbf{d_{Au\text{-}S}}$	2.51 Å
$\mathbf{d_{Cs\text{-}Au}}$	1.43 Å	0.23 Å	-	-
$\mathbf{d_{Mo\text{-}S}}$	1.10 Å	0.07 Å	$\mathbf{d_{Mo\text{-}S}}$	1.53 Å

Table 6.2: Interplanar spacings and relative uncertainties as estimated by the fitting of the experimental XRR curve in figure 6.10 and based on the model described in the text. The values are compared with corresponding distances from non-intercalated structure obtained by the fitting.

6.4 Deintercalation of MoS_2

As we have seen, a mild annealing of a few hundreds degrees after Cs adsorption on the surface promotes intercalation, which means intercalation is governed by a kinetic barrier.

Our hypothesis is that this energy is necessary for Cs to diffuse through natural defects and/or for creating defects that will act later as intercalation pathways. To further improve the efficiency of intercalation, it is tempting to increase the annealing temperature. Above 250°C however, another key process is activated: the moiré signal typical of a periodic lattice distortion re-appears in GIXRD and the MoS_2 peak shifts backwards, corresponding to a compression of the atomic lattice (figure 6.11a). After 600°C annealing and subsequent stabilization at room temperature, the reciprocal space location in the radial scan of the MoS_2 peak ($h = 1.8305$) is very similar to that of the as-grown case ($h = 1.8266$), and the moiré intensity is fully restored as it was before the intercalation. Also the specular rod shows a change in the intensity profile going in this sense: the wavelength of the oscillations in XRR increases upon the thermal treatment, suggesting a shorter distance between MoS_2 and the Au substrate (figure 6.11b-c). We deduce that between 300°C and 600°C, the intercalated Cs atoms can diffuse outside of the MoS_2 flakes, in other words they *de-intercalate*, and then desorb to vacuum. These evidences demonstrate that the Cs intercalation between MoS_2 and its Au(111) substrate is a reversible process. However, the current XRR image in figure 6.11b shows as well a more diffused background, sign of a higher surface disorder and probably linked to residual Cs contamination on the surface.

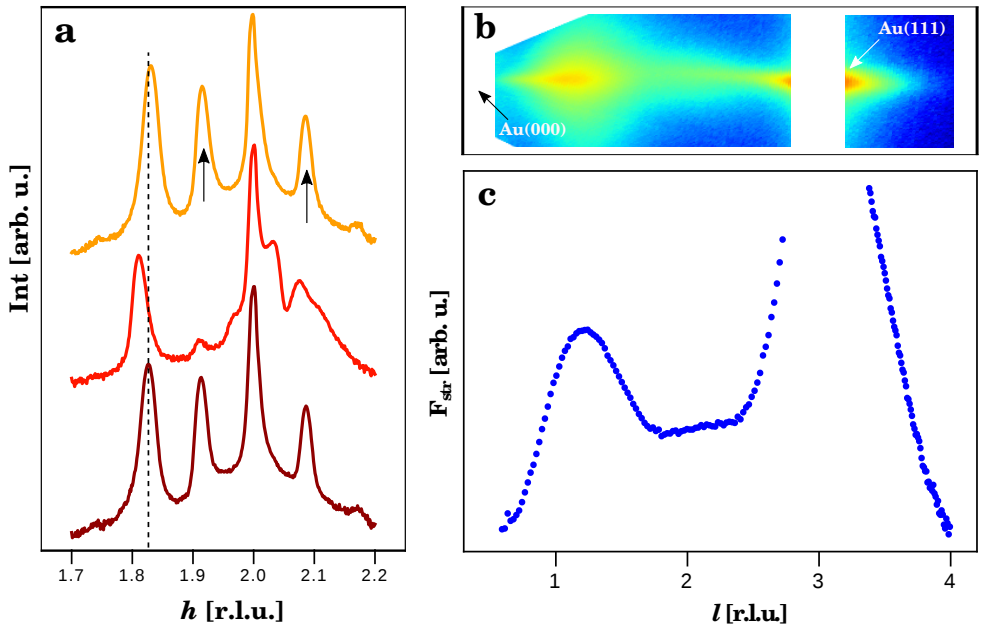

Figure 6.11: (a) radials scans along h axis in the sector between h=1.7 and h=2.3,containing the MoS_2 peak. From brown to yellow the curves correspond to the pristine grown MoS_2, the Cs intercalated one, and the deintercalated MoS_2 after annealing at 600°. (b,c) Specular rod analysis by XRR of the MoS_2/Au(111) sample after deintercalation at high temperatures: (b) two-dimensional view of the (0,0) specular rod intensity along l; (c) integrated structure factor F_{str} displayed along l.

6.5 Modifications of the electronic band structure upon intercalation

We expect that the lifting of the MoS_2 layer with respect to the Au(111) surface caused by the intercalation of Cs has strong influence on the electronic properties of MoS_2, not only concerning charge transfers that we already invoked, but also regarding the coupling of electronic bands of MoS_2 with its environment. The Cs 4d core level spectra were measured before and at two stages of the intercalation, with increasing Cs dose. Figure 6.12 compares the corresponding XPS data. Two peaks are observed for few-layer Cs on bare Au(111). They are 2.2eV apart and correspond to the expected spin-orbit splitting of the 3d level[27]. Their binding energy is about 600meV lower than for thick Cs, pointing to either charge transfers with Au or final state effects. In presence of MoS_2 flakes, the peaks develop two shoulders at low binding energies for small Cs doses, which evolve in well-separated peaks for larger doses (tripled with respect to the previous dose). The binding energies of the shoulders and peaks are about 840meV lower than on bare Au(111), and are ascribed to Cs atoms in contact to MoS_2, actually here intercalated between MoS_2 and Au(111). However, there is no straightforward argument to discriminate charge transfers effects, between Cs, MoS_2 and Au(111), and final state screening effects.

Intercalation has strong consequences on the electronic band structure of the system. We first address the case of MoS_2 /Au(111) before intercalation: figure 6.12b shows an ARPES cut in the band structure along the KΓKM direction of reciprocal space. The valence band (VB) of MoS_2, with a characteristic 130meV spin-orbit splitting at K point, is clearly seen. Its maxima at Γ and K points lie 1.58eV and 1.35eV respectively below Fermi level, while the conduction band minima is above Fermi level, consistent with a previous report[9]. After the intercalation of a first Cs deposit, the most obvious change in the band structure is observed at the Γ point, for the Au(111) electronic surface state lying close to Fermi level, which shifts down to lower binding energy (figure 6.12). Shifts of this kind have been observed with noble gas layers on Au(111)[28], and have been explained by the Pauli repulsion between the Au(111) surface state and the electrons of the layer deposited on top on the surface[29]. Careful analysis reveals that the MoS_2 valence band maxima at Γ points also shifts down, by 60meV, while no appreciable shift is found at the K point. No additional electronic band is observed that would correspond to Cs, consistent with our STM observations of a rather ill-ordered Cs superstructure on Au(111) (figure 6.12).

Tripling the Cs dose, which corresponds to fully-intercalated MoS_2, yields stronger changes in the electronic band structure of both Au(111) and MoS_2: the Au band close to the Fermi level (Γ point) and the MoS_2 valence band maximum at Γ point further shift down, for the latter by as much as 280meV. The photoemission signal corresponding to the MoS_2 valence band at the vicinity of the K point becomes weaker and broader, making it difficult to detect a possible down-shift. These observations are reminiscent of a previous study that explored charge transfers induced by potassium atoms adsorbed on MoS_2 /

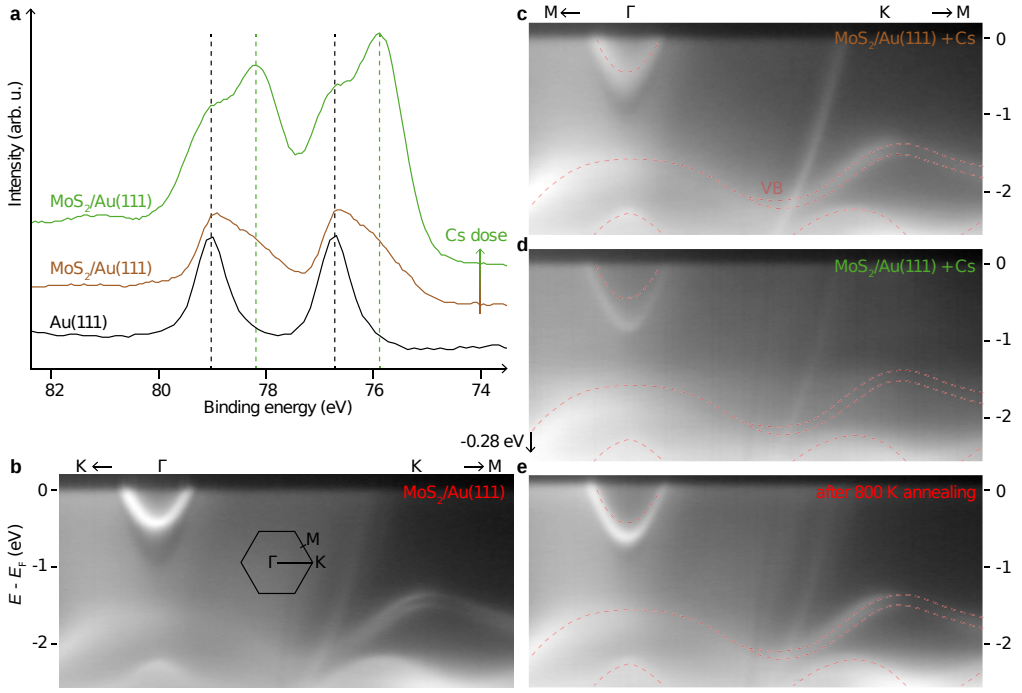

Figure 6.12: Electronic modifications in Cs and MoS_2 upon intercalation. (a) Cesium 4*d* core level spectra measured with a 130 eV photon energy after deposition on Au(111) (black curve) and MoS_2/Au(111) (brown and green curves, with increasing Cs dose); (b-e) photoemission intensity along high-symmetry reciprocal space directions (see inset in (b), with a 49 eV photon energy, for (b) pristine MoS_2/Au(111), and the same sample (c,d) exposed to an increasing Cs dose and (e) subsequently annealed to 800 K; the dotted lines mark the positions of the electronic bands in (b).

Au(111)[30]. In the two studies, the most prominent effects seem a non-rigid down-shift of the electronic band structure, with different magnitude at Γ and K points. The shifts are of the same order of magnitude with potassium and cesium, suggesting charge transfers (the Fermi level is changed) in the same range. The origin of the shifts can be qualitatively rationalised by inspecting the projection of the electronic states on the different orbitals in the system, which has been calculated by DFT for a (1×1) approximate model for MoS_2 on Au(111)[9]. The spin-orbit-split MoS_2 valence band close to K point is expected to be primarily of $Mo_{d_{x^2+d_{xy}}}$ character and the fact that it is not significantly shifted upon intercalation suggests that it is not related to a possible hybridization with the substrate's electronic band (the hybridization would be strongly affected by intercalation), which seems reasonable for these in-plane MoS_2 orbitals. In the energy range explored in figure 6.12, at Γ point the stronger contribution to the valence band stems from $Mo_{d_{z^2+d_{yz}}}$ out-of-plane orbitals, and these bands are indeed expected to be involved in the hybridization and charge transfers with the substrate or the alkali atoms, consistent with our observations (figure 6.12). The broadening of the valence band at K point after Cs intercalation points to a significant disorder in the system. This is consistent with our STM observations of a

disordered nanoscaled pattern for Cs in this case (figure 6.12). Strikingly, annealing the sample to 600°C allows to recover a well-defined valence band at K point (figure 6.12). This is an indication that the source of electronic disorder was indeed extrinsic to the MoS_2, namely due to the intercalant, and not due to the creation of defects in the dichalcogenide single-layer.

6.6 Conclusions and outlooks

With this work we demonstrated that Cs intercalation in UHV is a viable method to decouple both *structurally* and *electronically* nm-sized flakes of MoS_2 from their Au(111) substrate to which they are strongly coupled. This process, performed in UHV, is thermally activated and reversible - deintercalation is also thermally activated, but at higher temperatures. We found that Cs substantially dopes MoS_2 with electrons, and that this doping is a possible origin for a $\sim$0.85% expansion of the atomic lattice parallel to the surface.

A few questions remains unanswered. For instance, whether the electron-transfer towards MoS_2 is sufficient to trigger a 1H-to-1T transition, as often observed for bulk MoS_2 intercalated in solution, is still an open question. This question could be addressed by applying a detailled quantitative SXRD analysis and fitting of the structure factors measured along the diffraction rods of MoS_2 and (when present) the superstructure. However, ARPES data show clearly that no semiconductor-to-metal transitions occurred in our system. Reaching a control over the Cs dosing is a very compelling experimental issue, that could be eventually solved by calibrating the Cs deposition on alternative substrates where Cs reconstruction as function of the dose is measurable. Finally, understanding the intercalation mechanism and verifying its reproducibility also in presence of larger flakes represent other points to be checked.

Our work opens new perspectives towards the manipulation of 2D TMDCs. Similarly to in-solution strategies, intercalation could be exploited on MoS_2/Au(111) to facilitate the exfoliation of nanoscale flakes or full layers. Demonstrating further control on electronic or hole doping of MoS_2 with intercalated electro-donor or electro-acceptor species is another exciting goal. A number of species, to be intercalated with varying doses, are relevant here, among the vast catalog of alkali atoms, transition metals, and molecules. Finally, as extensively demonstrated with bulk compounds in the past, intercalation opens new doors to achieve a variety of two-dimensional phases, structural ones, magnetic ones, and even superconducting ones.

Bibliography

[1] S. Helveg, J. V. Lauritsen, E. Lægsgaard, I. Stensgaard, J. K. Nørskov, B. Clausen, H. Topsøe, and F. Besenbacher, "Atomic-scale structure of single-layer MoS_2 nanoclusters," *Physical Review Letters*, vol. 84, no. 5, p. 951, 2000.

[2] B. Radisavljevic, A. Radenovic, J. Brivio, V. Giacometti, and A. Kis, "Single-layer MoS_2 transistors," *Nature Nanotechnology*, vol. 6, no. 3, p. 147, 2011.

[3] A. Splendiani, L. Sun, Y. Zhang, T. Li, J. Kim, C.-Y. Chim, G. Galli, and F. Wang, "Emerging photoluminescence in monolayer MoS_2," *Nano Letters*, vol. 10, no. 4, pp. 1271–1275, 2010.

[4] S. Najmaei, Z. Liu, W. Zhou, X. Zou, G. Shi, S. Lei, B. I. Yakobson, J.-C. Idrobo, P. M. Ajayan, and J. Lou, "Vapour phase growth and grain boundary structure of molybdenum disulphide atomic layers," *Nature Materials*, vol. 12, no. 8, p. 754, 2013.

[5] C. M. Orofeo, S. Suzuki, Y. Sekine, and H. Hibino, "Scalable synthesis of layer-controlled WS_2 and MoS_2 sheets by sulfurization of thin metal films," *Applied Physics Letters*, vol. 105, no. 8, p. 083112, 2014.

[6] S. G. Sørensen, H. G. Füchtbauer, A. K. Tuxen, A. S. Walton, and J. V. Lauritsen, "Structure and electronic properties of in situ synthesized single-layer MoS_2 on a gold surface," *ACS Nano*, vol. 8, no. 7, pp. 6788–6796, 2014.

[7] S. S. Grønborg, S. Ulstrup, M. Bianchi, M. Dendzik, C. E. Sanders, J. V. Lauritsen, P. Hofmann, and J. A. Miwa, "Synthesis of epitaxial single-layer MoS_2 on au (111)," *Langmuir*, vol. 31, no. 35, pp. 9700–9706, 2015.

[8] H. Bana, E. Travaglia, L. Bignardi, P. Lacovig, C. E. Sanders, M. Dendzik, M. Michiardi, M. Bianchi, D. Lizzit, F. Presel, *et al.*, "Epitaxial growth of single-orientation high-quality MoS_2 monolayers," *2D Materials*, vol. 5, no. 3, p. 035012, 2018.

[9] A. Bruix, J. A. Miwa, N. Hauptmann, D. Wegner, S. Ulstrup, S. S. Grønborg, C. E. Sanders, M. Dendzik, A. G. Čabo, M. Bianchi, *et al.*, "Single-layer MoS_2 on au (111): Band gap renormalization and substrate interaction," *Physical Review B*, vol. 93, no. 16, p. 165422, 2016.

[10] N. Krane, C. Lotze, and K. J. Franke, "Moiré structure of MoS_2 on au (111): Local structural and electronic properties," *Surface Science*, vol. 678, pp. 136–142, 2018.

[11] N. Krane, C. Lotze, J. M. Läger, G. Reecht, and K. J. Franke, "Electronic structure and luminescence of quasi-freestanding MoS_2 nanopatches on au (111)," *Nano Letters*, vol. 16, no. 8, pp. 5163–5168, 2016.

[12] S. K. Mahatha, M. Dendzik, C. E. Sanders, M. Michiardi, M. Bianchi, J. A. Miwa, and P. Hofmann, "Quasi-free-standing single-layer WS_2 achieved by intercalation," *Physical Review Materials*, vol. 2, no. 12, p. 124001, 2018.

[13] R. Friend and A. Yoffe, "Electronic properties of intercalation complexes of the transition metal dichalcogenides," *Advances in Physics*, vol. 36, no. 1, pp. 1–94, 1987.

[14] M. S. Whittingham, "Electrical energy storage and intercalation chemistry," *Science*, vol. 192, no. 4244, pp. 1126–1127, 1976.

[15] G. Eda, H. Yamaguchi, D. Voiry, T. Fujita, M. Chen, and M. Chhowalla, "Photoluminescence from chemically exfoliated MoS_2," *Nano Letters*, vol. 11, no. 12, pp. 5111–5116, 2011.

[16] J. Barth, H. Brune, G. Ertl, and R. Behm, "Scanning tunneling microscopy observations on the reconstructed Au (111) surface: Atomic structure, long-range superstructure, rotational domains, and surface defects," *Physical Review B*, vol. 42, no. 15, p. 9307, 1990.

[17] A. Guinier, *X-ray diffraction in crystals, imperfect crystals, and amorphous bodies*. Courier Corporation, 1994.

[18] E. Vlieg, "Rod: a program for surface x-ray crystallography," *Journal of Applied Crystallography*, vol. 33, no. 2, pp. 401–405, 2000.

[19] E. Vlieg, "Surface and interface science, vol. 1, concepts and methods," 2012.

[20] R. W. G. Wyckoff, *Crystal structures*. Krieger, 1964.

[21] T. Brumme, M. Calandra, and F. Mauri, "First-principles theory of field-effect doping in transition-metal dichalcogenides: Structural properties, electronic structure, hall coefficient, and electrical conductivity," *Physical Review B*, vol. 91, no. 15, p. 155436, 2015.

[22] S. J. R. Tan, S. Sarkar, X. Zhao, X. Luo, Y. Z. Luo, S. M. Poh, I. Abdelwahab, W. Zhou, T. Venkatesan, W. Chen, *et al.*, "Temperature-and phase-dependent phonon renormalization in 1T' MoS_2," *ACS Nano*, vol. 12, no. 5, pp. 5051–5058, 2018.

[23] A. Andersen, S. M. Kathmann, M. A. Lilga, K. O. Albrecht, R. T. Hallen, and D. Mei, "First-principles characterization of potassium intercalation in hexagonal $2\,H-MoS_2$," *The Journal of Physical Chemistry C*, vol. 116, no. 2, pp. 1826–1832, 2012.

[24] J. L. LaRue, J. D. White, N. H. Nahler, Z. Liu, Y. Sun, P. Pianetta, D. J. Auerbach, and A. M. Wodtke, "The work function of submonolayer cesium-covered gold: A photoelectron spectroscopy study," *The Journal of Chemical Physics*, vol. 129, no. 2, p. 024709, 2008.

[25] J. Warmuth, A. Bruix, M. Michiardi, T. Hänke, M. Bianchi, J. Wiebe, R. Wiesendanger, B. Hammer, P. Hofmann, and A. A. Khajetoorians, "Band-gap engineering by Bi intercalation of graphene on Ir(111)," *Physical Review B*, vol. 93, no. 16, p. 165437, 2016.

[26] R. Somoano, V. Hadek, and A. Rembaum, "Alkali metal intercalates of molybdenum disulfide," *The Journal of Chemical Physics*, vol. 58, no. 2, pp. 697–701, 1973.

[27] H. Brauer, H. Starnberg, L. Holleboom, and H. Hughes, "In situ intercalation of the layered compounds TiS_2, ZrS_2 and VS_2," *Surface Science*, vol. 331, pp. 419–424, 1995.

[28] F. Forster, G. Nicolay, F. Reinert, D. Ehm, S. Schmidt, and S. Hüfner, "Surface and interface states on adsorbate covered noble metal surfaces," *Surface Science*, vol. 532, pp. 160–165, 2003.

[29] E. Bertel and N. Memmel, "Promotors, poisons and surfactants: Electronic effects of surface doping on metals," *Applied Physics A*, vol. 63, no. 6, pp. 523–531, 1996.

[30] J. A. Miwa, S. Ulstrup, S. G. Sørensen, M. Dendzik, A. G. Čabo, M. Bianchi, J. V. Lauritsen, and P. Hofmann, "Electronic structure of epitaxial single-layer MoS_2," *Physical Review Letters*, vol. 114, no. 4, p. 046802, 2015.

Chapter 7

Growth, structure and sulfurization of monolayer $PtSe_2$ on Pt(111)

7.1 Introduction

Single layer $PtSe_2$ is an indirect bandgap semiconductor with 1T structure, as opposed to the few-layers and bulk phases which have semimetal nature[1]. This fact is a notable example of thickness engineering achievable with TMDCs. Ideally, single and a-few-layers $PtSe_2$ can be embedded together in the same homojunction device and exploited for different functions using either their semiconducting or metallic properties according to their thickness.

The first direct synthesis in UHV of 2D $PtSe_2$ was reported by Wang et al.[1] in 2015 and it consists in a direct *selenization* of the Pt(111) surface (discussed later in the next section). As grown $PtSe_2$ has monolayer thickness and shows a well defined LEED pattern over the entire sample surface. Since then, other growth approaches have been reported, such as CVD[2], MBE[3], plasma assisted selenization[4] and thermally assisted conversion (TAC) of predeposited metal layers on insulators[5].

By virtue of the heavy mass of Pt and, consequently, the relatively strong spin-orbit coupling in the material, a variety of spin-related phenomena has been discussed in SL $PtSe_2$, such as helical spin texture, hidden spin polarization connected to spin-layer locking[6] and defect-related magnetism ordering (ferro/antiferromagnetism)[7; 8]. However, the presence of an inversion center in SL $PtSe_2$ prevents other effects to emerge, *e.g.* the Rashba effect. Such properties can be "switched on" by breaking the inversion symmetry in the system, for instance mechanically[9], electrostatically[10], or even chemically. In chapter 3 we reported how anionic substitution reactions have been used to tune the composition in TMDCs by substituting the chalcogen atoms with others of the same group. The process had the main purpose of engineering the TMDC bandgap[11; 12; 13], which can be varied continuously as function of the composition. This has led to a variety

of TMDC alloys of the type MX_xY_{1-x}, which are obtained mostly by annealing the pristine pure MX_2 material in the partial pressure of a suitable precursor of the Y element, enabling the substitution of the X atoms by the Y ones. As discussed in chapter 3, this approach can be used also to produce ordered *Janus* alloys, whereby chalcogen substitution occurs only for one of the two chalcogen layers. Ordered three-layers XMY compounds where the metal plane is sandwiched between two distinct X and Y chalcogen planes have been already synthesized[14; 15]. Notably, this configuration is vertically asymmetric and possesses an intrinsic cross plane electric dipole. Due to the broken inversion symmetry, Rashba splitting has been predicted in Pt based Janus TMDCs[16].

During this PhD thesis we synthesized SL epitaxial $PtSe_2$ by selenization of a Pt(111) single crystal surface, according to the method reported by *Wang et al.*[1]. We observed by GIXRD the growth of highly oriented single layer $PtSe_2$ epitaxially aligned with the Pt substrate and a long range order superstructure, extremely intense and extending in depth over many Brillouin zones of the reciprocal space. We quantitatively characterized the in-plane structure of the system by means of Patterson and model-and-fitting methods, pointing out that a significant deformation both in the $PtSe_2$ and in the uppermost substrate layer is present. Subsequently, we attempted the conversion of $PtSe_2$ into the corresponding Janus PtSeS material via the sulfurization of the as-grown $PtSe_2$. Strikingly, the combination of structural and chemical probes[1] demonstrated that the substitution of Se by S occurs in the top chalcogen layer with higher efficiency than in the bottom one, and does not alter much the in-plane structure of the pristine $PtSe_2$, leading - depending on the duration of the process - either to a Janus-like or a fully substituted $PtSe_2$, *i.e.* a quasi-PtS_2 layer, strongly pinned by the Pt subtrate.

This chapter is organized as follows: in the first section we will describe the growth and the quantitative structural characterization of SL $PtSe_2$ by analysing our SXRD data; in the second section we will discuss the results obtained after the sulfurization of the as-grown sample. We inform the reader that the contents of this work are still based on a *in-progress* analysis. Regarding the second half of this chapter results are discussed still from a phenomenological point of view. However, hypothesis and guidelines for the pursuit of the analysis are reported in the final section.

7.2 $PtSe_2$ growth by selenization of Pt(111)

7.2.1 *Operando* measurements during selenizations

SL $PtSe_2$ was grown by a two-step process based on the direct *selenization* of a Pt(111) surface according to the procedure described by Wang et al.[1] and schematized in figure

[1] chemical characterization has been performed by M. Gay and O. Renault by angle-resolved XPS at the CEA-LETI laboratories in Grenoble

7.1. We initially monitored the main steps of the preparation by RHEED (figures 7.1). Few nanometers of amorphous selenium (a-Se) were deposited in UHV on the Pt (111) surface until the typical (1×1) RHEED pattern blurred and finally disappeared (figure 7.1a-d). This stage was carried out by the team of M. Jamet at the CEA-INAC laboratories in Grenoble, where a selenium source was available. Subsequently, the sample was transferred to the INS2 chamber at BM32 by means of a UHV suitcase compatible with the two systems. Once inside the INS2 chamber, the a-Se/Pt(111) sample was slowly annealed from room temperature up to 370°C. During the annealing, the metal atoms in the uppermost substrate layers form covalent bonds with the selenium atoms at the interface, whereas the selenium in excess desorbes to the vacuum (figure 7.1e-f). In this manuscript we will use "*selenization*" to refer specifically to this step of the process, *i.e.* the annealing of the a-Se covered Pt sample.

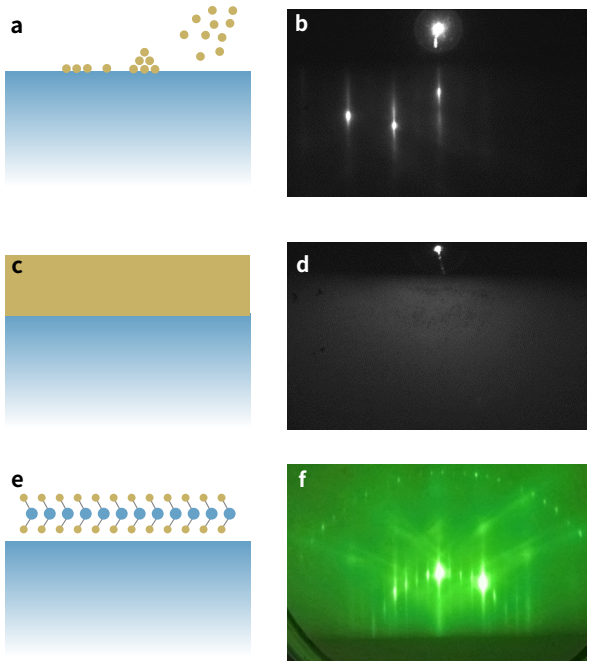

Figure 7.1: Sketch of the main steps during the selenization of Pt(111) surface (a,c,e), accompanied by RHEED pattern images taken at each stage ($[1\bar{1}0]$ azimuth, 15kV) (b,d,f): (a) selenium deposition on the Pt(111) surface; (b) RHEED pattern of the Pt(111) surface before Se deposition; (c) a thick layer (some nm) of amorphous selenium covers the sample; (d) RHEED diffractogram as it appears after selenium deposition; (e) a $PtSe_2$ single layer forms after annealing at 370°C of the selenium covered sample; (d) RHEED pattern of $PtSe_2$/Pt(111).

We monitored the selenization in real time through a sequence of X-ray rocking scans centered at $(h, k) = (0.74, 0.74)$, namely on the location where we expected the (110) $PtSe_2$ reflection in the case of an unstrained and non-rotated layer of $PtSe_2$ grown on Pt(111), assuming that the surface lattice parameters of Pt(111) and $PtSe_2$ are 2.77Å and 3.72Å, as in the respective relaxed bulk phases[1]. Selected rocking scans are shown in figure 7.2a. From blue to red, the temperature range goes from room temperature to 370°C, from which point we consider that the selenization is accomplished. Above 200°C

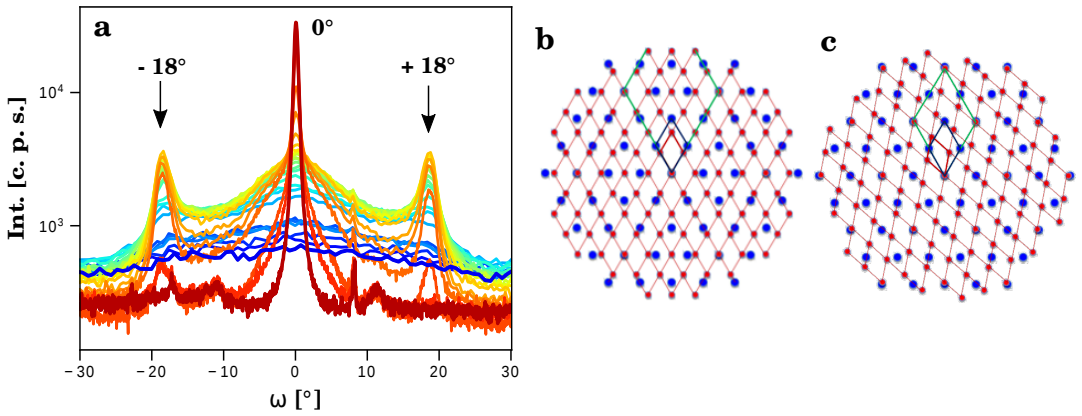

Figure 7.2: Selenization of the Pt(111) surface and formation of $PtSe_2$. (a) Rocking scans from room temperature (blue curve) up to 370°C (dark red curve) centered at $(h, k) = (0.74, 0.74)$ along the hh axis of Pt(111) in the reciprocal space; black arrows point out two signals rotated by ±18° from the hh axis, which correspond to metastable phases appearing (and disappearing) during the process; (b-c) Simplified real space model of overlayer Pt atoms (blue) on top of substrate Pt (red) in a perfectly aligned system (b) and in a ±18° rotated configuration (c).

two peaks appear at $\omega = \pm 18°$ out of the $h = k$ axis. The two peaks increase in intensity up to 330°C, then a third peak emerges at $\omega = 0°$, indicating the formation of a new phase perfectly aligned with the substrate. This peak increases in intensity at the expenses of the two at $\omega \pm 18°$ which finally disappear at 370°C. All along the selenization the background constantly reduces because of the desorption of the excess amorphous selenium.

Although at different omega values, all the diffraction peaks measured in the rocking scans ($\omega = \pm 18°$ and $\omega = 0°$) are located at the same distance from the reciprocal space origin - momentum transfer modulus $q = 3.862 \mathring{A}^{-1}$ - and can be associated to the same periodic length in real space, *i.e.* exactly the three quarters of the Pt(111) lattice. We deduced that they are reflections from different $PtSe_2$ domains, some epitaxially aligned with the Pt(111) and others ±18° rotated. The latter are interpreted as reflections from metastable rotational variants of $PtSe_2$ stabilized by kinetics in a small temperature window during growth. For small domain sizes in fact, the rotated epitaxy is preferred because it minimizes the overall epitaxial strain. Outside this window, at slightly higher temperatures, these domains seemingly abruptly re-orient and transform into the 0°-rotated ones, adopting the parallel aligned epitaxy. In this process, the size of the 0° domains increases, as evident in the decrease of the FWHM of the corresponding peak from 0.99 to 0.48° .

Figures 7.2b-c show a cartoon of the two domain configurations - respectively a $(\frac{3}{4} \times \frac{3}{4})$ and $(\frac{3}{4} \times \frac{3}{4})R18°$ reconstruction of Pt(111) surface - which correspond to two types of coincidences between overlayer (blue) and substrate (red) lattices. In the first case figures (7.2b) the supercell is fitted by (3×3) $PtSe_2$ and (4×4) Pt unit cells, as already observed by Wang et al.[1]

7.2.2 Diffraction characterisation of as-grown $PtSe_2$

When the 18° rotated peaks disappear from the rocking scan, the peak at 0° reaches the maximum intensity. At 370°C the rocking scan does not evolve anymore, presumably because selenium is either fully desorbed or bonded with Pt in $PtSe_2$. At this point we cooled the sample down to room temperature for the diffraction characterization. Figures 7.3a-b, show two 80° in-plane cuts of the reciprocal space measured before and after the selenization. It is straigthforward to verify that after the selenization the simple Pt(111) diffraction pattern (figure 7.3a), characterized by the typical three-fold symmetry, additionally has a set of sharp and intense spots corresponding to a (4×4) reconstruction extended over more than three Pt(111) Brillouin zones in reciprocal space (figure 7.3b). In figure 7.3c the radial scans of the diffracted intensity measured along h are also compared before and after selenization. Therein, Pt CTRs in the diffraction pattern of the selenized compound can be easily identified because of the exact superposition with the corresponding ones in the pristine Pt(111) pattern, whereas the $PtSe_2$ Bragg peaks are identified with a reciprocal lattice vector length which is three quarters of the latter. All the visible peaks, the aforementioned together with remaining ones, are perfectly aligned on a regular grid. Their separation is indicative of a 11.1Å long periodicity associated to the hexagonal superlattice discussed before and fitting exactly with 3×3 $PtSe_2$ and 4×4 Pt(111) surface unit cells. We indexed the reconstructed diffraction pattern so that Pt(111) and $PtSe_2$ reflections are labelled with multiple of 4 and 3 respectively. These observations are consistent with the analysis of *Wang et al*[1].

From accurate measurements of the radial scans we obtained a $PtSe_2$ surface lattice constant of (3.700 ± 0.002)Å, slightly compressed (∼ 0.7%) with respect to the relaxed bulk value (3.724Å)[17]. Strikingly, the superstructure satellites show significantly large intensity, comparable or even higher (see for instance the (700) peak), than the Bragg $PtSe_2$ peaks nearby (compare for instance with the (600) peak). The strong intensity measured for the superstructure satellites in $PtSe_2$/Pt(111) can only be explained if we assume significant atomic displacements in the lattice. This is confirmed also by the widely modulated intensity observed in the superstructure rods along the out-of-plane direction l, which increases when approaching integer l, namely Bragg conditions for the Pt substrate (7.4). As already discussed by *Croset et al.* for other surface systems[18], this indicates that the bulk periodicity plays a major role in the superstructure diffraction pattern. We can - for the moment qualitatively - interpret the surface lattice as strongly perturbed by structural deformations occurring both in-plane and out-of-plane, possibly extending deeply below the interface and involving several layers of the substrate. This scenario is far from what we expect from an ideal vdW epitaxy.

Figure 7.3d shows the rocking scan profiles of the $PtSe_2$(330) and Pt(440) reflections. Rocking scans represent a direct measurement of the mosaic spread in the epitaxial layer. From gaussian fitting of these scans, we measure a fairly narrow FWHM for the $PtSe_2$ peak (0.62°), roughly five times larger than the single crystal substrate peak. As with the case

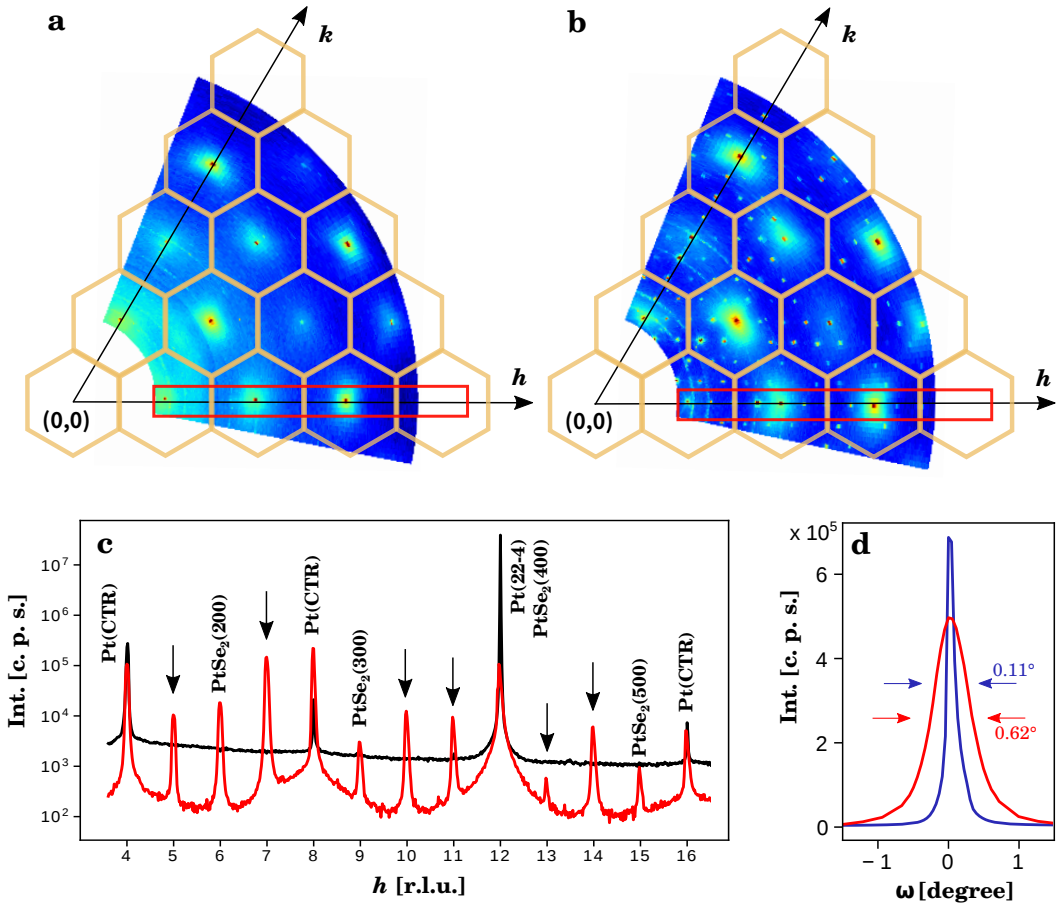

Figure 7.3: Comparison of the reciprocal space pattern before and after the selenization: (a-b) cuts of the reciprocal space parallel to the plane before (a) and after (b) the selenization; hexagonal cells correspond to Pt(111) Brillouin zones; (c) radial scan along h axis - as shown by the red boxes in the maps above - before (black) and after (red) the selenization; (d) rocking scans of Pt(440) reflection (blue) and $PtSe_2$(330) reflections (red).

of MoS_2/Au(111), $PtSe_2$/Pt(111) confirms that 2D TMDCs epitaxially grown on metals display lower mosaic spread compared to those grown on non-metallic substrates[19; 20; 21].

7.2.3 Modelling of the in-plane structure of $PtSe_2$

The number of measurable superstructure satellite peaks together with their sharp intensities make $PtSe_2$/Pt(111) a noteworthy case study for SXRD. These peaks are intense not only in the surroundings of the substrate CTRs - as it is common in many 2D surface systems including MoS_2/Au(111) and $ZrTe_2$/InAs(111) studied in the previous chapter - but all over the Pt(111) Brillouin zones visible in the map in figure 7.3. Based on this experimental evidence, we suppose that the origin of the as-measured diffraction pattern is due to wide deformations in the surface lattice, probably involving not only the $PtSe_2$ 2D layer but also some of the uppermost Pt substrate layers.

To investigate the nature of this deformation, we performed an extended set of mea-

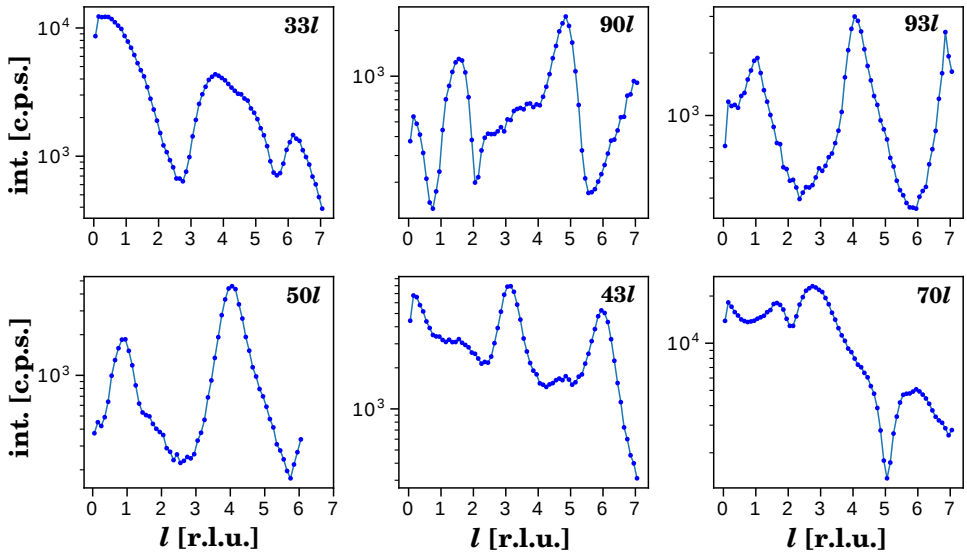

Figure 7.4: Diffraction intensity measured along the l out-of-plane direction perpendicular to the surface for selected (hk) diffraction rods of $PtSe_2$ (top row) and of the superstruture (bottom row).

surements of the scattered intensity along the direction l perpendicular to the sample surface (l-scans) for all the Pt CTRs, $PtSe_2$ rods and moiré rods centered on the (h, k) reflections shown in the map in figure 7.6, as well as many others centered at symmetrically equivalent positions in the reciprocal space plane but not visible in the map. In total 733 rods have been measured. Due to the small acceptance of the 2D detector at low out-of-plane angles we performed rocking scans to measure the rod intensity at small l-values (between $l = 0.01$ and l=1.04), whereas stationary scans were collected in the interval from $l = 0$ to $l = 7.05$. The integration of the intensity and the extraction of the structure factor rod profile out of the rocking scans have been performed with PyRod using classical methods as described in Ref.[22]. To analyze the stationary scans we used the methods developed by us and described at the end of chapter 4.

In SXRD the absolute atomic positions cannot be retrieved from the measured intensity because the phase of the scattered waves is unknown (see chapter 4). In order to trace back the surface structure, we applied an indirect method based on the *Patterson function*[23], of which we already spoke about in chapter 4. A Patterson function provides the mutual distances and angles between the atoms in the unit cell, which can be used then to build a first guess model of the structure. At this stage, we are interested in studying the atomic displacements occurring within the plane. To this purpose and for the sake of simplicity, we only calculated the in-plane Patterson function of all the rod intensities integrated between $l = 0.03$ and $l = 0.20$, but excluding the substrate CTRs. In fact, CTRs contain extra information from the bulk, as for instance the roughness and the registry of the surface layer with respect to the substrate, which would complicate the analysis. In total 733 reflections have been measured, of which 111 are non-equivalent by symmetry. The systematic error deduced from comparing non-equivalent reflection intensities is estimated at 13.4%. Figure 7.5 shows the Fourier map of the non-equivalent experimental in-plane

reflections after the integration of the rocking scans. The spot radius is proportional to the average structure factor of all the measured in-plane reflections that are equivalent according to the *p3m1* planar group, *i.e.* the planar group of the 1T-$PtSe_2$ structure projected on the plane. The Patterson function of the experimental data can be calculated with eq.(4.19) applied to the so-averaged structure factors. The result is reported by a contour plot map in figure 7.6a. A maximum at a given general position (x_0, y_0) in the contour plot marks a vector (x_0, y_0) corresponding to an interatomic distance between two atoms in the real structure projection. The continuous red line frame contains the unit cell of the Patterson map. It exhibits a *p6mm* symmetry, namely the symmetry of the 1T-$PtSe_2$ in-plane projection with an additional inversion axis, as expected since a vector connecting an atom A with an atom B is the inverse of the vector connecting B with A. The irreducible representation of the map is shown within the triangle having a red dashed line frame in figure 7.6a and zoomed in figure 7.6d. It contains the most significant interatomic vectors, listed in the figure with numbers from 0 to 4 in orange. To help us in the interpretation, we calculated the theoretical Patterson map of a freestanding $PtSe_2$ layer (figure 7.6b-c). Analog to the experimental case, we identified in the contour plot the irreducible unit cell (pink dashed triangle) and a reducible one (red dashed triangle), which is convenient for comparison with the experimental case. Besides the maximum at the origin (vector 0), which represents the distances of all the atoms with themselves, two other main vectors can be identified within the irreducible cell in figure 7.6c, namely vector 1 and 2. It is straightforward to verify that they correspond respectively to Pt-Pt and Pt-Se distances in the $PtSe_2$ unit cell (figure 7.6e). We can observe also other vectors in the reducible unit cell that correspond to non-nearest neighbors Pt-Pt and Pt-Se distances in the supercell (figure 7.6e)). Coming back to the experimental Patterson map and its irreducible representation in figure 7.6d, we can now compare the experimental interatomic vectors (in orange) with those obtained from the freestanding $PtSe_2$ model (in green) in figure 7.6c. It is straightforward to verify that some interatomic distances stretches, *e.g.* vectors 2 and 3 associated to Pt-Se distances, and others become shorter, *e.g.* vectors 1 associated to nearest neighbors Pt atoms. Moreover the relative angle between vector 4 and the other vectors has changed, indicating a displacement of a Se atom transverse to the other bonds, as shown in figure 7.6f. No maxima have been found that may correspond to vector 5 in figure 7.6f, probably because the distance it refers to is identical to a bulk Pt-Pt distance which is not taken into account by the Patterson function since the CTR reflections were removed from the Fourier map.

Globally, the Patterson analysis demonstrates that significant deformations characterize the superficial layers of the system. Although we associated some of the interatomic vectors to bonds in $PtSe_2$, the atomic displacements might not be confined to the dichalcogenide layer but involve also some of the substrate layers below. The information about the amplitude of the deformation at different levels of depth can be stored in the asymmetric shape of some maximum corresponding to Pt-Pt distances - for instance vector 1 in figure 7.6d. As we mentioned earlier, Patterson analysis is relevant to make a structure

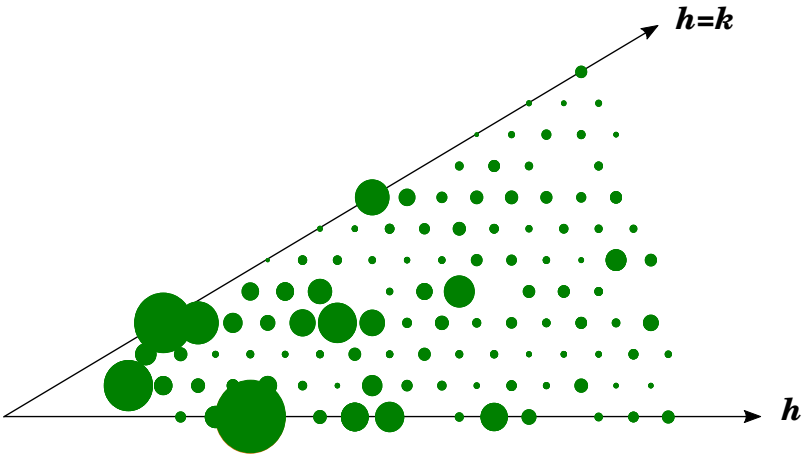

Figure 7.5: Fourier map of the averaged structure factors obtained from the experimental in-plane intensities integrated between $l = 0.03$ and $l = 0.20$ for each (h, k) shown position; the radius of each spot is proportional to the experimental structure factor; Pt substrate CTR and Bragg reflections are not considered.

guess model of the system, but it cannot directly give the real structure. To this purpose we built a model allowing atomic displacements along the bond axes of 1T-$PtSe_2$ unit cell, *i.e.* stretching and shrinking, consistent with the symmetry constraints imposed by the *p3m1* planar group.

The structural model we propose is a defined set of "surface" unit cells lying on "bulk" unit cells representing the substrate, as already made for MoS_2/Au(111) in chapter 6, with the difference that here atoms have (x, y) in-plane atomic displacements that are not negligible. The surface unit cell contains a single layer of $PtSe_2$ and two Pt(111) substrate layers where atoms are allowed to move in-plane. The bulk unit cells contains an ABC stacking of three Pt(111) planes according to the face centered cubic (fcc) packing, which is considered by the software as the periodic unit of an infinite pile of identical cells. The atomic positions in the bulk unit cells are fixed. We considered then 9 $PtSe_2$ unit cells and 16 Pt(111) unit cells composing the (3×3)$PtSe_2$ - (4×4)Pt(111) supercell described before. A set of displacement parameters (δx and δy) is assigned to all the atoms in the surface model. These parameters are not allowed to vary freely, but coherently with the constraints imposed by the symmetry elements of the *p3m1* planar group which 1T-$PtSe_2$ belongs to. The symmetry elements of the *p3m1* group can be found in the *International Table of Crystallography*[24]. From a careful analysis we deduce that Pt and Se atoms are allowed to shift only along the mirror axis, consistently with the hypothesis made as result of the Patterson map analysis. Then, we set the parameters of the fits accordingly. Other free parameters for the fit are in-plane Debye-Waller coefficients, which account for the thermal and static disorder in the system, and the atomic occupancies. The surface coverage is fixed to one, since in our data set Pt CTRs and any signal exclusively dominated by the free Pt surface have not been included. Finally the surface roughness is set to zero, since this information cannot be deduced from in-plane data. Considering 27 atoms in 9 $PtSe_2$ unit cells, 16 atoms in each substrate layer, the number of free parameters amounts to

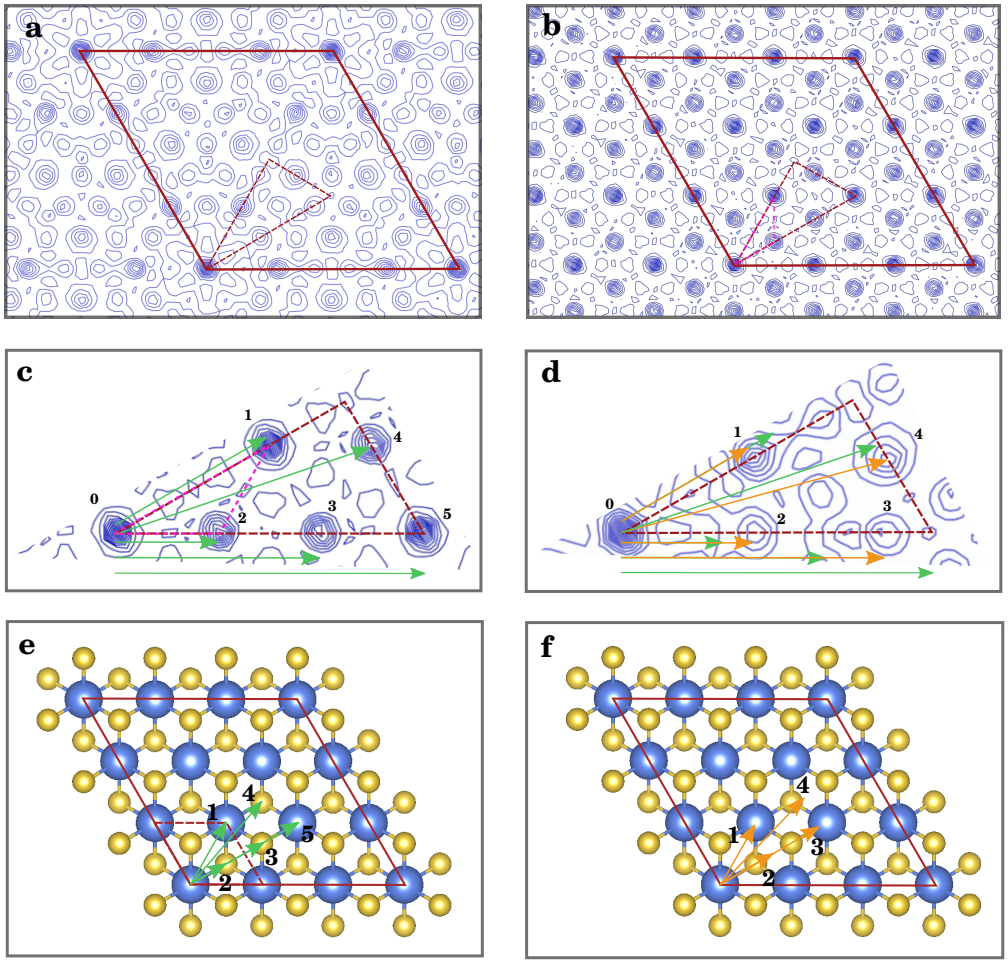

Figure 7.6: (a) Contour plot of the experimental Patterson map calculated using the in-plane structure factors of the Fourier map in figure 7.5; the asymmetric unit is shown with dashed red boundary; (b) Contour plot of the theoretical Patterson map calculated for a perfect (3×3) 1T-$PtSe_2$ cell; the asymmetric unit is shown with dashed pink boundary; a non-asymmetric unit useful for comparison with the case shown in (a) is also shown with dashed red boundary; (c) zoom on the (non)-asymmetric unit in (b); green arrows pointing to countour plot maxima represent interatomic vectors; (d) zoom on the asymmetric unit in (a); orange arrows pointing to countour plot maxima represent interatomic vectors; vectors from (c) are also reported for comparison; (e) (3×3) 1T-$PtSe_2$ cell model with theoretical interatomic vectors extracted from (c); (f) (3×3) 1T-$PtSe_2$ cell model with experimental interatomic vectors extracted from (d).

236. Thanks to the symmetry relationships - δx and δy associated to all the symmetrically equivalent atoms are a function of the same parameter "x" in the fit - the total amount can be reduced to 60.

We used this structural model to fit the in-plane structure factors shown in the Fourier map in figure 7.5. Using the atomic coordinates in the model, the ROD software calculated the structure factors at each given (h, k) position for $l = 0.108$, namely at the center of the integration interval, and by means of fit algorithms (*Levenberg-Marquartz* and *simulating annealing*), it varied the fit parameters to reach the best fit to the experimental data. Occupancies were left free to vary at the beginning, then, a few at a time, were fixed to one adjusting in parallel the corresponding Debye-Waller coefficients. Hereafter we limit to comment the main results obtained from the best fit.

The Fourier map in figure 7.7 compares the experimental structure factors (green semi-circles) with the calculated ones (yellow semi-circles) at each (h, k) center and globally establishes a good agreement between theory and experiment, estimated by an *R-factor* equal to 0.233. In figure 7.8 we compare the refined model (a,c,d) to the non-distorted one (b,d,f), firstly for the $PtSe_2$ layer only (figure 7.8a-b), then adding the topmost Pt(111) layer (figure 7.8c-d), and finally with both the Pt(111) layers underneath (figure 7.8e-f). In the $PtSe_2$ layer (figure 7.8) three Pt atoms (A,B,C, in grey) sit static on three high symmetry sites of the supercell: an *on top* site, an *fcc* site and *hcp* site, respectively. The other Pt atoms within the dichalcogenide layer (always in gray) shift along the mirror axes lines by displacement in the range of 0.4-0.55Å in the direction shown by the red arrows. In other words, there is a contraction of the nearest-neighbours Pt-Pt distance around the Pt(A). On the contrary, in the topmost substrate layer, Pt atoms (in orange) around the A center move oppositely to those in the dichalcogenide layer (pink arrows), namely expanding their distance from the sixfold axis position. Around B center the atoms displace moderately inwards, whereas around the C center they move widely and outwards. Regarding the Se atoms in the bottom (yellow) and in top (green) $PtSe_2$ layers, the displacements are more complex (figure 7.8a-b): shortly, the Pt-Se bonds are little contracted around B, largely expanded around A (only bottom layer Se) and C (only top layer Se). Overall, the amplitude of their displacements varies from almost zero to 0.55Å. Finally, in the second Pt substrate layer (figure 7.8e-f) the displacement amplitudes are smaller, varying between 0.02Å and 0.03Å.

The refined model is consistent with the hypothesis made on the basis of the Patterson analysis: significant contraction and expansion of the Pt-Pt distances, and in turn of the Pt-Se ones, occur both within the 2D layer and in the substrate - rather large in the former, moderate in the latter. The deformation does not propagate deeply inside the substrate: the Pt atoms in the second substrate layer have positions that almost match their bulk positions. One may want to obtain a better fit to the experimental data by including a third substrate Pt layer in the surface model, allowing atomic displacement more in depth. Although reasonable, the hypothesis is difficult to apply in practice. Adding a third layer means to increase the number of fit parameters from 60 to 97, thereby reducing the

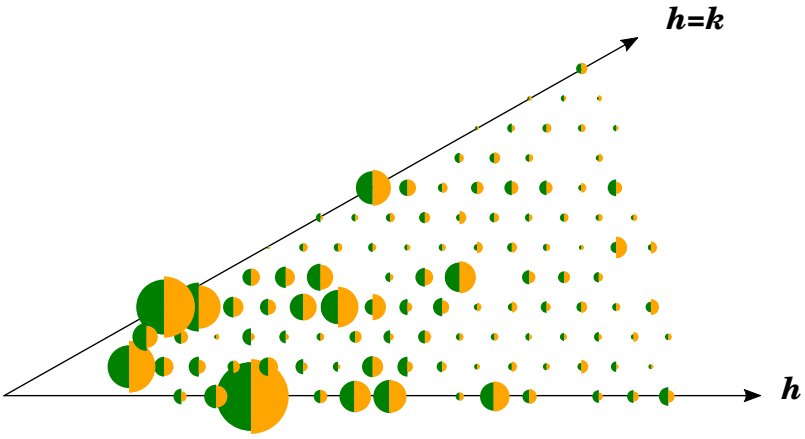

Figure 7.7: Fourier map of the experimental in-plane integrated structure factors (green semicircles) compared with the theoretical ones obtained by the fit procedure (orange semicircles); the radius of each spot is proportional to the structure factor; Pt substrate CTR and Bragg reflections are not considered.

reliability of the fit. Moreover in the model with two Pt atomic planes the single atomic displacements within the second substrate layers were as low as 0.02Å, namely 5% of the lowest displacement among the Pt atoms within $PtSe_2$. We expect that the deformation will be even lower in the third layer. For this reason we consider the refined model described above already a good representation of the real structure.

In-plane lattice deformations suggest a periodical modulation of the atomic heights within the supercell. A quantitative analysis of this kind requires new out-of-plane degrees of freedom δz to the atoms in the model and the integration and fitting of CTRs and superstructure rods along l in the reciprocal space. This analysis is currently in progress and we will not comment it here.

7.3 Selenium-by-sulfur substitution in 2D-$PtSe_2$

7.3.1 Annealing and sulfurization effects on $PtSe_2$ monitored by GIXRD

The thermal annealing in the partial pressure of a gaseous precursors of S has already been used to promote Se substitution in TMDcs, leading either to non-stoichiometric disordered alloys or, when suitable pressure and temperature conditions are used, to ordered *Janus* compounds. In this section we will describe the sulfurization of the $PtSe_2$/Pt(111) performed by annealing the as-grown sample in H_2S gas atmosphere inside the INS2 UHV chamber at BM32.

Firstly, we performed *in situ* measurements during annealing in UHV to determine the temperature window inside which $PtSe_2$ is stable. Figure 7.9 shows that the $PtSe_2$ structure is altered a few tens of degrees above the selenization temperature: the diffracted intensity of $PtSe_2$ and the peaks of the reconstruction constantly decreases over time and

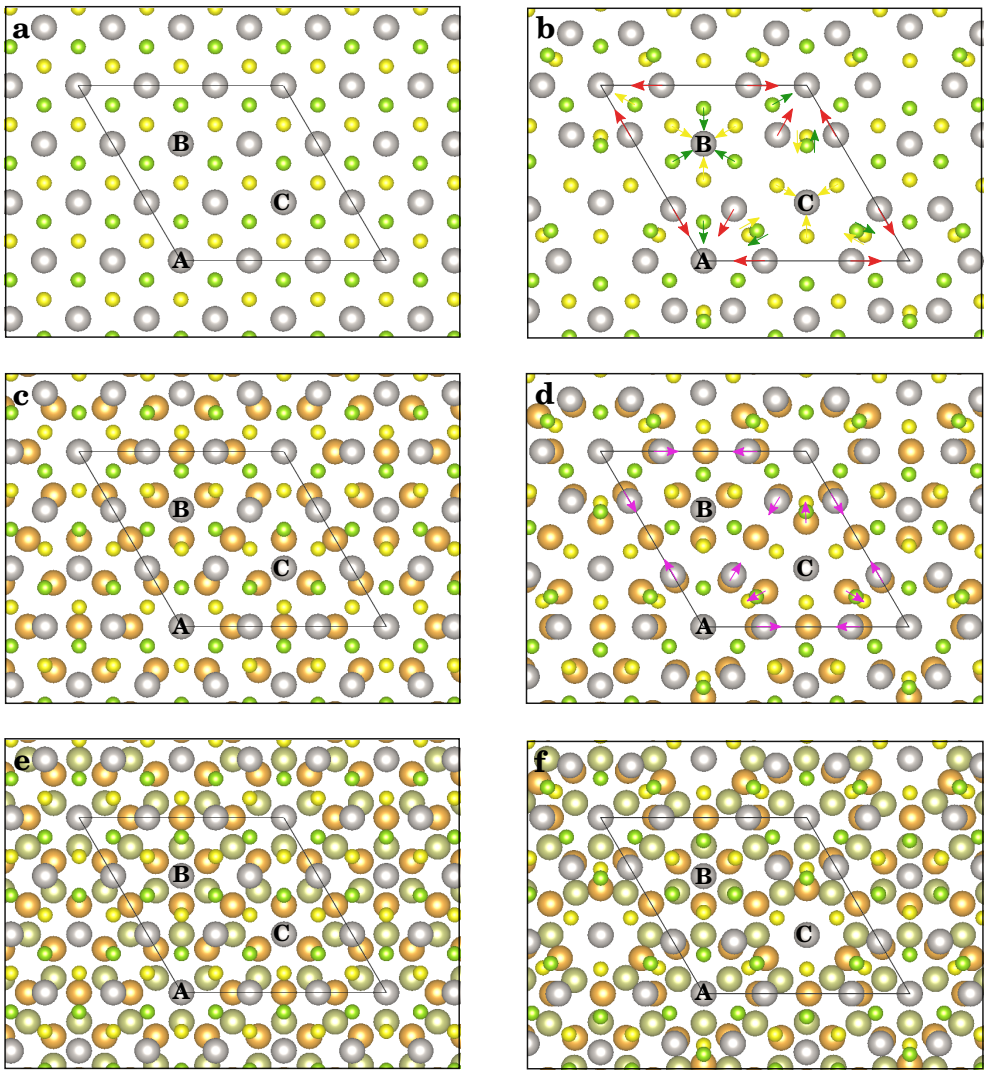

Figure 7.8: Refined structural model as obtained from the fit of the experimental data shown in the Fourier map in figure 7.5 (b-d-f) compared against an ideal non distorted model based on the (3×3)$PtSe_2$ - (4×4)Pt(111) superstructure (a-c-e). (a-b) only $PtSe_2$ layer is shown; (c-d) $PtSe_2$ and topmost substrate Pt(111) layer; (e-f) $PtSe_2$ with the two next substrate Pt(111) layers underneath. Pt atoms from $PtSe_2$ and from the first and second substrate Pt(111) layers are colored in grey, orange and green respectively, whereas top and bottom Se layers in $PtSe_2$ are in green and yellow. Arrows in (b) shows the movements of Pt (in red) and top and bottom Se (in green and yellow) within the $PtSe_2$ layer; Pink arrows in (d) show the movements of Pt atoms in the topmost Pt(111) substrate layer. Images are obtained with the VESTA software.

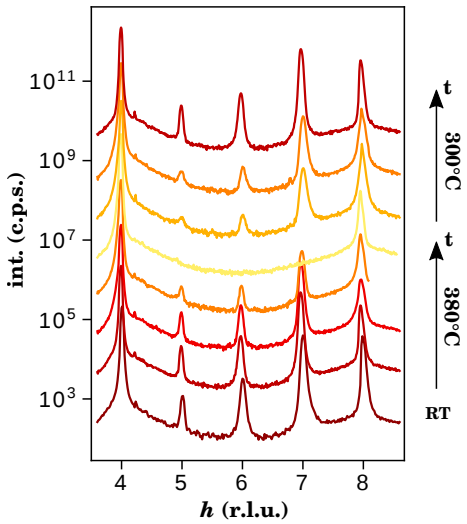

Figure 7.9: evolution of the diffraction pattern of $PtSe_2$ over time during annealing at 380°C (a few degrees above selenization temperature) and after stabilization at 300°C.

the process ends up with the total disappearing of the superstructure signal, namely with a complete loss of order or to $PtSe_2$ dissolution (red curve). Surprisingly, cooling down the sample to 300°C or below leads to $PtSe_2$ regeneration as visible in the re-appearance of the superlattice diffraction pattern (topmost curve). We propose two hypotheses to account for this phenomenon. First, because of the high temperature Se-Pt bonds are broken and the chalcogen floats on the Pt surface. Se is highly mobile on the surface and there is no ordered structure that can scatter X-rays coherently. A second hypothesis is based on some STM images of the $PtSe_2$ surface (not reported here) performed *ex-situ* with setup available at Institut Néel. These images reveal that, besides $PtSe_2$ islands, several nanometers thick islands of a different nature lie on the Pt surface. Very likely, selenium is not homogeneously deposited on the surface but it is present also in the form of three-dimensional clusters, which can potentially act as "Se reservoirs". We argue that an imbalance between Se loss, due to the desorption at high temperatures, and Se supply from the reservoirs might govern the dissolution/recovering process as a function of the annealing temperature. In the specific case of our experiments, below 380°C, Se atoms are provided by the clusters. Above 380°C instead, chalcogen desorption rate becomes important and the Se cluster reservoirs cannot compensate the ongoing formation of vacancies. The weak point of this hypothesis is that, if $PtSe_2$ Se was really desorbed from the surface because of the high temperatures, the same would happen for that stored in the clusters, leading at a certain point to the full consumption of the chalcogen. We observe instead that the $PtSe_2$ diffraction pattern can be reversibly suppressed and reformed for numerous cycles. Further investigations are thus needed to solve this issue.

Whichever of mechanism is at play, we wondered if the structural order in $PtSe_2$ can be restored regardless of the nature of the supplied chalcogen, e.g. by annealing the sample in S precursor partial pressure. Hydrogen sulfide (H_2S) gas has been widely used as sulfur

precursor in the synthesis of epitaxial 2D TMDCs on metallic Au substrates[25; 26; 27]. Noble metal substrates in fact are required to catalyze the dissociation of the H_2S molecules and provide elemental S to the reaction environment.

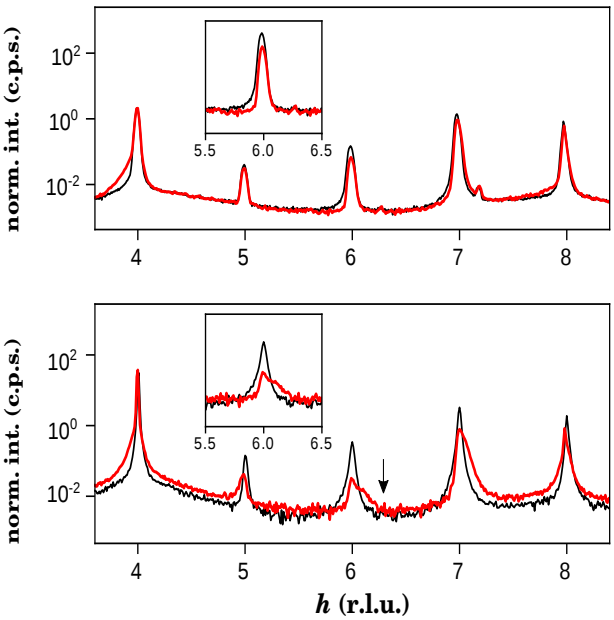

Figure 7.10: Radial scan along the h axis in the range of values from $h = 3.6$ to $h = 8.4$, containing peaks from $PtSe_2$, Pt substrate and the superstructure, before (black) and after (red) sulfurization of sample *S1* (top) and *S2* (bottom).

We exposed two $PtSe_2$ samples (hereafter referred to as *S1* and *S2*) to H_2S partial pressure and we monitored the sulfurization by GIXRD. The general approach, common in both cases, consisted in annealing the sample above 400°C in UHV and cooling it down to 400°C before injecting H_2S. The purpose of pre-annealing is to create a significant concentration of chalcogen vacancies. After a few cycles, the moiré and $PtSe_2$ peaks intensity in the diffraction patterns appears drastically reduced (approximately half the pristine sample). The main differences in the treatments applied to the two samples consists in the maximum annealing temperature used and in the number of cycles, while H_2S is supplied at the same partial pressure (10^{-4} mbar) for both cases. Regarding the two samples discussed here, *S1* underwent 3 cycles and the highest annealing temperature reached was 400°C. For *S2*, more drastic conditions were applied such as a higher number of cycles (5) and a higher maximum annealing temperature (up to 460°C). By GIXRD measurements we monitored the system to find signatures of either structural changes in the 2D layer due to the insertion of a small amount of S atoms in the original $PtSe_2$ lattice, *e.g.* strain, superstructure long range order loss, surface disorder, etc., or of even new phases characterized by different lattice parameters. In figure 7.10, radial scans along the h axis and within the sector containing the peaks from h=4 to h=8 compare the initial (as-grown $PtSe_2$) and final (sulfurized $PtSe_2$) diffraction patterns for *S1* and *S2*.

In the *S1* scan a moderate loss of intensity and a higher signal on the Pt CTR tail (at h=4) are visible upon the treatment, the latter suggesting scattering from a disordered surface. The same is also true for the *S2* sample, but in this case the peak signal is severely lower (about one tenth of the pristine intensity) and the background is higher. Moreover a new growing longitudinal component is visible at the higher h-values side of the peaks in *S2* radial scans, which can reasonably be attributed to a new phase formation with slightly shorter in-plane lattice parameter. However by GIXRD we do not have clear signatures of a successful substitution of Se by S. Surprisingly, no substantial modification of the pristine superstructure is observed both for *S1* and *S2*, demonstrating that the deformations within the Pt superficial layers are not affected by the thermal treatment in H_2S.

7.3.2 Angle resolved XPS analysis of sulfurized $PtSe_2$

Angle resolved x-ray photoemission spectroscopy (AR-XPS) measurements[2] have been performed afterwards on both S1 and S2 samples to estimate the concentration and the chemical nature of the atomic S found on the surface. In short, by reducing the photoelectron exit angle θ between the sample surface and the analyzer, the analysis depth decreases proportionally to $\sin(\theta)$. It follows that one can determine the relative depth between specific elements by comparing their atomic concentration at different angles. In our case, with this method we could not only detect if sulfur substitutes selenium in the TMDC, but also know if the substitution had occurred mostly in the top or in the bottom chalcogen layer. Figure 7.11 shows the deconvoluted XPS doublets of Se 3p and S 2p core levels for three different exit angles θ, *i.e.* 10°, 25° and 45° for the sample *S1*. To analyse the two sets of doublets, which are very close in binding energy, the spin-orbit splitting - a constant intrinsic property of the element - was fixed to 5.75 eV and 1.18 eV respectively for Se 3p and S 2p. Then, a Shirley background was subtracted from the raw data. From figure 7.11a to c, it is evident how the weight of the sulfur component increases when the exit angle decreases, while the opposite occurs for selenium, indicating that the sulfur atoms are mostly found closer to the surface than selenium. S and Se concentrations have been quantified rigorously, and their ratio (S/Se) diminishes as function of the depth, from 1.54 at 45° to 1.15 at the more grazing $\theta = 10°$(figure 7.11d). This result provides the main evidence that the annealing in H_2S partial pressure is a viable route for substituting Se atoms in (pre-annealed) $PtSe_2$/Pt(111) and that the substitution preferentially occurs in the top layer, consistent with what is expected for a *Janus* type SPtSe alloy. Noteworthy, our results do not exclude that Se-by-S substitution may have occurred even in the bottom layer, but it suggests that kinetics barriers are different for the two processes. Therefore, a careful control of the sulfurization (via pressure, temperature and exposition time) can

[2] All the (angle resolved) XPS measurements and analysis on the as-grown and sulfurized $PtSe_2$ samples (*S1* and *S2)* were carried out by M. Gay and O. Renault at the CEA-LETI laboratories. More detailes on the analysis will be found in the paper of this work, *Sant, R, Gay, M et al.* currently in preparation.

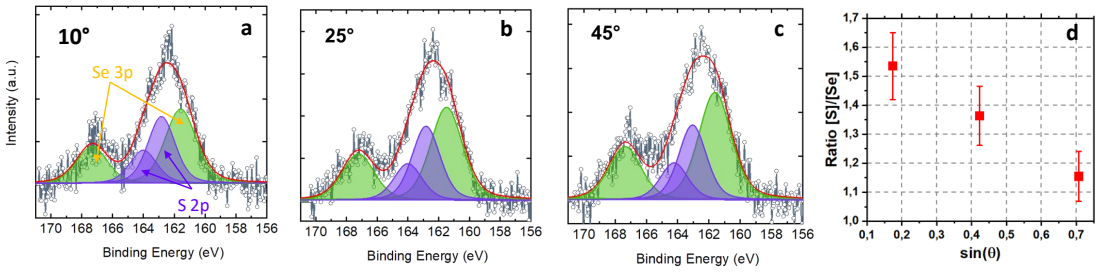

Figure 7.11: (a-c) Deconvoluted S 2p and Se 3p core levels (blue and green areas respectively) in the XPS spectra of sample *S1* measured at various exit angles: 10° (a), 25° (b) and 45° (c); (d) S/Se concentration ratio as function of the exit angles.

lead to a selective substitution of Se in one or both the chalcogen layers.

A confirmation of that is found with *S2*, where the more severe sulfurization conditions, *i.e.* longer process (five cycles instead of three) and higher annealing temperature (460°C instead of 400°C) led to a quasi-complete substitution of the selenium atoms in $PtSe_2$. In fact, a very low Se concentration (up to 3.5%) is measured by AR-XPS at 45°exit angle for the Se 3p and S 2p core levels. Se traces are even harder to detect at more grazing angles, namely more superficially, due to the very low signal.

7.3.3 Isostructure of the pristine and sulfurized $PtSe_2$

In spite of the drastic changes in the chemical composition of the two samples, *S1* and *S2*, which transforms from a pure selenide into a Janus type alloy and into an almost pure sulfide respectively, GIXRD demonstrates in both cases that the superlattice satellites observed in the pristine $PtSe_2$ are unchanged upon sulfurization. In other words, the PtSeS alloy found in *S1* and the almost fully S-substituted $PtSe_2$ in *S2* are apparently in the plane *isostructural* with the pristine $PtSe_2$, yet a non negligible loss of intensity is observed together with higher background, which suggests an increase of disorder and defects such as chalcogen vacancy, sulfur adsorbates on the surface, grain boundaries, etc. This can be asserted because of the absence of any other new significant reflection assignable either to a PtSeS alloy or to a PtS_2 phase. In fact, given the different (covalent) radii of Se and S atoms, respectively 1.16Å and 1.02Å, we would expect a contraction of the Pt-chalcogen bonds in the sulfurized structure with a consequent reduction of the lattice parameter to a value comprised between 3.70Å and 3.53Å according to the Vegard's law - experimental bulk PtS_2 lattice constants reported in the literature are between 3.53 and 3.54Å(compared to 3.72Å for bulk $PtSe_2$). If it is so, an additional reflection would be detectable in the radial scans reported in figures 7.10a-b, precisely between $h = 6.00$ and $h = 6.28$. Therein, the only new signature detectable by diffraction is a small shoulder in *S2* diffraction pattern coexisting with the pristine superstructure. This signal can neither explain the existence in the sample of isolated PtS_2 islands with freestanding lattice parameter, nor justify the formation of a PtSeS alloy since from the XPS analysis we did

not detect an appreciable amount of Se in the sample. Necessarily, the anionic exchange during thermal annealing in H_2S does not relax the in-plane strained Pt layers in the surface. We deduce that this picture is almost perfectly verified in *S1*, where substitution happens mostly in the outermost selenium layer. In the second sample *S2*, it comes with a severe reduction of intensity, *i.e.* structural order, and a certain distribution of lattice constants, *i.e.* the shoulder. In this case in fact S atoms have to diffuse through the very first Pt layer in order to occupy the atomic interstices underneath. It is worth noting that for PtS_2 to be in a 4:3 ratio with Pt(111) - conditions required by the superstructure - it should stretch its lattice parameter by 4.6%.

7.4 Conclusions and outlooks

In this chapter we described the synthesis of a 2D $PtSe_2$ epitaxial layer grown by selenization in UHV of a Pt(111) surface. The as-grown 2D layer preferentially aligns its high symmetry directions with those of the Pt(111) substrate and a long range order superstructure in a 3:4 lattice coincidence is observed, characterized by an intense diffraction pattern. Our analysis of the integrated in-plane projected intensities demonstrated that this diffraction pattern is the result of significant atomic displacements occurring both in the 2D layer and in the substrate. The system represents an interesting case of 2D TMDC strongly coupled to its substrate. Estimated displacements up to 0.55Å are observed in the $PtSe_2$ layer, which does not correspond to a situation of vdW epitaxy, but necessarily imply a strong interaction associated with a strain field propagating into the substrate. The displacement involves also the atoms in the outermost Pt layer. This surface atomic configuration is robust against the thermal treatments performed in H_2S atmosphere - as long as the temperature is not raised above 400°C - since the diffraction pattern remains unchanged even after the partial or total substitution of Se by S.

We also demonstrated how thermal annealing in H_2S atmosphere is a viable route to convert $PtSe_2$ into chalcogen alloys or even into an almost-stoichiometric PtS_2 phases, which are isostructural with the pristine material. Moreover, under suitable process conditions, Se-to-S substitution occurs restricted to the outermost $PtSe_2$, leading to an ordered *Janus* type alloy. *Janus* dichalcogenide materials have been the object of many computational works but few synthesis have been proposed so far. By virtue of their vertical chemical asymmetry, they should possess extra properties with respect to their binary analogs, enabling a certain number of forbidden-by-symmetry quantum effects, for instance a Rashba effect.

Bibliography

[1] Y. Wang, L. Li, W. Yao, S. Song, J. Sun, J. Pan, X. Ren, C. Li, E. Okunishi, Y.-Q. Wang, *et al.*, "Monolayer $PtSe_2$, a new semiconducting transition-metal-dichalcogenide, epitaxially grown by direct selenization of Pt," *Nano letters*, vol. 15, no. 6, pp. 4013–4018, 2015.

[2] Z. Wang, Q. Li, F. Besenbacher, and M. Dong, "Facile synthesis of single crystal $PtSe_2$ nanosheets for nanoscale electronics," *Advanced Materials*, vol. 28, no. 46, pp. 10224–10229, 2016.

[3] M. Yan, E. Wang, X. Zhou, G. Zhang, H. Zhang, K. Zhang, W. Yao, N. Lu, S. Yang, S. Wu, *et al.*, "High quality atomically thin $PtSe_2$ films grown by molecular beam epitaxy," *2D Materials*, vol. 4, no. 4, p. 045015, 2017.

[4] T.-Y. Su, H. Medina, Y.-Z. Chen, S.-W. Wang, S.-S. Lee, Y.-C. Shih, C.-W. Chen, H.-C. Kuo, F.-C. Chuang, and Y.-L. Chueh, "Phase-engineered $PtSe_2$-layered films by a plasma-assisted selenization process toward all $PtSe_2$-based field effect transistor to highly sensitive, flexible, and wide-spectrum photoresponse photodetectors," *Small*, vol. 14, no. 19, p. 1800032, 2018.

[5] C. Yim, K. Lee, N. McEvoy, M. O'Brien, S. Riazimehr, N. C. Berner, C. P. Cullen, J. Kotakoski, J. C. Meyer, M. C. Lemme, *et al.*, "High-performance hybrid electronic devices from layered $PtSe_2$ films grown at low temperature," *ACS nano*, vol. 10, no. 10, pp. 9550–9558, 2016.

[6] W. Yao, E. Wang, H. Huang, K. Deng, M. Yan, K. Zhang, K. Miyamoto, T. Okuda, L. Li, Y. Wang, *et al.*, "Direct observation of spin-layer locking by local rashba effect in monolayer semiconducting $PtSe_2$ film," *Nature communications*, vol. 8, p. 14216, 2017.

[7] A. Avsar, A. Ciarrocchi, M. Pizzochero, D. Unuchek, O. V. Yazyev, and A. Kis, "Defect induced, layer-modulated magnetism in ultrathin metallic $PtSe_2$," *Nature nanotechnology*, p. 1, 2019.

[8] W. Zhang, H. T. Guo, J. Jiang, Q. C. Tao, X. J. Song, H. Li, and J. Huang, "Magnetism and magnetocrystalline anisotropy in single-layer $PtSe_2$: interplay between strain and vacancy," *Journal of Applied Physics*, vol. 120, no. 1, p. 013904, 2016.

[9] T. Hu, F. Jia, G. Zhao, J. Wu, A. Stroppa, and W. Ren, "Intrinsic and anisotropic rashba spin splitting in janus transition-metal dichalcogenide monolayers," *Physical Review B*, vol. 97, no. 23, p. 235404, 2018.

[10] O. J. Clark, F. Mazzola, J. Feng, V. Sunko, I. Marković, L. Bawden, T. K. Kim, P. King, and M. S. Bahramy, "Dual quantum confinement and anisotropic spin split-

ting in the multivalley semimetal $PtSe_2$," *Physical Review B*, vol. 99, no. 4, p. 045438, 2019.

[11] Q. Ma, M. Isarraraz, C. S. Wang, E. Preciado, V. Klee, S. Bobek, K. Yamaguchi, E. Li, P. M. Odenthal, A. Nguyen, *et al.*, "Postgrowth tuning of the bandgap of single-layer molybdenum disulfide films by sulfur/selenium exchange," *ACS Nano*, vol. 8, no. 5, pp. 4672–4677, 2014.

[12] Q. Feng, N. Mao, J. Wu, H. Xu, C. Wang, J. Zhang, and L. Xie, "Growth of MoS_2(1-−x)Se_2x (x= 0.41–1.00) monolayer alloys with controlled morphology by physical vapor deposition," *ACS Nano*, vol. 9, no. 7, pp. 7450–7455, 2015.

[13] H. Taghinejad, D. A. Rehn, C. Muccianti, A. A. Eftekhar, M. Tian, T. Fan, X. Zhang, Y. Meng, Y. Chen, T.-V. Nguyen, *et al.*, "Defect-mediated alloying of monolayer transition-metal dichalcogenides," *ACS Nano*, vol. 12, no. 12, pp. 12795–12804, 2018.

[14] A.-Y. Lu, H. Zhu, J. Xiao, C.-P. Chuu, Y. Han, M.-H. Chiu, C.-C. Cheng, C.-W. Yang, K.-H. Wei, Y. Yang, *et al.*, "Janus monolayers of transition metal dichalcogenides," *Nature nanotechnology*, vol. 12, no. 8, p. 744, 2017.

[15] J. Zhang, S. Jia, I. Kholmanov, L. Dong, D. Er, W. Chen, H. Guo, Z. Jin, V. B. Shenoy, L. Shi, *et al.*, "Janus monolayer transition-metal dichalcogenides," *ACS Nano*, vol. 11, no. 8, pp. 8192–8198, 2017.

[16] Y. Cheng, Z. Zhu, M. Tahir, and U. Schwingenschlögl, "Spin-orbit-induced spin splittings in polar transition metal dichalcogenide monolayers," *EPL (Europhysics Letters)*, vol. 102, no. 5, p. 57001, 2013.

[17] R. W. G. Wyckoff, *Crystal structures*. Krieger, 1964.

[18] B. Croset, Y. Girard, G. Prévot, M. Sotto, Y. Garreau, R. Pinchaux, and M. Sauvage-Simkin, "Measuring surface stress discontinuities in self-organized systems with x rays," *Physical Review Letters*, vol. 88, no. 5, p. 056103, 2002.

[19] S. Aminalragia-Giamini, J. Marquez-Velasco, P. Tsipas, D. Tsoutsou, G. Renaud, and A. Dimoulas, "Molecular beam epitaxy of thin $HfTe_2$ semimetal films," *2D Materials*, vol. 4, no. 1, p. 015001, 2016.

[20] P. Tsipas, D. Tsoutsou, S. Fragkos, R. Sant, C. Alvarez, H. Okuno, G. Renaud, R. Alcotte, T. Baron, and A. Dimoulas, "Massless dirac fermions in $ZrTe_2$ semimetal grown on InAs(111) by van der waals epitaxy," *ACS Nano*, vol. 12, no. 2, pp. 1696–1703, 2018.

[21] M. T. Dau, M. Gay, D. Di Felice, C. Vergnaud, A. Marty, C. Beigne, G. Renaud, O. Renault, P. Mallet, T. Le Quang, *et al.*, "Beyond van der waals interaction: The case of $MoSe_2$ epitaxially grown on few-layer graphene," *ACS Nano*, vol. 12, no. 3, pp. 2319–2331, 2018.

[22] J. Drnec, T. Zhou, S. Pintea, W. Onderwaater, E. Vlieg, G. Renaud, and R. Felici, "Integration techniques for surface x-ray diffraction data obtained with a two-dimensional detector," *Journal of Applied Crystallography*, vol. 47, no. 1, pp. 365–377, 2014.

[23] I. Robinson and D. Tweet, "Surface x-ray diffraction," *Reports on Progress in Physics*, vol. 55, no. 5, p. 599, 1992.

[24] T. Hahn, U. Shmueli, and J. W. Arthur, *International tables for crystallography*, vol. 1. Reidel Dordrecht, 1983.

[25] S. S. Grønborg, S. Ulstrup, M. Bianchi, M. Dendzik, C. E. Sanders, J. V. Lauritsen, P. Hofmann, and J. A. Miwa, "Synthesis of epitaxial single-layer MoS_2 on Au(111)," *Langmuir*, vol. 31, no. 35, pp. 9700–9706, 2015.

[26] C. Sanders, F. Arnold, R. Stan, A. Bruix, S. Mahatha, H. Lund, M. Dendzik, D. Curcio, H. Bana, E. Travaglia, *et al.*, "Realization of vanadium sulfide compounds in the 2D limit," *Bulletin of the American Physical Society*, 2018.

[27] C. E. Sanders, M. Dendzik, A. S. Ngankeu, A. Eich, A. Bruix, M. Bianchi, J. A. Miwa, B. Hammer, A. A. Khajetoorians, and P. Hofmann, "Crystalline and electronic structure of single-layer TaS_2," *Physical Review B*, vol. 94, no. 8, p. 081404, 2016.

Chapter 8

General conclusions

Conclusions and outlooks relative to the specific topics discussed along this thesis have been already reported in the final sections of the respective chapters. In this last chapter we would like to offer some more general and transverse considerations by comparing the different studied cases.

In chapter 5 we characterized the structure of three transition metal ditellurides, *i.e.* $ZrTe_2$, $MoTe_2$ and $TiTe_2$, for the first time grown on InAs(111). Due to the epitaxial constraints, they all grew with expanded in-plane lattice constants. The residual strain is thought to be at the origin of the stability of the found phases, which are either not yet observed, *e.g.* the triclinic stacking in $MoTe_2$, or not supposed to exist at room temperature, *e.g.* the γ-orthorhombic phase found in $MoTe_2$ or the $2 \times 2 \times 2$ periodic lattice distortion linked to a charge density wave phase in $TiTe_2$. Our results indicate that 2D vdW materials like TMDCs are not immune from the influence of the substrate, at variance to what could have been thought in the context of vdW epitaxy. Moreover, the coupling between a 2D TMDC and its substrate can be very strong, such that significant deformations can be induced within the 2D layer. $PtSe_2$/Pt(111) is a noteworthy example, where large displacements occur both in the 2D layer and in the substrate, and the atomic configuration adopted by Pt atoms during the selenization is preserved despite the partial or even complete substitution of the Se atoms by S, which is expected instead to reduce the Pt-chalcogen bonding length and contract the structure.

As in the case of the ditellurides studied here, the nature of the substrate is an important growth parameter, used to induce a particular structure in the growing material. However, the epitaxial constraints and in general the strong coupling between overlayer and substrates sometimes might prevent 2D materials from displaying the desired properties which would be present instead in an ideal freestanding layer. We demonstrated that intercalation of alkali atoms between MoS_2 and the substrate is a way to structurally decouple the TMDC from its support. However, the insertion of guest species - Cs in our case - between the substrate and the overlayer might not be without any effect, as we identified charge transfer from the intercalated Cs towards MoS_2. Further investigation could however overcome this sorts of effects, for instance by choosing intercalant species

which do not dope the host layer but allow restoring the freestanding properties of the bulk material.

All the systems investigated in this manuscript comply only partially with the ideal vdW epitaxy criteria we listed in chapter 2. In fact for all the cases reported in this manuscript significant residual strain values were found, sometimes accompanied by strong local lattice distortions. Moreover, the mosaic spread measured for our materials grown either on semiconducting substrates, InAs(111), or metallic ones, Au and Pt (111) surfaces, is significantly lower than those measured in similar compounds grown on top of other vdW materials, *e.g.* graphene, or insulator substrates such as AlN. It suggests that the overlayers are locked to their supports. These observations support the idea that in all the systems reported in this manuscript epitaxy has a certain covalent character, and cannot be purely vdW. However, the interaction strength can be much different from one case to the other. In three of the five systems we studied, *i.e.* $ZrTe_2$, MoS_2 and $PtSe_2$, a superstructure pattern - that can be described in an analogy with an optical moiré effect - has been found, although different features can be pointed out. In $ZrTe_2$ and MoS_2 diffraction in-plane maps, it manifests with few satellites around the substrate crystal truncation rods or Bragg peaks, whereas in $PtSe_2$/Pt(111) it is in the form of a very extended pattern where all the peaks at fractional indices are visible. Satellites are rather intense for MoS_2, very intense for $PtSe_2$, but quite weak in the $ZrTe_2$ pattern. Finally, the size of the superlattice unit cell, *i.e.* the superperiodicity length, is also different in the three cases: it is large a dozen of unit cells for $ZrTe_2$ and MoS_2, whereas it is rather small in the case of $PtSe_2$/Pt(111) and fits exactly with 3×3 $PtSe_2$ unit cells and 4×4 Pt(111) unit cells.

Comparative quantitative analysis, possibly supported by theoretical calculations, would be required to get an exhaustive understanding of these structures. Unfortunately, in the case of $ZrTe_2$ we do not have sufficient data to attempt this study of the structure, whereas in the case of MoS_2, analysis is computationally very demanding in reason of the very large supercell size and in turn of the high number of atoms and fitting parameters eventually needed in a model. However, a DFT analysis performed on the MoS_2/Au(111) structure in parallel with this work - the analysis is still in progress at the moment of writing and not reported here - shows that the lateral displacement of Au atoms in the outermost substrate layers are more important than those of Mo atoms within MoS_2. This result suggests that the displacements of the Au atoms would bring a dominant Fourier component in the diffraction diagram, explaining why the diffraction pattern is characterized by satellite peaks centered around the Au reflections.

In $PtSe_2$/Pt(111), according to our analysis, Pt displacements are significant both in the outermost substrate layer and in the $PtSe_2$ 2D layer, translating a more complex Fourier pattern, which explains the long range order superstructure with many peaks all over inside all the Brillouin zones close and far from the origin in reciprocal space. The unusual intensity of the satellite peaks in $PtSe_2$/Pt(111) is most probably a consequence of the large atomic displacement in the lattices, as we found in our refined model. Such

displacements might be connected with the short superperiodicity length imposed by 4:3 commensurability of $PtSe_2$ and Pt(111) lattice parameters, but also the direct consequence of the selenization process, which can be seen as a segregation of part of the selenium atoms (the bottom layer) under the Pt surface, implying a considerable atomic rearrangement on the surface.

The experimental investigations carried out during this thesis establish with a good confidence that the epitaxial growth of 2D materials cannot be simplified within the framework of an ideal van der Waals epitaxy. The partial covalent character of the interface bonding leads to strained materials with sometimes strong local lattice deformation, whose strength can largely vary from one system to the other, as already seen in the case of graphene. This in turn influences the electronic properties.

To conclude, we want to highlight that strong strained 2D epitaxial systems that possess a structural superperiodicity, as $PtSe_2$/Pt(111) and $MoSe_2$/Au(111) studied here, can have also modulated chemical reactivity. In fact, specific atomic sites can act as "hot spots" for chemical functionalization, nanopatterning and catalysis. SXRD is a powerful tool to solve atomically thin layer structures and predict or provide explanations for the chemical behaviour of 2D materials. Our work aims at inspiring new SXRD studies of epitaxial 2D systems, not only TMDCs, and possibly at spurring the development of more effective technologies and softwares for their characterization and analysis. Necessarily, a complete characterization of the structure of 2D materials should not be limited to the analysis of the in-plane deformations, as it is reported in this manuscript for $PtSe_2$. Vertical modulations of the structure are also expected whose information are contained in the diffraction rods. The work that we described in chapter 7 for $PtSe_2$ is still in progress, and we aim at improving our model with new fits of the diffraction rod data we measured. The same considerations are valid also for MoS_2/Au(111) and they can contribute to enrich our understanding of this system.